

**COMPUTATIONAL ASPECTS OF A MULTISCALE MODELING
APPROACH FOR HETEROGENEOUS MATERIALS UNDER
MULTIPHYSICS LOADINGS**

BY

MUHAMMAD USAMA SIDDIQUI

A Dissertation Presented to the
DEANSHIP OF GRADUATE STUDIES

KING FAHD UNIVERSITY OF PETROLEUM & MINERALS

DHAHRAN, SAUDI ARABIA

In Partial Fulfillment of the
Requirements for the Degree of

DOCTOR OF PHILOSOPHY

In

MECHANICAL ENGINEERING

DECEMBER 2016

KING FAHD UNIVERSITY OF PETROLEUM & MINERALS

DHAHRAN- 31261, SAUDI ARABIA

DEANSHIP OF GRADUATE STUDIES

This dissertation, written by **Muhammad Usama Siddiqui** under the direction of his dissertation advisor and approved by his dissertation committee, has been presented and accepted by the Dean of Graduate Studies, in partial fulfillment of the requirements for the degree of **DOCTOR OF PHILOSOPHY IN MECHANICAL ENGINEERING**

	
Dr. Zuhair M. Gasem Department Chairman	Dr. Abul Fazal M. Arif (Advisor)
	
Dr. Salam A. Zummo Dean of Graduate Studies	Dr. Bekir S. Yilbas (Member)
	
	Dr. Anwar Khalil Sheikh (Member)
Date	
	Dr. Nouari Saheb (Member)
	
	Dr. M. Kalimur Rahman (Member)

© Muhammad Usama Siddiqui

2016



Dedicated to my family

ACKNOWLEDGEMENTS

In the Name of Allah, the Most Beneficent, the Most Merciful.

Praise belongs to Allah, the Lord of all the worlds (2) The All-Merciful, the Very-Merciful. (3) The Master of the Day of Requital. (4) You alone do we worship, and from You alone do we seek help. (5) Take us on the straight path (6) The path of those on whom You have bestowed Your Grace, Not of those who have incurred Your wrath, nor of those who have gone astray. (7)

Al-Fatiha

I begin with the name of Allah, the most beneficent, the most merciful. May Allah bestow peace on our beloved Prophet Mohammed (*peace and blessings of Allah be upon him*), and his family. I would not have been able to complete this work without the help of Allah who endowed me with health, courage, aptitude and patience.

During this work my wife and parents were a constant source of motivation and support. Their prayers, love and encouragement helped me to arrive at this milestone.

I am thankful to *King Fahd University of Petroleum and Minerals* which gave me the opportunity to pursue a doctorate degree and also for all the support I received in carrying out this research.

I would like to express my gratitude to my dissertation advisor *Dr. Abul Fazal M. Arif* for all he taught me, for his patience when I couldn't get things done and for his help when I needed it. I am also very thankful to my dissertation committee members *Dr. Bekir S. Yilbas, Dr. Anwar K. Sheikh, Dr. Nouari Saheb* and *Dr. M. Kalimur Rahman* for their involvement and encouragement. I am immensely thankful to *Dr. Syed Sohail Akhtar* and *Dr. Khaled Al-Athel* for their help and valuable comments. I would also like to thank *Dr.*

Hakeem Abbas from Research Institute at KFUPM and *Dr. M. A. Morsi* from chemistry department, KFUPM for their help during the experimental work.

Special thanks to my friends and all my colleagues in the Mechanical Engineering department for making my time in KFUPM memorable and wonderful.

TABLE OF CONTENTS

ACKNOWLEDGEMENTS	v
TABLE OF CONTENTS	vii
LIST OF TABLES	xiv
LIST OF FIGURES	xvi
THESIS ABSTRACT (ENGLISH)	xxx
THESIS ABSTRACT (ARABIC).....	xxxii
CHAPTER 1 INTRODUCTION.....	1
1.1 Background and Motivation	1
1.2 Homogenization schemes	6
1.2.1 Computational Homogenization.....	7
1.2.2 Mean Field Homogenization	8
1.3 Multiscale Methods.....	9
1.4 Representative Volume Element.....	11
1.5 Objectives of the Work	12
1.6 Approach and Outline of Work.....	13
CHAPTER 2 LITERATURE REVIEW.....	17
2.1 Linear Elastic Materials	17
2.2 Rate-Independent Plasticity	22
2.3 Rate-Dependent Material Behavior	25
2.4 Failure and Damage Modeling.....	29
2.5 RVE Generation and Size Determination	33

2.5.1 RVE Generation	33
2.5.2 Size Determination	37
2.6 Effective thermal conductivity estimation	39
2.6.1 Effective thermal conductivity of nanocomposites	41
2.7 Summary of literature Survey	43
CHAPTER 3 COMPUTATIONAL MICROSTRUCTURE GENERATION	45
3.1 Introduction.....	45
3.2 Random Placement Algorithm.....	46
3.3 Particle Kinematics Algorithm	50
CHAPTER 4 COMPUTATIONAL HOMOGENIZATION: METHODOLOGY	
AND APPLICATIONS.....	58
4.1 Introduction.....	58
4.2 Computational Homogenization Methodology.....	61
4.2.1 Elasticity	65
4.2.2 Rate-independent plasticity	66
4.3 RVE Size Determination.....	70
4.3.1 Elasticity	72
4.3.2 Rate-independent plasticity	76
4.4 Experimental Work.....	78
4.5 Model Validation	82
4.5.1 Elasticity homogenization	82

4.5.2 Rate-independent plasticity homogenization	83
4.6 Case Studies	87
4.6.1 Elasticity	87
4.6.2 Rate-independent plasticity	91
4.7 Concluding Remarks.....	97
CHAPTER 5 MEAN-FIELD HOMOGENIZATION: METHODOLOGY AND APPLICATIONS	98
5.1 Introduction.....	98
5.2 Modeling methodology	101
5.2.1 Elastoplastic response of metal-matrix nanocomposites	101
5.2.2 Constitutive modeling of metal matrix.....	106
5.2.3 Effect of process parameters on matrix crystallite size	114
5.3 Results and Discussion	118
5.3.1 Measured properties	118
5.3.2 Modeling of pure nanostructured aluminum	122
5.3.3 Modeling of elastoplastic response of aluminum matrix-alumina inclusion nanocomposites.....	125
5.3.4 Modeling of elastoplastic response of spark plasma sintered alumina matrix nanocomposites	132
5.4 Conclusions.....	139

CHAPTER 6 GENERALIZED EFFECTIVE MEDIUM THEORY: FORMULATION AND APPLICATIONS.....	141
6.1 Introduction.....	141
6.2 Framework of the Generalized Effective Medium Theory	145
6.2.1 Effective medium theory for composite with multiple inclusions	145
6.2.2 Effect of nanometer-sized inclusions on matrix and inclusion thermal conductivities.....	147
6.2.3 Two-scale approach for non-uniformly distributed inclusions	154
6.3 Case Studies	161
6.3.1 Effect of nanometer sized inclusions.....	164
6.3.2 Effect of inclusion orientation	170
6.3.3 Effect of non-uniform dispersion of inclusions.....	172
6.4 Application to polymer matrix composites with hybrid inclusions	174
6.4.1 Validation results for polymer matrix nanocomposites	175
6.5 Application to spark plasma sintered hybrid nanocomposites.....	181
6.5.1 Effective thermal conductivity of polycrystalline matrix.....	181
6.5.2 Validation and Results.....	183
6.6 Conclusions.....	191
CHAPTER 7 MULTISCALE MODELING: FORMULATION AND IMPLEMENTATION	193
7.1 Introduction.....	193

7.2 Overall Multiscale Modeling Algorithm	195
7.3 Macroscale Modeling.....	197
7.3.1 Macro-Micro Scale Transition	198
7.4 Microscale modeling.....	201
7.4.1 Micro-Macro scale transition	201
7.4.2 Mean-field homogenization based microscale modeling	204
7.4.3 Computational homogenization based microscale modeling	209
7.4.4 Hybrid Approach to Microscale Modeling	212
7.5 Multiscale model implementation in MATLAB/COMSOL.....	216
7.5.1 Macroscale model.....	220
7.5.2 Microscale model for computational homogenization based and hybrid approach	223
7.5.3 MATLAB Functions	224
7.6 Case Studies	227
7.6.1 Uniaxial extension	228
7.6.2 Bending	232
7.6.3 Computational efficiency of multiscale algorithms	235
7.7 Conclusion	238
CHAPTER 8 MULTISCALE MODELING: APPLICATION TO THERMAL BARRIER COATING	239

8.1 Introduction.....	239
8.2 Constitutive modeling – Thermo-elasto-viscoplasticity of porous top coat	242
8.2.1 Mean-field homogenization of thermo-elasto-viscoplastic materials	242
8.2.2 Application to J ₂ -elasto-viscoplasticity and creep models	245
8.2.3 Implementation approach in FEM.....	247
8.2.4 Validation of methodology	250
8.3 Model formulation	253
8.3.1 Geometry and FE model.....	253
8.3.2 Loadings and boundary conditions.....	256
8.3.3 Material models	258
8.4 Results and Discussion	262
8.4.1 Simplified Model.....	262
8.4.2 Turbine blade model.....	268
8.5 Concluding Remarks.....	286
CHAPTER 9 PERFORMANCE MODELING OF MEMBRANES.....	288
9.1 Introduction.....	288
9.2 Permeability-Selectivity analysis.....	291
9.2.1 Circular pores with size distribution	292
9.2.2 Elliptical pores with size and aspect ratio distribution.....	294
9.3 Effect of pore geometry on membrane performance	295

9.4 Membrane stretching	300
9.4.1 Finite element model for membrane stretching.....	300
9.4.2 Finite element modeling results	306
9.5 Effect of stretching on membrane performance.....	309
9.5.1 Effect of porosity dispersion quality on membrane performance	311
9.6 Conclusion	315
CHAPTER 10 CONCLUSIONS AND RECOMMENDATIONS	316
10.1 Conclusions.....	316
10.2 Recommendations for Future Work.....	321
REFERENCES.....	322
VITAE.....	346

LIST OF TABLES

Table 1.1. Application to different heterogeneous materials	16
Table 4.1. Density measurements for sintered samples	80
Table 4.2. Validation of Elastic Property Homogenization.	82
Table 4.3. Elastic properties for Alumina-Aluminum composite	89
Table 4.4. Voce-type hardening law parameters for Al-Cu-Mg (2080) - SiCp-T8 composite.	96
Table 5.1. Summary of mechanical properties of sintered samples	118
Table 5.2. 0.2% Yield stress prediction for spark plasma sintered samples.	123
Table 5.3. Sample crystallite sizes used in grain growth model parameter estimation. .	133
Table 5.4. Grain growth model parameters	134
Table 6.1. Properties used for Ge-Si nanocomposite.....	164
Table 6.2. Properties for alumina, aluminum and MWCNTs.....	168
Table 6.3. Properties used for Epoxy-Hybrid CNT-GNP nanocomposite.....	176
Table 6.4. Properties used for Epoxy-Hybrid CNT-GNP nanocomposite.....	179
Table 6.5. Dense material thermal conductivities of sintered alumina samples.	184
Table 6.6. Material properties of inclusions used in estimation model.	186
Table 6.7. Predicted effective thermal conductivities of sintered hybrid nanocomposite samples.....	187

Table 7.1. Material properties used in multiscale simulation.	227
Table 8.1. Material properties used for model validation.	251
Table 8.2. Mechanical properties of bond coat [189].	258
Table 8.3. Mechanical properties of dense top coat [189].	258
Table 8.4. Mechanical properties of TGO layer [189].	259
Table 8.5. Mechanical properties of substrate [190].	259
Table 8.6. Creep parameters for TBC materials [191].	259
Table 8.7. Thermal properties of all materials [184].	261
Table 9.1. Material properties of dense PET used in finite element model.	304
Table 9.2. Size distribution parameters for stretched membranes.	307

LIST OF FIGURES

Figure 1.1. Examples of heterogeneous materials (a) Composite [1] and (b) Thermal barrier coating [2].	2
Figure 1.2. Multiscale nature of a TBC coated turbine blade.....	3
Figure 1.3. Approaches for constitutive modeling of heterogeneous materials.	5
Figure 1.4. Basic flowchart of homogenization based multiscale methods.....	10
Figure 1.5. (a) 2-dimensional RVE of porous membrane and (b) 3-dimensional RVE of particulate composite.	12
Figure 1.6. Graphical summary of all works carried out in the dissertation.....	14
Figure 2.1. CNT representative volume element [27].	20
Figure 2.2. Development of CNT/polymer nanocomposite RVE [28].	21
Figure 2.3. Homogenization of granular materials – Cosserat continuum modeling	23
Figure 2.4. Fritzen et al.’s three-scale methodology [37].	24
Figure 2.5. Concurrent multiscale methodology of Ghosh et al. [58]	30
Figure 2.6. 2D RVE for DP steel [62].	32
Figure 2.7. (a) Actual Al ₂ O ₃ microstructure (b) Al ₂ O ₃ microstructure in black and white and (c) computational RME.....	34
Figure 2.8. RVE generation methodology of Takano et al. [32]	35
Figure 3.1. Example computational microstructures with 1% porosity and (a) 2.5% reinforcement (b) 10% reinforcement and (c) 20% reinforcement.....	48

Figure 3.2. Examples of computational microstructures generated using Particle kinematics algorithm. [(a) and (b) represent the complete domain and inclusion particles respectively. (1), (2) and (3) represent volume fractions 10%, 20% and 30% respectively].	52
Figure 3.3. Example microstructures showing maximum packing arrangements. [(1) and (2) show 2 particles and 4 particles having packing factors of 0.68 and 0.74 respectively. (a) and (b) show unit cell and a 2x2 arrangement of the unit cell respectively].	53
Figure 4.1. Applying periodic boundary conditions to microscale RVE.	63
Figure 4.2. Homogenization methodology	64
Figure 4.3. Elasticity modulus variation with inclusion volume fraction for $E_{inc}/E_{mat} = 2$ with (a) 1% reinforcement (b) 5% reinforcement (c) 10% reinforcement (d) 15% reinforcement (e) 20% reinforcement and (f) 25% reinforcement.	73
Figure 4.4. Elasticity modulus variation with inclusion volume fraction for $E_{inc}/E_{mat} = 5$ with (a) 1% reinforcement (b) 5% reinforcement (c) 10% reinforcement (d) 15% reinforcement (e) 20% reinforcement and (f) 25% reinforcement.	73
Figure 4.5. Elasticity modulus variation with inclusion volume fraction for $E_{inc}/E_{mat} = 10$ with (a) 1% reinforcement (b) 5% reinforcement (c) 10% reinforcement (d) 15% reinforcement (e) 20% reinforcement and (f) 25% reinforcement.	74

Figure 4.6. RVE Size convergence for Elastic modulus having(a) 1% reinforcement (b) 5% reinforcement (c) 10% reinforcement (d) 15% reinforcement (e) 20% reinforcement and (f) 25% reinforcement	75
Figure 4.7. RVE Size convergence for elastoplastic material behavior having (a) 1% reinforcement (b) 5% reinforcement (c) 10% reinforcement (d) 15% reinforcement (e) 20% reinforcement and (f) 25% reinforcement.	77
Figure 4.8. Optical micrographs of Aluminum with (a) 5 wt.% Alumina and (b) 10 wt.% Alumina.	79
Figure 4.9. SEM micrographs showing alumina particles inside aluminum matrix for (a) 5 wt.% Alumina and (b) 10 wt.% Alumina.	79
Figure 4.10. Stress-strain behavior of the sintered samples under compression.	81
Figure 4.11. Validation of plastic property homogenization with experimental data.	84
Figure 4.12. Comparison of predicted stress-strain response of computational microstructures with (a) 10 inclusion particles, (b) 50 inclusion particles, (c) 100 inclusion particles and (d) 150 inclusion particles with experimental response for 10 wt.% alumina composite.	86
Figure 4.13. Displacement contours for the six load vectors used for finding the elasticity matrix (a) ϵ_{xx} (b) ϵ_{yy} (c) ϵ_{zz} (d) ϵ_{xy} (e) ϵ_{xz} and (f) ϵ_{yz}	88
Figure 4.14. Effect of inclusion volume fraction.	90
Figure 4.15. RVE for 10%Alumina-Aluminum composite with 100 Alumina particles.	91
Figure 4.16. Stress-Strain curve for 10% Alumina-Aluminum composite.	92

Figure 4.17. Effective plastic strains in the RVE when macroscopic strain is (a) $\varepsilon_{y,loc}$	
(b) $2\varepsilon_{y,loc}$ (c) $3\varepsilon_{y,loc}$ (d) $4\varepsilon_{y,loc}$ (e) $5\varepsilon_{y,loc}$ and (f) 0.05.....	93
Figure 4.18. Effective plastic strains in the RVE at critical point when macroscopic	
strain is (a) $\varepsilon_{y,loc}$ (b) $2\varepsilon_{y,loc}$ (c) $3\varepsilon_{y,loc}$ (d) $4\varepsilon_{y,loc}$ (e) $5\varepsilon_{y,loc}$ and (f)	
0.05.....	94
Figure 4.19. Effect of Inclusion volume fraction on stress-strain response of Al-Cu-Mg	
(2080) - SiCp-T8 composite.	95
Figure 5.1. Two-step mean-field homogenization approach.	102
Figure 5.2. Effective stress and tangent Modulus update algorithm for Mean-field	
homogenization.....	105
Figure 5.3. Modeling Hall-Petch effect using (a) equation (5.14) and (b) equation	
(5.15) for Aluminum using data from Tsuji et al. [138] (Dataset 1) and	
Yu et al. [139] (Dataset 2).....	109
Figure 5.4. Crystallite size dependence of Voce hardening law parameters for	
Aluminum using data from Khan et al. [131].	112
Figure 5.5. Crystallite size dependence of Voce hardening law parameters for	
Aluminum using data from Farrokh and Khan [133].	113
Figure 5.6. Grain size reduction of pure Al during ball milling.	116
Figure 5.7. Transition of matrix metal crystallite size from as-received powder to	
sintered sample.....	117

Figure 5.8. Optical micrographs of Al samples sintered from (a) as-received Al powder (b) 24 hours milled Al powder.....	119
Figure 5.9. Stress-strain response of sintered samples under compression.	121
Figure 5.10. Comparison of modeled elastoplastic response of Aluminum with (a) Khan et al.'s experiments [131] and (b) Farrokh and Khan's experiments [133].....	124
Figure 5.11. Crystallite size dependence of Voce hardening law parameters (a) s_0 and s_A and (b) m and ϵ_0 for spark plasma sintered Aluminum samples.	125
Figure 5.12. Comparison of hardening model with experimentally determined hardening behavior of spark plasma sintered Aluminum.	126
Figure 5.13. Comparison of modeled stress-strain response of spark plasma sintered samples with experimental results.	128
Figure 5.14. Effect of matrix crystallite size on stress-strain response of Al-Al ₂ O ₃ nanocomposite.	130
Figure 5.15. Effect of inclusion (a) volume fraction and (b) particle size on stress-strain response of Al-Al ₂ O ₃ nanocomposite.	131
Figure 5.16. Comparison of grain growth model predictions with experimental results. (a) Effect of sintering time on grain growth in pure Al. (b) Effect of inclusion volume fraction on matrix grain growth in Al-Al ₂ O ₃ nanocomposite for a sintering time of 20 minutes.	135

Figure 5.17. Effect of sintering time on the elastoplastic response of 24 hours milled (a) pure Al, (b) Al-2% Al ₂ O ₃ composite, (c) Al-10% Al ₂ O ₃ composite and (d) Al-15% Al ₂ O ₃ composite. Sintering temperature is 823 K.....	137
Figure 5.18. Effect of sintering temperature on the elastoplastic response of 24 hours milled (a) pure Al, (b) Al-2% Al ₂ O ₃ composite, (c) Al-10% Al ₂ O ₃ composite and (d) Al-15% Al ₂ O ₃ composite. Sintering time is 20 minutes.....	138
Figure 6.1. Inclusion geometries and orientation for (a) Minnich and Chen [86] (b) Ordenez-Miranda et al. [87] and (c) generalized EMT - Current work. (d) A schematic representation non-uniformly distributed inclusions – Current work (inclusion sizes are not to scale).....	144
Figure 6.2. Calculating $\Lambda_{coll}^{inc.i}$ for (a) prolate inclusion and (b) oblate inclusion.....	152
Figure 6.3. Variation of collision mean free path $\Lambda_{coll}^{inc.i}$ with angle $\theta_{inc.i}$	153
Figure 6.4. Two-scale methodology for effective thermal conductivity estimation.....	155
Figure 6.5. Distribution of Si nanoparticle volume fraction in Ge matrix.....	156
Figure 6.6. Distribution of the effective thermal conductivity in the RVE.	157
Figure 6.7. Verification of RVE size for computational homogenization.....	159
Figure 6.8. Finite element mesh for computational homogenization.	160
Figure 6.9. Comparison of model predictions with experimental results for Al ₂ O ₃ - SiC composite [156].	162

Figure 6.10. Comparison of model predictions with experimental results for SiO ₂ - CNT composite [157].	163
Figure 6.11. Predicted effective thermal conductivity of Ge-Si nanocomposite compared to Monte Carlo (MT) simulations [86].....	165
Figure 6.12. Effective thermal conductivity of (a) Alumina-MWCNT and (b) Aluminum-MWCNT nanocomposites.....	168
Figure 6.13. Modified (a) Alumina matrix and (b) Aluminum matrix thermal conductivities in MWCNT nanocomposites with randomly oriented CNTs.....	169
Figure 6.14. Dependence of Ge-Si effective thermal conductivity on inclusion alignment for inclusion aspect ratio p equal to (a) 0.2 and (b) 5.	171
Figure 6.15. Effect of non-uniform dispersion on Ge-Si effective thermal conductivity.....	173
Figure 6.16. (a) Effective thermal conductivity of Epoxy - Hybrid CNT-GNP nanocomposite of Yu et al. (2008) (b) Variation of critical exponent.....	177
Figure 6.17. Effective thermal conductivity of Epoxy- Hybrid CNT-GNP nanocomposite of Yang et al. (2011).....	179
Figure 6.18. Effective thermal conductivity of Epoxy- Hybrid BNNT-BNNS nanocomposite of Yang et al. (2014).....	180
Figure 6.19. Predicted thermal conductivity of alumina as a function of its average crystallite size.....	185

Figure 6.20. (a) Comparison of predicted thermal conductivities of sintered hybrid nanocomposite samples with experimentally measured values (b) Absolute errors in predicted thermal conductivities.	187
Figure 6.21. Effect of matrix crystallite size on the effective thermal conductivity of sintered hybrid nanocomposite samples.	188
Figure 6.22. Effect of (a) SiC and (b) CNT volume fractions on the effective thermal conductivity of sintered hybrid nanocomposite samples ($d=100\text{nm}$ and porosity fraction=0).	189
Figure 6.23. Effect of porosity fraction on the effective thermal conductivity of sintered hybrid nanocomposite samples.	190
Figure 7.1. Assumption in multiscale methodology (a) Scale Separation (b) Local periodicity	195
Figure 7.2. (a) Scaling methodology (b) FEM implementation scheme for the Multiscale model.....	196
Figure 7.3. Two-step mean-field homogenization approach.	205
Figure 7.4. Effective stress and tangent Modulus update algorithm for Mean-field homogenization.....	208
Figure 7.5. Applying periodic boundary conditions to microscale RVE.....	211
Figure 7.6. One dimensional example of the Newton-Raphson scheme for nonlinear problems using (a) updated stiffness at each iteration and (b) constant stiffness.	214
Figure 7.7. Mean-field homogenization based multiscale modeling methodology	217

Figure 7.8. Computational homogenization based multiscale modeling methodology ..	218
Figure 7.9. Hybrid multiscale modeling methodology	219
Figure 7.10. Modified stress-strain equations for macroscale model.	221
Figure 7.11. MATLAB stress functions calls defined in macroscale model.	222
Figure 7.12. MATLAB tangent modulus function call defined in macroscale model. ..	222
Figure 7.13. An example RVE geometry with 10 vol.% spherical inclusions.	223
Figure 7.14. MATLAB function to solve microscale problem.....	225
Figure 7.15. MATLAB function to return tangent modulus components using microscale model solution.	226
Figure 7.16. Modeled plate dimensions.....	227
Figure 7.17. Applied boundary conditions for uniaxial extension.....	228
Figure 7.18. Solution to the uniaxial tension problem using computational homogenization based multiscale model.	229
Figure 7.19. Solution to the uniaxial tension problem using hybrid multiscale model. .	229
Figure 7.20. Solution to the uniaxial tension problem using mean field homogenization based multiscale model.	230
Figure 7.21. Computational homogenization based multiscale algorithm RVE solution for Gauss point at coordinates (0.003028,0.005528). (a) von Mises stress (b) Normal stress in x-direction (c) Normal stress in z- direction (d) Normal stress in y-direction (e) Shear stress in xy- direction.	231
Figure 7.22. Applied boundary conditions for bending	232

Figure 7.23. von Mises stress distribution in the plate under bending. (a) Computational homogenization based algorithm (b) Hybrid algorithm and (c) mean-field homogenization based algorithm.....	233
Figure 7.24. Representative RVE solutions for the plate bending problem.	234
Figure 7.25. Simulation times for (a) uniaxial extension and (b) bending problems using computational homogenization (CH) based algorithm, hybrid algorithm and mean-field homogenization (MFH) based algorithm.	236
Figure 7.26. Effect of number of parallel microscale solution (NP) on simulation time using computational homogenization (CH) based algorithm and hybrid algorithm.	237
Figure 8.1. Iterative algorithm for the determination of homogenized stress, tangent modulus and stress-temperature tensor.	249
Figure 8.2. Finite element models for validation containing (a) 5% (b) 10% and (c) 20% secondary phase.	250
Figure 8.3. Validation of homogenization methodology. Cases (a)-(c) are for 5%, 10% and 20% viscoplastic-viscoplastic composite respectively and cases (d)-(f) are for porous viscoplastic materials with 5%, 10% and 20% porosity fractions respectively.	252
Figure 8.4. Actual turbine blade [188].....	254
Figure 8.5. (a) Simplified model (b) Model of actual turbine blade.....	254

Figure 8.6. (a) Schematic representation of the various materials in the coated blade	
(b) Arrangement of integration point through the thickness of layered shell elements.	255
Figure 8.7. Loading and boundary conditions on (a) simplified model (b) Turbine blade model.	257
Figure 8.8. Variation of ambient temperatures in convective boundary conditions.	257
Figure 8.9. Uniaxial tension test of porous top coat at a strain rate of 10^{-5} s^{-1} and a temperature of 1000°C . (a) von Mises stress (b) effective creep strain.....	260
Figure 8.10. Steady-state temperature drops across the TBC for various amounts of top coat porosities.	263
Figure 8.11. 1st principle stress in the bond coat at the TGO interface. (a), (b), (c) and (d) represent 0%, 10%, 20% and 30% porosity in the top coat. (1) and (2) represent results at the end of heating and the end of cooling.	265
Figure 8.12. 1st principle stress in the top coat at the TGO interface. (a), (b), (c) and (d) represent 0%, 10%, 20% and 30% porosity in the top coat. (1) and (2) represent results at the end of heating and the end of cooling.	266
Figure 8.13. Effective creep strain evolution during a single cycle in (a)topcoat (b) TGO and (c) bond coat using the simplified model (TC: top coat)	267
Figure 8.14. Steady-state temperature distribution on the top coat outer surface. (a), (b), (c) and (d) represent 0%, 10%, 20% and 30% porosity in the top coat.	269

Figure 8.15. Steady-state temperature distribution at the bond-substrate interface. (a), (b), (c) and (d) represent 0%, 10%, 20% and 30% porosity in the top coat.	270
Figure 8.16. Steady-state temperature distribution in the blade substrate. (a), (b), (c) and (d) represent 0%, 10%, 20% and 30% porosity in the top coat. .	271
Figure 8.17. Characteristic regions in a turbine blade.	272
Figure 8.18. Steady-state temperature distribution on (a) trailing edge, (b) the leading edge, (c) the suction side and (d) the pressure side.....	273
Figure 8.19. 1st principle stress in the bond coat at the TGO interface. (a), (b), (c) and (d) represent 0%, 10%, 20% and 30% porosity in the top coat. (1), (2) and (3) represent times at the end of initial cooling, at the end of heating and the end of final cooling.	275
Figure 8.20. 1st principle stress in the top coat at the TGO interface. (a), (b), (c) and (d) represent 0%, 10%, 20% and 30% porosity in the top coat. (1), (2) and (3) represent times at the end of initial cooling, at the end of heating and the end of final cooling.	276
Figure 8.21. Variation of 1st principle stress with time in the YSZ phase of top coat at a point on the trailing edge. (TC: top coat).....	278
Figure 8.22. Variation of 1st principle stress with time in the (a) top coat (b) TGO and (c) bond coat for TBC system with dense top coat at a point on the trailing edge.	279

Figure 8.23. Maximum tensile stress variation with number of thermal cycles for the YSZ phase of top coat. (TC: top coat).	280
Figure 8.24. Effective creep strain in the top coat at the end of final cooling. (a), (b), (c) and (d) represent 0%, 10%, 20% and 30% porosity in the top coat.	282
Figure 8.25. Effective creep strain in the TGO layer at the end of final cooling. (a), (b), (c) and (d) represent 0%, 10%, 20% and 30% porosity in the top coat.	282
Figure 8.26. Effective creep strain in the bond coat at the end of final cooling. (a), (b), (c) and (d) represent 0%, 10%, 20% and 30% porosity in the top coat.	283
Figure 8.27. Effective creep strain evolution at the trailing edge during a single thermal cycle in (a) top coat (b) TGO and (c) bond coat using the turbine blade model (TC: top coat).	284
Figure 8.28. Variation of 1st principle stress with time in the TGO layer at a point on the trailing edge. (TC: top coat).....	285
Figure 9.1. Microstructure of a (a) phase-inversion PES membrane (b) track-etched membrane [196].	289
Figure 9.2. Effect of pore aspect ratio on permeability-selectivity trade-off.....	298
Figure 9.3. Effect of pore size distribution on permeability-selectivity trade-off.	299
Figure 9.4. Membrane geometry with finite element mesh.	301
Figure 9.5. Applying periodic boundary conditions to a microscale RVE.....	304
Figure 9.6. Applied temperature and strain load.....	305
Figure 9.7. (a) Major and (b) minor axes size distribution for stretched membranes.....	307

Figure 9.8. Deformed geometries of stretched membranes for (a) 15% stretch, (b) 30% stretch, (c) 40% stretch and (d) 50% stretch.	308
Figure 9.9. Effect of membrane stretching on permeability-selectivity trade-off.	310
Figure 9.10. Porous membrane RVEs with controlled porosity dispersion.....	312
Figure 9.11. Normalized nearest neighbor distances in membrane RVEs with controlled porosity dispersion.....	313
Figure 9.12. Effect of porosity dispersion on permeability-selectivity trade-off for (a) 30% stretch and (b) 50% stretch.	314

ABSTRACT (ENGLISH)

NAME:	Muhammad Usama Siddiqui
TITLE:	Computational aspects of a multiscale modeling approach for heterogeneous materials under Multiphysics loadings
MAJOR FIELD:	MECHANICAL ENGINEERING
DATE OF DEGREE:	DECEMBER 2016

Modeling of heterogeneous materials at multiple length scales has developed in recent years. The main issue is in identifying the relationships which bridge these various length scales. The area of multi-scale modeling is concerned with developing the relationships between the various length and time scales. The main aim of multi-scale methodologies is to predict and quantify the macroscopic behavior of a material through the modeling of its micro- or nano-structure which may be heterogeneous, anisotropic and even multi-phase.

The aim of the current work is the formulation of methodologies for the property estimation and constitutive modeling of heterogeneous materials. To achieve this, computational tools for the determination of homogenized thermo-mechanical properties and constitutive behavior of heterogeneous materials have been developed and validated against experimental results. A multi-scale modeling approach has also been formulated that can utilize homogenization techniques to predict the constitutive response of materials at integration points of finite element models.

For the estimation of homogenized structural properties of heterogeneous materials, two homogenization methodologies namely computational homogenization and mean-

field homogenization, have been formulated, implemented and validated against experimental results for particulate composites. An improvement to the mean-field homogenization approach has been proposed to include the effect of nanometer sized inclusions, nanometer sized matrix grains as well as sintering parameters. Using the model, it was concluded that the matrix grain size reduction is the main strengthening mechanism for metal matrix nanocomposites.

For thermal conductivity estimation, a new generalized effective medium theory model has been formulated that is capable of including the effects of multiple nanometer-sized inclusions, orientations of inclusions, shapes of inclusions and the effect of non-uniformly dispersed inclusions. The model has been validated against experimental results for polymer matrix nanocomposites and spark plasma sintered ceramic matrix nanocomposites.

The thermo-mechanical homogenization approaches have also been used in the formulation and implementation of an efficient multiscale finite element model. The multiscale method has been used to study the thermo-mechanical performance of a turbine blade coated with thermal barrier coating as a function of varying levels of porosity in the top coat layer of the coating system. It is concluded that top coat porosity plays an important role in lowering the temperature of the turbine blade and relieving stresses in it. Additionally, the trailing edge of the blade has been identified as the critical region in the turbine blade.

ABSTRACT (ARABIC)

ملخص الرسالة

الإسم :	محمد أسامة صديقي
العنوان :	الجوانب التحسببية المتعلقة بطريقة البرامج التحسببية للمحاكاة متعددة المستويات المطبقة علي المواد الغير متجانسة والمعرضة لأحمال متنوعة
التخصص :	قسم الهندسة الميكانيكية
تاريخ منح الدرجة :	ديسمبر 2016

زاد الإهتمام في السنوات الأخيرة بالمستويات المختلفة للأبعاد المكانية التي تحكم ميكانيكا المواد، حيث يهتم الباحثون بإيجاد وتعريف العلاقات التي تربط بين هذه المستويات المختلفة من الأبعاد والأطوال، وذلك نسبة لأن مجال تصميم البرامج التحسببية للمحاكاة متعددة المستويات يعني بإيجاد هذه العلاقات بين المستويات البعدية والطولية المختلفة، وكذلك المستويات الزمنية المختلفة. الهدف الأساسي من الطرق المتبعة في هذا المجال هو حساب وتوقع سلوك المواد في المستوي المجهرى، وذلك عن طريق محاكاة هياكل هذه المواد في أبعاد صغيرة تصل إلي مايكروميتر أو حتي نانوميتر، وقد تكون المواد في هذا المستوي البعدي غير متجانسة، أو قد تكون خصائصها غير متساوية في كل الإتجاهات، كما أنها قد تحتوي علي عدة أطوار أو حالات مختلفة للمادة وليست حالة واحدة.

الهدف من هذه الدراسة هو تطوير طرق تحسببية يمكنها تقدير خصائص المواد، وإنشاء نموذج تحسبي تأسيسي قادر علي التعامل مع المواد الغير متجانسة. من أجل تحقيق أهداف هذه الدراسة تم تطوير أدوات تحسببية تقوم بحساب الخصائص الإلكتروميكانيكية المتجانسة للمواد الغير متجانسة، وتم التحقق من صحة هذه الأدوات التحسببية بمقارنة نتائجها مع قراءات أخذت من تجارب معملية. تم تطوير نموذج تحسبي ذو مستويات بعدية متعددة، بحيث يمكنه إستخدام الأدوات التحسببية الخاصة بحساب الخصائص المتجانسة التي تم تطويرها، والإستفادة منها في توقع وحساب سلوك المواد عند نقاط التكامل الخاصة بنموذج العناصر المنتهية.

من أجل تقدير الخصائص الهيكلية المتجانسة للمواد الغير متجانسة، تم تطوير طريقتين لحساب التجانس، الطريقة الأولى هي عملية التجانس التحسينية، والطريقة الثانية هي تجانس الحقل المتوسط، وكذلك تم تطبيق الطريقتين والتحقق من عملهما عن طريق المقارنة مع بعض القراءات العملية الحقيقية، وذلك للمواد المركبة الحبيبية. تم إقترح تطوير علي طريقة تجانس الحقل المتوسط بحيث تمكنها من توقع تأثير الحبيبات صغير الحجم للمادة ذات النسبة الأكبر في المواد المركبة والتي يصل قطرها الي عدة نانوميترات، والحبيبات ذات الحجم الصغير للمادة ذات النسبة الأقل في المواد المركبة أيضا ، وكذلك تأثير متغيرات عملية تصليب المواد من الباودر (sintering) . بإستخدام هذا النموذج التحسيني، تم الوصول للخلاصة التالية : أن تقليل حجم حبيبات المادة ذات النسبة الأكبر من عناصر المواد المركبة، له التأثير الأقوي في زيادة قوة المادة المركبة والتي يكون العنصر الأساسي فيها عبارة عن معدن.

لتقدير وحساب الموصلية الحرارية للمواد المركبة، تم تطوير نموذج جديد يستخدم طريقة تعميم المتوسط الفعّال، وهذه الطريقة الجديدة قادرة علي حساب تأثير الأحجام النانومترية الصغيرة لمختلفة لعناصر المواد المركبة في الموصلية الحرارية للمادة المركبة، وكذلك تأثير إتجاهات حبيبات عناصر المادة المركبة، وأشكالها، وكذلك تأثير هذه الحبيبات حتي إن لم تكن موزعة بانتظام في المادة المركبة. تم التحقق من عمل هذا النموذج التحسيني وذلك بمقارنة نتائج مع بعض التجارب العملية التي أجريت علي مادة مركبة نانومترية ذات عنصر أساسي من البوليمر، وكذلك علي مادة ذات عنصر أساسي من السيراميك، مصنعة بطريقة تصليب المواد من الباودر بإستخدام حرارة البلازما (SPS).

تم إستخدام طرق حساب الخصائص الميكانيكية الحرارية المتجانسة في تطوير وتطبيق نموذج عناصر منتهية متعدد المستويات. طريقة المستويات المتعددة تم أستخدامها لدراسة الأداء السلوك الميكانيكي الحراري الخاص بريشة توربين تم طلاؤها بطلاء عازل حراري يحتوي علي عدة أحجام من المسامات في الطبقة العليا للطلاء. من نتائج هذه الدراسة أن المسامية في الطبقة العليا من الطلاء تلعب دورا مهما في خفض درجة حرارة الريشة وبالتالي إزالة بعض الإجهادات الموجودة في الريشة. وكذلك من نتائج الدراسة أن الحافة الخلفية للريشة تعتبر من المناطق الحرجة في الريشة..

CHAPTER 1

INTRODUCTION

1.1 BACKGROUND AND MOTIVATION

Over the last few decades, the need for materials with application-optimized properties has increased dramatically. In many cases, materials found in nature, do not have the desired combination of properties which has led to the development of man-made materials. For example, in the aerospace industry which requires materials to satisfy the conflicting properties of high strength and low weight to minimize fuel consumption and still satisfy the minimum structural design criteria, heterogeneous materials are used. Heterogeneous materials are materials that are composed of several different materials (phases) or the same material in different states. Examples include composites, polycrystals, multilayered coatings, etc. Figure 1.1 shows microstructures of a ceramic composite and a multi-layered coating as two examples of heterogeneous materials.

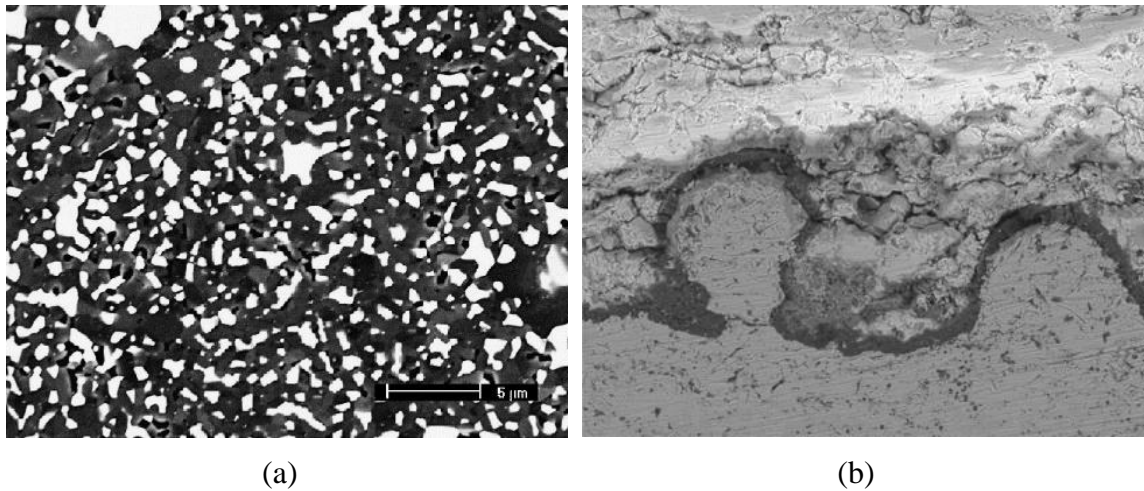


Figure 1.1. Examples of heterogeneous materials (a) Composite [1] and (b) Thermal barrier coating [2].

Heterogeneous materials allow the material designers to tailor their properties by incorporating different phases into the microstructure of the heterogeneous material. By introducing different phases, properties such as stiffness, strength, toughness, electrical and thermal conductivities can be improved. Since the length scale of the structures made from these heterogeneous materials is usually much larger than the characteristic lengths of the phases present in the materials, the performance of the materials needs to be determined considering these various length scale. Hence, these materials are considered as multiscale. An example showing the multiscale nature of heterogeneous materials is given in Figure 1.2. The figure shows a turbine blade coated with thermal barrier coating (TBC). TBC is composed of a multi-layer system to provide optimum thermo-mechanical performance. The length scale of the thickness of TBC layers is orders of magnitude smaller than the length scale of the turbine blade. The performance of the TBC coated turbine blade depends to details that exist in multiple length scales and therefore it is considered to be multiscale.

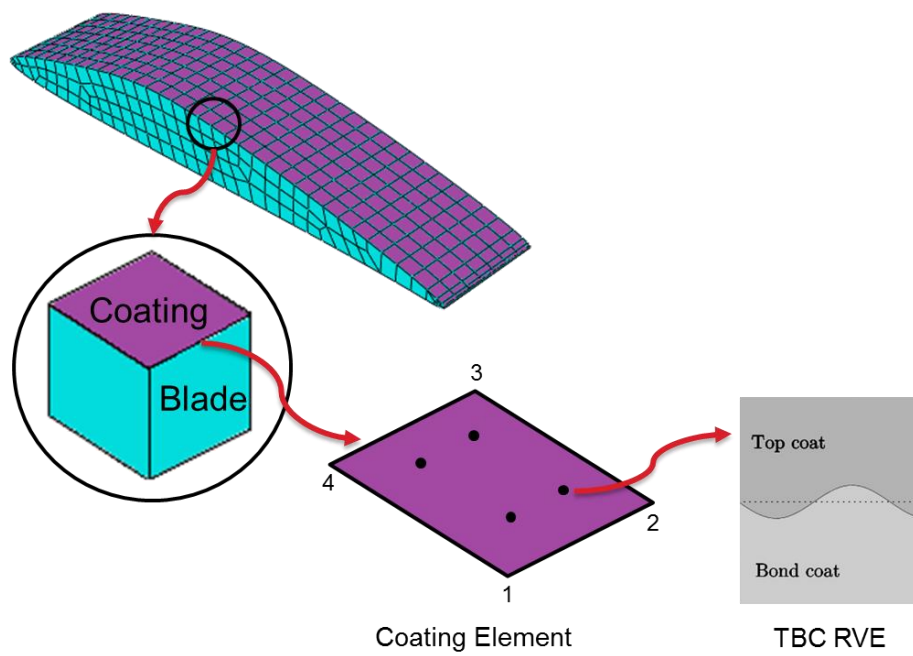


Figure 1.2. Multiscale nature of a TBC coated turbine blade.

The design and development of heterogeneous material with desired properties requires a careful control of the microstructure of the material and a thorough understanding of the effects of the microstructural parameters on its properties. Traditional methodology for designing these multiscale materials is through experimental trial and error. This method requires large amounts of experiments to be conducted to understand the microstructure-property relationships and for the optimization of desired properties. The use of computer modeling and simulation in the design of these materials can provide a supplementary tool to the experimental method that can help improve design times and lower costs by lowering the number of experiments that need to be conducted.

For material design and property estimation, computer modeling and simulation can be utilized in two different ways. The first method involves the determination of effective material properties and constitutive behavior of the heterogeneous material through the use of various homogenization techniques. These homogenized properties can then be used at the macroscale for analysis the performance of the macroscale structure. In the second method, the properties and constitutive behavior of the heterogeneous material are not explicitly determined. Rather, the simulation is performance on all related length scale. The three approaches for constitutive modeling of heterogeneous materials are shown graphically in Figure 1.3.

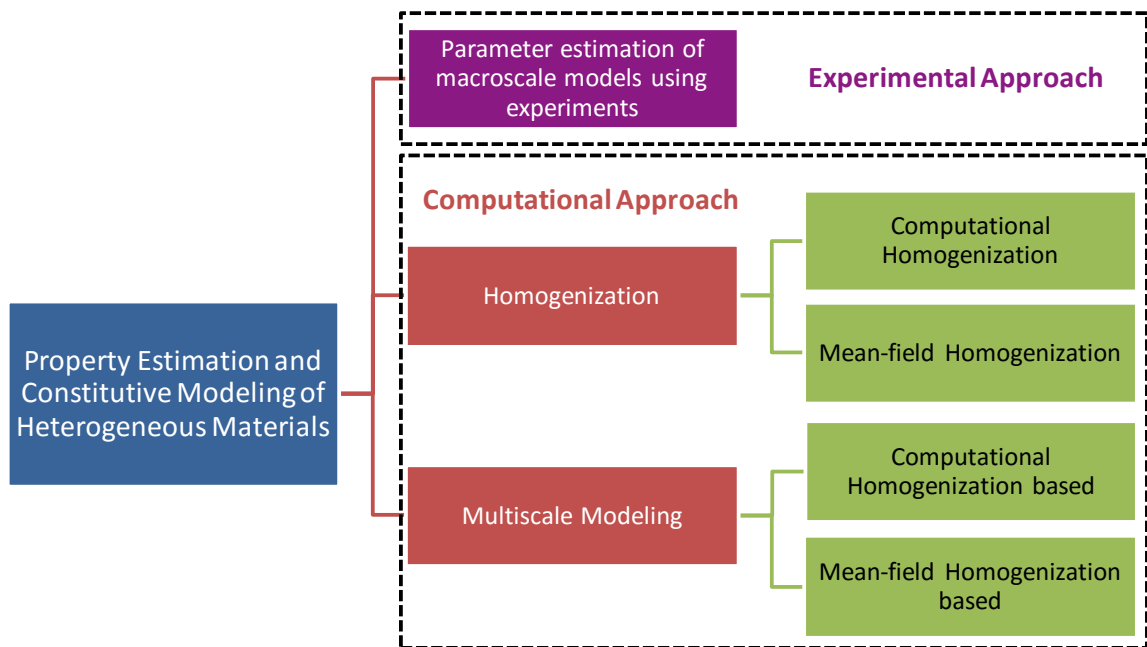


Figure 1.3. Approaches for constitutive modeling of heterogeneous materials.

1.2 HOMOGENIZATION SCHEMES

As discussed in the last section, heterogeneous materials have features that exist on multiple length scales. Homogenization refers to determination of effective properties at the larger scale (macroscale) using the information available at the lower scale (microscale). The first homogenization techniques were formulated for the determination of elastic properties of heterogeneous materials. These include methods such as the Voigt-Reuss bounds, the variational principle, the Mori-Tanaka scheme and the self-consistent scheme.

In the context of structural mechanical, the transition between micro- and macro-scales means the determination of effective stress and strain tensors using the microscale stress and strain fields. Such a transition is generally represented by equation (1.1)

$$\begin{aligned}\bar{\varepsilon} &= \frac{1}{V} \int \varepsilon dV \\ \bar{\sigma} &= \frac{1}{V} \int \sigma dV\end{aligned}\tag{1.1}$$

where σ is the Cauchy stress, ε is the true strain and the over-bar denotes homogenized values.

Application of methods such as finite element analysis at the macroscale requires the use of the constitutive behavior of the heterogeneous material. But the constitutive model $\bar{\sigma} = \bar{\sigma}(\bar{\varepsilon})$ is generally not easy to develop if one has to take the microstructural effects

into account. Various types of homogenization methods have been extensively employed in multiscale methods to describe the mechanical behaviors of real heterogeneous materials by taking into account the length scale difference between the macrostructure and the individual microstructure components. These homogenization schemes fall into two major categories: mean-field homogenization and computational homogenization. Both these techniques provide certain advantages and disadvantages when compared to the other. Computational homogenization provides the full-field of all concerned field variables within the microstructure. Therefore, it provides high level of details. On the other hand, the full-field solution takes high computational time compared to the mean-field homogenization techniques in which only the average value of each field variable is determined within each phase present in the microstructure. But, this improved in computational efficiency comes at the cost of level of details captured.

1.2.1 Computational Homogenization

In computational homogenization, the boundary value problem in micro-field fluctuation \tilde{w} given by equations (1.2) and (1.3) is solved.

$$\varepsilon = \bar{\varepsilon} + \nabla_x \tilde{w} \quad (1.2)$$

$$\nabla \cdot \sigma = 0 \quad (1.3)$$

In applying the boundary conditions, three things are possible. (i) \tilde{w} is set to zero throughout the domain, (ii) \tilde{w} is set to zero at the boundary or (iii) periodicity is assumed in which points on the opposite sides of the boundary with equal and opposite normal have

the same fluctuations. Therefore, the degrees of freedom offered to the domain and hence the compliance increase from condition (i) to condition (iii). Additionally, the constitutive relation for each phase present in the microstructure needs to be included in the solution.

Any appropriate numerical technique such as finite element method, Fourier series, meshless methods, etc. may be used to solve the problem. Once the microscale solution is completed, homogenization is carried out using equations (1.1) to determine the macroscale solution. An appropriate constitutive model can also be determined from the macroscale solution if required. Several authors have presented algorithms for the implementation of computational homogenization schemes using finite element method [3–5].

1.2.2 Mean Field Homogenization

In mean-field homogenization, only average solution fields, equations (1.4), in the microscale domain are determined. This is done by assuming the microscale domain as a system of inclusions particles embedded in a matrix.

$$\begin{aligned}\bar{\varepsilon} &= \frac{1}{V} \int \varepsilon dV = \frac{1}{V} \sum v_{\alpha} \langle \varepsilon \rangle_{\alpha} \\ \bar{\sigma} &= \frac{1}{V} \int \sigma dV = \frac{1}{V} \sum v_{\alpha} \langle \sigma \rangle_{\alpha}\end{aligned}\tag{1.4}$$

The seminal work for mean-field homogenization techniques was carried out by Eshelby [6] who determine the strain field in an ellipsoidal inclusion embedded in an infinite matrix. From his work, several techniques have been formulated such as the self-

consistent schemes originally suggested by Kroner [7], the scheme by Mori and Tanaka [8] and the Differential Method [9]. The basic working principle of all self-consistent methodology is the same. The first step in the homogenization is of strain localization in which the average strains within the phases of the heterogeneous material are determined using the macroscale strain. This is represented by equation (1.5). Once the localized strains are known, the constitutive behavior of the individual phases can be determined. The homogenized stress can then be determined using equation (1.4).

$$\varepsilon^\alpha = A_\alpha : \bar{\varepsilon} \quad (1.5)$$

where the tensor A_α is strain localization tensor that depends on the homogenization scheme.

1.3 MULTISCALE METHODS

In recent years, significant emphasis has been laid on multiscale modeling of heterogeneous materials in which the constitutive behavior at the larger scale is derived using either the full-field or mean-field solution of a boundary value problem at the lower scale and carrying out homogenization. Graphically, the method is presented in Figure 1.4.

The microscale problem is a classical boundary value problem for which any appropriate solution technique (mean-field homogenization or computational homogenization) may be used. At the macro-scale, the constitutive response is a priori unknown. Also, no assumptions are required at the macro level.

Multiscale methods work under two assumptions. The first assumption is of scale separation. According to this assumption, the macroscale and microscale model must exist on different length scale. The difference in the length scales needs to be large enough that the microscale model can be represented as a single material point in the macroscale model. The second assumption is of local periodicity. According to this assumption, the microstructure of the material and the associated RVE is assumed to be locally periodic. Although, the microstructure can be dependent on macroscale location.

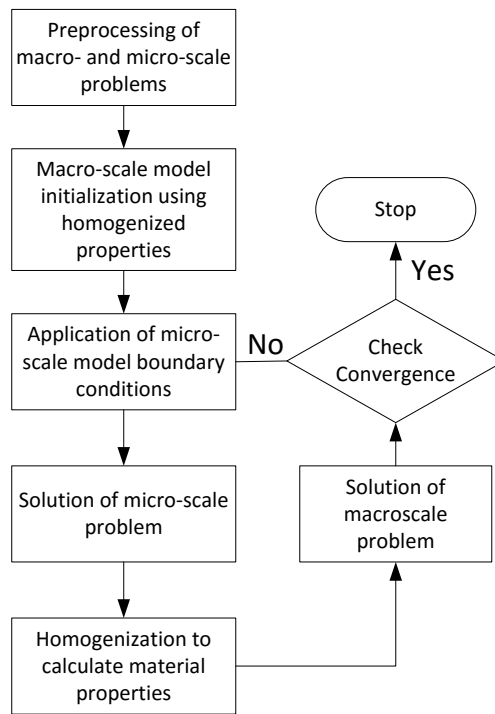


Figure 1.4. Basic flowchart of homogenization based multiscale methods.

1.4 REPRESENTATIVE VOLUME ELEMENT

The concept of the representative volume element (RVE) was first introduced by Hill [10] and since then it has found extensive applications in determining the properties of materials based on their microstructures [11–14].

It is defined as the minimal material volume that has the same properties as the bulk material. A basic property of the RVE is that increasing of this volume does not lead to changes in the predicted properties and the constitutive behavior of the material. The size of the RVE must be chosen sufficiently large compared to the characteristic length of the microstructure. The characteristic length could be the size of the grains if a polycrystalline material is being modeled. For composites, the characteristic length is usually taken as the size of the inclusion particles.

Determining the correct size of the RVE is a key issue in the use of computational homogenization methodologies. Ideally, the size of the RVE should be as small as possible to ensure good computational efficiency but large enough to be statistically representative of the material. Several authors have focused solely on this issue in order to understand the relationship between the prediction accuracy and the determination of correct RVE size based on application [11,15,16]. Once the RVE has been developed, it can then be used to study the mechanical behavior of the material at the microscale [13,14,17] or can be used in a multiscale approach to include the microstructural effects at the macroscale [18–20]. Two example RVEs are shown in Figure 1.5.

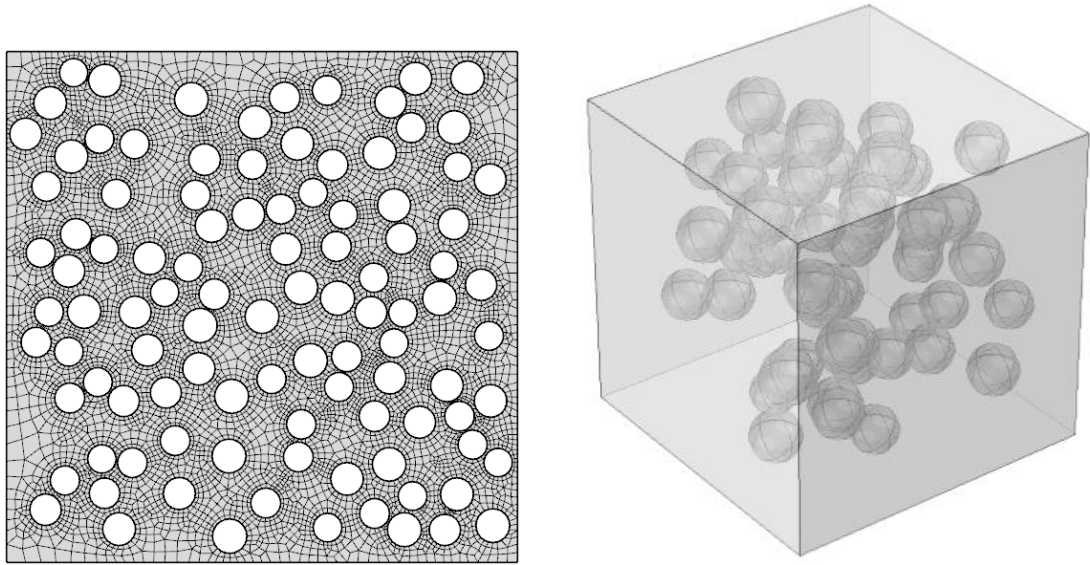


Figure 1.5. (a) 2-dimensional RVE of porous membrane and (b) 3-dimensional RVE of particulate composite.

1.5 OBJECTIVES OF THE WORK

The objectives of the work include the following.

1. Development of computational tools capable of predicting mechanical and thermal properties of heterogeneous materials.
2. The formulation and implementation of a computationally efficient multiscale methodology capable of predicting the multiphysics response of heterogeneous materials.
3. The demonstration of the effectiveness of the developed methodologies for various applications such as coatings, membranes and composites.

1.6 APPROACH AND OUTLINE OF WORK

The current work involves the formulation of methodologies for the property estimation and constitutive modeling of heterogeneous materials and the application of these methodologies to novel applications such as nanocomposites, coatings and membranes. In view of the objectives, the work has been divided into two main parts. In the first part, methodologies for the determination of homogenized material properties and constitutive behavior of heterogeneous materials have been presented. Several applications of the formulated methodologies have also been presented. In the second part, the homogenization techniques implemented in the first part are used for the formulation of multiscale modeling methodologies. An application of the multiscale method to the thermo-mechanical modeling of a turbine blade coated with thermal barrier coating is also presented. A graphical summary of all works carried out in the dissertation are presented in Figure 1.6 which also shows how the various works are inter-connected.

All modeling approaches presented in the current work are formulated under the assumption of continuum materials. As such, these approaches are only valid as long the continuum assumption holds. If the system under consideration does not satisfy the continuum assumption, the use of the formulated methodologies can lead to large errors in the predictions.

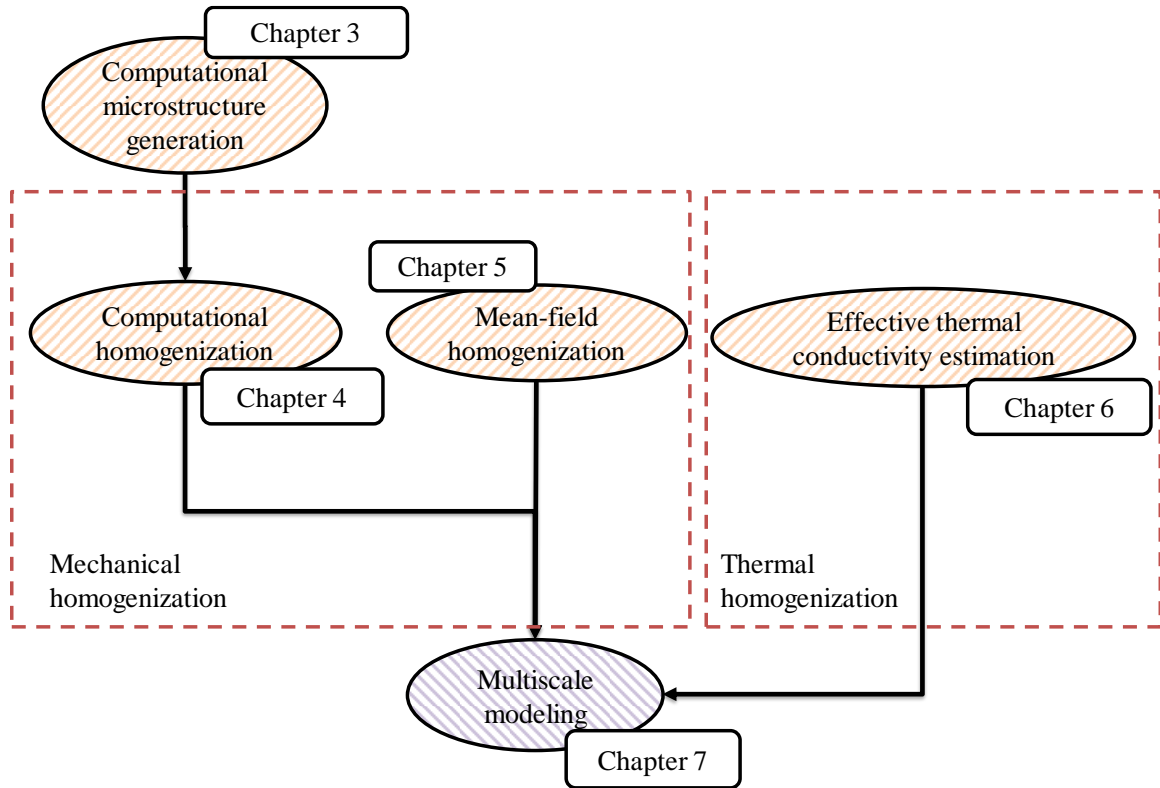


Figure 1.6. Graphical summary of all works carried out in the dissertation.

The dissertation is organized into a total of 10 chapters. Each chapter has been written in a way that it can be read independently. Chapter 2 presents a literature review of homogenization methodologies and multiscale modeling approaches for various types of material behaviors. Chapter 3 presents the algorithms used for generating computational microstructures of heterogeneous materials which are needed in carrying out computational homogenization. In chapter 4, the computational homogenization approach is presented along with an application to elasticity and elastoplasticity of particulate composites. The chapter presents the complete work flow that needs to be adopted for carrying out computational homogenization including RVE generation, its size determination and property estimation. In chapter 5, a mean-field homogenization approach is presented. The presented formulation extends the mean-field homogenization approach to metal-matrix particulate nanocomposites incorporating the effects of inclusion particles and matrix crystallite size. Chapter 6 presents the generalized effective medium theory for the estimation of effective thermal conductivity of particulate nanocomposites. The presented formulation extends the effective medium theory to multi-inclusion nanocomposites with randomly oriented particles and non-uniform dispersion. In chapter 7, the multiscale methodology is presented. The computational efficiency and accuracy of three different multiscale models have been analyzed and compared in this chapter. Chapter 8 presents the multiscale modeling of a turbine blade coated with thermal barrier coating. Chapter 9 presents an application of the RVE generation algorithm in modeling polymeric ultrafiltration and microfiltration membranes. The generated membrane microstructures have been used to analyze the effect of membrane stretching on the permeability-selectivity

tradeoff of ultrafiltration and microfiltration membranes using a new formulated model. Finally, the conclusions and recommendations for possible future work are presented in chapter 10. All the applications of the current work are presented in Table 1.1.

Table 1.1. Application to different heterogeneous materials

Application		Computational Technique	Purpose	Chapter
Composites	Metal matrix composite	Computational homogenization	Elastic and Elasto-plastic constitutive behavior	4
	Metal matrix nanocomposites	Mean field homogenization	Elasto-plastic constitutive behavior	5
	Ceramic and polymer matrix nanocomposites	Effective medium theory	Effective thermal conductivity	6
Coating	Thermal barrier coating	Multi-scale modeling	Effect of top coat porosity on thermo-mechanical performance	8
Membrane	Micro- and ultra-filtration membranes	Computational microstructure generation	Effect of stretching on membrane performance	9

CHAPTER 2

LITERATURE REVIEW

This chapter presents a literature review to establish the state-of-the-art of the homogenization schemes and multiscale modeling of various types of constitutive behaviors of heterogeneous materials.

2.1 LINEAR ELASTIC MATERIALS

Cho et al. [21] used computational homogenization to determine the thermoelastic properties for regular and random microstructures. They generated computational two phase RVEs using the random morphology description function (RMDF) similar to Vel and Goupee [22]. They used the developed computational RVEs to determine the homogenized properties, study the effect of variations in particle shapes and orientation on the orthotropic properties and to study the response of a beam composed of a dual phase material. For determining the homogenized properties, Cho et al. utilized the principle of superposition by applying two sets of boundary conditions in order to determine the homogenized orthotropic properties.

Griffiths et al. [23] Monte-Carlo simulations to study the effect of porosity fraction and pore size of the effective elastic properties of geomaterials. They evaluated the elastic modulus and Poisson's ratio using a finite element model. Using the developed model, a probabilistic analysis of the elastic properties of the material was carried out using Monte-Carlo simulations. They later extended the methodology to foundation problems involving a footing on an elastic foundation containing voids.

Dong and Bhattacharyya [24] used two dimensional RVE models along with finite element simulations to estimate the elastic moduli of clay/polymer nanocomposites. They studied the influence of parameters such as clay content, clay aspect ratios, dispersion patterns as well as the interphase material properties on the material behavior. Two dimensional FE models were developed in ANSYS with the clay platelets represented as unidirectional. Several arrangements of the platelets were considered: periodic, staggered and random. All constituents were considered as isotropic and linear elastic. Virtual uniaxial tests were performed to find out the elastic modulus of the nanocomposites as follows.

$$E_c = \frac{\sigma}{\varepsilon_o} = \frac{\sum_{i=1}^n F_i}{\varepsilon_o (1)(3b)} = \frac{\sum_{i=1}^n F_i}{3b\varepsilon_o} \quad (2.1)$$

The elastic modulus was defined as the average stress divided by the average strain where the average stress was calculated in terms of the nodal forces at the boundary.

An adaptive multiscale methodology was presented by Vernerey et al. [25]. The main objective for their methodology is to find the optimum balance between numerical and homogenization accuracies. Numerical accuracy improves as the element size reduces while homogenization accuracy improves when RVE size increases. Among the two of these, the RVE size is usually governed by the microstructural features and the material behavior that is being modeled while the element size can be adjusted as required. Vernerey et al. suggest that when the element size is sufficiently larger than the RVE size, effective properties obtained through the computational homogenization of the RVE can be used. This is in agreement with the discussions by Geers et al. [26] on computational homogenization which put restriction on the maximum size of the RVE allowed. But if the element size and the RVE size comparable, the microstructure itself needs to be included in the macroscale model. Therefore, in some regions in the macroscale models, multiscale methods are used to determine the effective constitutive behavior of the materials while in other regions, the microstructural features are directly included in the macroscale model.

The alternative to using computational homogenization is mean-field homogenization approaches which for linear elastic materials have matured significantly for the decades and can be confidently used for the property estimation of elastic heterogeneous materials. A good comparison of various mean-field homogenization methods for determining the effective material properties is presented by Klusemann and Svendsen [9] in which they carried out comparisons of the several classical schemes including Mori Tanaka model, Hashin-Shtrikman bounds, the Lielens method and the self-consistent scheme and two relatively new schemes, the effective self-consistent scheme and the Interaction direct

derivative method, with direct FE simulation results. Their results showed that the interaction direct derivative method provided the best results.

Ayatollahi et al. [27] developed models for predicting the nonlinear constitutive behavior of single-walled CNTs using finite element simulations. They also developed an equivalent beam element for studying SWCNTs and developed a representative volume element for modeling the mechanical behavior of CNTs under tensile, bending and torsional loads. The RVE consisted of the equivalent CNT element surrounded by an interphase region and the matrix as shown in Figure 2.1.

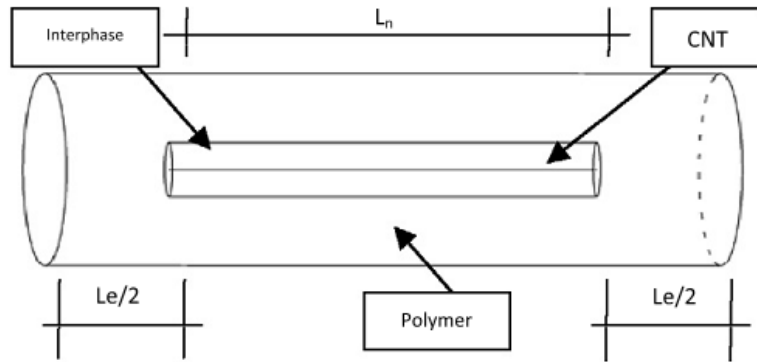


Figure 2.1. CNT representative volume element [27].

Tserpes et al. [28] developed a multiscale RVE for modeling CNT/polymer nanocomposites. The proposed approach started by finding a nonlinear equivalent continuum stress-strain response of individual CNTs using molecular dynamics simulations, finite element analysis and polynomial curve fitting. The CNT/polymer composite is then represented by a RVE in which the CNT is represented by beam elements which are surrounded by solid elements for matrix material. The steps are shown

graphically in Figure 2.2. Tserpes et al. also included the effect of interfacial debonding in their model. This was done by comparing the shear stress on the CNT-polymer interface with the interfacial shear strength (ISS) of the composite and removing the elements for which the shear stress exceeded the ISS.

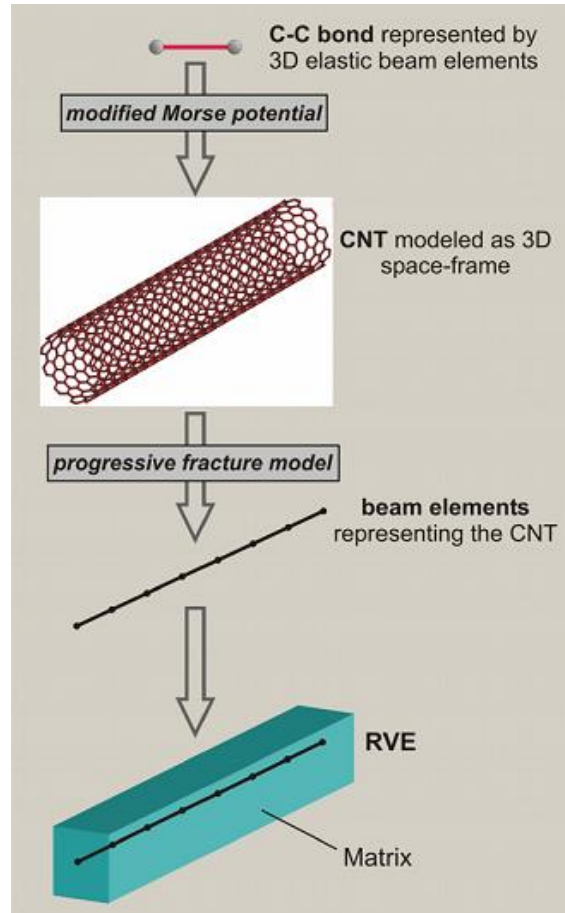


Figure 2.2. Development of CNT/polymer nanocomposite RVE [28].

Liu and Chen [12,17] used computational homogenization to determine the effective elastic properties of CNT nanocomposites. In their work, they considered cylindrical RVEs containing single CNTs of various lengths. Using continuum mechanics, they formulated

a methodology to estimate the effective properties of the nanocomposite and used finite element method with three sets of boundary conditions to calculate these properties.

Ni and Chiang [29] developed a homogenization process to predict the anisotropic elastic properties heterogeneous materials. They considered only the microstructure of the constituents in the media to be highly interconnected and correlated instead of having dispersed inclusions. They adapted the phase-field micro elasticity model of Wang et al. [30] to attain the eigenstrain field which is then used in the homogenization process. The homogenization approach is therefore based on the work of Eshelby [6].

Takano et al. [31,32] used asymptotic expansion homogenization method to predict the elastic properties of porous Alumina and found the predict values to have about 1% error when compared with the experimentally measured values. They later used the homogenization method in a two-scale model to simulate the four-point bending test.

2.2 RATE-INDEPENDENT PLASTICITY

Galli et al. [20,33] used computational homogenization for studying the elasoplastic response of metal-matrix particulate composites. Their work comprised a methodology for the generation of computational RVEs and the homogenization of the thermoelastic and plastic properties of the composites. For the generation of the computational RVE, Galli et al. developed an algorithm to introduce reinforcement particles into the mesh instead to meshing a geometry containing the particles in a matrix.

Li et al. [34] presented the Hill's lemma for the macro-micro homogenization of gradient-enhanced Cosserat media. As seen in the work of Kousnetsova et al. [3] for the gradient enhanced multiscale methods, not only stresses and strains but also their gradients are transferred from one scale to another. Using the Hill's lemma for Cosserat media, conditions for applying kinematic, static and mixed boundary conditions on the microscale model are derived and are shown to satisfy both the Hill's lemma as well as the average field conditions. In [35], Li et al. used their gradient-enhanced homogenization method [34] for the homogenization of discrete particle assemblies represented by equivalent Cosserat continuum as shown in Figure 2.3.

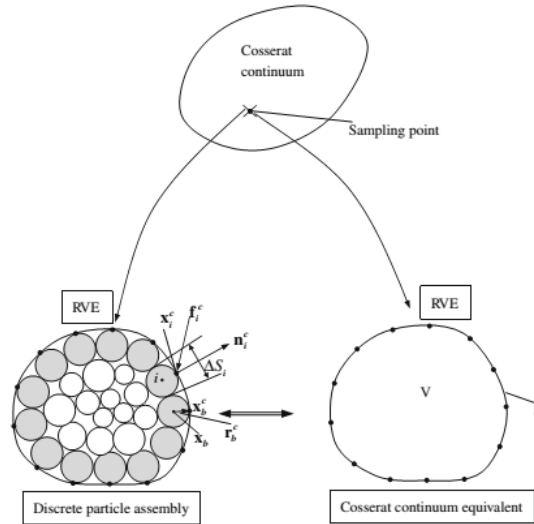


Figure 2.3. Homogenization of granular materials – Cosserat continuum modeling

Fritzen et al. [36] used computational homogenization methodology to study the macroscopic constitutive behavior of porous materials with spherical porosities. They compared the results of the computational homogenization with the results of analytical

model and found that the results were close for small porosity volume fractions. In [37], Fritzen et al. extended their work to study the asymptotic stress response of Green-type porous materials and to calculate the effective yield surface as a function of the microscale material behavior and porosity fraction. They developed a two-scale model as assumed scale separation between the two scales. At the microscale, the materials were assumed to be incompressible while at the macroscale, compressibility of the materials was present due to the presence of porosity. Fritzen et al. extended their model to a three-scale model in order to account for porosity at two different scales. The three-scale methodology is presented in Figure 2.4.

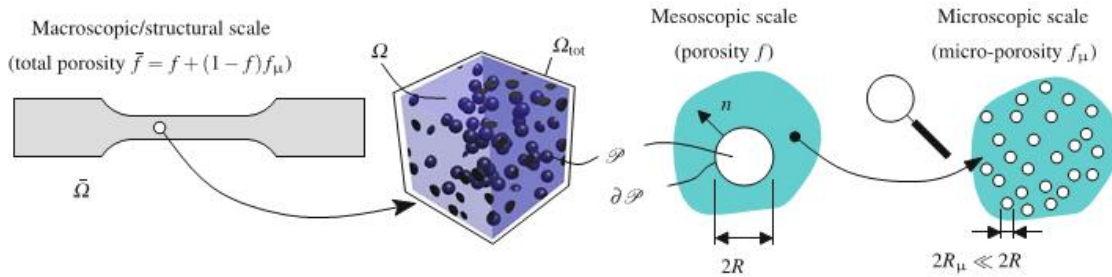


Figure 2.4. Fritzen et al.'s three-scale methodology [37].

Danas and Aravas [38] presented a multiscale methodology to model the rate-independent elasto-plastic response of porous materials at finite deformations. The methodology is based on a self-consistent mean-field homogenization technique capable of predicting not only the constitutive behavior of the materials but also the evolution of the microstructure. The microstructure is defined by general ellipsoidal pores which result in the material behaving anisotropically.

Brenner [39] used augmented Lagrangian fast Fourier transform to solved for the homogenized material properties of composites with coupled constitutive laws. He considered the case of a piezoelectric material and solved for the overall response of the material. As possible applications, he applied the developed methodology on porous materials and fiber-reinforced composites and validated the methodology by comparing it with experimental results.

Doghri et al [40] used mean field homogenization schemes to predict the elastoplastic response of two-phase composite materials under small strain conditions. They compared their results with the results of direct numerical simulations. They also tried several methods for the calculation of tangent moduli and studied their influence on the results.

Yuan and Fish [41] presented a methodology for the implementation of computational homogenization based multiscale models in ABQUS CAE using user defined functions. There model utilizes the ABAQUS FE solver to solve the macroscale as well as the microscale problems and couples the two at macroscale integration points using a user defined material (UMAT) subroutine. In order to validate the developed methodology, they compared the results of the two-scale model with the results of a single-scale model that used a very fine mesh and found good agreement between the two.

2.3 RATE-DEPENDENT MATERIAL BEHAVIOR

For the multiscale modeling of rate-dependent material behavior, relatively little work has been done. Like other material behaviors, the works can be divided in two main

approaches. These are computational homogenization for effective material properties [42–46] or complete multiscale models [47–51].

Benseddiq et al. [42] used computational homogenization to determine the effective hyperelastic-viscoplastic material behavior of rubber toughened polymers. They used a simple single particle reinforced unit cell as the microscale mode. The hyperelastic material behavior was modeled using the Money-Rivlin model while a power-law type model was used for viscoplastic strain rate. They studied the effect of rubber volume fraction, strain rate as well as rubber cavitation on the effective properties of the RT polymers.

Haasemann and Ulbricht [43] used computational homogenization to find effective viscoelastic and viscoplastic material models for composite materials. In order to find the relaxation tensors required in the viscoelastic material model, the Laplace-Carson transformation was applied to the material models of all microscopic constituent phases, the homogenization relaxation in the s-domain were determined and the inverse transforms were applied. For viscoplastic materials, an addition step of linearization was required which was carried out using affine formulation. The homogenized material response was then calculated incrementally.

Ohno et al. [44] used computational homogenization to develop an effective constitutive model for pore-pressurized open-pore metallic structures under small strains and finite deformations. In their work, they provided equations to calculate macroscale stresses and strains using microscale solutions for the case when porosity and pore pressure exists. Using the effective stress and strains, relations were described for macroscale

viscoplastic strain rate which were verified by comparing the results with direct FE simulations.

van der Sluis et al. [45] used computation homogenization to find effective properties of elasto-viscoplastic materials and used it to find the effective material properties of a porous material. In their work, van der Sluis used the Perzyna's model for viscoplasticity along with the von Mises yield criterion and have presented a complete iterative implementation strategy for the microscale material model in finite element environment. Using the microscale model and computational homogenization, the macroscale stress-strain behavior was predicted and used to calculate the effective material properties of the material.

Tsuda et al. [46] also used computational homogenization to determine an effective constitutive model of a plate-fin structure and validated the developed macroscopic model against homogenized stress-strain response.

Carrere et al. [47] used multiscale modeling to predict the material behavior of SiC reinforced Titanium MMCs. Their model took into account the viscoplastic behavior of Titanium and the interfacial behavior between the SiC particles and the matrix. The interfacial behavior was modeled using a cohesive zone model whose parameters were determined by the authors experimentally. The stress localization step carried out in the work took into account the inelastic material behavior, thermal effects and damage. The homogenization step used was the standard volume-averaging method.

Feyel and Chaboche [48] used multiscale finite element analysis to model the elasto-viscoplastic material behavior of SiC-Ti composites. Standard volume averaging methods were used to carry out homogenization. They used the perturbation method for the calculation of the consistent tangent modulus. As applications of the developed mode, four-point bending test and a rotor subjected to centrifugal loading were simulated.

In another work, Feyel [49] presented a multiscale modeling methodology for generalized continua which are important when the assumption of scale separation does not hold. As an example, they showed the application of the methodology for Corresat media and presented the required localization and homogenization equations. It is important to note here that the generalized continuum is only used at the macroscale and the microscale model still uses the classical continuum.

Khan and Muliana [50] developed a multiscale model of functionally graded viscoelastic materials under thermomechanical loadings. In their work, they developed equations of effective thermo-mechanical properties and developed a methodology for the multiscale solution of the stresses and temperature distribution in the thermomechanical problem.

In [52,53], Doghri et al., presented the affine homogenization schemes for the homogenization of heterogeneous materials with viscoplastic phases. Their methodology involved the linearization of the constitutive behavior of the viscoplastic materials using the affine relationship. They also presented a general solution for the affine strain increment that can be applied to any viscoplastic model.

Molinari et al. [54–57] presented a homogenization scheme for the homogenization of heterogeneous materials with viscoplasticity. Their main contribution was the interaction law which can be used to determine the relationship between the macroscale strain rates and localized strain rates in the matrix and the inclusions. The interaction law can be used in conjunction with self-consistent or Mori-Tanaka approaches to homogenization for determining the homogenized properties of polycrystalline materials and composites respectively.

Matou and Maniatty [51] developed a multiscale model too predict the hyperelastic-viscoplastic behavior of polycrystalline materials undergoing finite deformations. In their work, the authors focused on the formulation of the multiscale finite element problem using variational methods and the development of an implementation scheme for the method. In order to show the capability of the model, the authors used the model to predict the macroscale stress strain response and the texture evolution of an aluminum alloy under plane strain and simple shear loading and compared their results with those predicted by Taylor’s approach.

2.4 FAILURE AND DAMAGE MODELING

Ghosh et al. [18] developed an adaptive concurrent multi-level methodology for the multiscale analysis of elastic composites and extended the model to include damage initiation and growth in [58]. They divided their entire solution domain into three different types of levels of computation: level-0 for homogeneous macroscopic analysis, level-1 for

asymptotic homogenization using microscopic RVE and level-2 for pure microscopic analysis. Level-1 in the methodology served as a bridge between the purely macroscopic level-0 and purely microscopic level-2. They defined criteria for switching from level-0 to level-1 and from level-1 to level-2. The various levels of computation in the multiscale methodology of Ghosh et al. is shown in Figure 2.5. The methodology of Ghosh et al. allows the study of composites in which localization is occurring in an efficient manner since the detailed analysis is carried out only in regions of high localization.

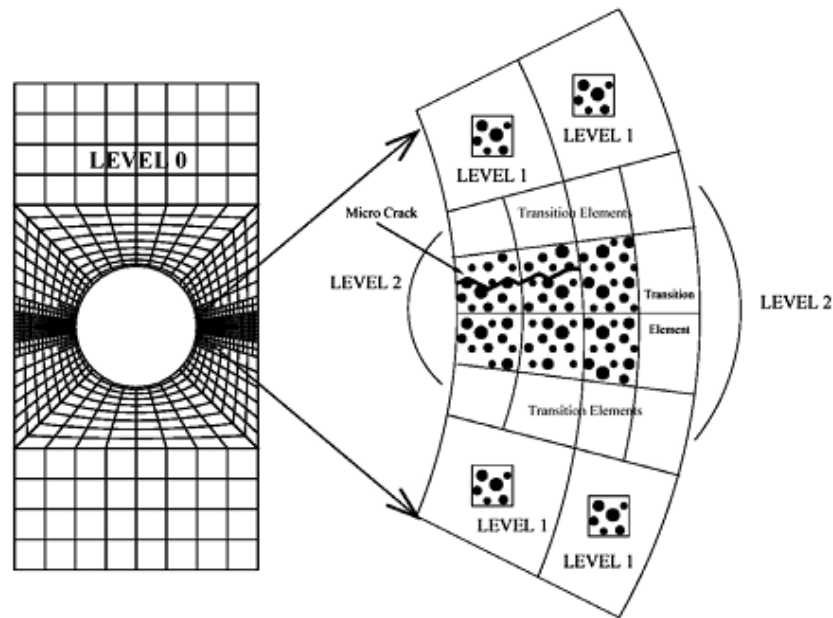


Figure 2.5. Concurrent multiscale methodology of Ghosh et al. [58]

Sanchez et al. [5] presented a multiscale methodology called the failure-oriented multiscale variational formulation for modeling materials undergoing softening and strain localization. Their multiscale methodology is actually a combination of two multiscale sub-

models; a classical computational homogenization based multiscale model for stable regime and a multiscale model for regions in the model undergoing failure.

Kim and Lee [14] used RVE-based micromechanical modeling and a mean-field homogenization technique considering the finite Eshelby tensor [6] to model fibre-reinforced composites with elastic material response with damage. For the validation of the developed methodology, they compared their results with Hashin's theoretical bounds. They extended their work to elastoplastic material behavior in [59].

In [60], Nguyen et al. developed a methodology for extracting the macroscale traction-separation behavior of quasi-brittle materials through the homogenization of a microscale RVE for both cohesive and adhesive cracks. They proposed a methodology to relate the microscale localized damage to macroscale discontinuous cracking.

Nguyen et al. extended their work in [4] to include the behavior of both the macroscopic bulk as well as the crack in the same algorithm. In their overall algorithm, the homogenization of the bulk region was carried out using standard computational homogenization procedures similar to for example Geers et al. [61] while the macroscale cracking was modeled using the approach laid out in [60]. They validated the accuracy of the algorithm by comparing the results with a reference solution for mode I failure.

Uthaisangsuk et al. [62] used computational homogenization to determine the homogenized macroscale response of dual phase (DP) and triple phase (TRIP) steel and to study their inter-phase fracture and damage. They developed 2D RVEs using experimental

micrographs for DP steel while 3D micrographs for DP and TRIP steels were generated computationally. Shows the steps involved in the generation of the 2D RVE for DP steel.

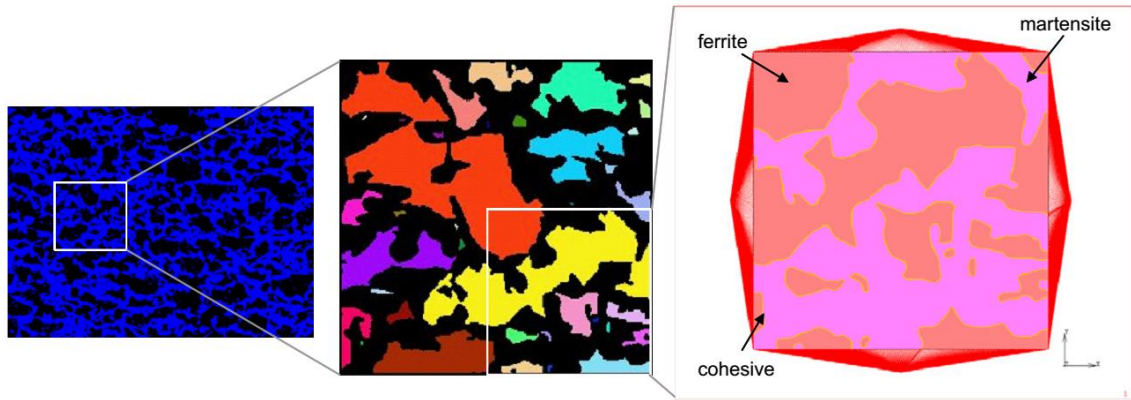


Figure 2.6. 2D RVE for DP steel [62].

Greco et al. [63] developed a multiscale method for failure analysis of periodic fiber-reinforced composites. Their model comprises two scales and is capable of predicting the initiation and propagation of cracks at the fiber-matrix interface. As a first step, no cracking is assumed in the model and macroscale problem is solved using homogenized linear elastic properties from the microscale. Using the macroscopic solution, the microscale problem is solved at each integration point. If a criterion of crack initiation is met at any integration point, the RVE at that point is replaced with a new RVE with an initial crack and its properties are recalculated and the crack propagation problem is solved for that RVE.

Vel and Goupee [22] extended their model to carry out the multiscale analysis of heterogeneous materials for the prediction of local failure at the microscale level [64]. They

used the model to develop the initial failure envelope of the heterogeneous material by directly relating the macroscopic failure to the microscopic failure.

2.5 RVE GENERATION AND SIZE DETERMINATION

The representative volume element (RVE) is the smallest sample of a heterogeneous material that can accurately represent the material's behavior. An RVE can therefore be used to determine effective material properties of heterogeneous materials. Two important aspects of RVEs i.e. generation and correct size determination have been discussed below.

2.5.1 RVE Generation

It is important that an RVE can accurately capture all morphological features of the material in order to predict the correct material behavior. In practice, RVEs are generated either computationally with predefined parameters such as porosity fraction, reinforcement fraction, reinforcement distribution type, etc. or they are generated by digitizing actual microstructures. Capturing actual microstructures results in a more detailed but also a much more complex RVE.

For the microscale homogenization, Wu et al. [65] digitized the microstructure of hardened cement paste (HCP) using a microCT scanner and its effective thermal conductivity was calculated. For the mesoscale, they developed computational RVEs using the take-and-place algorithm.

Vel and Goupee [22] used random morphology description function to generate computational representative material elements (RMEs) that were found to have the same morphology as actual metal matrix and ceramic matrix composites. A comparison of the computational RMEs with the actual microstructure of Al/Al₂O₃ is shown in Figure 2.7.

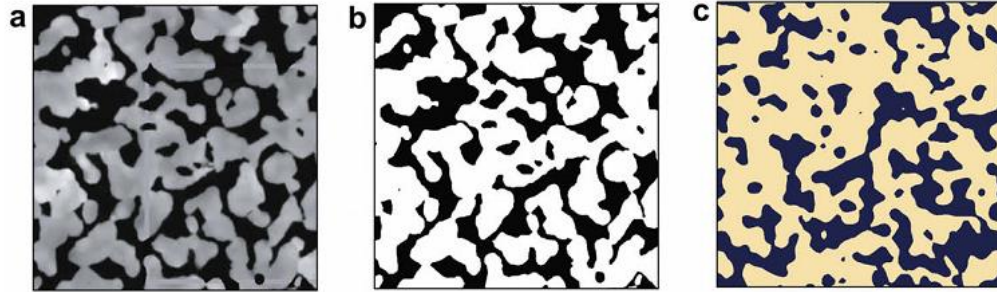


Figure 2.7. (a) Actual Al₂O₃ microstructure (b) Al₂O₃ microstructure in black and white and (c) computational RME

To generate the geometry of their microscale model, Takano et al. [31,32] used digital images of the microstructure cross section to generate a three-dimensional voxel-based mesh. The methodology is graphically shown below in Figure 2.8.

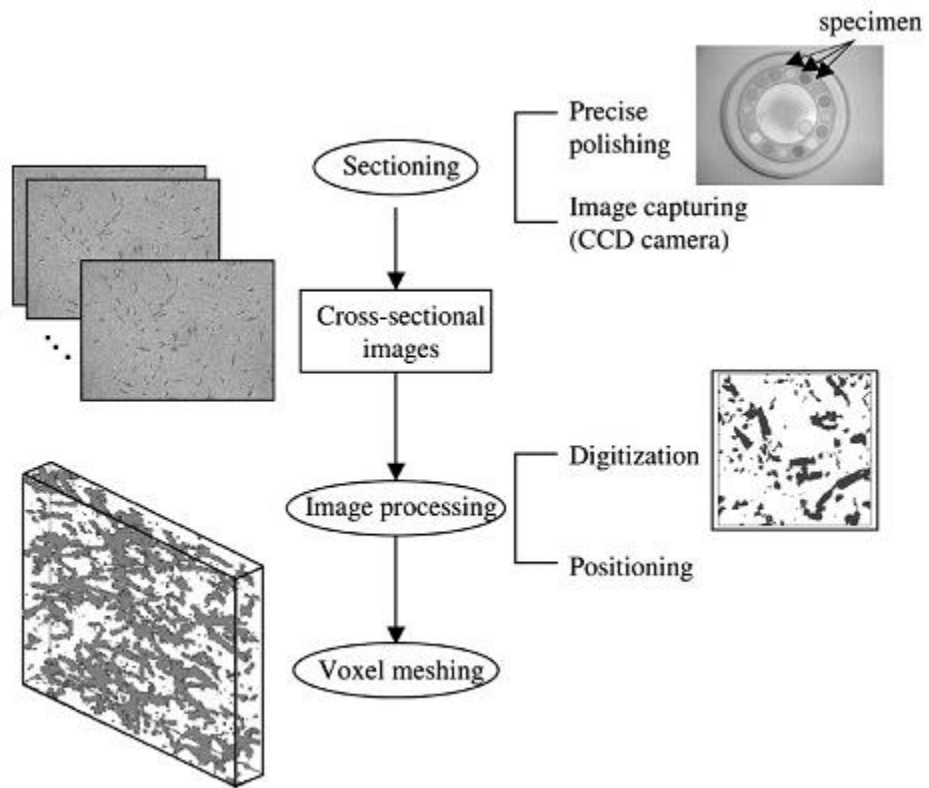


Figure 2.8. RVE generation methodology of Takano et al. [32]

Galli et al. [20,33] used computational homogenization for studying the macroscale behavior of particle-reinforced metal matrix composites (PRMMCs). Their work comprises a methodology for the generation of computational RVEs and the homogenization of the thermoelastic and plastic properties of the composites. For the generation of the computational RVE, Galli et al. developed an algorithm to introduce reinforcement particles into the mesh instead of meshing a geometry containing the particles in a matrix. Their methodology for RVE generation proved to be faster and more efficient than the latter. For the homogenization of thermo-elastic properties,

Nguyen et al [66], for the computational homogenization of concrete, implemented the cement hydration model in C++ framework to develop computational microstructures for concrete paste. The images of the computational RVEs were meshed using the software OOF and used as the microscale model for the multiscale modeling of concrete.

Toulemonde et al. [19] used computational homogenization to determine the effective elastic properties of concrete. To generate computational RVEs, they used the Monte Carlo method and Fuller curves which give a set of inclusions based on constraints like the required volume fraction and periodicity condition for microstructure morphology. The RVE is meshed independent of the positioning of the inclusions with tetrahedrons. Next, the properties of the elements are assigned based on the positions of inclusions and inter-phase regions.

Conventionally, RVEs considered in micromechanical modeling are cubic for three-dimensional problems and square for two-dimensional problems. Gluge et al. [67]

conducted a study to see the influence of the shape of the RVE on the results. They argue that using spherical RVEs instead of cubic RVEs is more advantageous because in spherical RVEs the bias of specific boundary conditions is reduced since the surface-to-volume ratio is smaller and material-independent anisotropy is not induced due to the application of boundary conditions. For an elasto-plastic composite with hard inclusions, they developed both cubic as well as spherical RVEs and found the size convergence to be much faster in the spherical RVE.

For granular materials, Stroeven et al. [15] provided a methodology for the determination of the minimum size of the RVE that can be used for the micromechanical modeling of material. They modeled grain distribution using SPACE software package and carried out finite element simulation on the generated geometries. Next, using a statistical method, they identify the correct size of the RVE for determining a particular material property up to a certain level of statistical accuracy.

2.5.2 Size Determination

The determination of the correct minimum size of an RVE is an essential step in the development of an efficient and accurate microscale model. For linear materials, RVEs always exist and the required minimum size can be determined. For other situations, the existence of the RVE needs to be checked.

Gitman et al. [16] has provided a very good discussion on the existence and size determination of RVEs. They considered three different regimes of material behavior: elastic, hardening and softening. They found that RVEs always exist for elastic and

hardening materials but the size of the RVE for hardening materials is much larger than elastic materials. According to the work of Gitman et al., RVEs do not exist for softening materials.

Galli et al. [20,33] studied the variation of the predicted elasticity tensor and the thermal expansion coefficients with the size of the RVE as well as the volume fraction of reinforcement particles. They found that an RVE size around five times larger than the average particle size was required for the homogenization of thermo-elastic properties. For the homogenization of the plastic response, they formulated a methodology to predict the macroscale nonlinear stress-strain response of the material using the microscale model simulations. They validated the approach by comparing the predicted response with experimental results and found good agreement. They also found that the RVE size requirement increase from 5 times to 15 times the average particle size in cases when plasticity is present.

Salahouelhadj and Haddadi [68] carried out a study to estimate the RVE size requirement for copper polycrystals using finite element based polycrystal plasticity modeling. They studied the variation of the macroscopic stress-strain response with RVE size. They also studied the dependence of this variation with the reached stress value and the strain rate and found very weak dependence on both.

2.6 EFFECTIVE THERMAL CONDUCTIVITY ESTIMATION

The problem of estimation of the effective thermal conductivity of heterogeneous materials has been widely studied. Early work in the area were done by Maxwell [69] and Lord Rayleigh [70] who studied the thermal conductivities of composites with low concentrations of inclusions. Their works were later extended by Hasselman and Johnson [71] and Benveniste [72] who studied the effects of thermal boundary conductance on the effective thermal conductivity of the composite. Recently, expressions for the effective thermal conductivity of composites with inclusions of different shapes have been presented by Nan et al. [73]. For spherical inclusion, the equations presented by Nan et al. is,

$$\frac{k_{eff}}{k_h} = \frac{k_i(1+2\alpha) + 2k_h + 2\phi[k_i(1-\alpha) - k_h]}{k_i(1+2\alpha) + 2k_h - \phi[k_i(1-\alpha) - k_h]} \quad (2.2)$$

where k_{eff} , k_h and k_i are the thermal conductivities of composite, host matrix and the inclusion particles respectively. ϕ is the inclusion volume fraction and α is a modified thermal boundary resistance parameter defined as $\alpha = R_{TB}k_h/(d/2)$ where R_{TB} is the thermal boundary resistance and d is the inclusion diameter.

Bruggeman [74] derived a model for the effective thermal conductivity of a composite when the inclusion concentration was high. His model was later extended by Every et al. [75] to include the effect of thermal boundary conductance. The differential form of the equation by Every et al. is given by (2.3) which when integrated leads to the implicit

equation (2.4) for the effective thermal conductivity of the composite. Modifications to the model by Every et al. to include the effect of particle shape have also been presented [76].

$$dk_{eff} = \frac{3k_{eff} [k_i(1-\alpha) - k_{eff}] d\phi}{(1-\phi) [k_i(1+2\alpha) + 2k_{eff}]} \quad (2.3)$$

$$(1-\phi)^3 = \left(\frac{k_h}{k_{eff}} \right)^{(1+2\alpha)/(1-\alpha)} \left(\frac{k_{eff} - k_i(1-\alpha)}{k_h - k_i(1-\alpha)} \right)^{3/(1-\alpha)} \quad (2.4)$$

Another approach, which has recently gained popularity, is the use of computational homogenization for the estimation of the effective thermal conductivity of composites. Computational homogenization requires the solution of a microscale boundary value problem. When appropriate boundary conditions are applied, the effective thermal conductivity of the composite can be determined using equation (6.28). Moumen et al. [77] and Wu et al. [65] applied computational homogenization scheme for the determination of effective thermal conductivities of porous media and concrete respectively.

$$k_{eff} = \frac{\langle q \rangle_1 \langle \nabla T \rangle_1 + \langle q \rangle_2 \langle \nabla T \rangle_2 + \langle q \rangle_3 \langle \nabla T \rangle_3}{\langle \nabla T \rangle_1^2 + \langle \nabla T \rangle_2^2 + \langle \nabla T \rangle_3^2} \quad (2.5)$$

where $\langle \bullet \rangle = \frac{1}{|V|} \int_V \bullet dV$ and V is the domain volume.

2.6.1 Effective thermal conductivity of nanocomposites

Although the approaches mentioned above have been widely utilized for the estimation of effective thermal conductivity of composites, their application to nanocomposites can lead to large errors [1]. The reason for this is the decrease of the thermal conductivities of the host and the inclusions due to increased interface scattering.

One method for the estimation of effective thermal conductivity of nanocomposites is the Monte Carlo simulation method. Tian and Yang [78] used phonon transport Monte Carlo simulation to determine the thermal conductivity of Si-Si and Si-Ge nanowire composites. Jeng et al. [79] used the Monte Carlo simulation to estimate the effective thermal conductivity of Si-Ge nanocomposites. An application of the Monte Carlo simulation method to polymer-CNT nanocomposite was presented by Duong et al. [80] who found good agreement between their estimated effective thermal conductivity and the experimental values.

Another approach for the determination of effective thermal conductivity is using the Boltzmann transport equation. Yang and Chen [81] applied Boltzmann transport equation for modeling Si nanowire – Ge nanocomposites. Hsieh et al. [82] used Boltzmann transport equation for modeling compacted type Si-Ge nanocomposites. Xu and Li [83] combined lattice dynamics with Boltzmann transport equation to study the effect of strain on the thermal conductivity of Si nanowire- Ge nanocomposite. Lee et al. [84] presented a methodology for the solution of Boltzmann transport equation using extended finite element method and used it for the determination of the effective thermal conductivity of

complex Si-Ge microstructures. Maute et al. [85] also used XFEM for the solution of the Boltzmann transport equation and applied a topology optimization algorithm to find the optimum shape and size of Si inclusions in a Ge host to achieve the minimum effective thermal conductivity.

The final approach found in literature is the modified effective medium theory models. In this approach, presented by Minnich and Chen [86] for spherical inclusions and later extended by Ordonez-Miranda et al. [87] for spheroidal inclusions, modified thermal conductivities of the matrix and inclusions are first calculated and then used in the effective medium theory. Minnich and Chen used the modified values of matrix and inclusion thermal conductivities in Nan et al.'s EMT for spherical inclusions and found good agreement between the effective thermal conductivities predicted by the modified EMT and Monte Carlo simulations. Minnich and Chen's modified effective medium theory is shown in equation (2.6).

$$k_{eff}(\Phi, d) = k_h(\Phi) \frac{k_i(d)(1 + 2\alpha(\Phi, d)) + 2k_h(\Phi) + 2(\Phi d/6)[k_i(d)(1 - \alpha(\Phi, d)) - k_h(\Phi)]}{k_i(d)(1 + 2\alpha(\Phi, d)) + 2k_h(\Phi) - (\Phi d/6)[k_i(d)(1 - \alpha(\Phi, d)) - k_h(\Phi)]} \quad (2.6)$$

where $k_h(\Phi)$ and $k_i(d)$ are the modified thermal conductivities of the matrix and inclusions respectively, defined by equations (2.7), Φ is the interface density, Λ is the mean free path of phonons, C is the specific heat capacity, v is the phonon group velocity and d is the inclusion size.

$$\begin{aligned}
k_h &= \frac{1}{3} C_h \nu_h \frac{1}{\left(1/\Lambda_{h,bulk}\right) + (\Phi/4)} \\
k_i &= \frac{1}{3} C_i \nu_i \frac{1}{\left(1/\Lambda_{i,bulk}\right) + (1/d)}
\end{aligned} \tag{2.7}$$

One important aspect missing from all approaches presented above is the ability to include non-uniform distribution of inclusions.

2.7 SUMMARY OF LITERATURE SURVEY

In the current work, an extensive literature survey was carried out in order to determine the state of the art in the areas of homogenization methodologies and multiscale modeling approaches. In the literature survey homogenization techniques and multiscale approaches were found for a variety of material constitutive behaviors including elasticity [21,24], elastoplasticity [18,33,40,88], softening behavior [60,66,89], viscoelastic behavior [90–93] and viscoplasticity [52,53,57,94,95]. Homogenization approaches for thermal conductivity estimation of heterogeneous materials were also found [71,73,75] including modifications to these models for nanocomposites [86,87]. The applications of these homogenization and multiscale approaches were found in the areas of composites [58,64,96,97], porous media [31,32] and concrete [4,60,66].

During the literature review, it was found that there are several steps involved in carrying out the property estimation of heterogeneous materials including computational microstructure generation, RVE size determination and property estimation. There is a lack of unified approaches carrying out all these steps inside a single algorithm. It was also

found out that there is a lack of homogenization tools for the property estimation of nanocomposites. In particular, tools for determining the elastoplastic response of particulate nanocomposites and effective thermal conductivity of multi-inclusion particulate nanocomposite have shortcomings in the available literature. Additionally, applications of the homogenization tools in novel areas such as membranes and coatings need further investigation.

CHAPTER 3

COMPUTATIONAL MICROSTRUCTURE GENERATION

3.1 INTRODUCTION

The most common algorithm used for the generation of computational composite microstructures is the Random Sequential Adsorption (RSA) algorithm [98]. The algorithm starts by randomly assigning the position of the first reinforcement. The remaining reinforcement particles are placed one by one. If any new particle is found to be in contact with previously placed particles, it is redrawn. The process is repeated for the remaining inclusions. Another approach for reinforcement placement in a matrix based on molecular dynamics was proposed by Lubachevsky et al. [99,100]. The method starts by generating all the reinforcement particles in the matrix together at the start of the algorithm. All particles are assigned random locations and zero radii and are put into motion by assigning random velocities to them. The algorithm increases the particles sizes at a fixed rate and also detects collisions between the particles and between particles and the faces of the RVE. The simulation ends when the desired volume fraction is achieved. A similar algorithm was formulated by Ghossein and Lévesque [101].

In the present work, two computational microstructure generation algorithms were implemented. The first algorithm is similar to the Random sequential adsorption algorithm.

The second is the algorithm presented by Ghossein and Lévesque [101]. The details of the algorithms are presented in the sections below.

3.2 RANDOM PLACEMENT ALGORITHM

The Random placement algorithm implemented in the current work is similar to the RSA algorithm [98] but extends the capability to multiple types of inclusions/porosity and variable sizes of inclusion particles and pores. The methodology is presented in algorithms 3.1 to 3.3. It is capable of placing two different phases which can be inclusions and/or porosity in a matrix up to a volume fraction of around 30%.

The inputs to the algorithm include the target weight fraction of inclusions (wf_{inc}), target volume fraction of porosity (vf_{pore}), average inclusion size (r_{inc}), target number of inclusions (N_{inc}), target number of pores (N_{pore}) and matrix and inclusion densities. Using the inputs, the target inclusion volume fraction (vf_{inc}), domain volume (V_{domain}), domain edge length (L_{domain}) and the average pore size (r_{pore}) are calculated using equations (3.1) to (3.4).

$$vf_{inc} = \frac{\rho_{comp}}{\rho_{inc}} wf_{inc} \quad (3.1)$$

$$V_{domain} = \frac{4}{3} \pi r_{inc}^3 \frac{N_{inc}}{vf_{inc}} \quad (3.2)$$

$$L_{domain} = \sqrt[3]{V_{domain}} \quad (3.3)$$

$$r_{pore} = \sqrt[3]{\frac{vf_{pore} V_{domain}}{N_{pore} \frac{4}{3} \pi}} \quad (3.4)$$

The algorithm starts by randomly placing the first inclusion particle in the matrix with a radius equal to the average inclusion radius. The remaining particles are sequentially placed. To determine the radius of a newly placed particle, its distance from all previously placed particles is calculated to determine its maximum allowable radius and a random radius is generated within the maximum allowable limit. The inclusion particles are placed until the volume fraction of the inclusions is equal to the desired value and the number of particles do not exceed the target number of inclusion particles by more than five percent. Next, the pores are randomly placed in sequence following a similar approach.

Three example computational microstructures generated using the algorithm implemented in *MATLAB* are shown in Figure 3.1. In these microstructures, 10 pores with a target porosity of 1% are generated along with 100 inclusions with a target inclusion volume fraction of 2.5%, 10% and 20%.

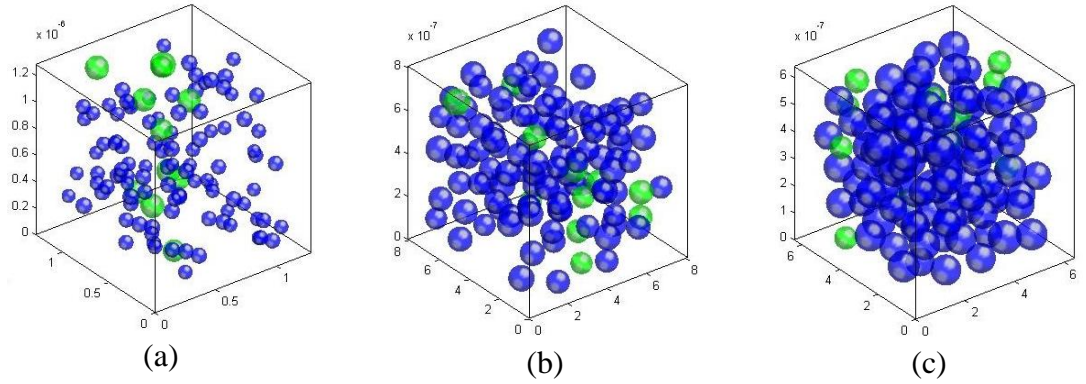


Figure 3.1. Example computational microstructures with 1% porosity and (a) 2.5% reinforcement (b) 10% reinforcement and (c) 20% reinforcement

Algorithm 3.1 – Computational microstructure generation - Main Algorithm

-
1. Calculate inclusion volume fraction vf_{inc} using equation (3.1), domain volume V_{domain} using equation (3.2) and L_{domain} using equation (3.3).
 2. Calculate average pore size, r_{pore} , using equation (3.4).
 3. Generate a random location for the center of first inclusion within the range $1.2r_{inc} \leq (x_{inc,i}, y_{inc,i}, z_{inc,i}) \leq L_{domain} - 1.2r_{inc}$ and assign it a radius of r_{inc} .
 4. Calculate current inclusion weight fraction using,

$$vf_{inc,current} = \frac{4}{3} \frac{\pi r_{inc,1}^3}{V_{domain}} \quad (3.5)$$

5. Set $N_{inc,current} = 1$, $i = 2$ and $trials = 0$.
 6. Generate $(N_{inc} - 1)$ inclusions using algorithm A3 with $xx = inc$.
 7. Set $N_{pore,current} = 0$, $i = 1$, $vf_{pore,current} = 0$ and $trials = 0$.
 8. Generate N_{pore} pores in the RVE using algorithm A3 with $xx = pore$.
-

Algorithm 3.2 – Computational microstructure generation - Inclusion and Pore Placement algorithm

1. While $vf_{xx,current} < vf_{xx}$ and $i < 1.02N_{xx} + 1$ and $trials \leq trials_{max}$, do:

a. Generate a random location for next inclusion

$$1.2r_{xx} \leq (x_{xx,i}, y_{xx,i}, z_{xx,i}) \leq L_{domain} - 1.2r_{xx}.$$

b. Calculate maximum allowed radius $r_{xx,max}$ of RVE using algorithm A4.

c. If $r_{xx,max} > 0.9r_{xx}$:

i. Generate a random radius for the inclusion in the range

$$0.9r_{xx} \leq r_{xx,i} \leq r_{xx,max}.$$

ii. Update inclusion volume fraction using the following equation.

$$vf_{xx,current} = vf_{xx,current} + \frac{\frac{4}{3}\pi r_{xx,i}^3}{V_{domain}} \quad (3.6)$$

iii. If $vf_{xx,current} > vf_{xx}$:

1. Recalculate $r_{xx,i}$ using the following equation.

$$r_{xx,i} = \sqrt[3]{\frac{(vf_{xx} - vf_{xx,current})V_{domain}}{\frac{4}{3}\pi}} \quad (3.7)$$

2. If $r_{xx,i} < 0.9r_{xx}$, set $r_i = 0.9r_{inc}$.

iv. Set $N_{xx,current} = i$

v. Increment i .

d. Increment $trials$.

-
1. Set $r_{xx,max} = 0$.
 2. For $j=1$ to $N_{inc,current}$, do:
 - a. Calculate distance d between $(x_{xx,i}, y_{xx,i}, z_{xx,i})$ and $(x_{inc,j}, y_{inc,j}, z_{inc,j})$.
 - b. Calculate $r_{temp} = d - r_{inc,j}$.
 - c. If $j=1$ or $r_{temp} < r_{xx,max}$, set $r_{xx,max} = r_{temp}$.
 3. If $xx=pore$:
 - a. For $j=1$ to $N_{pore,current}$, do:
 - i. Calculate distance d between $(x_{xx,i}, y_{xx,i}, z_{xx,i})$ and $(x_{pore,j}, y_{pore,j}, z_{pore,j})$.
 - ii. Calculate $r_{temp} = d - r_{pore,j}$.
 - iii. If $r_{temp} < r_{xx,max}$, set $r_{xx,max} = r_{temp}$.
 4. If $r_{xx,max} > 1.1r_{xx}$, set $r_{xx,max} = 1.1r_{xx}$.
-

3.3 PARTICLE KINEMATICS ALGORITHM

The particle kinematics based algorithm was presented by Ghossein and Lévesque [101] and has been implemented in the current work. The algorithm starts by randomly placing all inclusion particles in a cubic volume. The initial volume of each particles is set as zero. Each particle is assigned a rate of growth and an initial velocity. A time domain simulation is then performed to track the motion of the particles through the cubic volume. During the simulation, collisions between two particles and between a wall and a particle

are tracked. If two particles collide, their velocities are adjusted following the law of conservation of linear momentum. If a particle collides with a wall, a secondary particle is introduced on the opposite side wall to ensure periodicity with the microstructure. The methodology is represented by Algorithms 3.4 to 3.8. Algorithm 3.4 gives the overall scheme. Algorithms 3.5 and 3.6 are used for particle-particle and particle-wall collision detection respectively. Algorithm 3.7 is used for the determination of post particle-particle collision velocities. Algorithm 3.8 is used for the creation of secondary periodic particles after particle collision with walls.

Example microstructures generated using the particle kinematics algorithm are shown in Figure 3.2. The figure shows three cases of 10%, 20% and 30% inclusion volume fractions. For each case, the number of inclusion particles was set as 50. The algorithm has no limitation on the maximum volume fraction of inclusion particles and is capable of generating microstructures with maximum packing for a given number of inclusion particles. To validate this point, two additional microstructures were generated. The first one had two particles and a volume fraction of 68%. The second one had four particles and a volume fraction of 74%. The results are shown in Figure 3.3. As shown in the figure, the generated microstructures exactly match the maximum packing arrangements of 2 spheres (BCC) and 4 spheres (FCC).

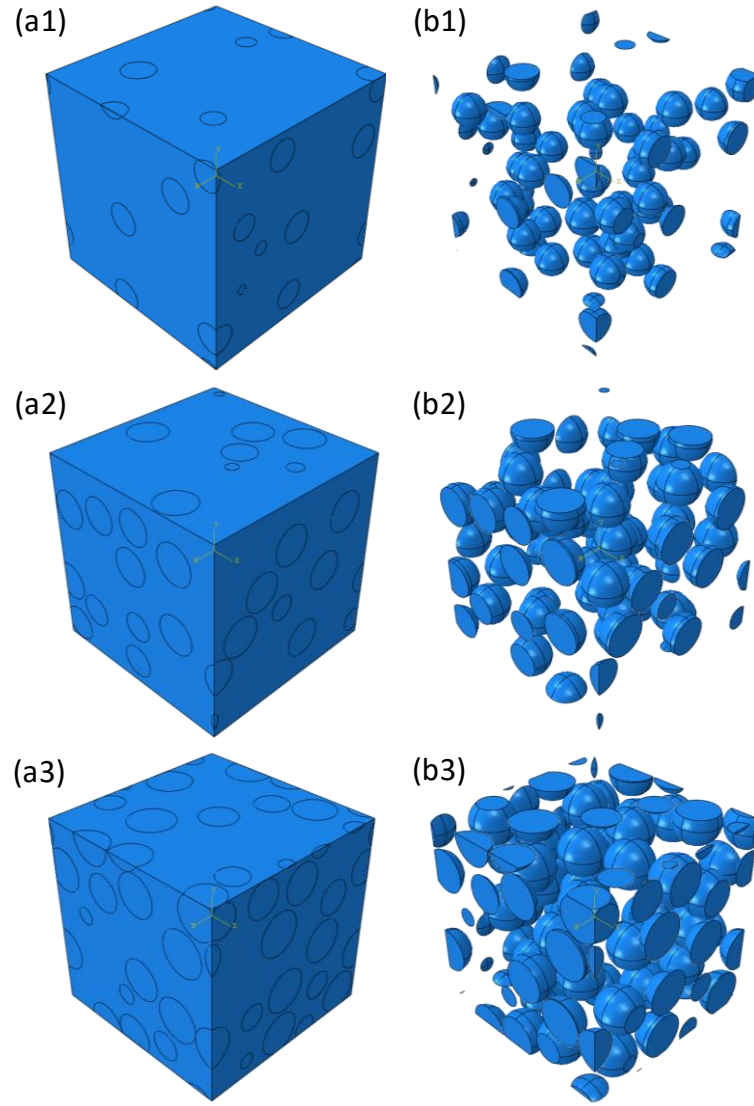


Figure 3.2. Examples of computational microstructures generated using Particle kinematics algorithm. [(a) and (b) represent the complete domain and inclusion particles respectively. (1), (2) and (3) represent volume fractions 10%, 20% and 30% respectively].

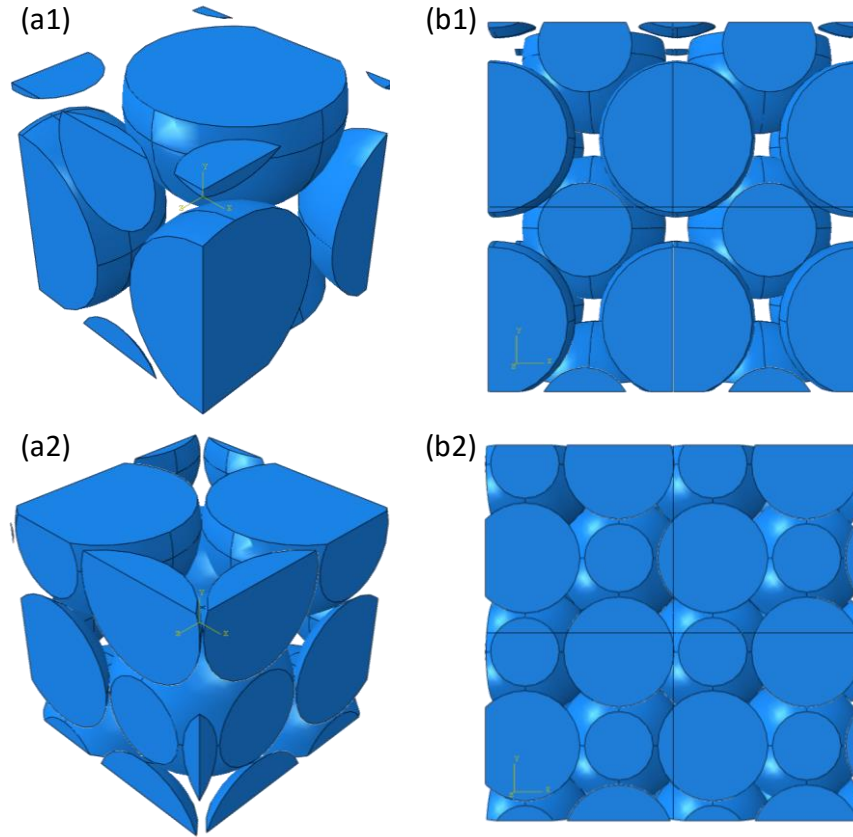


Figure 3.3. Example microstructures showing maximum packing arrangements. [(1) and (2) show 2 particles and 4 particles having packing factors of 0.68 and 0.74 respectively. (a) and (b) show unit cell and a 2x2 arrangement of the unit cell respectively].

Algorithm 3.4– Particle kinematics main algorithm

-
1. Calculate inclusion volume fraction vf_{inc} using equation (3.1), domain volume V_{domain} using equation (3.2) and L_{domain} using equation (3.3).
 2. For each particle i from 1 to N , *do*:
 - i. Assign a random location \vec{r}_i^0 .
 - ii. Assign a random velocity \vec{v}_i^0 .
 - iii. Assign zero initial radius R_i^0 .
 3. Initialize time iteration $n = 1$, time $t^0 = 0$ and actual inclusion volume fraction $vf_{actual} = 0$.
 4. Using algorithm 3.5, determine time increment for next particle-particle collision t_c .
 5. Using algorithm 3.6, determine time increment for next particle-wall collision t_s .
 6. Set $\Delta t^n = \min(t_s, t_c)$.
 7. For each particle I from 1 to N , *do*:
 - i. Update particle position, $\vec{r}_i^{n+1} = \vec{r}_i^n + \vec{v}_i^n \Delta t^n$.
 - ii. Update particle radius, $R_i^{n+1} = R_i^n + a_i \Delta t^n$.
 8. If $\Delta t^n = t_c$,
 - i. Calculate new particle velocities for colliding particles using algorithm 3.7.
 Else if $\Delta t^n = t_s$,
 - i. Produce secondary periodic particles for the particle colliding with a wall using algorithm 3.8.
 9. Compute new volume fraction $vf_{actual} = \frac{1}{L^3} \sum_{i=1}^N \frac{4}{3} \pi (R_i^{n+1})^3$
 10. If $vf_{actual} < vf_{inc}$,
 - i. Update iteration $n = n + 1$ and go to step 4.
-

Algorithm 3.5– Particle-Particle collision detection algorithm

1. For each particle pair i and j :

- i. Calculate $\Delta\vec{r}^n$ and $\Delta\vec{v}^n$.
- ii. Calculate α, β and γ where,

$$\begin{aligned}\alpha &= \|\Delta\vec{v}^n\|^2 - (a_i - a_j)^2 \\ \beta &= \Delta\vec{r}^n \cdot \Delta\vec{v}^n - (R_i^n - R_j^n)(a_i - a_j) \\ \gamma &= \|\Delta\vec{r}^n\|^2 - (R_i^n - R_j^n)^2\end{aligned}$$

- iii. If $(\beta \leq 0$ or $\alpha < 0)$ and $\beta^2 - \alpha\gamma \geq 0$:

$$\tau_{ij} = \alpha^{-1} \left[-\beta - \sqrt{\beta^2 - \alpha\gamma} \right]$$

Else:

No collision ($\tau_{ij} = \infty$)

- 2. Select the minimum time, $t_c = \min(\tau_{ij})$
-

Algorithm 3.6– Particle-wall collision detection algorithm

1. For each particle i from 1 to N :

i. For walls $k=1$ to 6

a. If particle i does not intersect wall k , then

$$\tau_{ik} = \begin{cases} \left[R_i^n - r_i^n(k) \right] \left[v_i^n(k) - a_i \right]^{-1} & \text{for } k \in \{1, 2, 3\} \\ \left[L - R_i^n - r_i^n(k-3) \right] \left[v_i^n(k-3) - a_i \right]^{-1} & \text{for } k \in \{4, 5, 6\} \end{cases}$$

b. If $\tau_{ik} < 0, \tau_{ik} = \infty$.

2. Select the minimum time, $t_s = \min(\tau_{ik})$

Algorithm 3.7– Post-collision velocity algorithm

1. Assume particles i and j are colliding.

2. Compute unit vector $u = (\vec{r}_i^{n+1} - \vec{r}_j^{n+1}) / \|\vec{r}_i^{n+1} - \vec{r}_j^{n+1}\|$.

3. Decompose the particle velocities into parallel ($^{\parallel}$) and normal ($^{\perp}$) components where,

$$^{\parallel}v_z^n = (\vec{v}_z^n \cdot \vec{u})\vec{u} \quad \text{and} \quad ^{\perp}\vec{v}_z^n = \vec{v}_z^n - ^{\parallel}\vec{v}_z^n \quad \text{where } z = \{i, j\}$$

4. Compute the new particle velocities using,

$$\begin{aligned} \vec{v}_i^{n+1} &= \left[^{\parallel}\vec{v}_i^n + (a_i + a_j)u \right] + ^{\perp}\vec{v}_i^n \\ \vec{v}_j^{n+1} &= \left[^{\parallel}\vec{v}_j^n - (a_i + a_j)u \right] + ^{\perp}\vec{v}_j^n \end{aligned}$$

5. If particle z has Q periodic images, then:

i. For q from 1 to Q

$$^q\vec{v}_z^{n+1} = \vec{v}_z^{n+1}$$

Algorithm 3.8– Secondary periodic particle generation algorithm

-
1. Assume particle i collided with m walls
 2. If $m=1$, $P=1$
 Else if $m=2$, $P=3$
 Else if $m=3$, $P=7$
 3. Create P periodic images of particle i .
 4. For $p=1$ to P ,

$$\begin{aligned} {}^p\vec{r}_i^{n+1} &= \vec{r}_i^{n+1} + \vec{h} \\ {}^p\vec{v}_i^{n+1} &= \vec{v}_i^{n+1} \end{aligned}$$

where the vector \vec{h} provides the relative displacement of the secondary periodic particles.

CHAPTER 4

COMPUTATIONAL HOMOGENIZATION:

METHODOLOGY AND APPLICATIONS

4.1 INTRODUCTION

The design and development of metal-matrix composites requires a careful control of the microstructure of composite and a thorough understanding of the effects of the microstructural parameters on the properties of the composite. Computer modeling and simulation plays a key role in the design of these materials since it provides a fast, low cost and efficient tool to study the effects of various parameters on the properties of the composite.

Various types of homogenization methods have been extensively employed to determine the mechanical behaviors of heterogeneous materials by taking into account the length scale difference between the macrostructure and the individual microstructure components. These homogenization schemes fall into two major categories: mean-field homogenization and computational homogenization. Although mean-field homogenization

schemes are much more computationally efficient than the computational homogenization schemes, homogenization in nonlinear regimes using mean-field approaches is more cumbersome. In recent years, significant emphasis has been laid on computational homogenization techniques which are essentially solutions of finite element boundary value problem.

An important aspect of the computational homogenization approach is the correct selection of the representative volume element (RVE). A key issue in the use of RVEs in determining material properties is the determination of the size of the microstructure domain for which the predicted results are representative of the macroscale properties. Several authors have focused solely on this issue in order to understand the relationship between the prediction accuracy and the determination of correct RVE size based on application [11,15,16]. Once the RVE has been developed, it can then be used to study the mechanical behavior of the material at the microscale [13,14,17,102,103] or can be used in a multiscale approach to include the microstructural effects at the macroscale [18–20,104].

Several authors have presented homogenization methodologies for the estimation of the properties of the composite. Cho et al. [21] used computational homogenization to determine the thermoelastic properties for regular and random microstructures. They generated computational two-phase RVEs using the random morphology description function (RMDF) and used the developed computational RVEs to determine the homogenized properties, study the effect of variations in particle shapes and orientation on the orthotropic properties and to study the response of a beam composed of a dual phase

material. For determining the homogenized properties, Cho et al. utilized the principle of superposition by applying two sets of boundary conditions in order to determine the homogenized orthotropic properties. Ni and Chiang [29] developed a homogenization process to predict the anisotropic elastic properties heterogeneous materials. They considered the microstructure of the constituents to be highly interconnected and correlated instead of having dispersed inclusions. They adapted the phase-field micro elasticity model of Wang et al. [30] to attain the eigenstrain field which is then used in the homogenization process. Their homogenization approach is therefore based on the work of Eshelby [6].

Galli et al. [20,33] used computational homogenization to study the macroscale behavior of particle-reinforced metal matrix composites. Their work comprises a methodology for the generation of computational microstructures and the homogenization of the thermoelastic and plastic properties of the composites. For the generation of the computational microstructures, Galli et al. developed an algorithm to introduce reinforcement particles into the mesh instead of meshing a geometry containing the particles in a matrix. Brenner [39] used augmented Lagrangian fast Fourier transform to solve for the homogenized material properties of composites with coupled constitutive laws. He considered the case of a piezoelectric material and solved for the overall response of the material. As possible applications, he applied the developed methodology on porous materials and fiber-reinforced composites and validated the methodology by comparing the model predictions with experimental results. Doghri et al [40] used mean field homogenization schemes to predict the elastoplastic response of two-phase composite materials under small strain conditions. They compared their results with the results of

direct numerical simulations. They also tried several methods for the calculation of tangent moduli and studied their influence on the results.

This chapter presents the formulation of a unified approach for carrying out all steps necessary for numerical prediction of the constitutive behavior of metal matrix composites. In this regard, methodologies to carry out all necessary steps required for computational homogenization have been presented. This includes methodologies for the size determination of representative volume elements and the determination of elastic and elastoplastic properties of particulate composites using the generated RVEs. Validation of the approach has been carried out using experimental elastoplastic stress-strain response of sintered Al-Al₂O₃ composite samples. As an application of the methodology, the effect of inclusion volume fraction on the homogenized macroscopic properties is studied and effective macroscale material models for the composites are determined.

4.2 COMPUTATIONAL HOMOGENIZATION METHODOLOGY

The computational homogenization methodology relies on the solution of a finite element model of the microstructures of heterogeneous materials. Therefore, the solution domain consists of a representative volume element of the heterogeneous material. The size of the RVE is statistically determined to accurately represent the overall macroscopic response of the material. This RVE contains all constituent phases of the material and the constitutive behaviors of all phases present are explicitly defined. Periodic boundary conditions are applied to the microscale model using constraint equations. For a two

dimensional RVE, shown in Figure 4.1, the constraint equations are given as equations (4.1)-(4.5). For a three-dimensional RVE, a simple extension of the same method can be used. Constraint equations (4.1)-(4.5) ensure the periodicity of the displacement field solution within the RVE. To allow relative displacement between the boundaries due to straining of the RVE, reference nodes are added to the RVE which are defined as additional degrees of freedom in the RVE. The relative displacement at the periodic boundaries are tied to the reference nodes. Therefore, these reference nodes can be used to apply strain loads (in terms of displacement) to the RVE. It is important to note here that, for the application of periodic boundary conditions, the geometry of the finite element model does not need to be periodic.

$$\bar{u}_2 - \bar{u}_1 - \bar{u}_{ref_1} = 0 \quad (4.1)$$

$$\bar{u}_4 - \bar{u}_1 - \bar{u}_{ref_2} = 0 \quad (4.2)$$

$$\bar{u}_3 - \bar{u}_1 - \bar{u}_{ref_1} - \bar{u}_{ref_2} = 0 \quad (4.3)$$

$$\bar{u}_{right,noedges} - \bar{u}_{left,noedges} - \bar{u}_{ref_1} = 0 \quad (4.4)$$

$$\bar{u}_{top,noedges} - \bar{u}_{bottom,noedges} - \bar{u}_{ref_2} = 0 \quad (4.5)$$

where \bar{u} denotes the displacement vectors and ref_1 and ref_2 are reference nodes.

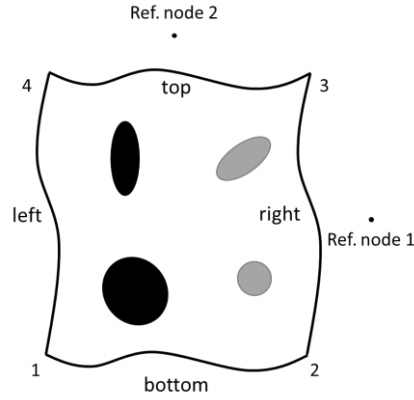


Figure 4.1. Applying periodic boundary conditions to microscale RVE

The overall homogenization methodology is presented in Figure 4.2. The steps involved in the methodology are computational microstructure generation, FE model generation, RVE size determination and homogenization. The methodology starts by assuming an initial domain size for the computational microstructure. For the assumed size, n random realizations of the microstructure are generated and converted to finite element models. Computational homogenization is carried to determine the concerned properties using the FE models of all realizations of the microstructure. Finally, the RVE size convergence criterion is checked. If the criterion is met, the initial domain size is considered representative of the macroscale material. Otherwise, the domain size is increased and the process is repeated again.

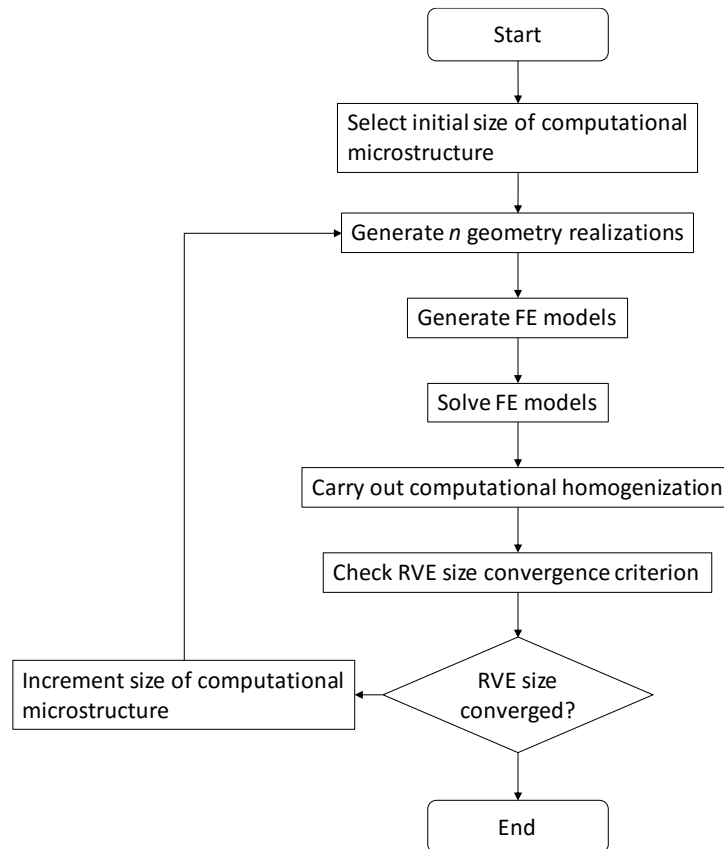


Figure 4.2. Homogenization methodology

4.2.1 Elasticity

In its most general form, elasticity can be represented using the 4th order elasticity tensor C_{ijkl} which has 81 components. Because of the existence of minor symmetries in the tensor, the number of independent components reduces to 36. These 36 components can be conveniently written in the form of a 6x6 matrix. The independent components in the elasticity tensor further reduces to 21 due to the existence of major symmetry in the tensor. In the matrix form, this results in a symmetric 6x6 matrix.

For homogenization of elastic materials, the homogenized elasticity matrix \bar{C} , given by equation (4.6), is calculated by applying six different macroscopic strain vectors (three in case of two-dimensional model) to the microscale RVE. Each strain vector, shown in equation (4.7), applies only one strain component as a load to the RVE and provides one column of the tangent modulus. This is done by first carrying out homogenization of the stress field using equation (4.8) which calculates the volume averaged stress components, $\bar{\sigma}_{ij}$, within the RVE. The elements C_{ij} of the elasticity matrix are then calculated by dividing $\bar{\sigma}_{ij}$ components with ε_0 as shown in equation (4.9).

$$\bar{C} = \frac{d\sigma}{d\varepsilon} = \begin{bmatrix} C_{11} & C_{12} & C_{13} & C_{14} & C_{15} & C_{16} \\ C_{12} & C_{22} & C_{23} & C_{24} & C_{25} & C_{26} \\ C_{13} & C_{23} & C_{33} & C_{34} & C_{35} & C_{36} \\ C_{14} & C_{24} & C_{34} & C_{44} & C_{45} & C_{46} \\ C_{15} & C_{25} & C_{35} & C_{45} & C_{55} & C_{56} \\ C_{16} & C_{26} & C_{36} & C_{46} & C_{56} & C_{66} \end{bmatrix} \quad (4.6)$$

$$\bar{\varepsilon} = \left\{ \begin{pmatrix} \varepsilon_o \\ 0 \\ 0 \\ 0 \\ 0 \\ 0 \end{pmatrix}, \begin{pmatrix} 0 \\ \varepsilon_o \\ 0 \\ 0 \\ 0 \\ 0 \end{pmatrix}, \begin{pmatrix} 0 \\ 0 \\ \varepsilon_o \\ 0 \\ 0 \\ 0 \end{pmatrix}, \begin{pmatrix} 0 \\ 0 \\ 0 \\ \varepsilon_o \\ 0 \\ 0 \end{pmatrix}, \begin{pmatrix} 0 \\ 0 \\ 0 \\ 0 \\ \varepsilon_o \\ 0 \end{pmatrix}, \begin{pmatrix} 0 \\ 0 \\ 0 \\ 0 \\ 0 \\ \varepsilon_o \end{pmatrix} \right\} \quad (4.7)$$

$$\bar{\sigma}_{ij} = \frac{1}{V} \int_V \sigma_{ij} dV \quad (4.8)$$

$$C_{ij} = \frac{\bar{\sigma}_{ij}}{\varepsilon_0} \quad (4.9)$$

where ε_0 is a small strain increment, σ_{ij} are the components of the stress field in the RVE and V is the RVE volume.

Although the computational homogenization methodology is more computationally intensive than techniques such as mean-field homogenization [9,105] and rule-of-mixtures [106], it is much general and applicable to a wider class of microstructures. Whereas, simplified approaches are limited to inclusions with regular shapes, the computational homogenization approach is not bound by any such limitation.

4.2.2 Rate-independent plasticity

The calculation of the homogenized elastoplastic response of heterogeneous materials requires two steps. These include the determination of the stress $\sigma_{y,loc}$ at which localized yielding starts and the stress strain curve. The yield stress $\sigma_{y,loc}$ needs to be iteratively

determined by applying the correct strain load to the RVE that results in the onset of yielding at any point within the RVE. This strain load is not known at the beginning of the calculation and needs to be determined iteratively during the solution with the range $(0, \sigma_{y,m}/E_m)$ using algorithm 4.1. $\sigma_{y,m}$ and E_m are the yield stress and Young's modulus of the matrix.

The algorithm starts by applying an initial strain load of $\sigma_{y,m}/2E_m$ to the RVE. The resulting total strain and elastic strain components are homogenized using equations (4.10) and (4.11) respectively which calculate the volumetric averages of the strain components. The plastic strain components and the effective plastic strain are calculated using equation (4.12) and (4.13) respectively. If the effective plastic strain is lower than a threshold value, the homogenized effective stress in the RVE, calculated using equation (4.14), is considered the yield stress of the composite. It is important to note that to carry to computational homogenization of any field, it needs to be continuous. Since plastic strains are localized, homogenized plastic strains cannot be determined by directly carrying out computational homogenization. Therefore, they are determined using equation (4.12) as the difference of the total and elastic strains.

$$\bar{\varepsilon}_{ij} = \frac{1}{V} \int_V \varepsilon_{ij} \quad (4.10)$$

$$\bar{\varepsilon}_{e,ij} = \frac{1}{V} \int_V \varepsilon_{e,ij} \quad (4.11)$$

$$\bar{\varepsilon}_{p,ij} = \bar{\varepsilon}_{ij} - \bar{\varepsilon}_{e,ij} \quad (4.12)$$

$$\bar{\varepsilon}_{p,eff} = \sqrt{\frac{1}{2} \left(\left(\bar{\varepsilon}_{p,11} - \bar{\varepsilon}_{p,22} \right)^2 + \left(\bar{\varepsilon}_{p,11} - \bar{\varepsilon}_{p,33} \right)^2 + \left(\bar{\varepsilon}_{p,22} - \bar{\varepsilon}_{p,33} \right)^2 + 6 \left(\bar{\varepsilon}_{p,12}^2 + \bar{\varepsilon}_{p,13}^2 + \bar{\varepsilon}_{p,23}^2 \right) \right)} \quad (4.13)$$

$$\bar{\sigma}_{eff} = \sqrt{\frac{1}{2} \left(\left(\bar{\sigma}_{11} - \bar{\sigma}_{22} \right)^2 + \left(\bar{\sigma}_{11} - \bar{\sigma}_{33} \right)^2 + \left(\bar{\sigma}_{22} - \bar{\sigma}_{33} \right)^2 + 6 \left(\bar{\sigma}_{12}^2 + \bar{\sigma}_{13}^2 + \bar{\sigma}_{23}^2 \right) \right)} \quad (4.14)$$

where ε_{ij} are the strain components and subscripts e , p , and eff stand for elastic, plastic and effective.

Once the stress and strain at the localized yielding point are known, the remaining stress-strain curve can be determined by applying incremental strain loads to the RVE. The points on the curve can also be fitted to a standard hardening function and its parameters determined.

Algorithm 4.1 – Determination of Localized Yield Stress

-
1. Set lower and upper limits of strains as:

$$lower = 0$$

$$upper = \frac{\sigma_{y,m}}{E_m}$$

2. Set counter = 0.

3. While counter < max. iterations

- a. Set uniaxial strain load $e_{xx} = (upper + lower)/2$

- b. Solve the RVE problem.

- c. Calculate the homogenized total strain ε_{ij} and elastic strain $\varepsilon_{e,ij}$ components using equations (4.10) and (4.11) respectively.

- d. Calculate the homogenized plastic strain components $\varepsilon_{p,ij}$ using equation (4.12).

- e. Calculate the effective plastic strain $\varepsilon_{p,eff}$ using equation (4.13).

- f. If $\varepsilon_{p,eff} < 10^{-8}$, break loop.

- g. If $\varepsilon_{p,eff} > 10^{-8}$, set $upper = e_{xx}$. Else set $lower = e_{xx}$.

- h. Increment counter.

4. Calculate homogenized stress components σ_{ij} using equation (4.8).

5. Calculate the yield stress which is equal to the effective homogenized stress using equation (4.14).
-

4.3 RVE SIZE DETERMINATION

In the computational microstructure generation algorithms presented in the last chapter, the size of the computational domain is governed by the desired number of inclusions in the domain. Before carrying out computational homogenization using the computational microstructures, a convergence study is required to determine the necessary number of inclusions that need to be included in the domain so that it is representative of the macroscale material. The size of this representative domain, or RVE, depends strongly on the material property being homogenized. An RVE used for one material property is not directly applicable to other properties without verification of its size requirement. In general, the required sizes of RVEs increase with material nonlinearity as will be seen in this section for the cases of elasticity and elastoplasticity.

A methodology to statistically determine the size of the RVE was presented by Gitman et al. [16] and was applied in the current work to determine the required RVE sizes for the determination of the elastic and inelastic properties of a composite. The applied methodology can be summarized in the following steps.

1. Select the domain sizes to be generated. In the present case, this means the selection of the number of inclusions in the domain.
2. Generate multiple microstructure realizations of the same size. In the present case, five random microstructures were generated for each domain size.

3. Perform finite element simulation and carry out computational homogenization to determine the desired property.
4. Carry out statistical analysis by calculating the *chi-square criterion* (χ^2) using equation (4.15).

$$\chi^2 = \frac{\sum_{i=1}^n (a_i - \langle a \rangle)^2}{\langle a \rangle} \quad (4.15)$$

where a_i is the property under consideration for realization i , n is the total number of realizations of the same size and $\langle a \rangle$ is the mean value of the property under consideration.

A lower chi-square value indicates less variation in homogenized property among random realizations of the same size. If the *chi-square criterion* is below a threshold value, the domain can be considered an RVE. Gitman et al. [3] suggested using at least five random domain realizations for the calculation of the *chi-square criterion* and suggested using a threshold value of 0.1. In the RVE generation algorithm used, the positions of the particles in the RVE are generated using uniform distribution functions which is defined by two parameters. If five random realizations are generated for each size, the number of degrees of freedom = *number of random realizations - parameters controlling particle distribution - 1* = 5 - 2 - 1 = 2. For two degrees of freedom, a *chi-square* value of 0.1 represents an accuracy of 95% [107]. In the presented work, a threshold of 0.01 was selected which represents an accuracy of greater than 99%.

4.3.1 Elasticity

To determine the required size of the RVE for the determination of elastic properties, computational microstructures were generated with 10, 50, 100, 200 and 300 inclusions for volume fractions of 1%, 5%, 10%, 15%, 20% and 25%. No porosities were considered. The elastic modulus and the Poisson's ratio of the matrix were set to 50 GPa and 0.3 respectively. The elastic modulus of the inclusion was varied between two to ten times the elastic modulus of the matrix while its Poisson's ratio was fixed at 0.3. This allowed the effect of the property mismatch on the RVE size to be analyzed.

Five random microstructure realizations ($n=5$) were generated for each case. Computational homogenization was carried out and the *chi-square criterion* was calculated for the homogenized elastic modulus. The variation of the homogenized elastic modulus with inclusion volume fraction are shown in Figures 4.3 to 4.5 for E_{inc}/E_{mat} equal to 2, 5 and 10 respectively. The convergence results are presented in Figure 4.6. As can be seen from Figure 4.6, inclusion volume fractions 1%, 5% and 10% are converged for 10 particles. For 15% inclusions, the required number of particles is 10 for E_{inc}/E_{mat} equal to 2 and 50 for E_{inc}/E_{mat} equal to 5 and 10. For 20% inclusions, 50 inclusion particles are required for all elasticity modulus ratios. Finally, for 25% inclusion fraction, the required number of inclusion particles are 50, 100 and 200 for E_{inc}/E_{mat} equal to 2, 5 and 10 respectively.

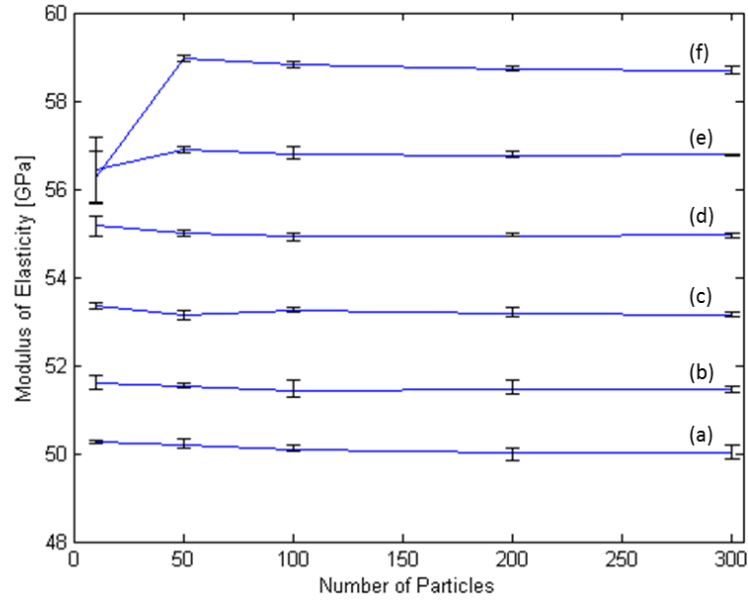


Figure 4.3. Elasticity modulus variation with inclusion volume fraction for $E_{inc}/E_{mat} = 2$ with (a) 1% reinforcement (b) 5% reinforcement (c) 10% reinforcement (d) 15% reinforcement (e) 20% reinforcement and (f) 25% reinforcement.

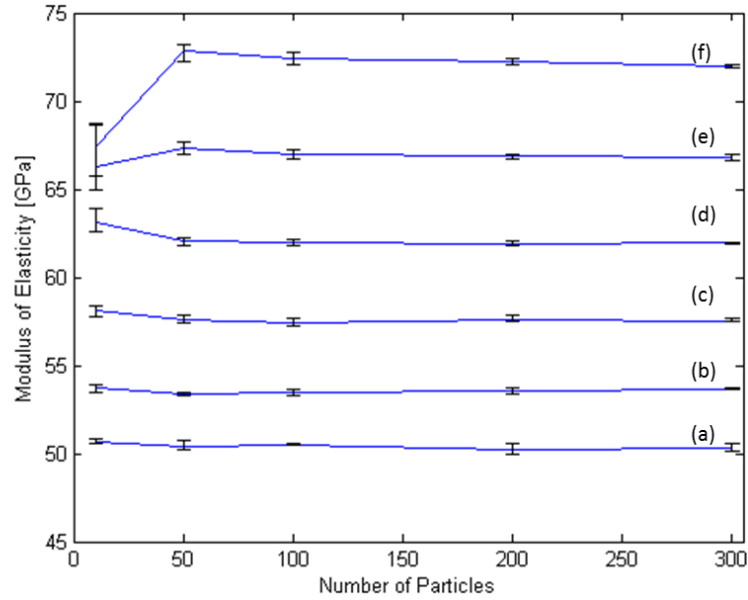


Figure 4.4. Elasticity modulus variation with inclusion volume fraction for $E_{inc}/E_{mat} = 5$ with (a) 1% reinforcement (b) 5% reinforcement (c) 10% reinforcement (d) 15% reinforcement (e) 20% reinforcement and (f) 25% reinforcement.

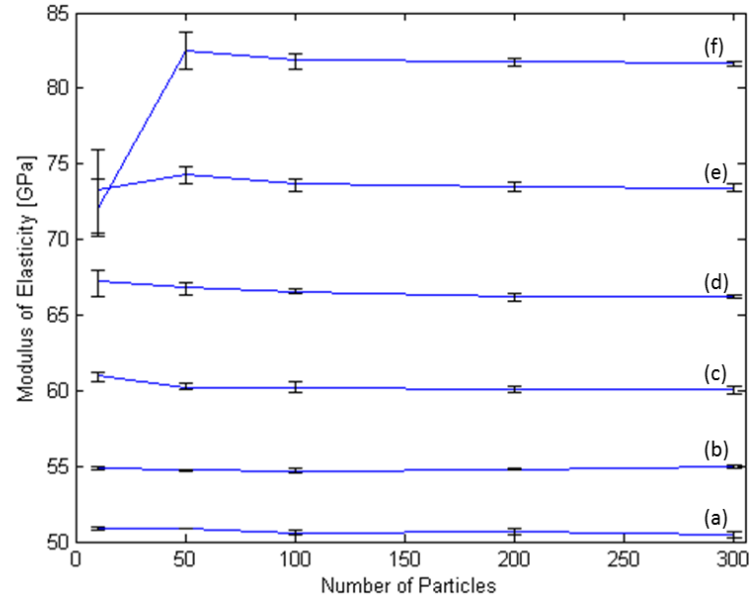
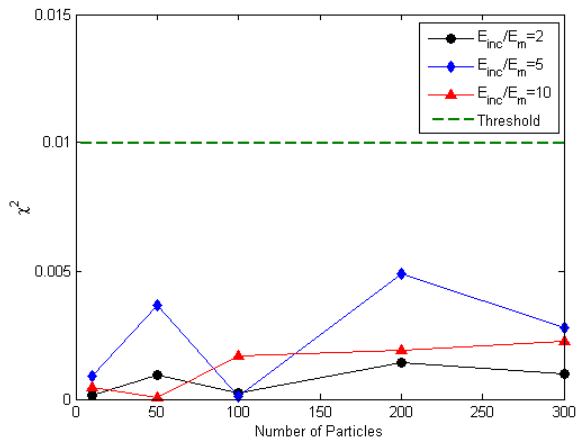
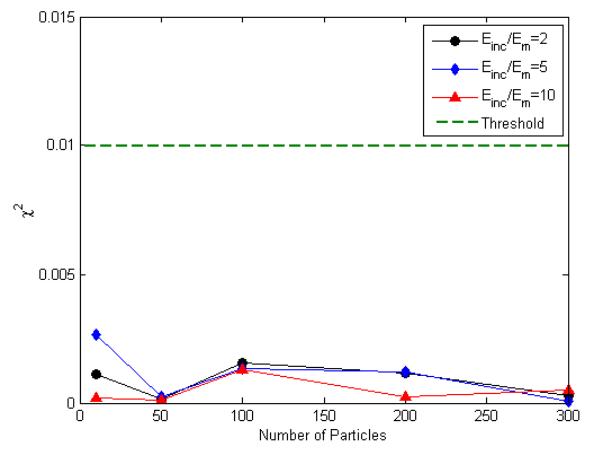


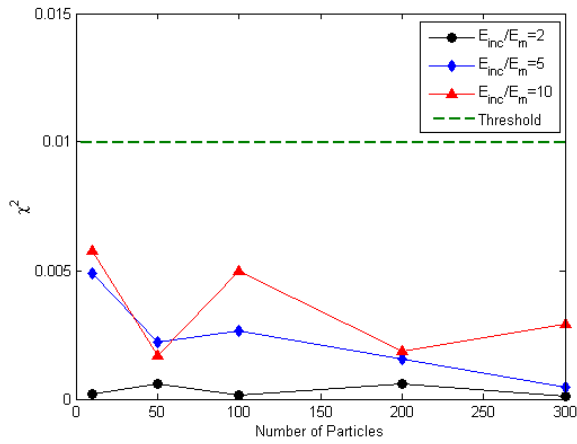
Figure 4.5. Elasticity modulus variation with inclusion volume fraction for $E_{inc}/E_{mat} = 10$ with (a) 1% reinforcement (b) 5% reinforcement (c) 10% reinforcement (d) 15% reinforcement (e) 20% reinforcement and (f) 25% reinforcement.



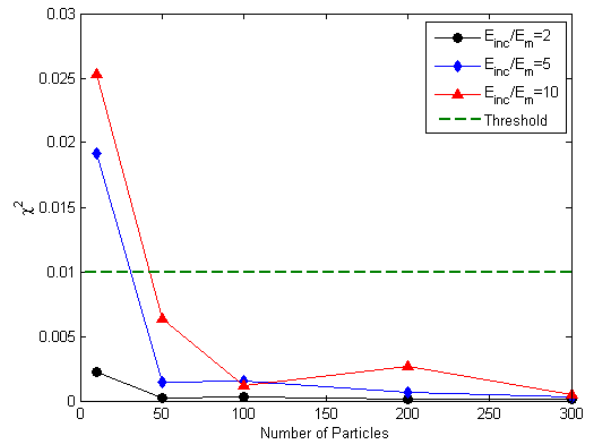
(a)



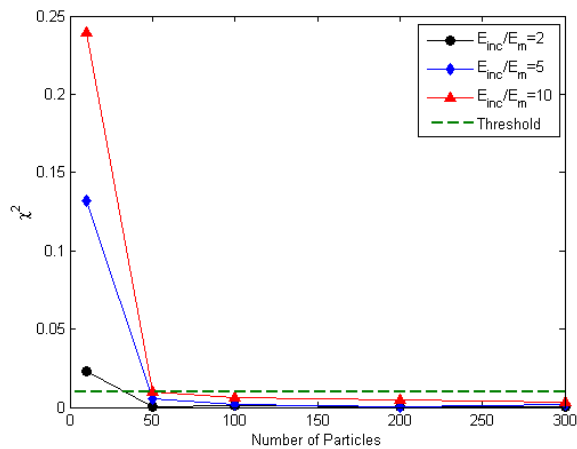
(b)



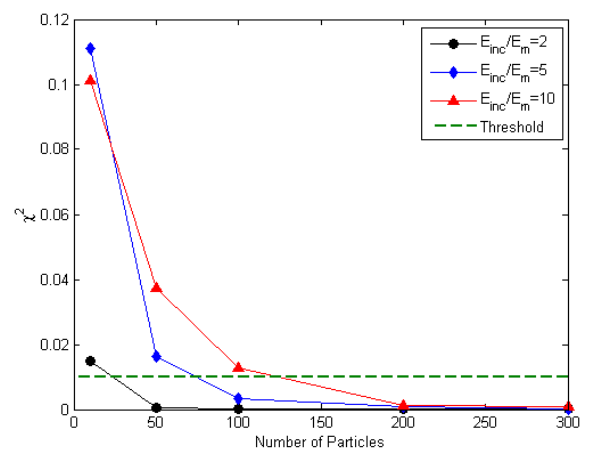
(c)



(d)



(e)



(f)

Figure 4.6. RVE Size convergence for Elastic modulus having (a) 1% reinforcement (b) 5% reinforcement (c) 10% reinforcement (d) 15% reinforcement (e) 20% reinforcement and (f) 25% reinforcement

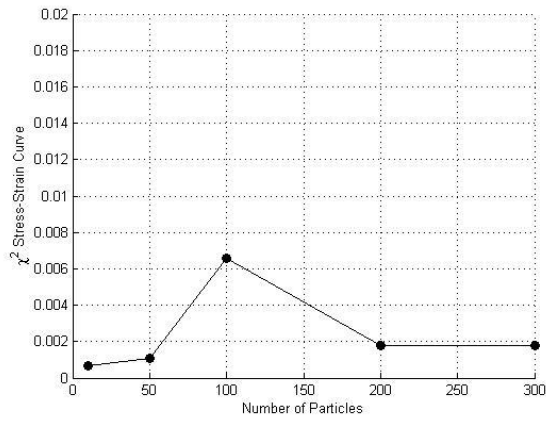
4.3.2 Rate-independent plasticity

To determine the RVE size required for homogenization of the elastoplastic properties of composites, the case of Aluminum-Alumina composite was considered. Aluminum matrix was modeled as bilinear elastoplastic with a yield stress of 246.4 MPa and tangent modulus of 139.5 MPa. Sets of five microstructure realizations ($n=5$) were generated for volume fractions 1%, 5%, 10%, 15%, 20% and 25% having 10, 50, 100, 200 and 300 particles. Finite element simulations were performed and the homogenized stress-strain curves were determined. The average *chi-square criterion* for the stresses at m points along the stress-strain curve was calculated using equation (4.16) and is shown in Figure 4.7.

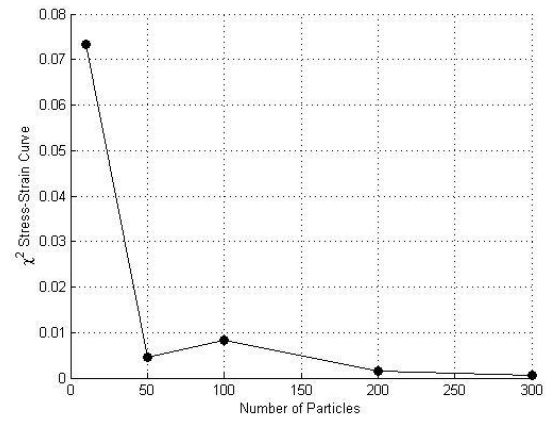
$$\chi^2 = \frac{1}{m} \sum_{j=1}^m \frac{\sum_{i=1}^n (\sigma_j^i - \langle \sigma \rangle_j)^2}{\langle \sigma \rangle_j} \quad (4.16)$$

where n and m are the number of random RVE realizations and number of points on the stress-strain curve respectively.

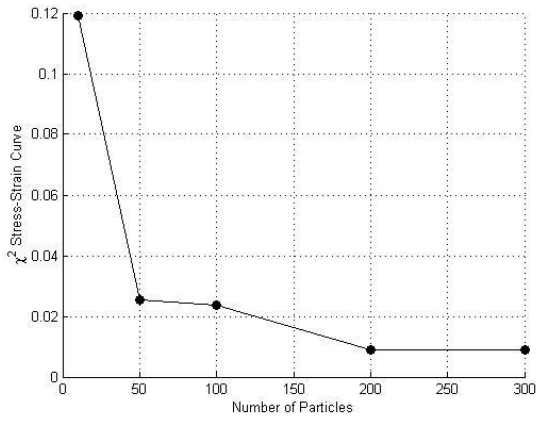
The results show that for 1%, the predicted stress-strain curve is converged for 10 particles. 5% volume fraction of inclusions requires 50 particles and 10%, 15% and 20% volume fractions require 200 particles for convergence. For 25% volume fraction, no significant improvement was observed between 100 and 300 particles. The final *chi-square* value was 0.1 which is higher than the threshold value of 0.01 used in the current work but still provides an accuracy of 95% for the case of five random realizations with two degrees of freedom.



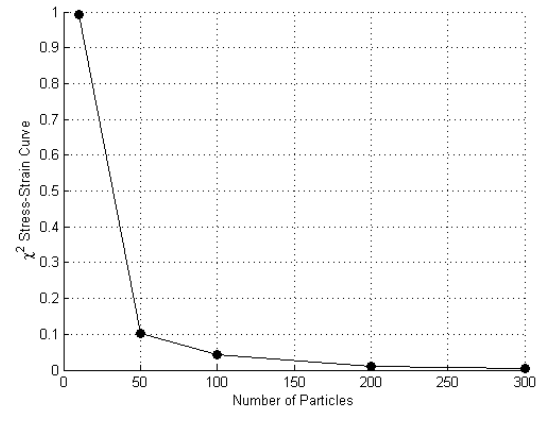
(a)



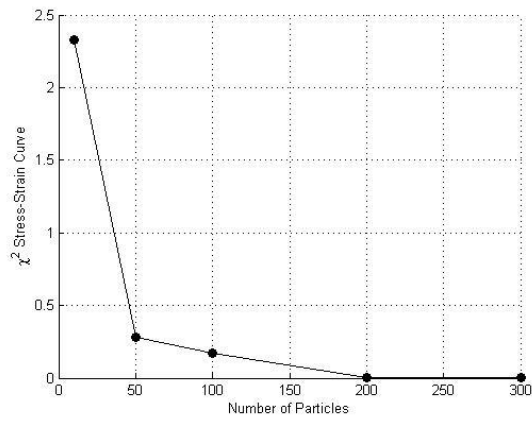
(b)



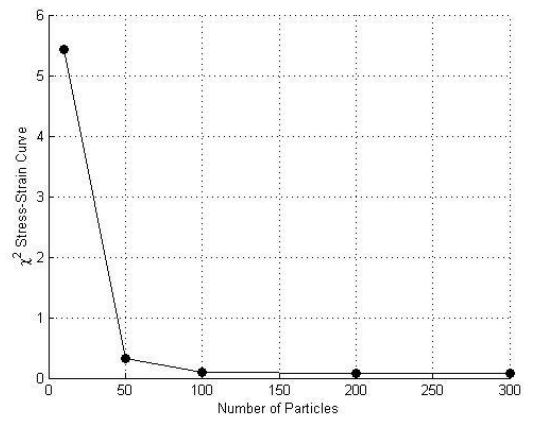
(c)



(d)



(e)



(f)

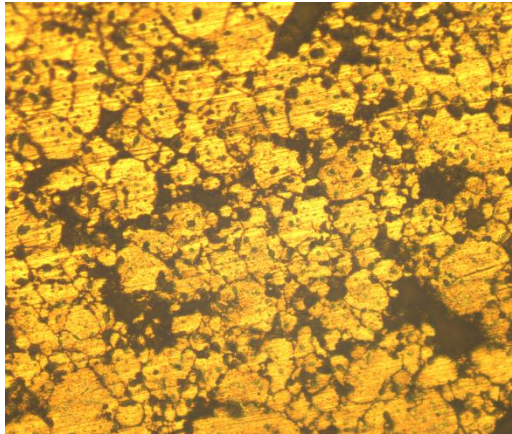
Figure 4.7. RVE Size convergence for elastoplastic material behavior having (a) 1% reinforcement (b) 5% reinforcement (c) 10% reinforcement (d) 15% reinforcement (e) 20% reinforcement and (f) 25% reinforcement.

4.4 EXPERIMENTAL WORK

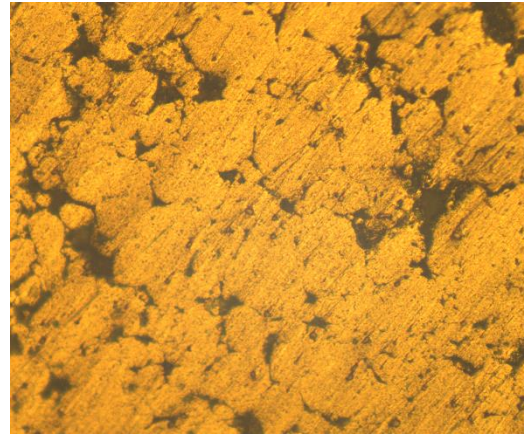
In order to validate the homogenization methodology, aluminum matrix composites with alumina reinforcement were sintered. The average particle size of alumina used was 300 nm. In total, three samples were prepared: a pure aluminum sample and samples with 5 wt.% and 10 wt.% Alumina.

Proper proportions of the matrix and reinforcement particles were mixed in a jar mill for 10 minutes to ensure proper mixing. The powder mixture was compacted and the green compacts were sintered in Argon environment at a temperature of 600°C. The sintering time was set as 60 and 120 minutes for 5 wt.% and 10 wt.% alumina respectively. It is important to note here that the objective of the experimental work was not to sinter fully dense samples but to validate the modeling approach. Therefore, the sintering times were varied to get different levels of porosities in the sintered samples.

The sintered composite samples were analyzed using optical and scanning electron microscopy techniques. The optical micrographs, presented in Figure 4.8, show that 5 wt.% alumina composite has smaller grain sizes and higher porosity than the 10 wt.% alumina composite. The distribution of alumina particles in the aluminum matrix is shown in the SEM micrographs presented in Figure 4.9.



(a)

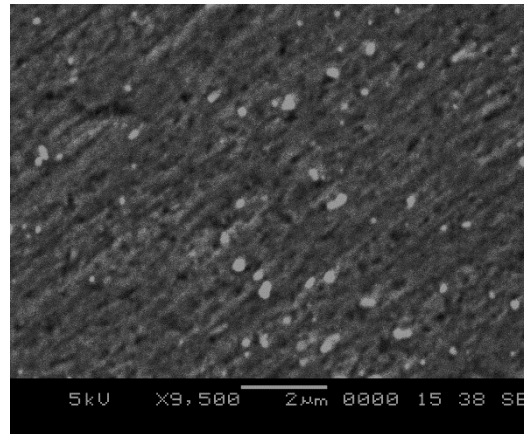


(b)

Figure 4.8. Optical micrographs of Aluminum with (a) 5 wt.% Alumina and (b) 10 wt.% Alumina.



(a)



(b)

Figure 4.9. SEM micrographs showing alumina particles inside aluminum matrix for (a) 5 wt.% Alumina and (b) 10 wt.% Alumina.

Densities of the sintered samples were measured using the Archimedes principle. It was found that the 5 wt.% alumina composite was highly porous with a porosity volume fraction of 23.32% while the 10 wt.% alumina composite had a porosity of 9.76%. These measurements agree with the findings of optical micrographs which showed the 5 wt.% alumina composite to be more porous than the 10 wt.% alumina composite.

Table 4.1. Density measurements for sintered samples

Sample	Theoretical density [g/cm³]	Measured density [g/cm³]	Porosity volume fraction
Aluminum	2.7	2.5518	5.49%
5 wt. % Alumina	2.74	2.1008	23.32%
10 wt.% Alumina	2.79	2.5175	9.76%

Finally, compression tests were carried out on the three samples. The stress strain behavior of the three samples is presented in Figure 4.10. It can be seen in the figure that the 5 wt.% alumina composite sample shows lower levels of stress than that in the pure aluminum sample. This is due to the high level of porosity in the composite sample. On the other hand, the 10 wt.% alumina composite shows a stress-strain response comparable to that of the pure aluminum sample. This can be explained by the fact that the effect of porosity and alumina cancel each other out.

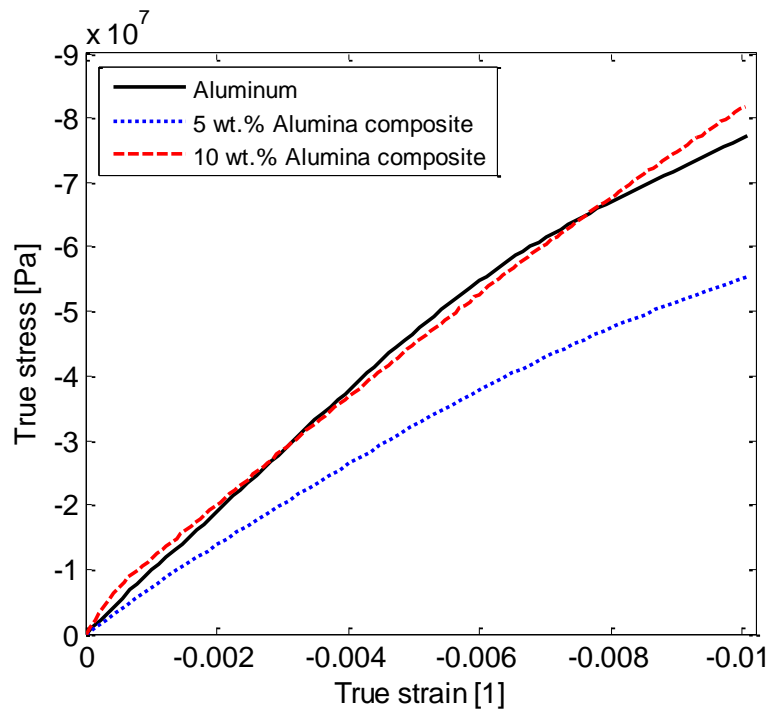


Figure 4.10. Stress-strain behavior of the sintered samples under compression.

4.5 MODEL VALIDATION

4.5.1 Elasticity homogenization

For validation of the methodology, results of Gudlur et al. [108] were selected. In their work, Gudlur et al. used object oriented finite element method code (OOF2) to determine the homogenized properties using actual microstructures of the composite. They selected four 50 μm x 50 μm cross sections of the SEM images of the composite and solved for the properties using OOF2. The results of Gudlur et al.'s work is given in Table 4.2 along with the results obtained using the current methodology. As can be seen from Table 4.2, the model shows good agreement with the results of Gudlur et al. In fact, the results of Gudler et al. show a greater scatter between the properties computed using different microstructure images than the current work since they did not carry out a study to determine the required size of the domain required for it to be considered an RVE.

Table 4.2.Validation of Elastic Property Homogenization.

RVE Number	Inclusion VF%	Porosity VF%	E [GPa]		Difference
			Gudlur et al.[108]	Current Work	
RVE 1	20.2	0.4	83.28	85.82	3.05%
RVE 2	21.7	0.1	86.67	87.16	0.56%
RVE 3	20.9	0.7	83.70	86.74	3.63%
RVE 4	21.2	0.0	88.05	92.26	4.78%

4.5.2 Rate-independent plasticity homogenization

For the validation of elastoplastic homogenization methodology, the homogenized stress-strain response of the sintered Aluminum-Alumina composite samples was estimated using the proposed methodology and compared with the experimental stress-strain response of the composites. The matrix was model as elastoplastic and the inclusions were modeled as elastic. The elastic modulus of the alumina inclusion and its Poisson's ratio were taken as 370 GPa and 0.22 respectively. The properties of aluminum matrix were estimated from the experimental stress-strain curve. A voce-type hardening law, as shown in equation (4.17), was fitted to the data to estimate the hardening law.

$$\sigma_y = 44 + (93.25 - 44)(1 - \exp(-\varepsilon_p / 0.002927)) + 3545.55\varepsilon_p \text{ MPa} \quad (4.17)$$

Since the matrix properties were estimated from the experimental data, the modeled matrix material already included the effect of the porosity present in the aluminum sample. Therefore, the matrix material was assumed to have a density of 2.5518 g/cm³. The porosity volume fractions of the 5 wt.% and 10 wt.% alumina composite samples were recalculated as 19.23% and 4.64% respectively and used in the algorithm to generate computational microstructures.

The validation results are shown in Figure 4.11 and show good agreement between the homogenization and experimental results.

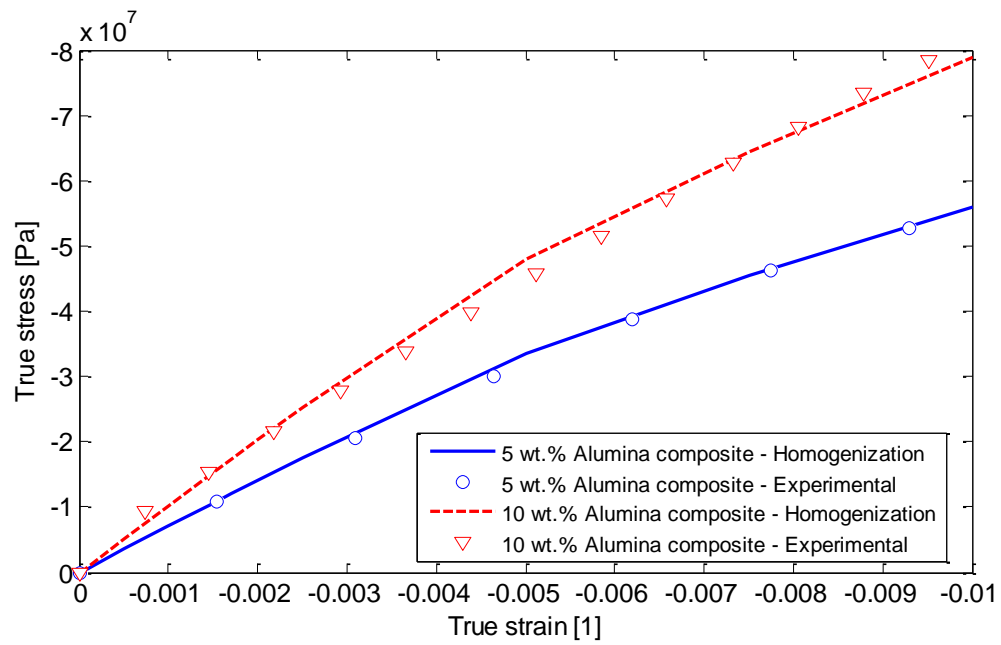
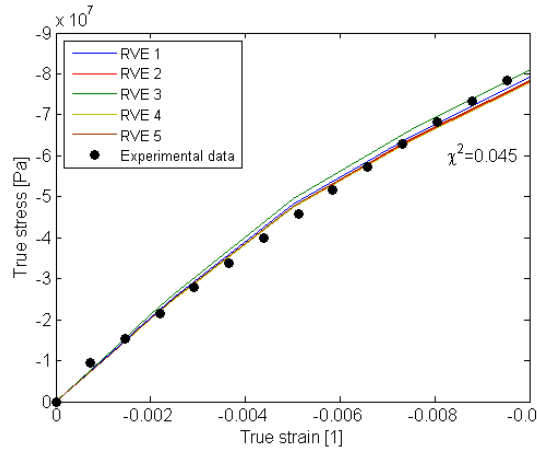


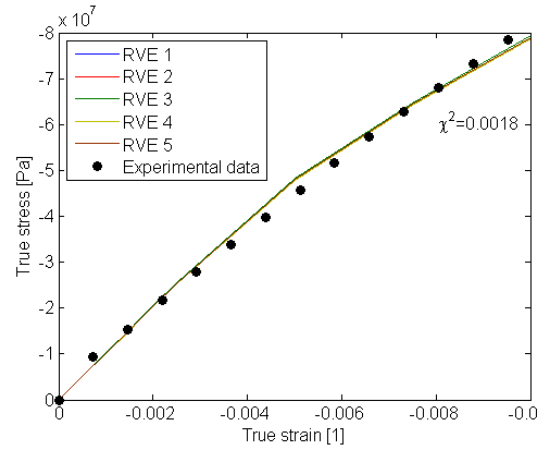
Figure 4.11. Validation of plastic property homogenization with experimental data.

4.5.2.1 Effect of microstructural domain size on prediction accuracy

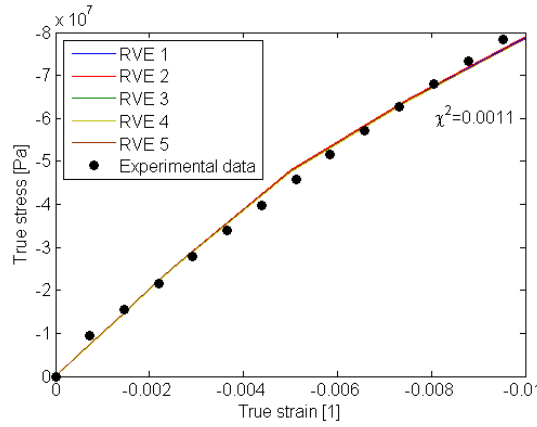
A study to determine the correct RVE size for the homogenization of elastoplastic material response is presented in section 4. Finding the correct domain size is critical for obtaining repeatable results using random computational microstructures. In this section, the prediction repeatability for various microstructural domain sizes is analyzed by comparing the predicted stress-strain response to the experimental one for 10 wt.% alumina composite. It should be noted that 10 wt.% of alumina corresponds to 6.69% volume fraction. The comparison is shown in Figure 4.12. The figure also shows the chi-square value for each case.



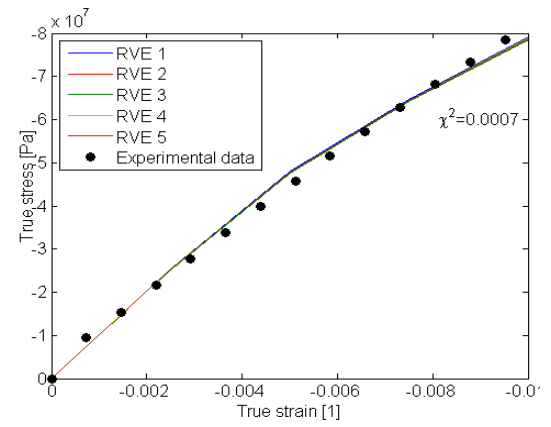
(a)



(b)



(c)



(d)

Figure 4.12. Comparison of predicted stress-strain response of computational microstructures with (a) 10 inclusion particles, (b) 50 inclusion particles, (c) 100 inclusion particles and (d) 150 inclusion particles with experimental response for 10 wt.% alumina composite.

4.6 CASE STUDIES

The following sections present the application of the formulated homogenization methodologies to study the effect of inclusion volume fraction on the bulk properties of the composite.

4.6.1 Elasticity

In this section, the effect of the inclusion volume fraction on the homogenized elastic modulus of the composite are presented following the discussion on one detailed case. Figure 4.13 shows the displacement contours on the RVE as a result of the six strain vectors shown in equations (4.7) with $\varepsilon_o = 1$. As is clear from the figure, each strain load vector in equations (4.7) applies only a single type of strain on the RVE. The homogenized stress vectors in these cases each provide one column of the elasticity matrix. The complete homogenized elasticity matrix of the RVE is given in equation (4.18).

$$E = \begin{bmatrix} 115.73 & 58.38 & 58.67 & 0.06 & -0.06 & -0.08 \\ 58.38 & 115.16 & 58.51 & -0.01 & 0.03 & 0.04 \\ 58.67 & 58.51 & 115.90 & -0.02 & -0.06 & 0.02 \\ 0.06 & -0.01 & -0.02 & 28.29 & -0.03 & 0.02 \\ -0.06 & 0.03 & -0.06 & -0.03 & 28.49 & -0.02 \\ -0.08 & 0.04 & 0.02 & 0.02 & -0.02 & 28.36 \end{bmatrix} GPa \quad (4.18)$$

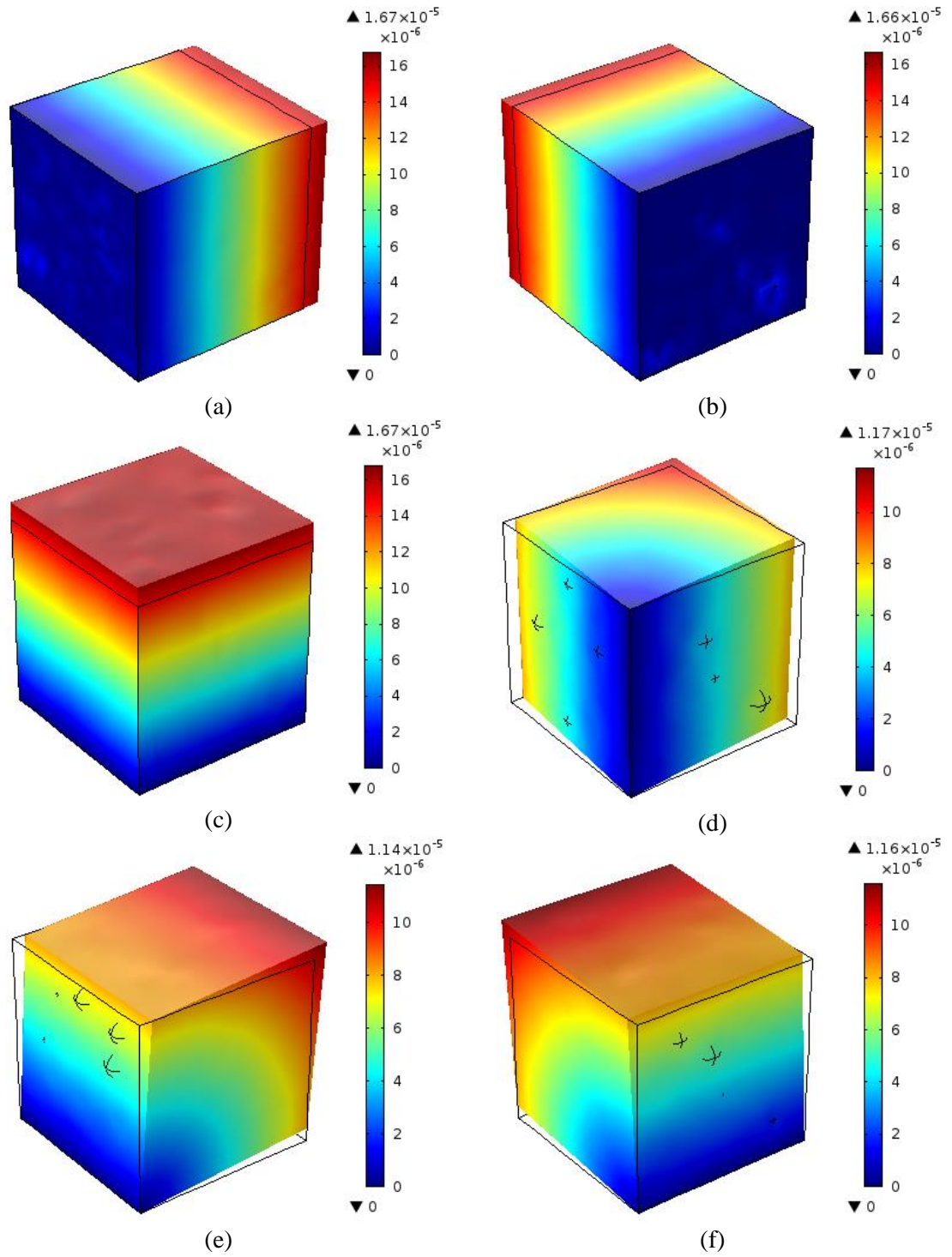


Figure 4.13. Displacement contours for the six load vectors used for finding the elasticity matrix (a) \mathcal{E}_{xx} (b)

\mathcal{E}_{yy} (c) \mathcal{E}_{zz} (d) \mathcal{E}_{xy} (e) \mathcal{E}_{xz} and (f) \mathcal{E}_{yz}

4.6.1.1 Effect of inclusion volume fraction

In order to further validate the model and to study the effect inclusion volume fraction on the macroscale elastic properties, Alumina-Aluminum composites with inclusion volume fractions of 1%, 2.5%, 5%, 10%, 15%, 20% and 25% were modeled using the computational homogenization approach. A total of 300 inclusions were introduced in the matrix. The porosity fraction was set at 0. The homogenized elastic modulus was compared to those predicted by the Mori Tanaka model and the self-consistent model. The upper and lower bounds of the elastic modulus of were also calculated using the rule of mixtures. The homogenized properties are presented in Table 4.3 and the comparison is presented in Figure 4.14. The results show that the computational homogenization approach presented in the current work and self-consistent mean-field homogenization show very close agreement. In comparison, the Mori Tanaka approach under-predicted the elastic moduli of the composite at higher inclusion volume fractions.

Table 4.3. Elastic properties for Alumina-Aluminum composite

Inclusion volume fraction	E [GPa]	ν
1%	65.42	0.348
5%	70.49	0.342
10%	76.26	0.337
15%	82.93	0.330
20%	90.23	0.324
25%	98.22	0.316

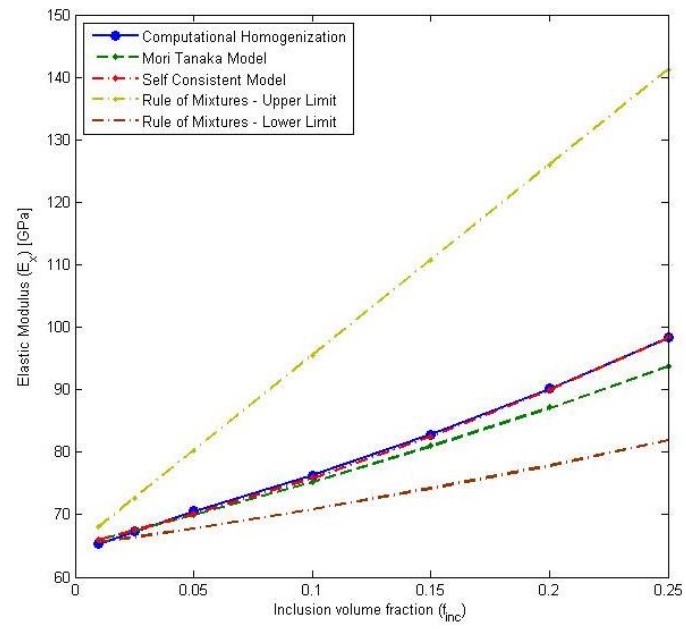


Figure 4.14. Effect of inclusion volume fraction.

4.6.2 Rate-independent plasticity

In this section, the results of computational homogenization of elastoplastic material response of metal matrix composite materials is presented. First, one case is discussed in detail. The results of a parametric study are then presented to show the effect of inclusion volume fraction on the predicted properties. For the detailed study, the case of 10% Alumina-Aluminum composite with 100 particles was selected. The geometry of the RVE is shown in Figure 4.15. The material properties used are reported in section 4.2.

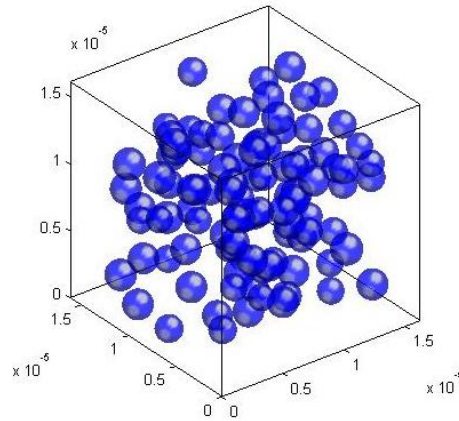


Figure 4.15. RVE for 10%Alumina-Aluminum composite with 100 Alumina particles.

The homogenized stress-strain curve for the composite is shown in Figure 4.16. The localized yielding of the matrix begins at macroscopic strain $\epsilon_{y,loc}$ but the macroscopic stress-strain curve does not show a yielding behavior until after $3\epsilon_{y,loc}$. Therefore, a macroscopic experiment to measure the stress-strain response of the composite will not be able to capture the localized yielding in the matrix. The effective plastic strains in the RVE at various macroscopic strains is shown in Figure 4.17. As can be seen from Figure 4.17(a)-

(c), the yielding is localized around the inclusions up to $3\varepsilon_{y,loc}$ while Figure 4.17(d)-(f) show bulk yielding in the matrix. This agrees with the macroscopic stress-strain curve shown in Figure 4.16. The effective plastic strains at the point of initial localized yielding are shown in Figure 4.18.

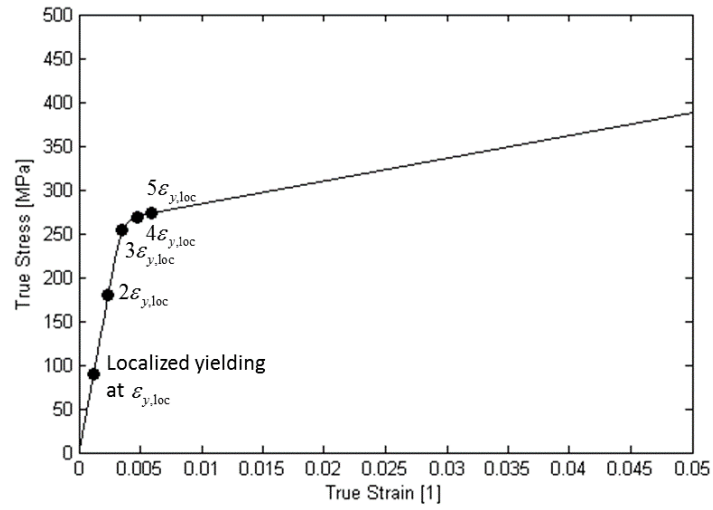


Figure 4.16. Stress-Strain curve for 10% Alumina-Aluminum composite.

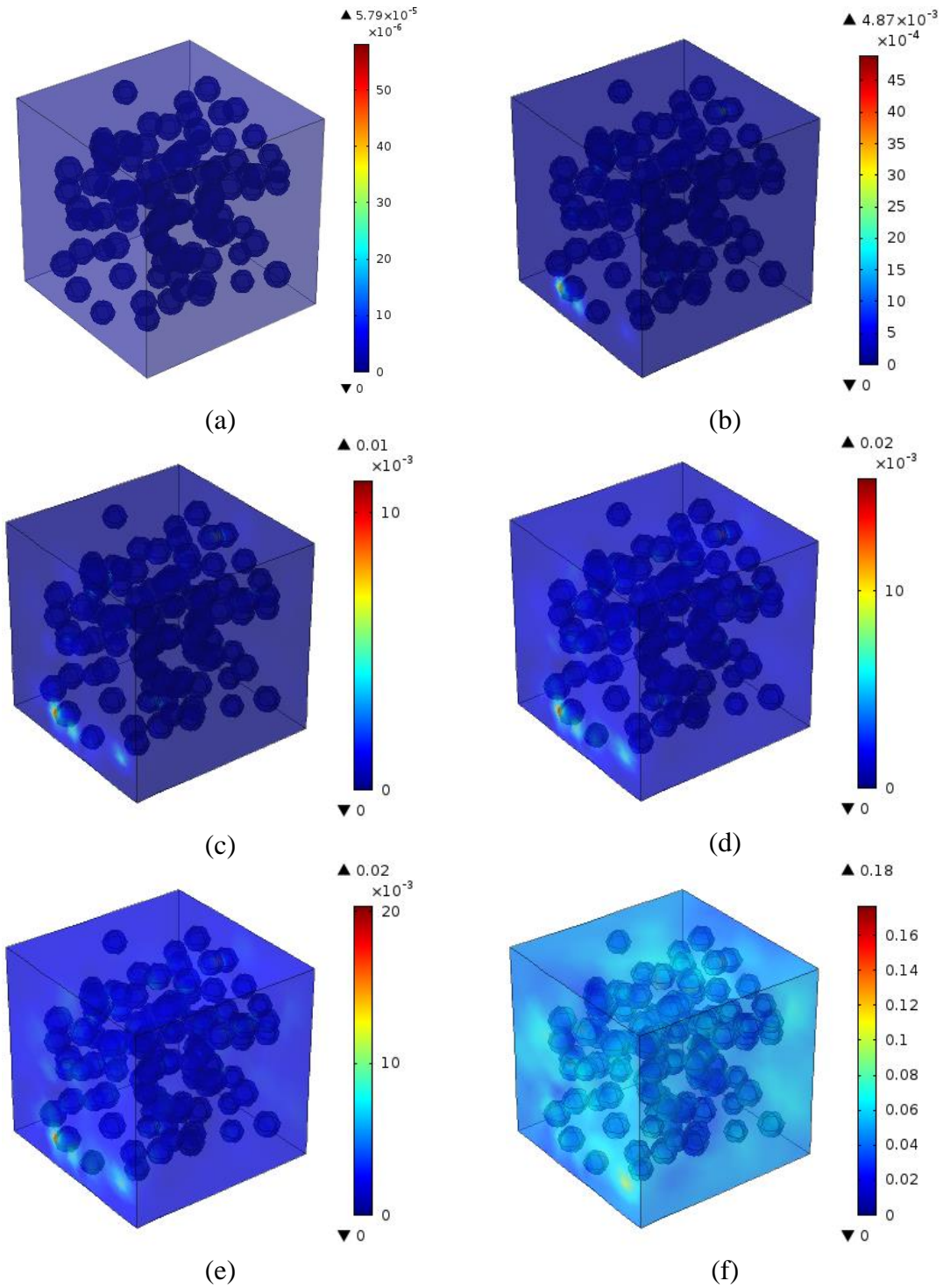


Figure 4.17. Effective plastic strains in the RVE when macroscopic strain is (a) $\epsilon_{y,loc}$ (b) $2\epsilon_{y,loc}$ (c) $3\epsilon_{y,loc}$ (d) $4\epsilon_{y,loc}$ (e) $5\epsilon_{y,loc}$ and (f) 0.05 .

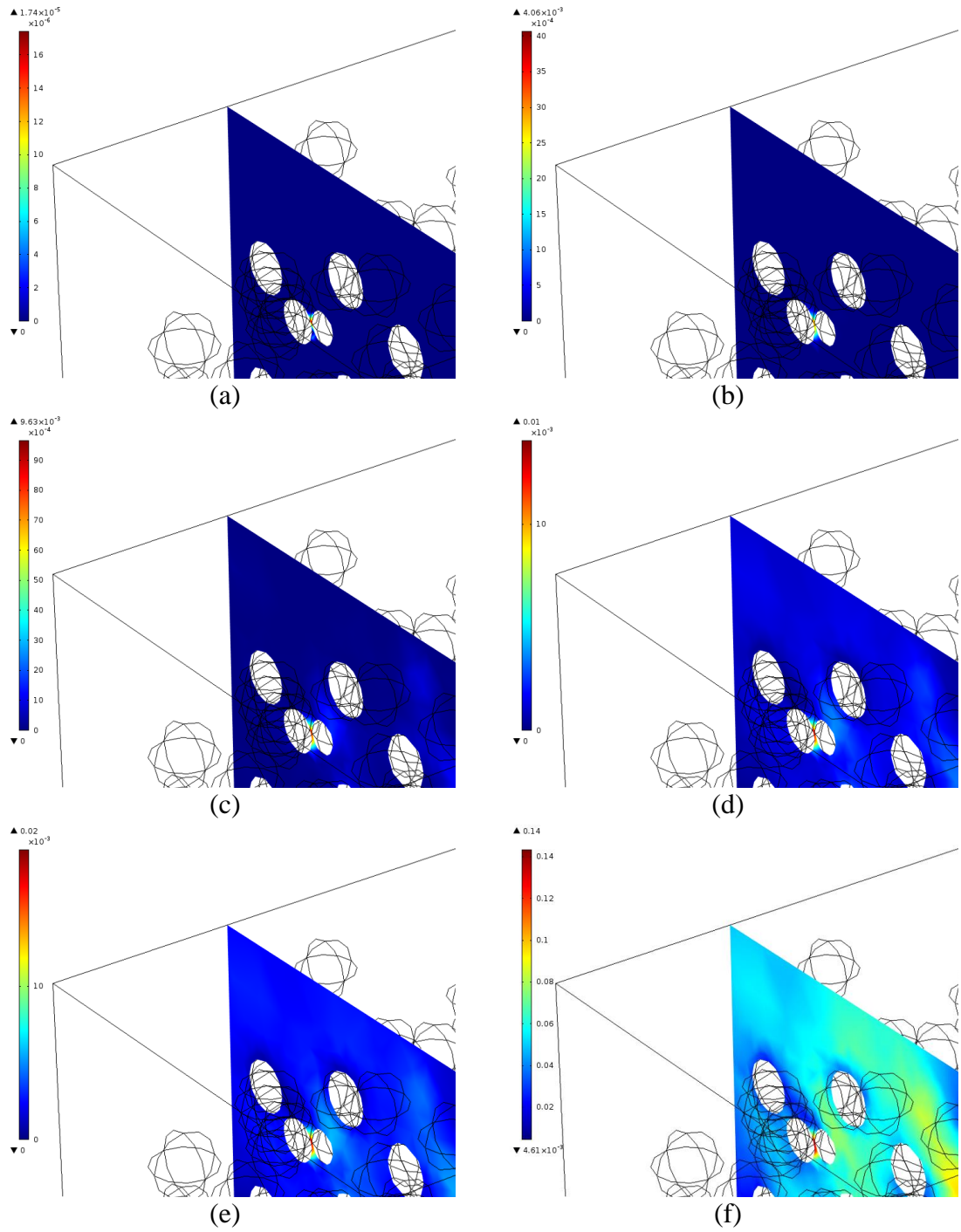


Figure 4.18. Effective plastic strains in the RVE at critical point when macroscopic strain is (a) $\varepsilon_{y,loc}$ (b)

$2\varepsilon_{y,loc}$ (c) $3\varepsilon_{y,loc}$ (d) $4\varepsilon_{y,loc}$ (e) $5\varepsilon_{y,loc}$ and (f) 0.05.

4.6.2.1 Effect of inclusion volume fraction

To study the effect of inclusion volume fraction on the stress strain response of a composite, the case of Al-Cu-Mg(2080)-SiCp-T8 [109] was analyzed. The matrix was model as elastoplastic and the inclusions were modeled as elastic. The elastic modulus and the yield stress of the matrix were determined from the experimental stress-strain curve of the matrix provided by Chawla and Shen [109] and were found to be 79.3 GPa and 485.8 MPa respectively. The experimental hardening behavior of the matrix was also used in the simulation. The elastic modulus of the inclusion and its Poisson's ratio were 415 GPa and 0.225 respectively. The effect of inclusion volume fraction on the stress-strain response of the composite is shown in Figure 4.19.

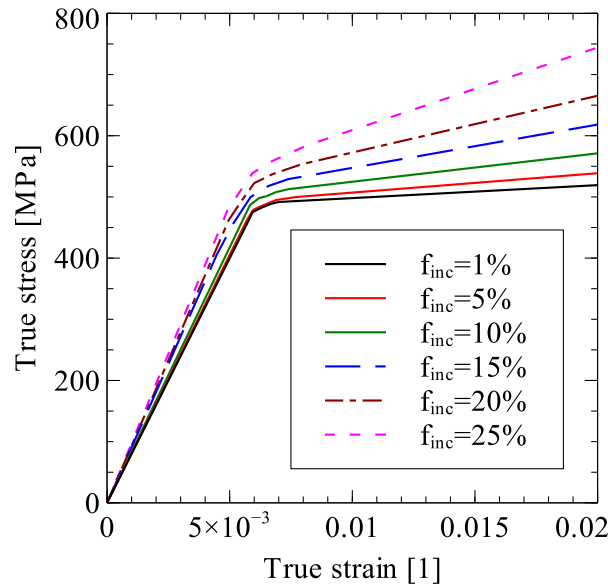


Figure 4.19. Effect of Inclusion volume fraction on stress-strain response of Al-Cu-Mg (2080) - SiCp-T8 composite.

Using the results of computational homogenization, bulk yield stress and parameters of a hardening rule can also be determined. Here, the parameters of a Voce-type hardening law, given by equation (4.19) are determined using a Trust-Region optimization algorithm in *MATLAB*. The parameters of the hardening law are shown in Table 4.4.

$$\sigma_y = \sigma_o + (\sigma_A - \sigma_o)(1 - \exp(-\varepsilon_p / \varepsilon_o)) + m\varepsilon_p \quad (4.19)$$

Table 4.4. Voce-type hardening law parameters for Al-Cu-Mg (2080) - SiC_p-T8 composite.

Inclusion volume fraction	σ_o [MPa]	σ_A [MPa]	m[GPa]	ε_o
1%	485	489.5	1.295	0.001625
5%	488	497.3	1.976	0.002778
10%	497.6	513.6	2.823	0.004156
15%	507.8	532.2	4.180	0.004711
20%	518.9	553.5	5.673	0.005551
25%	531.7	579.5	8.485	0.006016

4.7 CONCLUDING REMARKS

In this chapter, a numerical methodology for the estimation of the elastoplastic material properties of metals matrix composites was presented and validated with experimental results.

As part of the approach, a methodology to determine the minimum RVE size required for correct property estimation was presented. The methodology was used to determine required RVE sizes for the determination of elastic properties for a variety of property contrast and for the determination of elastoplastic response using the example of Al-Al₂O₃ composite. It was found that homogenization of nonlinear properties like plasticity require larger RVEs than linear properties such as elasticity.

The formulated computational homogenization methodology was used for the estimation of elastic and rate-independent elastoplastic properties of metal matrix composites and validated. The effect of inclusion volume fraction on the bulk material properties of the composite was investigated and, effective material models were determined that can represent the bulk constitutive response of the composites.

CHAPTER 5

MEAN-FIELD HOMOGENIZATION: METHODOLOGY

AND APPLICATIONS

5.1 INTRODUCTION

Metal matrix nanocomposites (MMNCs) are very promising materials that are seeing significant interest from investigators worldwide due to their suitability to a wide range of applications. MMNCs show higher strength and stiffness compared to conventional composites while maintaining the ductility of the metals. The use of a variety of matrix metals having several types of nanoscale inclusions has been reported in the literature. The most commonly reported metals matrices include Aluminum [110–115], Magnesium [116–118], Copper [119] and their alloys. For inclusions, the use of ceramic compounds such as SiC [111,120,121], Al₂O₃ [113–115,119,122], and CNTs [117,123–125] has been extensively reported.

MMNCs show significant enhancement of mechanical properties at very low volume fractions of reinforcements [126]. This is because several new strengthening

mechanisms come in play as the reinforcement size is reduced to the nanometer scale. These include the load transfer effect, Hall-Petch strengthening, Orowan strengthening and property mismatch. Because of the load transfer effect, the strength of the soft matrix material is enhanced when the load is transferred to the stiffer and harder reinforcement. Hall-Petch strengthening occurs due to the interaction of dislocations with the grain boundaries. The fact that polycrystalline materials are stronger than single crystals was first reported by Hall [127] and Petch [128] in the early 1950s. Orowan strengthening [116,126,129] occurs due to the interaction of the reinforcement particles with dislocations causing dislocation bowing leading to Orowan loops. Finally, the property mismatch [116,118,126,129] causes the generation of geometrically necessary dislocations (GNDs) during straining. The overall strengthening of the nanocomposites is a combination of the above-mentioned strengthening mechanisms.

Several models to estimate the strength of nanocomposites and nanostructured metals, in general, have been reported in the literature [116,118,129–133]. Dunstan and Bushby [130] have presented a comprehensive analysis of various equations that can be used to model Hall-Petch effect using several data sets from literature. Khan et al. [131], using experimental results for Al and Fe, showed that as crystallite size is reduced, the parameters of Hall-Petch equation change. They also formulated a crystallite size, strain rate, and temperature dependent hardening law for nano-crystalline metals. An improved version of the model was presented by Farrokh and Khan [133]. For estimating the yield strength of metal matrix nanocomposites, Zhang and Chen [118] formulated a model that incorporated the effects of load transfer strengthening, Orowan strengthening and dislocation density

strengthening mechanisms. Sanaty-Zadeh [129] compared Zhang and Chen's model with a modified Clyne model and found out that Zhang and Chen's model under-predicted the yield strength of nanocomposites because it did not take into account the Hall-Petch effect. Mirza and Chen [116] presented an improved model that also took into account the Hall-Petch effect.

Although a number of models have been formulated to investigate the effect of nanometer sized inclusions and nanometer sized matrix grains on the strength of composites, these models do not predict the complete elastoplastic response of the composite. Moreover, the effect of process parameters such as sintering time and temperature on the strength and elastoplastic behavior of the composite have not been investigated using modeling approach. In this chapter, a methodology to model the elastoplastic response of spark plasma sintered metal matrix particulate nanocomposites is presented. The methodology comprises of two main parts: a model for estimation of average matrix crystallite size in spark plasma sintered metal matrix composites and elastoplasticity constitutive model for the composite based on matrix crystallite size and inclusion particle size. The elastoplasticity constitutive model can take into account the effects of matrix crystallite size, inclusion particle size and inclusion and porosity volume fractions on the elastoplastic stress-strain response of metal matrix nanocomposites. The grain growth model can be used to calculate the average crystallite size of the metal-matrix as a function of sintering time, sintering temperature, inclusion volume fraction and inclusion size. The formulated methodology has been validated against experimentally measured crystallite sizes and stress-strain responses of ball-milled and spark plasma

sintered Al-Al₂O₃ nanocomposite samples synthesized by Nouari et al. [134]. Additional validation of the methodology against the experimental stress-strain response of nanostructured aluminum reported in the literature has also been carried out.

5.2 MODELING METHODOLOGY

The elastoplastic response of metal matrix nanocomposites depends on the intrinsic properties of the matrix and inclusions and on the interactions between the metal matrix and inclusions particles. The constitutive behavior of the metal matrix itself is a function of average crystallite size of the matrix and the size and properties of the inclusion particles. In general, any modeling approach for predicting the elastoplastic response of nanocomposites must relate the microstructural features to the bulk properties of the composite.

In the current work, the overall elastoplastic response of the nanocomposite was estimated using mean-field homogenization approach presented in section 5.2.1. The effect of composite microstructure on the constitutive behavior of the metal matrix is presented in section 5.2.2. In section 5.2.3, models to estimate the effect of ball milling and sintering parameters on the microstructure of composite are presented.

5.2.1 Elastoplastic response of metal-matrix nanocomposites

In the current work, the incremental mean-field modeling approach of Doghri and Tinel [88] who proposed a two-step mean-field homogenization approach for modeling materials with multiple heterogeneities approach was used. For the estimation of elastoplastic

response, the mean-field homogenization methodology was incrementally applied to the nanocomposite during a numerical uniaxial compression test in order to determine the stresses and the tangent modulus of the composite at each strain increment.

In order to model composites with multiple inclusions (or porosity), the first step of the homogenization approach was to divide the microstructure into pseudo grains each containing only one type of inclusion (or porosity). Mean-field homogenization was carried for all pseudo grains to determine the effective stresses and tangent modulus in each grain. Finally, homogenization was carried out across all grains to determine the overall effective stresses and tangent modulus of the heterogeneous material. The two-step homogenization approach is shown graphically in Figure 5.1.

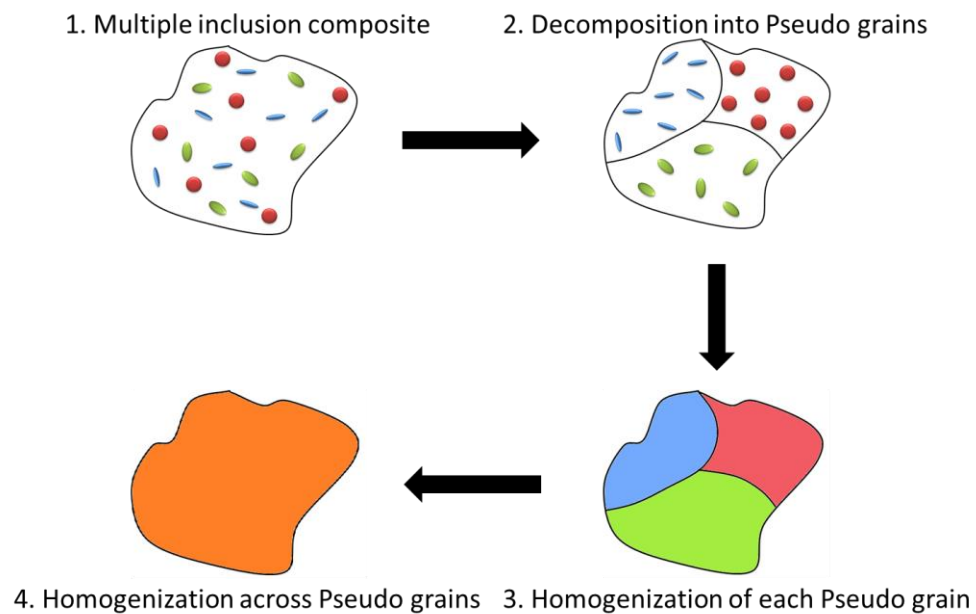


Figure 5.1. Two-step mean-field homogenization approach.

For a microstructure containing N types of inclusions i having volume fractions φ_i , the microstructure was divided into N pseudo grains with each pseudo grain having only one type of inclusion. Within each pseudo grain, the inclusion volume fraction φ_{inc} was set equal to $(1 - \varphi_0)$, where φ_0 is the volume fraction of the matrix.

Macroscale strain increments were applied to each pseudo-grain as the boundary condition. Using the mean-field strain localization relations, the strain increments in the inclusion and matrix were estimated using,

$$\begin{aligned}\Delta \varepsilon_{inc} &= A_{inc} \Delta \varepsilon_M \\ \Delta \varepsilon_{mat} &= (\Delta \varepsilon_M - \varphi_{inc} \Delta \varepsilon_{inc}) / (1 - \varphi_{inc})\end{aligned}\tag{5.1}$$

where φ_{inc} is the volume fraction of inclusion phase, A_{mat} and A_{inc} are the matrix and inclusion strain localization tensors defined by,

$$\begin{aligned}A_{mat} &= \left[(1 - \phi_{inc}) I_4 + \phi_{inc} B_a \right]^{-1} \\ A_{inc} &= B_a : A_{mat} \\ B_a &= \left[I_4 + S : C_{mat,alg}^{-1} (C_{inc,alg} - C_{mat,alg}) \right]^{-1}\end{aligned}\tag{5.2}$$

where I_4 is the 4th order tensor identity, S is the Eshelby tensor [6] and $C_{mat,alg}$ and $C_{inc,alg}$ are the algorithmic tangent moduli of the matrix and inclusion for the current strain increment.

Using the matrix and inclusion strain increments, the stresses in the matrix and inclusion and the corresponding tangent moduli were estimated using the constitutive models of the matrix and inclusion. Finally, the effective stress and tangent modulus of the pseudo-grain were estimated using equation (5.3) and (5.4) respectively.

$$\sigma_{eff,i} = \varphi_{inc} \sigma_{inc} + (1 - \varphi_{inc}) \sigma_{mat} \quad (5.3)$$

$$C_{eff,alg,i} = \varphi_{inc} C_{inc,alg} : A_{inc} + (1 - \varphi_{inc}) C_{mat,alg} : A_{mat} \quad (5.4)$$

Since the strain increments and the algorithmic tangent moduli of the matrix and inclusion are implicitly related, an iterative scheme was used to solve for the stresses and strains in the pseudo grains. At the beginning of the iterations, the inclusion strain increment was assumed to be equal to the macroscale strain increment. Using this value, the entire process was completed once. At the end of the step, the inclusion strain increment was recalculated using the updated parameters. The iterative process was stopped once the difference between the inclusion strain increment at the beginning and the end of an iteration was within tolerance. The iterative scheme is shown in Figure 5.2.

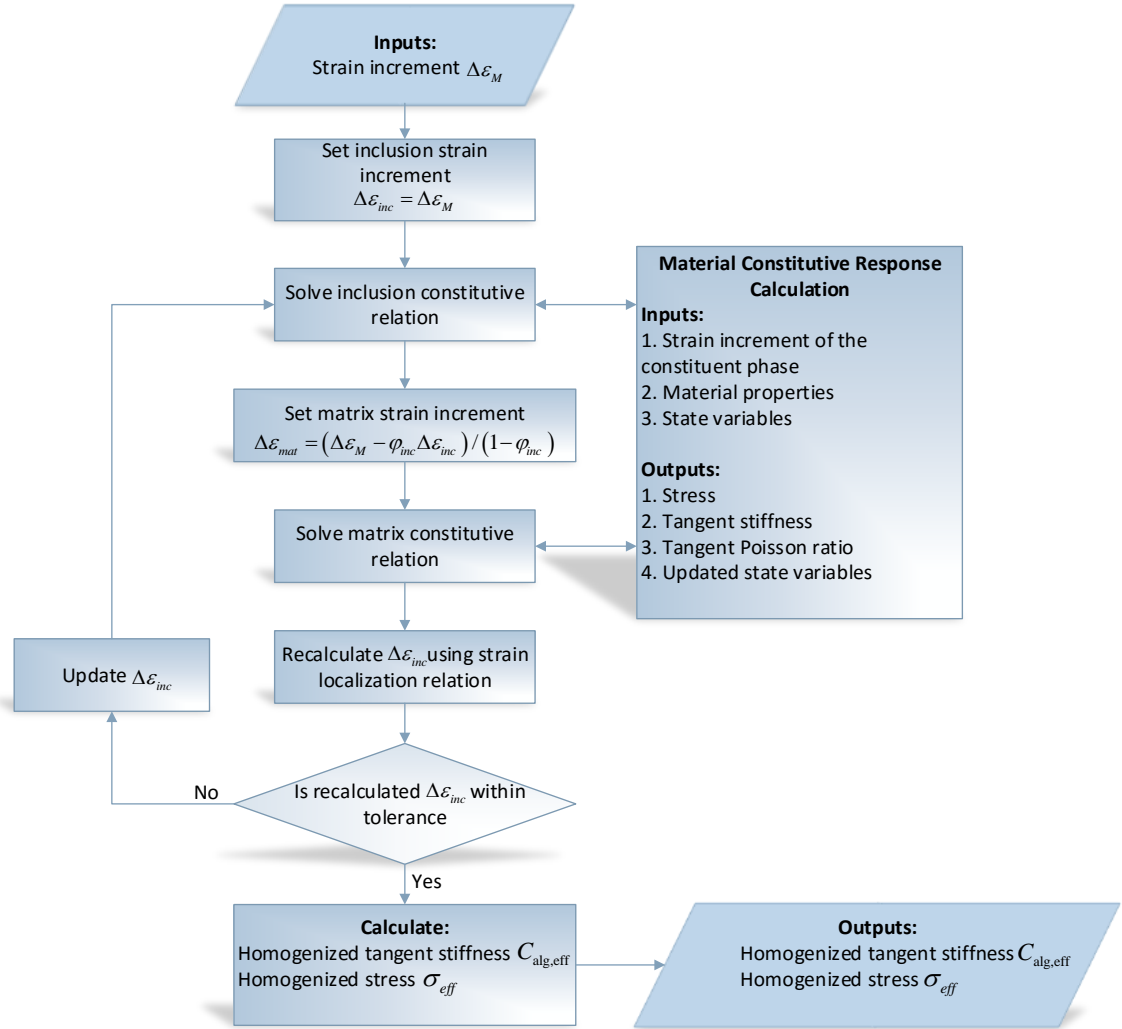


Figure 5.2. Effective stress and tangent Modulus update algorithm for Mean-field homogenization.

Once the effective stresses and tangent moduli of all pseudo grains had been calculated, the macroscale stresses and tangent modulus were calculated using Voigt homogenization across all the pseudo grains using equations (5.5) and (5.6).

$$\sigma_M = \sum_{i=1}^N \frac{\varphi_i}{1 - \varphi_0} \sigma_{eff,i} \quad (5.5)$$

$$C_{alg,M} = \sum_{i=1}^N \frac{\varphi_i}{1 - \varphi_0} C_{eff,alg,i} \quad (5.6)$$

5.2.2 Constitutive modeling of metal matrix

The properties of the metal matrix are a function of the average crystallite size of the matrix as well as the size of the inclusion particles embedded in it. The strengthening of the metal matrix with a reduction in its grain size is referred to as Hall-Petch effect. The strengthening due to hard nanometer-sized inclusions embedded in the matrix occurs through the Orowan strengthening and dislocation density strengthening mechanisms [116,126,132,135].

The elastoplastic constitutive behavior of the metal matrix was defined by equations (5.7)-(5.9).

$$\sigma = C : \varepsilon_{el} \quad (5.7)$$

$$\varepsilon_{el} = \varepsilon - \varepsilon_{pl} \quad (5.8)$$

$$\varepsilon = \frac{1}{2} \left[(\nabla u)^T + \nabla u + (\nabla u)^T \nabla u \right] \quad (5.9)$$

where σ is the true stress, C is the elasticity tensor and $\varepsilon, \varepsilon_{el}$ and ε_{pl} are the total, elastic and plastic strain tensors.

The rate-independent plasticity of the matrix material was modeled using a voce-type hardening model. The model is defined by equations (5.10)-(5.13) .

$$\dot{\varepsilon}_p = \dot{\varepsilon}_{p,eff} \frac{\partial F}{\partial S} \quad (5.10)$$

$$F = \sigma_{mises} - \sigma_y \quad (5.11)$$

$$\sigma_y = \sigma_0 + (\sigma_A - \sigma_0) \left(1 - \exp(-\varepsilon_{p,eff} / \varepsilon_0) \right) + m \varepsilon_{p,eff} \quad (5.12)$$

$$\dot{\varepsilon}_{p,eff} \geq 0, F(\sigma, \sigma_{ys}) \leq 0, \dot{\varepsilon}_{p,eff} F = 0 \quad (5.13)$$

where ε_p is the plastic strain tensor, $\varepsilon_{p,eff}$ is the von Mises effective plastic strain, σ_{mises} is the von Mises stress, σ_{y0} and σ_y are the initial and current yield stress and σ_A , m and ε_0 are parameters used in the hardening law.

5.2.2.1 Effect of matrix crystallite size

The Hall-Petch effect is most commonly represented using either the widely used equations (5.14) or equations (5.15) [130,135]. The use of yield strains instead of yield stress allows comparison between datasets in which the elastic moduli are different. Dunstan and Bushby [130] have argued that equations (5.15) are more closely related to the physical mechanisms acting to increase the strength of the material.

$$\begin{aligned} \sigma_y &= \sigma_{y0} + k_\sigma / \sqrt{d} \\ \varepsilon_y &= \varepsilon_{y0} + k_\varepsilon / \sqrt{d} \end{aligned} \quad (5.14)$$

$$\begin{aligned}\sigma_y &= \sigma_{y0} + k_\sigma \frac{\ln(d/a_0)}{d/a_0} \\ \varepsilon_y &= \varepsilon_{y0} + k_\varepsilon \frac{\ln(d/a_0)}{d/a_0}\end{aligned}\tag{5.15}$$

where d is the average grain size, a_0 is lattice parameter of the matrix metal, σ_y and ε_y are the yield stress and yield strain and σ_{y0} , ε_{y0} , k_σ and k_ε are material parameters.

It has been previously reported that as the grain size is reduced, the simple relationship of equation (5.14) does not hold [131,136,137]. Khan et al. [131] showed that below a threshold value, the parameters of the Hall-Petch equation change. In Figure 5.3, equations (5.14) and (5.15) have been fitted to two different data sets from literature [138,139]. The fitted relationships are also shown in the figure. The data in Figure 5.3 represents average grain sizes from 330nm to 41 μ m. The bilinear relationship is clearly visible in Figure 5.3(a) in which the parameters for equation (5.14) change at a grain size of 1.6 μ m and 4.4 μ m for datasets 1 and 2 respectively. Equation (5.15), on the other hand, is able to capture the entire range of crystallite sizes using one set of parameters.

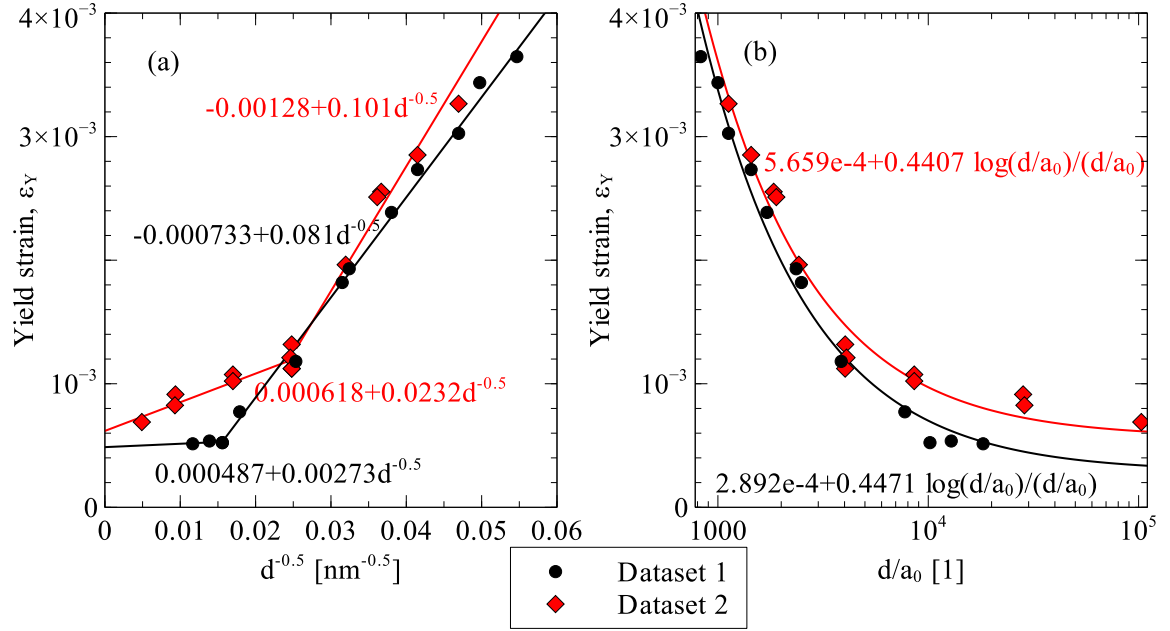


Figure 5.3. Modeling Hall-Petch effect using (a) equation (5.14) and (b) equation (5.15) for Aluminum using data from Tsuji et al. [138] (Dataset 1) and Yu et al. [139] (Dataset 2).

5.2.2.2 Effect of nanometer-sized inclusions

Orowan strengthening of the metal matrix due to the presence of nanometer-sized inclusions was modeled using equation (5.16) [116,126,129].

$$\Delta\sigma_{y,OR} = \frac{0.13b_{mat}G_{mat}}{d_{inc}\left(\sqrt[3]{1/2\phi_{inc}} - 1\right)} \ln\left(\frac{d_{inc}}{2b_{mat}}\right) \quad (5.16)$$

where $\Delta\sigma_{y,OR}$ is the increment in yield strength of the metal matrix due to Orowan strengthening, b_{mat} is the burger's length of the matrix, G_{mat} is the shear modulus of the matrix and d_{inc} is the inclusion size.

The enhancement due to elastic modulus (EM) and coefficient of thermal expansion (CTE) mismatch was modeled using equation (5.17) [116,118,126,129].

$$\begin{aligned} \Delta\sigma_{y,CTE+EM} &= M\beta G_{mat}b_{mat}\left(\sqrt{\rho^{CTE}} + \sqrt{\rho^{EM}}\right) \\ \rho^{CTE} &= \frac{A\Delta\alpha\Delta T\phi_{inc}}{b_{mat}d_{inc}(1-\phi_{inc})} \\ \rho^{EM} &= \frac{6\phi_{inc}}{\pi d_{inc}}\varepsilon \end{aligned} \quad (5.17)$$

where ρ^{CTE} and ρ^{EM} are the dislocation densities generated due to CTE and EM mismatch respectively, $\Delta\alpha$ is the CTE mismatch between matrix and inclusion and ΔT is the difference between processing and testing temperatures, M is the Taylor's factor ($\approx \sqrt{3}$), β ($=1.15$) is a constant and A is a geometric factor ranging from 10 to 12 depending on the shape of inclusion particles. Its value is 12 for spherical inclusions.

5.2.2.3 Overall strength of the metal matrix

The overall strengthening of the metal matrix is a combination of all of the above mechanisms. Several ways for the determination of the overall strengthening effect have been reported in the literature [116,118,126,129]. These range from models that consider the strengthening mechanisms to be additive to models which consider the synergic effects of the various mechanisms. In the current work, the Clyne model [129,140], shown in equation (5.18), was used to determine the overall strengthening of the matrix. It should be noted that load transfer strengthening and porosity do not affect the constitutive behavior of the metal matrix and are directly taken care of during mean-field homogenization.

$$\Delta\sigma_y = \sqrt{\Delta\sigma_{OR}^2 + \Delta\sigma_{CTE}^2 + \Delta\sigma_{EM}^2 + \Delta\sigma_{Hall-Petch}^2} \quad (5.18)$$

5.2.2.4 Matrix crystallite size and inclusion particle size dependent hardening of metal matrix

The hardening behavior in metals can be modeled using several types of models. Widely used models include bilinear hardening, power-law hardening, and Voce hardening law. In the current work, an approach was developed to incorporate the grain size effect into the voce hardening law of metals. The Voce hardening law, shown in equation (5.12), has four parameters, σ_0 , σ_A , m and ε_0 that control the shape of the hardening curve in which the parameter σ_0 is the initial yield stress of the material at the onset of yielding.

In the current work, the experimental data of Khan et al. [131] and Farrokh and Khan [133] was used to study the effect of matrix crystallite size on the hardening law

parameters. It is important to note here that Khan et al. [131] reported crystallite sizes of ball-milled aluminum powder and not the sintered samples. Therefore, their results cannot be directly correlated with other data sets. The variation of hardening model parameters is shown in Figures 5.4 and 5.5 for Khan et al.'s data and Farrokh and Khan's data respectively. The results of both datasets revealed that three of the four parameters, σ_0 , σ_A and m , showed bilinear variation with $1/\sqrt{d}$. The fourth parameter, ε_0 , showed deviation from the bilinear behavior. But, as will be shown in the results, a bilinear approximation of ε_0 still provides good agreement with experimental data.

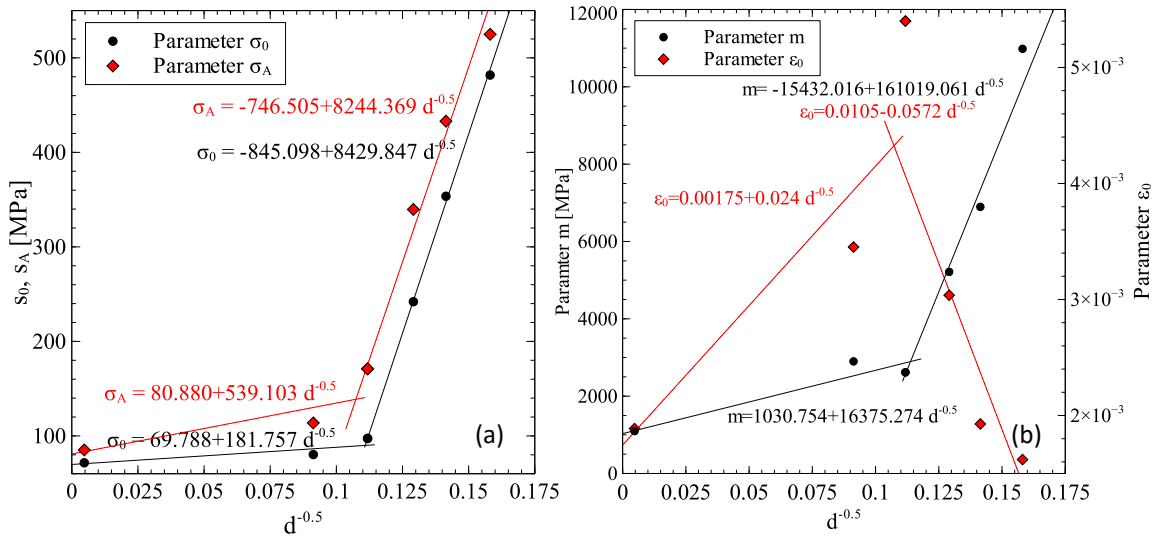


Figure 5.4. Crystallite size dependence of Voce hardening law parameters for Aluminum using data from Khan et al. [131].

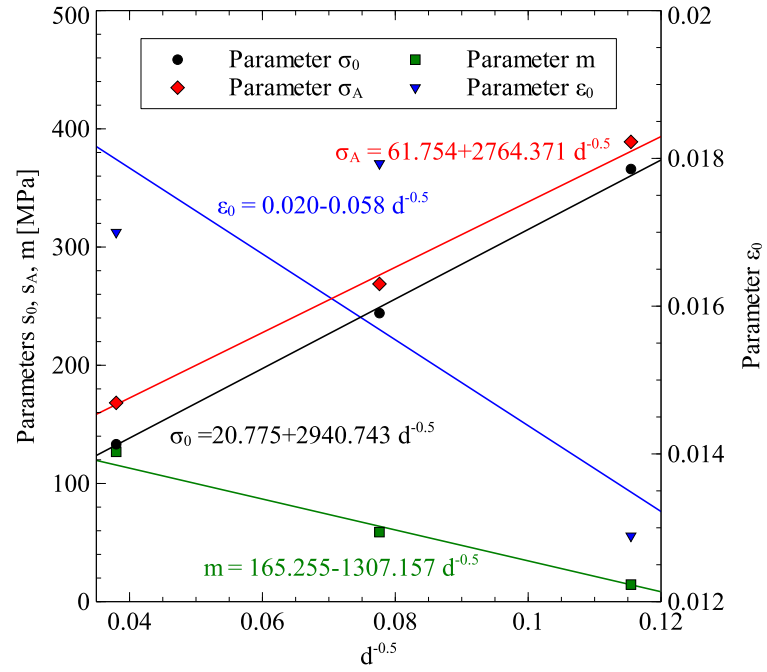


Figure 5.5. Crystallite size dependence of Voce hardening law parameters for Aluminum using data from Farrokh and Khan [133].

Based on the fact that all parameters in the hardening function show a dependence of matrix crystallite size, the hardening function of the matrix was modified as,

$$\sigma(\varepsilon_{p,eff}) = \sigma_0(d) + \{\sigma_A(d) - \sigma_0(d)\} \left[1 - \exp\{-\varepsilon_{p,eff} / \varepsilon_0(d)\} \right] + m(d) \varepsilon_{p,eff} \quad (5.19)$$

where the crystallite size dependence of the model parameters is defined by Hall-Petch type equations (5.20).

$$\begin{aligned} \sigma_0(d) &= \sigma_0^* + k_{\sigma_0} / \sqrt{d} \\ \sigma_A(d) &= \sigma_A^* + k_{\sigma_A} / \sqrt{d} \\ m(d) &= m_0^* + k_m / \sqrt{d} \\ \varepsilon_0(d) &= \varepsilon_0^* + k_{\varepsilon_0} / \sqrt{d} \end{aligned} \quad (5.20)$$

To include the effect of nanometer-sized inclusions into the hardening function, the Clyne model, defined by equation (5.18), was applied to parameters σ_0 and σ_A of the hardening function since these two parameters represent stresses. Equations (5.21) define the two parameters as a function of matrix crystallite size, inclusion particle size and inclusion volume fraction.

$$\begin{aligned} \sigma_0(d, d_{inc}, \varphi_{inc}) &= \sigma_{0, \text{large grains}} + \Delta \sigma_0(d, d_{inc}, \varphi_{inc}) \\ \sigma_A(d, d_{inc}, \varphi_{inc}) &= \sigma_{A, \text{large grains}} + \Delta \sigma_A(d, d_{inc}, \varphi_{inc}) \end{aligned} \quad (5.21)$$

5.2.3 Effect of process parameters on matrix crystallite size

The properties of particulate nanocomposites are a strong function of the crystallite size of the matrix material. This crystallite size is, in turn, a function of the process parameters used in the synthesis of the nanocomposite. A commonly used approach in the fabrication

of particulate metal matrix nanocomposites involves the step of ball-milling the matrix and inclusion powder together followed by the step of high-temperature consolidation such as hot pressing, hot extrusion or spark plasma sintering. The process parameters of both these steps determine the final crystallite size of the matrix.

The grain size reduction during ball milling can be easily captured by a double exponential function as shown in equation (5.22). Data of grain size reduction of Aluminum powder during ball milling from two different sources was used in the current work. Khan et al. [131] carried out high energy ball milling at 100 rpm with a ball to powder ratio of 20:1 to make nanostructured Al. In the experiments during current work, ball milling of Al powder was carried out at 200 rpm with a ball to powder ratio of 10:1. As shown in Figure 5.6, equation (5.22) can capture a reduction as well as an increase in grain size. The parameters a_1 , a_2 , a_3 and a_4 will depend on the ball-milling process parameters as well as the properties of the powder being milled.

$$d_{milled} = a_1 \exp(a_2 t) + a_3 \exp(a_4 t) \quad (5.22)$$

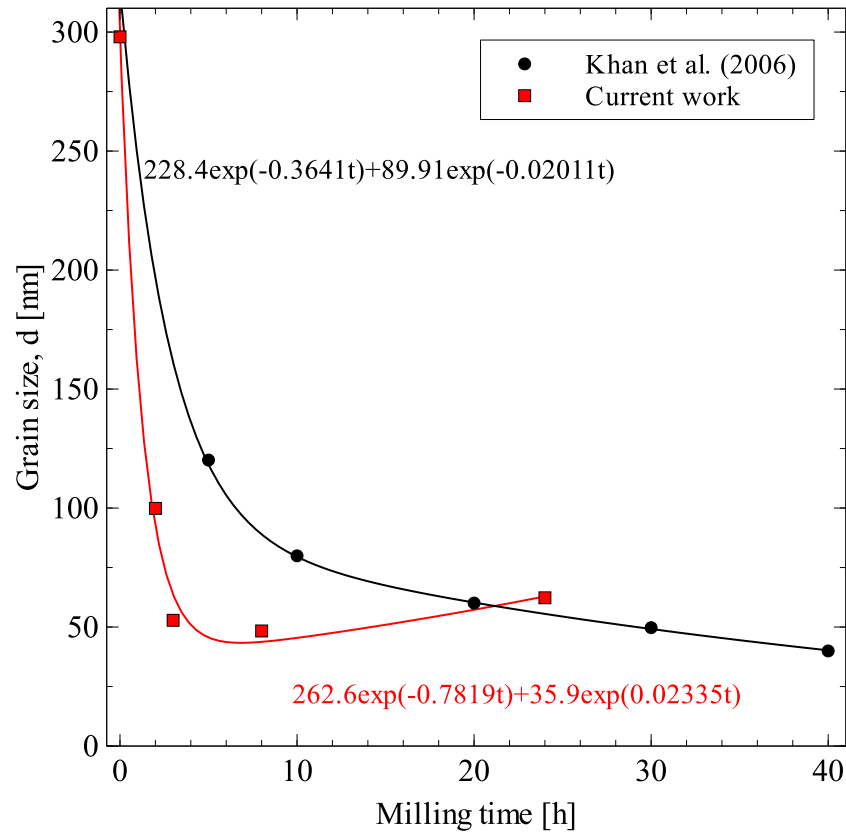


Figure 5.6. Grain size reduction of pure Al during ball milling.

The grain growth during the sintering process was modeled using the proposed equation (5.23). In equation (5.23), the first term in the first parenthesis takes into account the effect of grain size on the grain growth rate and the second term in the first parenthesis takes into account the effect of Zener pinning effect [112,141,142] due to nanoscale inclusion within the metal matrix. This effect is directly proportional to the inclusion volume fraction and inversely proportional to the inclusion size [143]. Equation (5.23) is similar to the differential form of grain growth models used by Zhou et al. [144] and Ye et al. [145] with the additional effect of Zener pinning.

$$\frac{dG}{dt} = \left(\frac{k_0}{G^n} - k_{inc} \frac{\phi_{inc}}{d_{inc}} \right) \exp\left(\frac{-Q_G}{RT}\right), \quad G(0) = d_{milled} \quad (5.23)$$

where G is the average grain size of the matrix during sintering, d_{milled} is the initial grain size, T is the sintering temperature, R is the universal gas constant and k_0 , k_{inc} and Q_G are material parameters.

Equations (5.22) and (5.23) can be used to determine the average crystallite size of ball milled and sintered samples. The transition of matrix metal crystallite size from as-received powder to sintered sample is shown graphically in Figure 5.7.

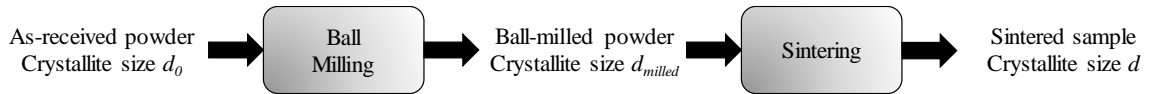


Figure 5.7. Transition of matrix metal crystallite size from as-received powder to sintered sample.

5.3 RESULTS AND DISCUSSION

5.3.1 Measured properties

A summary of properties of composite samples sintered by Nouari et al. [134] is provided in Table 5.1. Mechanical alloying of pure aluminum for 24 h decreased its crystallite size from 298 to 62.24 nm. As for the composite, milling for 24 h and the addition of 10 vol. % of Al₂O₃ nanoparticles reduced the crystallite size of the α -aluminum phase to 32.69 nm. Sintering of the as-received aluminum, the mechanically alloyed aluminum, and the mechanically alloyed Al- 10vol.% of Al₂O₃ nanocomposite increased the crystallite size of the α -aluminum phase to 366, 108.18, and 53.4 nm, respectively. This indicates that Al₂O₃ nanoparticles, on the one hand, acted as grinding medium and enhanced the milling effect, and on the other hand, acted as grain growth inhibitors during sintering.

Table 5.1. Summary of mechanical properties of sintered samples

Sample	Porosity fraction (%)	Crystallite size (milled powder) (nm)	Crystallite size (sintered sample) (nm)	Vickers hardness (MPa)	Yield strength (.2% offset) (MPa)	Compressive Strength (MPa)
Al (as received)	0.2	298	366	326.3	74.33±21	204.43 ± 16
Al (24 hours milled)	2.98	62	108	421	166.9-224.0	371.69 ± 69
Al- 10% Al ₂ O ₃ (24 hours milled)	3.43	33	53	1309.7	311.40±44	432.87 ± 91

The as-received pure aluminum and pure aluminum milled for 24 h had relative density values of 98.8 and 97.02 %, respectively. Milling for 24 h and addition of 10 vol.% Al_2O_3 reduced the relative density of 96.57 %. This could be due to the fact that sintering of nano-composite powders become more difficult at higher fractions of ceramic nanoparticles. Figure 5.8 shows optical micrographs of pure Al samples sintered using as-received and 24 hours milled Al powders.

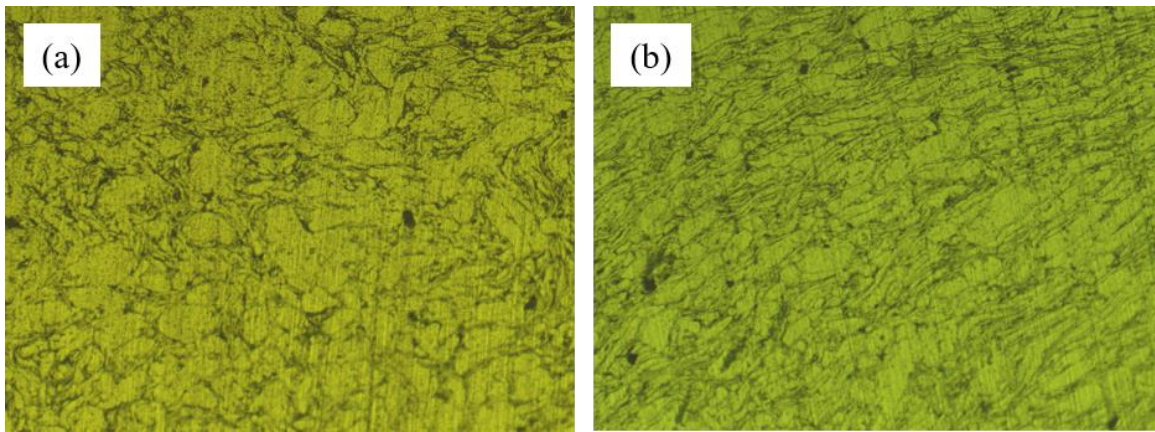


Figure 5.8. Optical micrographs of Al samples sintered from (a) as-received Al powder (b) 24 hours milled Al powder.

The sintered as-received aluminum and the 24 h mechanically alloyed aluminum had Vickers hardness values of 326.3 and 421 MPa, respectively. The Al-10 vol.% Al₂O₃ composite had a Vickers hardness of 1309.7 MPa. The monolithic un-milled aluminum had a yield strength of 74.33 MPa. Milling for 24 h increased the yield strength to 200.46 MPa. The addition of 10 vol.% Al₂O₃ and milling for 24 h increased the yield strength to 311.40 MPa. The compressive strength of the monolithic un-milled aluminum was 204.43 MPa. Milling for 24 h increased the strength to 371.69 MPa. The addition of 10 vol.% Al₂O₃ and milling for 24 h increased the strength to 432.87.4 MPa. The stress-strain response of the sintered samples under compression is presented in Figure 5.9 in which the average stress-strain response of each sintered sample (calculated using compression tests on multiple cylindrical specimens from the same sample) is presented along with variation in the stress-strain response. The increase in hardness, yield strength and compressive strength can be attributed to the small grain size of the matrix (Hall-Petch theory), the presence of nanoparticles (Orowan strengthening), an increase in dislocations' density, load transfer from the matrix to the reinforcement, and strain gradient [126,146,147].

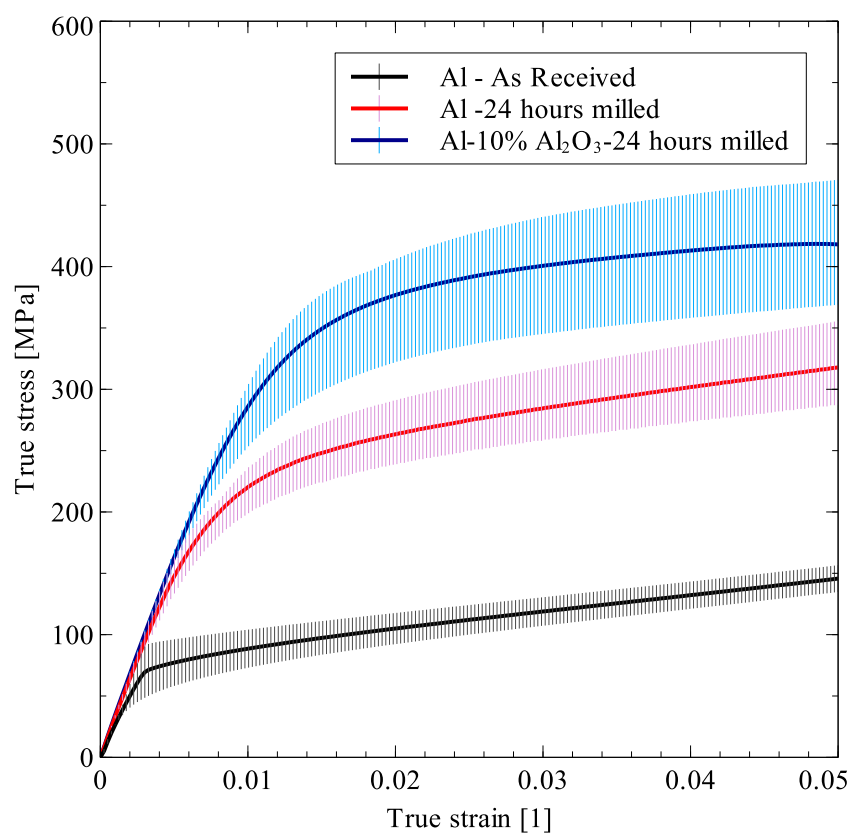


Figure 5.9. Stress-strain response of sintered samples under compression.

5.3.2 Modeling of pure nanostructured aluminum

A comparison of the 0.2% yield stress of pure aluminum samples sintered in the current work with predicted values using Hall-Petch relationships (5.14) and (5.15) is presented in Table 5.2. The predicted yield strains are multiplied with the experimentally determined elastic moduli of the sintered samples to calculate yield stresses. In the work of Farrokh and Khan [133], the sintered samples had a different elastic modulus than current work. Therefore, the Hall-Petch relationship (5.14) using their data was scaled to the modulus of elasticity of samples in current work. It can be seen from the results that equations (5.14) and (5.15) using datasets 1 and 2 both provided excellent predictions for spark plasma sintered aluminum samples of as-received Al powder ($d=366\text{nm}$). For the 24 hours ball-milled and spark plasma sintered aluminum sample ($d=108\text{nm}$), equation (5.14) provided better estimates than equation (5.15). This is because a crystallite size of 106nm is smaller than those in datasets 1 and 2. The slope of equation (5.15) increases as d/a_0 increases which result in an overestimation of yield stress. Equation (5.14) using Farrokh and Khan's data underestimated the yield stresses.

Table 5.2. 0.2% Yield stress prediction for spark plasma sintered samples.

Method	Crystallite size			
	366nm		106nm	
	Yield strain	Yield stress	Yield strain	Yield stress
	[1]	[MPa]	[1]	[MPa]
Experimental – Current work	0.00229	74.33±21	0.00617	166.9-224.0
Eq.(5.14) - Dataset 1 [138]	0.00350	82.46	0.00706	205.02
Eq.(5.14) - Dataset 2 [139]	0.00400	94.24	0.00844	245.10
Eq.(5.15) - Dataset 1 [138]	0.00365	85.99	0.00964	279.82
Eq.(5.15) - Dataset 2 [139]	0.00388	91.38	0.00978	283.97
Eq.(5.14) - Farrokh & Khan's data	0.00243	56.32	0.00423	120.83

The complete elastoplastic response of pure Al samples under compression was modeled using the constitutive model defined in section 3.2 for the pure Al samples sintered by Khan et al. [131] and Farrokh and Khan [133]. The parameters of the crystallite size dependent hardening law were taken from Figures 5.4 and 5.5 for Khan et al.'s data and Farrokh and Khan's data respectively. The modeling results are presented in Figure 5.10 for Khan et al.'s and Farrokh and Khan's experimental results. The modeling results that the crystallite size dependent hardening law presented in the current work is able to accurately capture the effect of crystallite size on the elastoplastic response of nanostructured metals. The assumption of linear dependence of parameter ε_0 on the inverse of square root of crystallite size did not adversely affect the model results and the results had good agreement with experimental data.

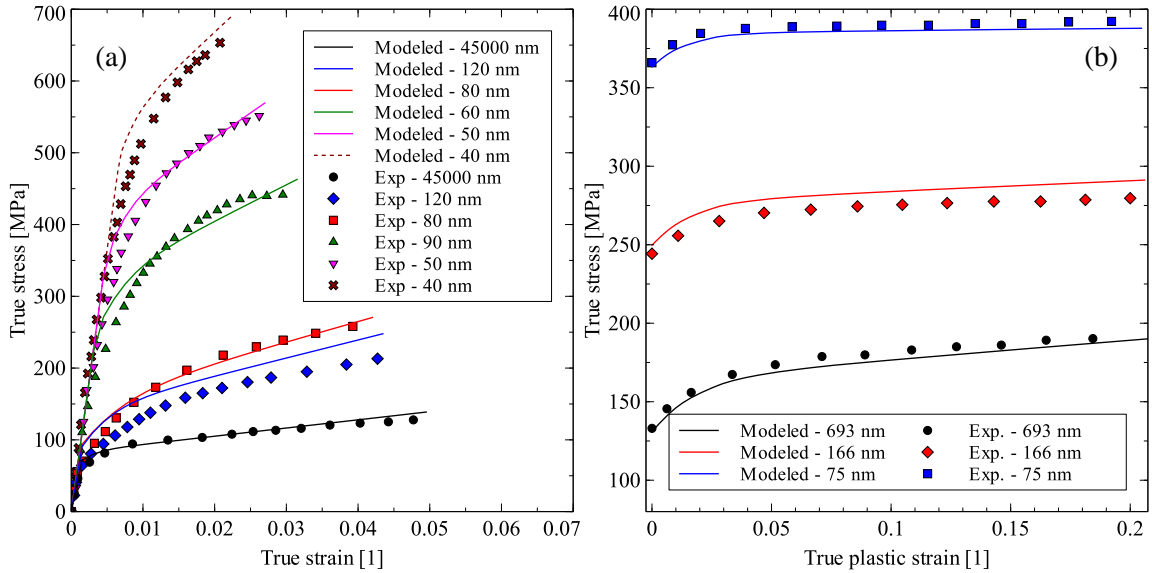


Figure 5.10. Comparison of modeled elastoplastic response of Aluminum with (a) Khan et al.'s experiments [131] and (b) Farrokh and Khan's experiments [133]

5.3.3 Modeling of elastoplastic response of aluminum matrix-alumina inclusion nanocomposites

Using the stress-strain curves of sintered aluminum samples made using as-received aluminum powder and 24 hours milled aluminum powder, the crystallite size dependence of hardening law parameters was determined. The variation of the hardening law parameters with the inverse of the square root of crystallite size is shown in Figure 5.11 in which the fitted Hall-Petch type relationships for all parameters is also shown. A comparison of the modeled hardening behavior of two pure Al sintered samples is plotted in Figure 5.12 along with the experimental hardening behavior of the samples.

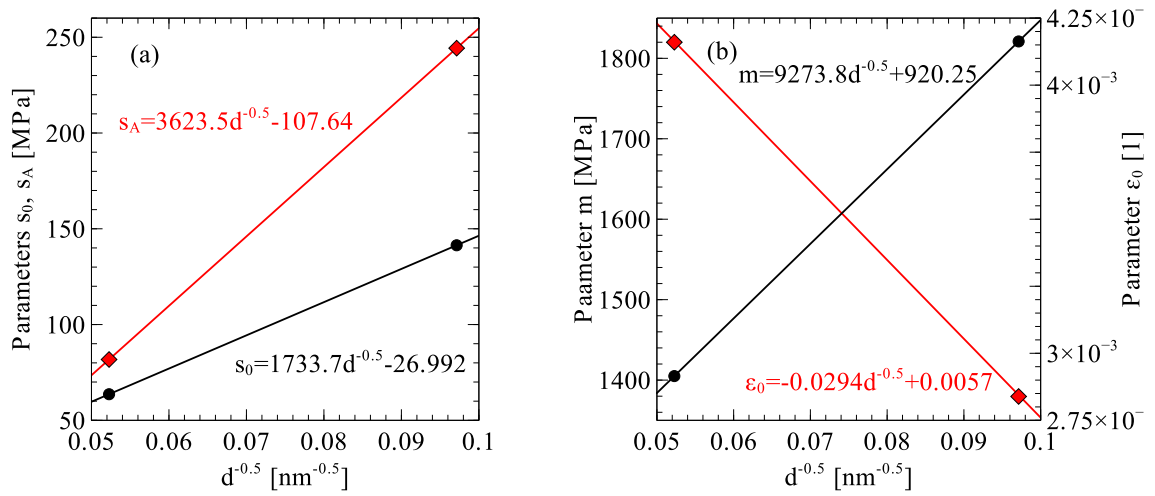


Figure 5.11. Crystallite size dependence of Voce hardening law parameters (a) s_0 and s_A and (b) m and ϵ_0 for spark plasma sintered Aluminum samples.

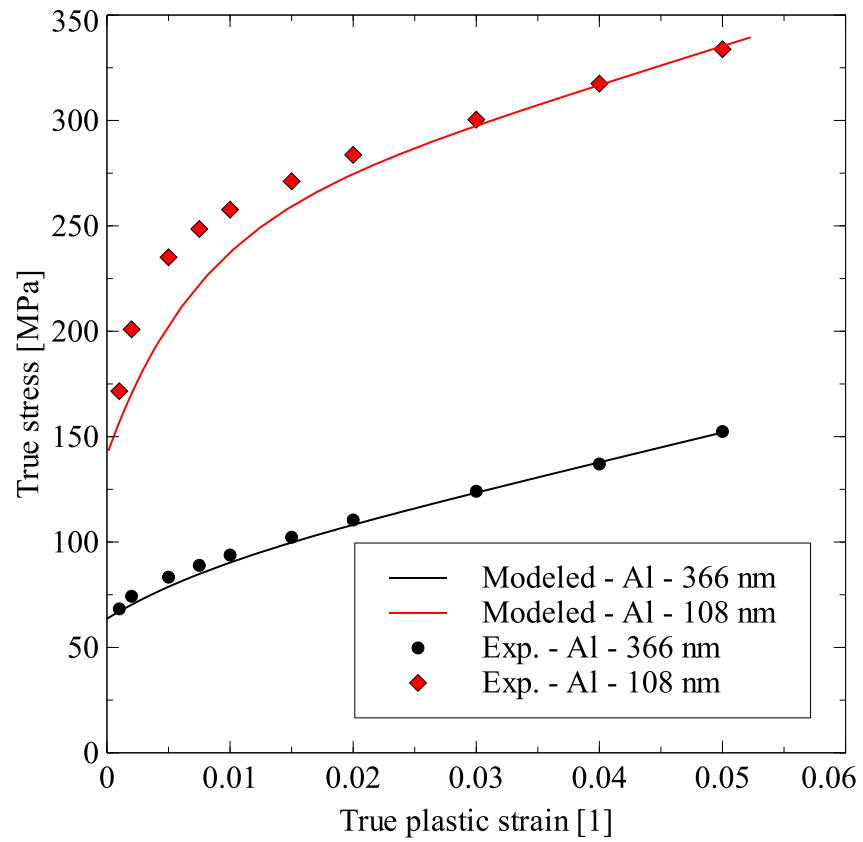


Figure 5.12. Comparison of hardening model with experimentally determined hardening behavior of spark plasma sintered Aluminum.

In order to model the stress-strain response of the Al-10% Al₂O₃ sample, the parameters m and ε_0 were scaled using the Hall-Petch type relationships shown in Figure 5.11 for the average crystallite of Al matrix in the sintered composite (53.4 nm). For determining parameters s_o and s_A , the Clyne model represented by equation (5.18) was used. Three strengthening mechanisms were incorporated into the parameters: Hall-Petch effect, Orowan strengthening and dislocation density effect due to the coefficient of thermal expansion mismatch. The Clyne model calculates the overall change in the two parameters s_o and s_A . This difference needs to be added to the parameters of the coarse-grained material in order to determine the new parameters. Since no coarse-grained samples were made in the current work, the equations for s_o and s_A were extrapolated to determine the parameter values from which the change was calculated. The parameter values at an average crystallite size of 549.1 nm were used since at this value, s_o and s_A have an equal value of 46.99 MPa. At higher crystallite sizes, s_o comes out greater than s_A which is physically not possible.

For an average inclusion particle size of 150nm, inclusion volume fraction equal to 10% and a shear modulus of 10.74 GPa (calculated using $E=29.04$ GPa and $\nu=0.35$), the contributions of Orowan strengthening and dislocation density strengthening were found out to be equal to 9.33MPa and 103.98MPa. The contribution of Hall-Petch effect to s_o and s_A for an average crystallite size of 53.4 nm were 163.26 MPa and 341.23 MPa respectively. By applying the Clyne model, parameters s_o and s_A were found out to be equal to 240.26 MPa and 403.55 MPa respectively. Parameter m and ε_0 were determined to be equal to 2189.32

MPa and 0.001677 respectively. The modeled stress-strain responses of all sintered samples are presented in Figure 5.13.

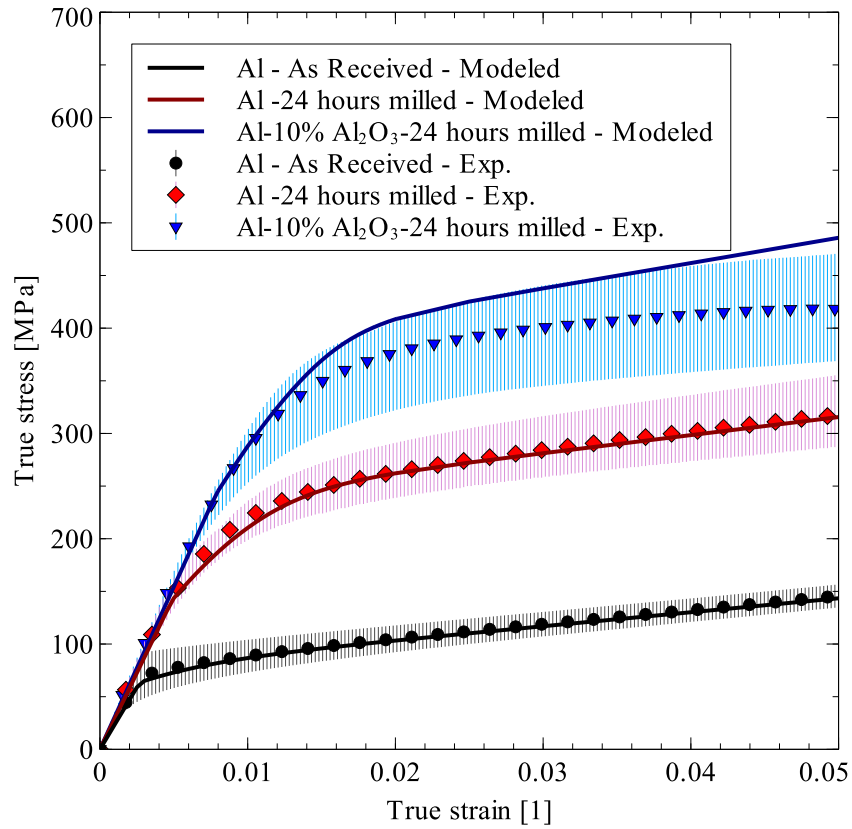


Figure 5.13. Comparison of modeled stress-strain response of spark plasma sintered samples with experimental results.

In order to analyze the relative contributions of Hall-Petch effect and Orowan and dislocation density strengthening, parametric studies were carried out to study the effects of inclusion volume fraction, inclusion particle size and matrix crystallite size on the stress-strain response of the Al-Al₂O₃ nanocomposite. Varying inclusion volume fraction and particle size affects the contributions of Orowan strengthening and dislocation density strengthening while varying matrix crystallite size affects the contribution of Hall-Petch effect.

The results of the parametric studies are shown in Figures 5.14 and 5.15. The results of the parametric studies show that the biggest contributing factor to the enhancement of yield strength and flow stress of Al-Al₂O₃ nanocomposite is the Hall-Petch effect. As the crystallite size was reduced from 300nm to 50nm, the 0.2% yield strength of the composite increased from 141 MPa to 373 MPa for an inclusion volume fraction of 5% and inclusion particle size equal to 150 nm. The contribution of Hall-Petch effect becomes especially high for ball-milled composites since ceramic inclusion particles act as an additional grinding medium for the metal matrix powder reducing its crystallite size.

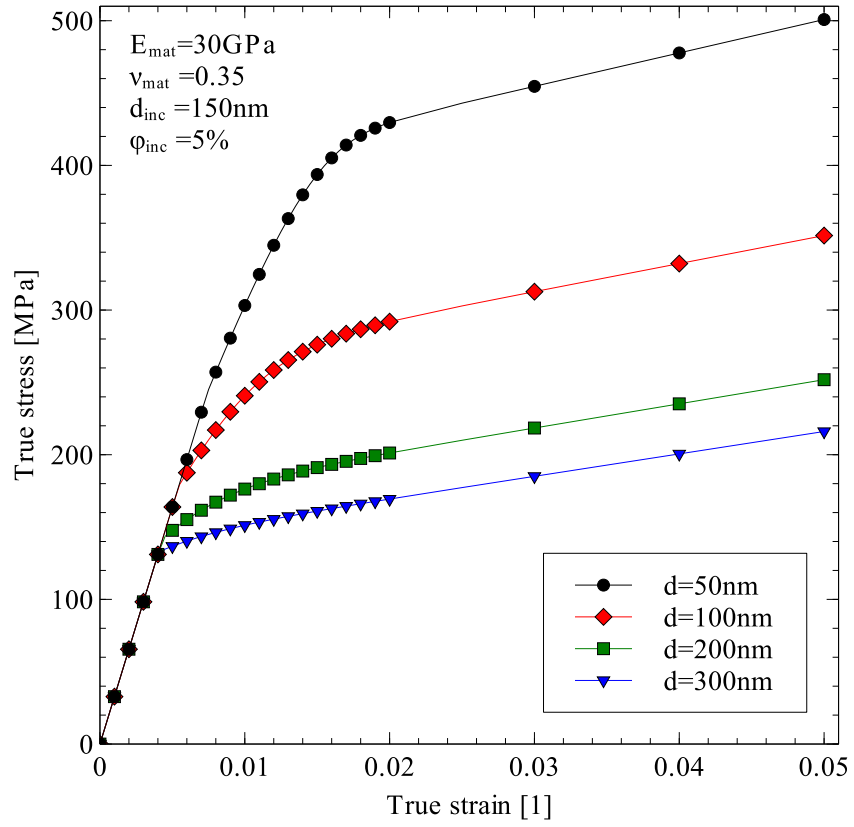


Figure 5.14. Effect of matrix crystallite size on stress-strain response of Al-Al₂O₃ nanocomposite.

For inclusion, there are two parameters, volume fraction and particle size, which affect the strength of the nanocomposite. Increasing the inclusion volume fraction provided a relatively smaller improvement compared to the Hall-Petch effect. Adding 10% inclusion improved the 0.2% yield strength from 205 MPa to 256 MPa. Reduction in inclusion particle size also resulted in improvement in composite strength. For Al-Al₂O₃ nanocomposite, the improvement was found to be more significant for particle sizes under 100 nm. When the inclusion size was reduced from 150 nm to 100 nm the 0.2% yield strength increases from 230 MPa to 240 MPa. For inclusion particle sizes 50 nm and 25 nm, the 0.2% yield strength of the composite was 265 MPa and 306 MPa respectively.

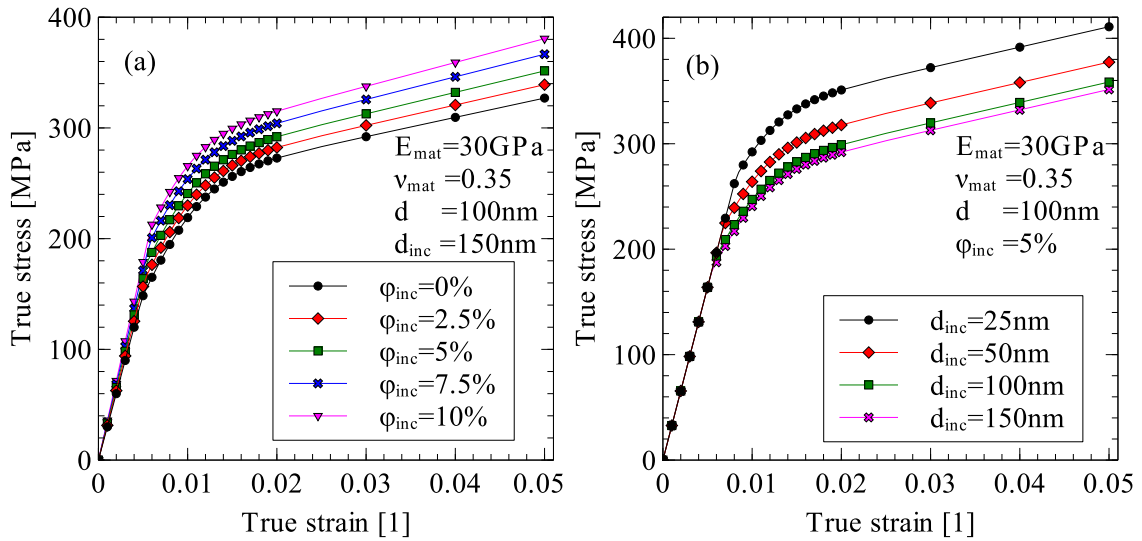


Figure 5.15. Effect of inclusion (a) volume fraction and (b) particle size on stress-strain response of Al-Al₂O₃ nanocomposite.

5.3.4 Modeling of elastoplastic response of spark plasma sintered alumina matrix nanocomposites

In order to determine the three model parameters in equation (5.23) used for calculating grain growth, additional pure aluminum and composite samples were made using spark plasma sintering. For 24 hours milled pure aluminum, additional samples were made using sintering times of 5 minutes, 10 minutes and 15 minutes. Additional composite samples were made with 2% and 15% alumina and a ball-milling time of 24 hours. The sintering temperature was kept constant at 550°C for all samples. In total, five new samples were made in addition to the three samples that have been mentioned before. The average crystallite sizes of all sintered samples used in the parameter estimation all listed in Table 5.3.

Table 5.3. Sample crystallite sizes used in grain growth model parameter estimation.

Sample	Crystallite size [nm]	
	Before sintering	After sintering
Pure Al – As received – 20 minutes sintered	298	366
Pure Al – 24 hours milled – 5 minutes sintered	62	66
Pure Al – 24 hours milled – 10 minutes sintered	62	87
Pure Al – 24 hours milled – 15 minutes sintered	62	93
Pure Al – 24 hours milled – 20 minutes sintered	62	108
Al-2% Al ₂ O ₃ -24 hours milled – 20 minutes sintered	40	83
Al-10% Al ₂ O ₃ -24 hours milled – 20 minutes sintered	33	53
Al-15% Al ₂ O ₃ -24 hours milled – 20 minutes sintered	28	42

The grain growth model was implemented using an explicit Range-Kutta method [148] in MATLAB. Estimation of the model parameters was carried out using the Nelder-Mead simplex search algorithm [149] by minimizing the total *root-mean-squared error* in the final crystallite size prediction for all samples. The estimated model parameters are listed in Table 5.4. A comparison of the predicted crystallite sizes with experimentally measured sizes is shown in Figure 5.16. The figure shows that the proposed grain growth model is able to accurately model the effects of sintering time as well as inclusion volume fraction.

Table 5.4. Grain growth model parameters

Parameter	Value
k_0	$5 \times 10^{-3} \text{ nm}^{0.691} / \text{s}$
k_{inc}	$14.94 \times 10^{-3} \text{ nm}^2 / \text{s}$
Q_G	125.12 kJ/mol
n	-0.309

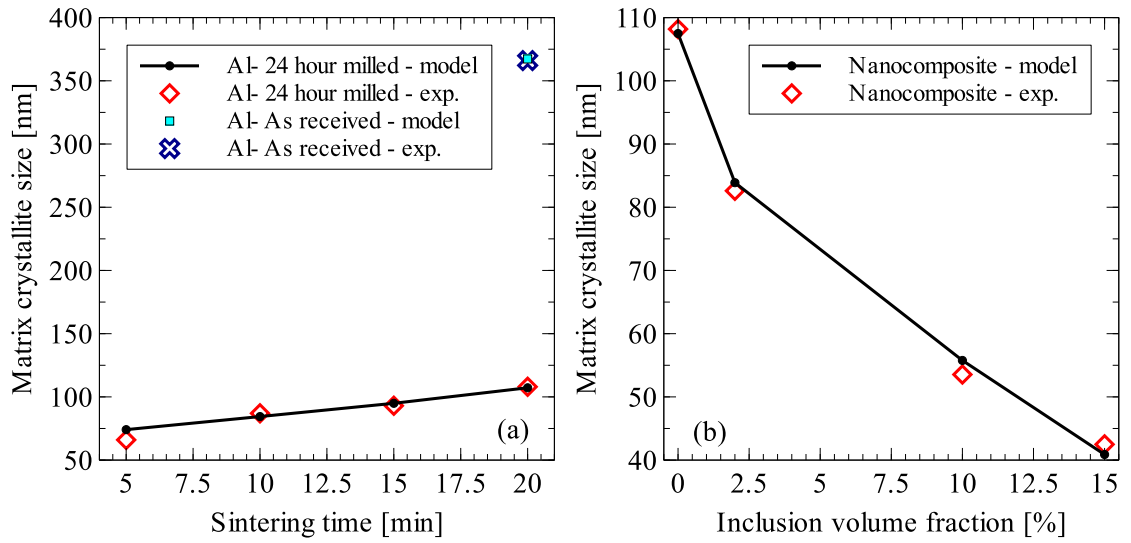


Figure 5.16. Comparison of grain growth model predictions with experimental results. (a) Effect of sintering time on grain growth in pure Al. (b) Effect of inclusion volume fraction on matrix grain growth in Al-Al₂O₃ nanocomposite for a sintering time of 20 minutes.

Using the grain growth model in combination with the elastoplasticity model, parametric studies were carried out to study the effect of sintering time and temperature on the elastoplastic response of Al-Al₂O₃ nanocomposites. The initial crystallite sizes for all modeled cases were taken from Table 5.3. The inclusion particle size was taken as 150 nm and the porosity fraction for all cases was assumed to be equal to 2%. Same porosity volume fraction was used for all cases since it has been previously shown that same amount of porosity is obtained in the sintering time range of 5 to 20 minutes [134]. The results of the parametric studies are shown in Figure 5.17 and Figure 5.18 which show the effects of sintering time and sintering temperature respectively. The results show that increasing the sintering temperature and time beyond what is required for good densification would result in a decrease in the strength of the material. In the current study, when the sintering time was increased from 5 minutes to 20 minutes while keeping the sintering temperature constant at 823 K, the 0.2% yield strength reduced from 217 MPa to 189 MPa for the 24 hours milled pure Al sample, from 263 MPa to 229 MPa for 2% alumina composite, from 387 MPa to 350 MPa for 10% alumina composite and from 507 MPa to 463 MPa for 15% alumina composite. An increase in the sintering temperature from 798 K to 873 K with a sintering time of 20 minutes reduced the 0.2% yield strength from 174 MPa to 143 MPa for the 24 hours milled pure Al sample, from 215 MPa to 179 MPa for 2% alumina composite, from 322 MPa to 280 MPa for 10% alumina composite and from 420 MPa to 374 MPa for 15% alumina composite.

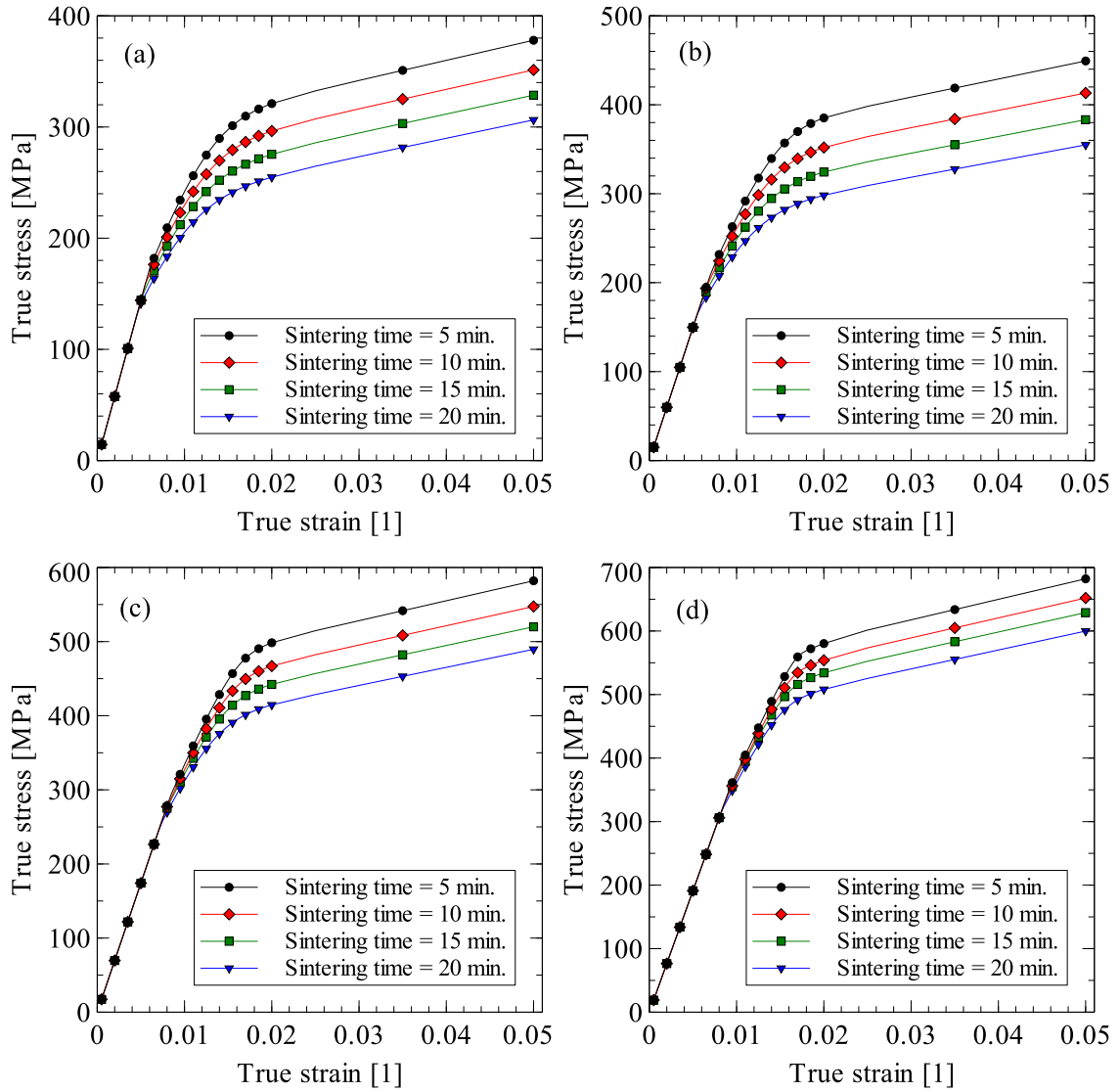


Figure 5.17. Effect of sintering time on the elastoplastic response of 24 hours milled (a) pure Al, (b) Al-2% Al₂O₃ composite, (c) Al-10% Al₂O₃ composite and (d) Al-15% Al₂O₃ composite. Sintering temperature is 823 K.

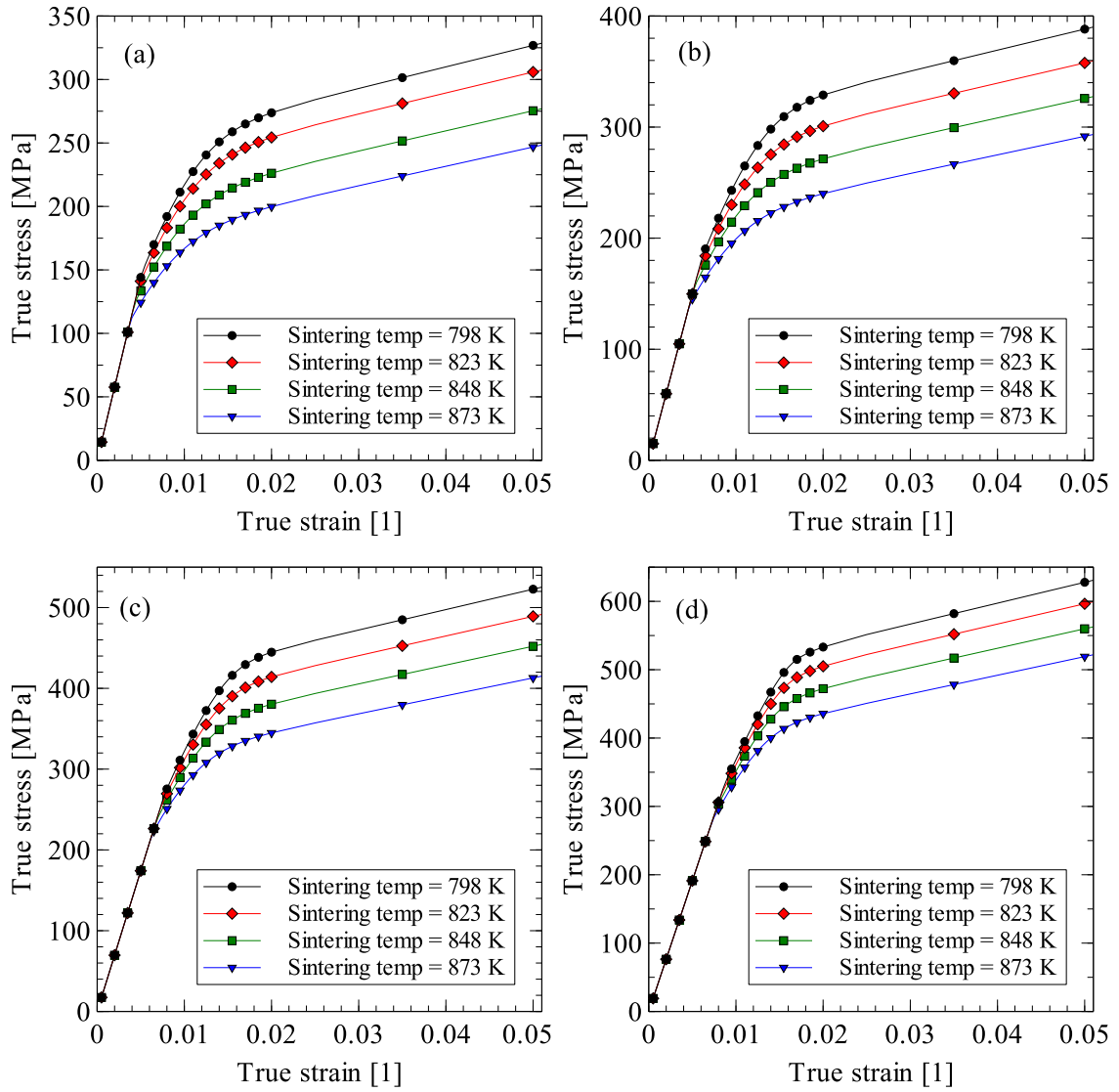


Figure 5.18. Effect of sintering temperature on the elastoplastic response of 24 hours milled (a) pure Al, (b) Al-2% Al₂O₃ composite, (c) Al-10% Al₂O₃ composite and (d) Al-15% Al₂O₃ composite. Sintering time is 20 minutes.

5.4 CONCLUSIONS

In the current work, a methodology to model the constitutive response of elastoplasticity in spark plasma sintered nanostructured metals and metal-matrix nanocomposites has been presented. The formulated methodology incorporates the effect of Hall-Petch strengthening, Orowan strengthening, dislocation density strengthening, load transfer strengthening and porosity using a mean-field homogenization approach along with a plasticity hardening function for the metal matrix that is dependent on the metal matrix crystallite size, inclusion particle size and inclusion and porosity volume fractions. The effect of process parameters is incorporated into the model using a grain growth model that can estimate the average matrix crystallite size as a function of sintering time, sintering temperature, inclusion size and inclusion volume fraction.

The formulated methodology was validated against experimentally determined crystallite sizes and elastoplastic response of nanostructured aluminum and aluminum matrix-alumina reinforced nanocomposite synthesized using ball milling and spark plasma sintering. Additional validations of the proposed hardening function were carried out against the elastoplastic response of nanostructured aluminum taken from literature. Both validations showed that the proposed methodology is able to accurately capture the dependence of elastoplastic response of nanostructured metals and metal-matrix nanocomposites on the metal matrix crystallite size, inclusion particle size and inclusion and porosity volume fractions.

Using the formulated methodology, parametric studies were carried out by varying matrix crystallite size, inclusion particle size and inclusion volume fraction to determine the relative contributions of various strengthening mechanisms in a metal matrix nanocomposite. It is found out that major contribution to strengthening comes from the Hall-Petch strengthening. Reduction in inclusion particle size improved the strength of the nanocomposite as expected but the improvement was relatively more significant below a particle size of 100nm. On the other hand, increasing the inclusion volume fraction increased the strength of the nanocomposite almost linearly.

Parametric studies were also conducted to study the effect of sintering time and temperature on the elastoplastic stress-strain response of metal-matrix nanocomposites. From the results, it was concluded that the sintering time and temperature should be set at the minimum required values for good densification. Unnecessarily increasing the sintering time and temperature results in a decrease in the strength of the sintered material.

CHAPTER 6

GENERALIZED EFFECTIVE MEDIUM THEORY:

FORMULATION AND APPLICATIONS

6.1 INTRODUCTION

Typically, the process of heat conduction is treated using the classical Fourier law. Although the Fourier law is widely applied, its application to systems with characteristic lengths comparable to or lower than the mean free path of the energy carriers (phonons or electrons) will lead to large errors in in any or all variables in the system such as the thermal conductivity, temperature and the temperature gradient [150]. Examples of such systems include nanoparticles, nanowires or thin films. The reason for the inapplicability of the Fourier law for nanostructures is that during heat conduction in such systems, equilibrium conditions are not achieved and therefore, a local temperature gradient cannot be established. Without a temperature gradient, Fourier law is not applicable and thermal conductivity, which relates heat flux to the temperature gradient, is meaningless. However, if one is interested in the heat conduction in a domain much greater than the mean free path

of the energy carriers, the Fourier law may still be applied with an effective value of thermal conductivity. An example of such a case can be a nanocomposite where the domain under consideration can be considerably larger than the characteristic length of the nanoparticles.

The problem of estimation of the effective thermal conductivity of composite materials has been widely studied. Early works in the area were done by Maxwell [69] and Lord Rayleigh [70] who studied the thermal conductivities of composites with low concentrations of inclusions. Their works were later extended by Hasselman and Johnson [71] and Benveniste [72] who studied the effects of thermal boundary conductance on the effective thermal conductivity of the composite. Bruggeman [74] derived a model for the effective thermal conductivity of a composite when the inclusion concentration was high. His model was later extended by Every et al. [75] to include the effect of thermal boundary conductance. Modifications to the model by Every et al. to include the effect of particle shape have also been presented [76]. Expressions for the effective thermal conductivity of composites with dilute concentrations of inclusions of different shapes have been presented by Nan et al [73]. The major drawbacks of the effective thermal conductivity approaches presented above include the limitation of using inclusions of regular shapes, inability to handle non-uniformly dispersed inclusions and percolating inclusions and large errors in results when dealing with nanocomposites [150]. To overcome the inability of handling percolating inclusions, Prasher et al. [151,152] and Evans et al. [153] presented a three-level homogenization methodology capable of handling clustering of inclusions.

To reduce the errors in effective medium theory predictions for nanocomposites, a modified effective medium theory was presented by Minnich and Chen [86] for spherical inclusions and was extended by Ordonez-Miranda et al. [87] for spheroidal inclusions. In this approach, modified thermal conductivities of the matrix and inclusions are first calculated and then used in the effective medium theory. Minnich and Chen used the modified values of matrix and inclusion thermal conductivities in Nan et al.'s EMT for spherical inclusions and found good agreement between the effective thermal conductivities predicted by the modified EMT and Monte Carlo simulations. The shortcomings of the modified effective medium theory approach include inability to handle multiple inclusions, randomly oriented inclusions and non-uniformly distributed inclusions. Other approaches used for the estimation of effective thermal conductivity of nanocomposites include the Monte Carlo simulation method [78–80], molecular dynamics [154] and the Boltzmann transport equation [81–85].

This chapter presents the formulation of a generalized effective medium theory (EMT) which can be used to determine the effective thermal conductivity of particulate nanocomposites. The proposed effective medium theory overcomes several shortcomings in the effective medium theory approaches reported in literature. These include capabilities to include effect of multiple nanometer-sized inclusions, effect of oriented (randomly or at any angle relative to heat flow direction) spheroidal, cylindrical or platelet inclusions and the effect of non-uniformly dispersed inclusions. Figure 6.1 graphically shows the capability of the formulated generalized effective medium theory in comparison to those proposed by Minnich and Chen [86] and Ordonez-Miranda et al. [87]. The work also

presents applications of the formulated methodology for the estimation of the effective thermal conductivity of polymer nanocomposites with hybrid inclusions and ceramic nanocomposites with hybrid inclusions.

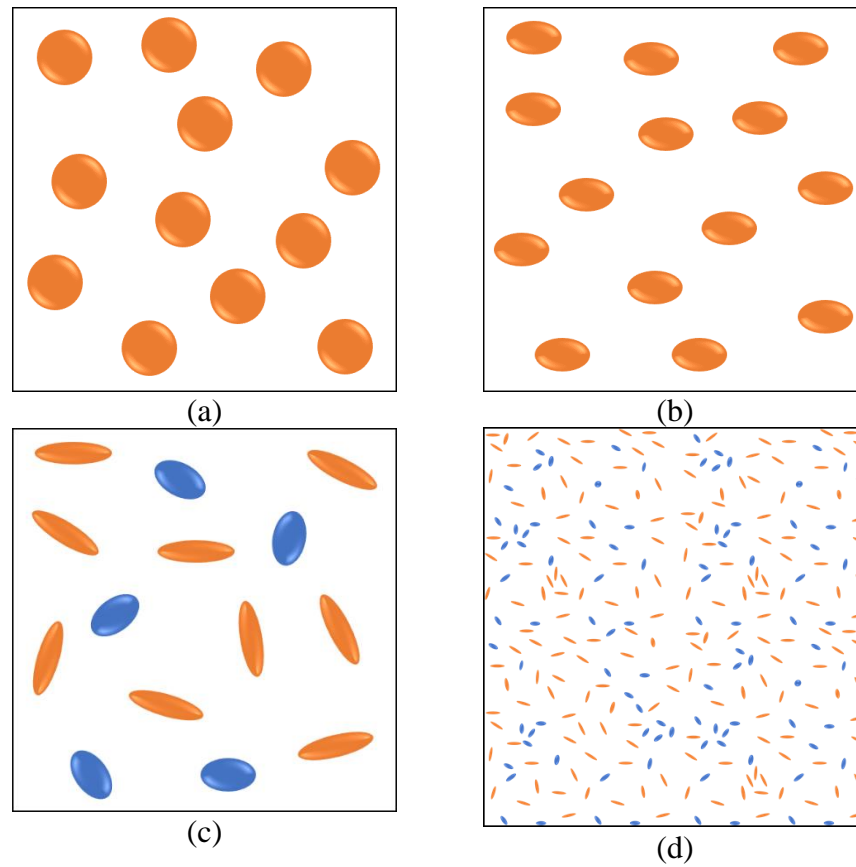


Figure 6.1. Inclusion geometries and orientation for (a) Minnich and Chen [86] (b) Ordóñez-Miranda et al. [87] and (c) generalized EMT - Current work. (d) A schematic representation non-uniformly distributed inclusions – Current work (inclusion sizes are not to scale).

6.2 FRAMEWORK OF THE GENERALIZED EFFECTIVE MEDIUM THEORY

The formulation of the generalized effective medium theory is presented in this section. First, the effective medium theory formulation for multiple inclusions is presented. Second, the effect of multiple nanometer-sized inclusions on the thermal conductivity is derived. Lastly, a two-scale approach to handle non-uniformly dispersed inclusions is presented.

6.2.1 Effective medium theory for composite with multiple inclusions

To derive the effective medium theory for composites with multiple inclusions, a two-phase composite was first considered. The thermal conductivity of the composite was assumed to vary from point to point according to the function $\mathbf{K}(\mathbf{r}) = \mathbf{K}^0 + \sum_n \delta\mathbf{K}_n(\mathbf{r})$ where \mathbf{K}^0 is the constant part of thermal conductivity function and $\delta\mathbf{K}_n(\mathbf{r})$ is the fluctuation in thermal conductivity due to inclusion particle n . For inclusions of a single kind, the effective thermal conductivity of the composite was determined by Nan et al. [73,155]. Their model can easily be extended for multiple types of inclusions. The effective thermal conductivity of the composite can then be calculated using equations (6.1)-(6.9) which are valid for spheroidal inclusions of multiple types.

$$\begin{aligned}
K_{eff,11} = K_{eff,22} = K_{mat} & \frac{2 + \sum_{i=1}^N \varphi_i \left[\beta_{11}^i (1 - L_{11}^i) \left(1 + \langle \cos^2 \theta \rangle^i \right) + \beta_{33}^i (1 - L_{33}^i) \left(1 - \langle \cos^2 \theta \rangle^i \right) \right]}{2 - \sum_{i=1}^N \varphi_i \left[\beta_{11}^i L_{11}^i \left(1 + \langle \cos^2 \theta \rangle^i \right) + \beta_{33}^i L_{33}^i \left(1 - \langle \cos^2 \theta \rangle^i \right) \right]} \\
K_{eff,33} = K_{mat} & \frac{1 + \sum_{i=1}^N \varphi_i \left[\beta_{11}^i (1 - L_{11}^i) \left(1 - \langle \cos^2 \theta \rangle^i \right) + \beta_{33}^i (1 - L_{33}^i) \left(\langle \cos^2 \theta \rangle^i \right) \right]}{1 - \sum_{i=1}^N \varphi_i \left[\beta_{11}^i L_{11}^i \left(1 - \langle \cos^2 \theta \rangle^i \right) + \beta_{33}^i L_{33}^i \langle \cos^2 \theta \rangle^i \right]}
\end{aligned} \tag{6.1}$$

$$\begin{aligned}
K_{c,11}^i &= \begin{cases} K_{inc,i} / \left(1 + \gamma_{11}^i L_{33}^i K_{inc,i} / K_m \right), & \text{for platelet inclusions} \\ K_{inc,i} / \left(1 + \gamma_{11}^i L_{11}^i K_{inc,i} / K_m \right), & \text{for other shapes} \end{cases} \\
K_{c,33}^i &= \begin{cases} K_{inc,i} / \left(1 + \gamma_{33}^i L_{11}^i K_{inc,i} / K_m \right), & \text{for cylindrical inclusions} \\ K_{inc,i} / \left(1 + \gamma_{33}^i L_{33}^i K_{inc,i} / K_m \right), & \text{for other shapes} \end{cases}
\end{aligned} \tag{6.2}$$

$$L_{11}^i = L_{22}^i = \begin{cases} \frac{p^{i^2}}{2(p^{i^2} - 1)} - \frac{p^i}{2(p^{i^2} - 1)^{3/2}} \cosh^{-1} p^i, & \text{for } p^i \geq 1 \\ \frac{p^{i^2}}{2(p^{i^2} - 1)} + \frac{p^i}{2(1 - p^{i^2})^{3/2}} \cos^{-1} p^i, & \text{for } p^i < 1 \end{cases} \tag{6.3}$$

$$\beta_{kk}^i = \frac{K_{c,kk}^i - K_m}{K_m + L_{kk}^i (K_{c,kk}^i - K_m)} \tag{6.4}$$

$$\langle \cos^2 \theta \rangle^i = \frac{\int \rho^i(\theta) \cos^2 \theta \sin \theta d\theta}{\int \rho^i(\theta) \sin \theta d\theta} \tag{6.5}$$

$$\gamma_{kk}^i = \begin{cases} (2 + 1/p^i) \alpha_k, & \text{for } p^i \geq 1 \\ (1 + 2p^i) \alpha_k, & \text{for } p^i < 1 \end{cases} \quad (6.6)$$

$$L_{33}^i = 1 - 2L_{11}^i \quad (6.7)$$

$$\alpha_k^i = R_{TB}^i K_m / a_k^i \quad (6.8)$$

$$p^i = a_3^i / a_1^i \quad (6.9)$$

where φ_i is the volume fraction, a_1^i and a_3^i are the particle radii, p^i is the aspect ratio, R_{TB}^i is the interfacial thermal resistance, $K_{inc. i}$ is the thermal conductivity of inclusion of type i . K_{mat} is the thermal conductivity of the matrix. $\langle \cos^2 \theta \rangle^i$ is a factor defining the orientation of inclusion of type i .

6.2.2 Effect of nanometer-sized inclusions on matrix and inclusion thermal conductivities

The effect of multiple nanometer-sized inclusions oriented in any random direction on the thermal conductivities of the matrix and inclusions can be calculated by extending the approach of Minnich and Chen [86]. According to their approach, the addition of the nanometer-sized particles modifies the thermal conductivities of the matrix and the inclusions. The modified thermal conductivities are calculated by first calculating the effective mean free path of the energy carriers (phonons or electrons) in the matrix or the inclusions using Matthiessen's rule.

$$\frac{1}{\Lambda_{x,eff}^y} = \frac{1}{\Lambda_{x,bulk}^y} + \frac{1}{\Lambda_{x,coll}^y} \quad (6.10)$$

where x can be p or e for phonons or electrons respectively and y can be mat for the matrix or $inc.i$ for the i th inclusion.

The bulk mean free paths, $\Lambda_{x,bulk}^y$ for a material are known quantities. The unknown quantity in equation (6.10) is the collision mean free path, Λ_{coll}^y , defined as the average distance travelled by the energy carriers between collisions. Once the effective mean free paths of the energy carriers have been calculated, the modified thermal conductivities of the matrix and inclusions can be calculated using,

$$K_x^y = \frac{1}{3} C_x^y v_x^y \Lambda_{x,eff}^y \quad (6.11)$$

To calculate the collision mean free paths of the matrix, Λ_{coll}^{mat} , consider N types of inclusions embedded in the matrix. The density of the inclusions in the matrix, n_i , can be calculated using equation (6.12).

$$n_i = \frac{N}{V} = \frac{\varphi_i}{V_i} \quad (6.12)$$

where N is the number of inclusions in a sample of volume V and V_i is the volume of a single particle of inclusion type i .

Assuming $A_{\perp 1} = \max(A_{\perp 1}, A_{\perp 2}, A_{\perp 3}, \dots, A_{\perp N})$, where $A_{\perp i}$ is the collisions cross-section area of the i th inclusion type, the number of inclusions of type i that an energy carrier (phonon or electron) will encounter in a volume $A_{\perp 1}L$ is $n_i A_{\perp 1}L$. The matrix collision mean free path is therefore,

$$\Lambda_{coll}^{mat} = \frac{L}{(n_1 + n_2 + \dots + n_N)A_{\perp 1}L} \quad (6.13)$$

By replacing the expressions for n_i in equation (6.13), we get,

$$\Lambda_{coll}^{mat} = \frac{1}{(\varphi_1 + r_{V2}\varphi_2 + \dots + r_{VN}\varphi_N)\sigma_{\perp 1}} \quad (6.14)$$

where $r_{Vi} = V_i / V_1$ and $\sigma_{\perp 1} = A_{\perp 1} / V_1$. Equation (6.14) reduces to Ordonez-Miranda et al.'s formulation [87] when only a single inclusion is considered that is when $\varphi_i = 0$ for $i = 2, 3, \dots, N$. It is also interesting to note that in equation (6.14), the relative sizes of the inclusions, represented by r_{Vi} , will determine their contribution to the collision mean free path for the matrix.

Applying Mattheissen's rule, the effective mean free path of energy carriers in the matrix is,

$$\Lambda_{x,eff}^{mat} = \frac{\Lambda_{x,bulk}^{mat}}{1 + \Lambda_{x,bulk}^{mat} (\varphi_1 + r_{V2}\varphi_2 + \dots + r_{VN}\varphi_N)\sigma_{\perp 1}} \quad (6.15)$$

The modified thermal conductivity of the matrix material can be calculated using equation (6.11) which leads to equation (6.16),

$$K_x^{mat} = \frac{K_{x,bulk}^{mat}}{1 + \Lambda_{x,bulk}^{mat} (\varphi_1 + r_{V2}\varphi_2 + \dots + r_{VN}\varphi_2) \sigma_{\perp 1}} \quad (6.16)$$

The total matrix thermal conductivity is given by equation (6.17).

$$K_{mat} = K_p^{mat} + K_e^{mat} \quad (6.17)$$

The cross-sectional area in the path of the energy carrier was calculated by considering a general spheroidal inclusion particle placed at an angle θ in the direction of heat flow. Such an inclusion projects an area A_{\perp} perpendicular to the direction of the heat flow. To calculate this cross-sectional area, we start with the general equation of an ellipsoid,

$$(\mathbf{x} - \mathbf{c})^T \mathbf{R}^T \mathbf{A} \mathbf{R} (\mathbf{x} - \mathbf{c}) = 1 \quad (6.18)$$

where $\mathbf{x} = [x, y, z]^T$, \mathbf{c} is the vector defining the center of the ellipsoid, \mathbf{R} is the rotation matrix and \mathbf{A} is 3×3 matrix with diagonal terms $(1/a_1^2, 1/a_2^2, 1/a_3^2)$. Assume a spheroid ($a_1 = a_2$) centered at the origin ($\mathbf{c} = [0, 0, 0]^T$) and rotated about the y-axis by an angle θ (a rotation about the x-axis will provide the same result). To calculate the area of the ellipse projected on the global 12 plane, we need to calculate its major and minor axes of the projection. This can be done by replacing $y = 0$ and determining the derivative dx/dz . The x-intercepts can be determined by setting the numerator equal to zero which leads to the

points $(\pm b_1, 0)$. Similarly, y-intercepts are determined by setting the denominator equal to zero, which leads to the points $(0, \pm b_2)$.

Therefore, the collision cross-sectional area for spheroidal inclusions can be calculated using equation (6.19).

$$A_{\perp} = \pi b_1 b_2 \quad (6.19)$$

For the inclusions, the collision mean free path depends only on the size and orientation of the inclusion itself. If the angle θ^i is 0° or 90° , the collision mean free path for inclusion particles can be calculated using equations (6.21) or (6.22) respectively [87]. In general, for any angle between 0° and 90° , equation (6.20) can be used to calculate the collision mean free path of inclusion particles. Figure 6.2 shows the reasoning behind equation (6.20). For randomly oriented inclusions, the average orientation of the inclusions can be estimated from $\langle \cos^2 \theta \rangle^i = 1/3$ as $\langle \theta^i \rangle = \cos^{-1}(1/\sqrt{3})$. It should be noted that equation (6.20) provides an approximate mean free path for the inclusion particles. If a more accurate analytical solution is available for the mean free path through ellipsoidal inclusions at an angle, it should be used instead.

$$\Lambda_{coll}^{inc.i} = \begin{cases} \min\left(\frac{c_{12}^{inc.i}}{\sin \theta^i}, c_{33}^{inc.i}\right), & \text{for } p^i \geq 1 \\ \min\left(\frac{c_{33}^{inc.i}}{\cos \theta^i}, c_{12}^{inc.i}\right), & \text{for } p^i < 1 \end{cases} \quad (6.20)$$

$$c_{12}^{inc.i} = \begin{cases} \frac{8a_1^i (1+\varepsilon^2) K_{ellip}(-\varepsilon^2) - (1-\varepsilon^2) E_{ellip}(-\varepsilon^2)}{3\pi\varepsilon \sqrt{1+\varepsilon^2} + \operatorname{arcsinh}(\varepsilon)}, & \text{for } p^i < 1 \\ \frac{8a_1^i (1-\varepsilon^2) K_{ellip}(\varepsilon^2) - (1+\varepsilon^2) E_{ellip}(\varepsilon^2)}{3\pi(i\varepsilon) \sqrt{1-\varepsilon^2} + \operatorname{arcsinh}(i\varepsilon)}, & \text{for } p^i \geq 1 \end{cases} \quad (6.21)$$

$$c_{33}^{inc.i} = \begin{cases} \frac{4a_3^i \sqrt{(1+\varepsilon^2)^3} - 1}{3\varepsilon \sqrt{1+\varepsilon^2} + \operatorname{arcsinh}(\varepsilon)}, & \text{for } p^i < 1 \\ \frac{4a_3^i \sqrt{(1-\varepsilon^2)^3} - 1}{3(i\varepsilon) \sqrt{1-\varepsilon^2} + \operatorname{arcsinh}(i\varepsilon)}, & \text{for } p^i \geq 1 \end{cases} \quad (6.22)$$

where ε is the eccentricity given by,

$$\varepsilon = \begin{cases} \sqrt{1-p^{i^2}}, & \text{for } p^i < 1 \\ \sqrt{p^{i^2}-1}, & \text{for } p^i \geq 1 \end{cases} \quad (6.23)$$

and $K_{ellip}(\)$ and $E_{ellip}(\)$ are elliptic integrals of first and second kind.

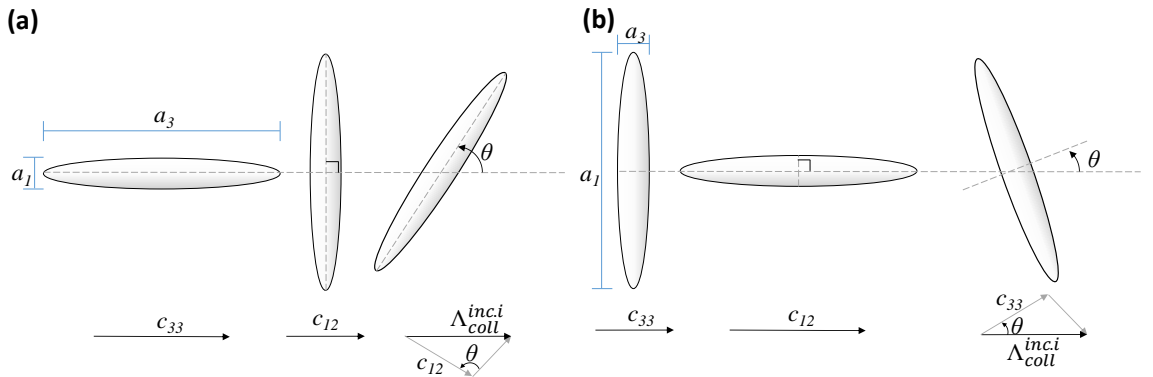


Figure 6.2. Calculating $\Lambda_{coll}^{inc.i}$ for (a) prolate inclusion and (b) oblate inclusion.

The variation of $\Lambda_{coll}^{inc.i}$ with angle θ^i is shown in Figure 6.3 for spheroid aspect ratios 0.1, 1 and 10.

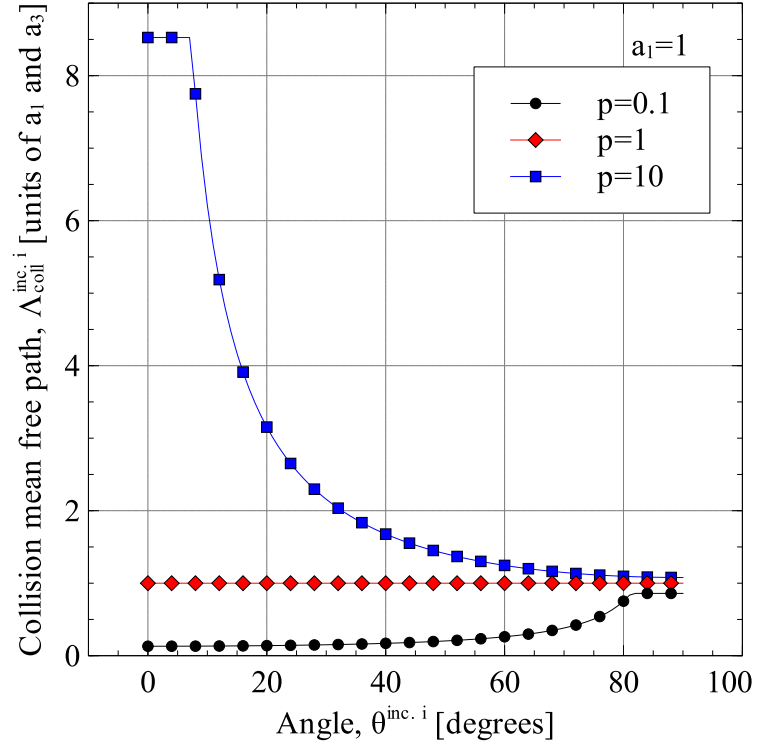


Figure 6.3. Variation of collision mean free path $\Lambda_{coll}^{inc.i}$ with angle $\theta^{inc.i}$.

The effective mean-free-path of the energy carriers in the inclusion particles was calculated by applying the Matthiessen's rule.

$$\Lambda_{x,\text{eff}}^{inc.i} = \frac{\Lambda_{x,bulk}^{inc.i}}{1 + \Lambda_{x,bulk}^{inc.i} / \Lambda_{coll}^{inc.i}} \quad (6.24)$$

The modified thermal conductivities of the inclusions can be calculated using equation (6.25) which are derived by replacing the effective mean free paths of the energy carriers in equation (6.11).

$$K_x^{inc.i} = \frac{K_{x,bulk}^{inc.i}}{1 + \Lambda_{x,bulk}^{inc.i} / \Lambda_{coll}^{inc.i}} \quad (6.25)$$

The total thermal conductivity for inclusion i is given by equation (6.26).

$$K_{inc.i} = K_p^{inc.i} + K_e^{inc.i} \quad (6.26)$$

6.2.3 Two-scale approach for non-uniformly distributed inclusions

A major drawback of the effective medium theory approach is its inability to handle non-uniform dispersion of inclusions. In the current work, a two-scale approach is proposed that combines the EMT approach at the lower scale with computational homogenization [65,77] at the upper scale to introduce the effect of non-uniform dispersion of inclusions in the matrix on the effective thermal conductivity of the composite.

The application of the method requires a quantitative knowledge of inclusion distribution in the matrix. This could a statistical parameter like standard deviation of

inclusion volume fraction that can be used to develop an RVE for computational homogenization. The distribution could also be experimentally determined using material characterization techniques. An important point is that the distribution needs to be measured at a larger length scale than the inclusion size. As an example, if the inclusions are nanometer sized, the distribution is determined at the micrometer length scale. The two-scale methodology is presented in Figure 6.4.

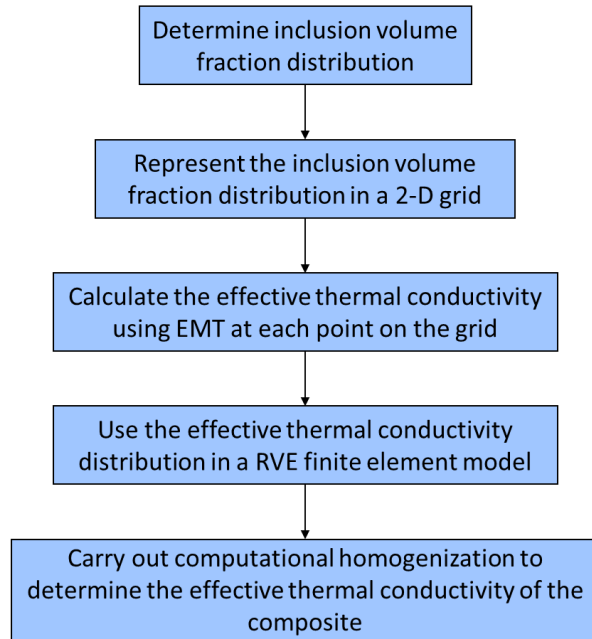


Figure 6.4. Two-scale methodology for effective thermal conductivity estimation.

In the first two steps in the methodology, the variation of inclusion volume fraction at different points in the composite is determined and represented in the form of a grid of points for each inclusion. As a result, the distribution of inclusions in the composite can be shown as in Figure 6.5, which shows the distribution of a nanometer sized Si inclusion in Ge matrix. Because of the scale separation requirement, each point in the grid represents the composite material having a certain volume fraction of inclusions. In the example considered in the figure, the average inclusion volume fraction in the Ge–Si RVE was 5% and the standard deviation of the volume fraction in the microscale domain was 1%. The distribution of the effective thermal conductivity in the RVE determined using the generalized effective medium theory is shown in Figure 7.

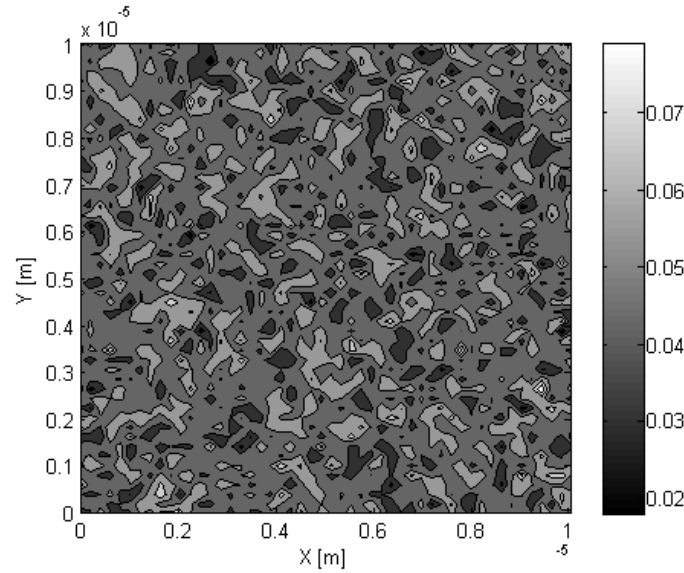


Figure 6.5. Distribution of Si nanoparticle volume fraction in Ge matrix.

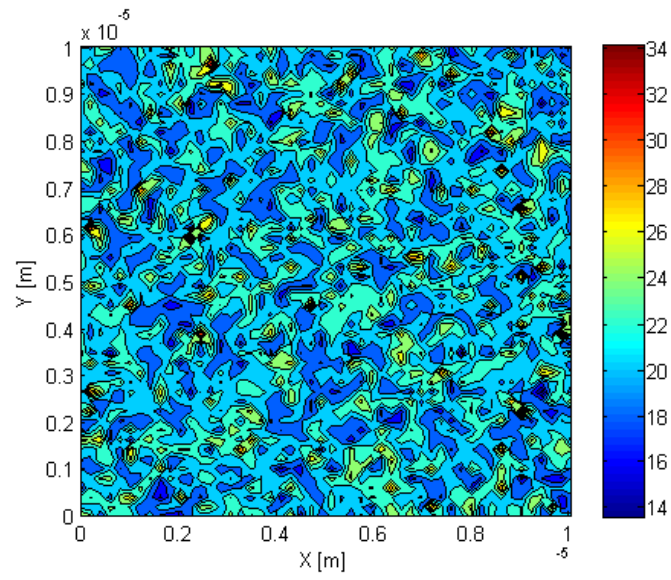


Figure 6.6. Distribution of the effective thermal conductivity in the RVE.

The final step in the methodology is to apply computational homogenization to estimate the overall effective thermal conductivity of the composite. An important aspect of the accuracy of computational homogenization results is the correct determination of the RVE size required for homogenization. In the current work, the validity of the RVE size used was determined using the methodology presented by Gitman et al. [16]. Gitman and coworkers suggested the calculation of a variation coefficient, known as the *chi-square criterion* (χ^2) using Equation (6.27). If the *chi-square criterion* is below a threshold value, the homogenization results are considered to be independent of RVE size. A threshold of 0.1 was selected in the present study as suggested by Gitman and coworkers.

$$\chi^2 = \frac{\sum_{i=1}^n (a_i - \langle a \rangle)^2}{\langle a \rangle} \quad (6.27)$$

where a_i is the homogenized property under consideration for RVE realization i , n is the total number of random RVE realizations of the same size and $\langle a \rangle$ is the mean value of the property under consideration.

For the computational homogenization problem of the current work, the parameter χ^2 was determined for multiple average inclusion volume fractions and multiple dispersion non-uniformity values (modeled using standard deviation of inclusion volume fraction). The results of this study are presented in Figure 6.7. From the results, it was concluded that the use of RVEs of 10 μm edge length will result in homogenized thermal conductivity values which are independent of the RVE size. Therefore, this RVE size was used.

Computational homogenization was carried using COMSOL/MATLAB. A mesh convergence study was conducted to determine the number of elements required for results to be independent of the element size. It was found that increasing the number of elements beyond 50×50 did not result in any significant change in the results. The final mesh having 50×50 elements used in the current work to carry out computational homogenization is shown in Figure 6.8.

The effect of distribution non-uniformity was incorporated into the mesh using an interpolation function which applied the thermal conductivity distribution, as shown in Figure 6.6, to the integration points in the finite element mesh. It is important to note here that due to the condition of scale separation, the inclusion particles were not explicitly modeled in the geometry of the finite element domain. A temperature gradient was applied along the x- and y-directions of the RVE and Equation (6.28) was used to determine the effective thermal conductivity of the composite.

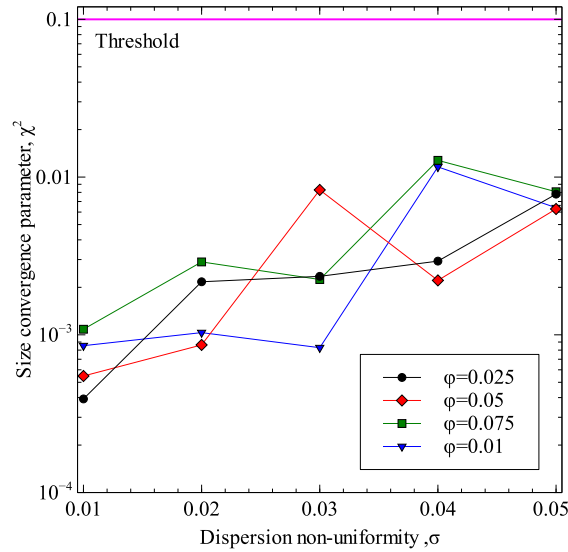


Figure 6.7. Verification of RVE size for computational homogenization.

$$K_{eff} = \frac{\langle q \rangle_{11} \langle \nabla T \rangle_{11} + \langle q \rangle_{22} \langle \nabla T \rangle_{22} + \langle q \rangle_{33} \langle \nabla T \rangle_{33}}{\langle \nabla T \rangle_{11}^2 + \langle \nabla T \rangle_{22}^2 + \langle \nabla T \rangle_{33}^2} \quad (6.28)$$

where q is the heat flux, ∇T is the temperature gradient, $\langle \bullet \rangle = \frac{1}{|V|} \int_V \bullet dV$ and V is the domain volume.

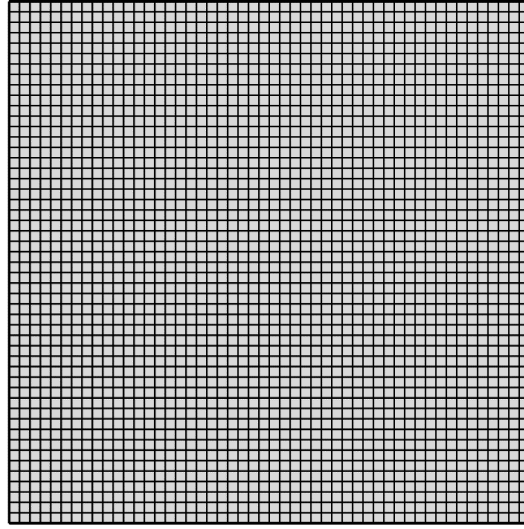


Figure 6.8. Finite element mesh for computational homogenization.

For the example of 5% Ge–Si composite considered above, the overall effective thermal conductivity of the composite was determined to be 21.41 W/m·K. For the case when inclusion distribution was uniform, the effective thermal conductivity was determined to be 21.06 W/m·K.

6.3 CASE STUDIES

In this section, the generalized effective medium theory formulated above is applied to different particulate composites to show its various capabilities. Before using the formulated model to carry out various studies, the model was validated against two experimental datasets for Al₂O₃–SiC platelet composite [156] and SiO₂–CNT composite [157]. The results of these validations are presented in Figure 6.9 and Figure 6.10 for Al₂O₃–SiC composite and SiO₂–CNT composite respectively. For both validations, the matrix thermal conductivity was set as the experimentally determined value and the inclusion dimensions were taken from the original experimental data. The model predictions were calculated by varying the thermal interface resistance in the range of 1×10^{-8} to 8×10^{-8} m²·K/W. This was done to take into account the variation in thermal interface resistance that can occur due to change in process parameters, the source of raw materials and can even vary greatly from sample to sample [158]. Model predictions for both composites showed good agreement with experimental measurements.

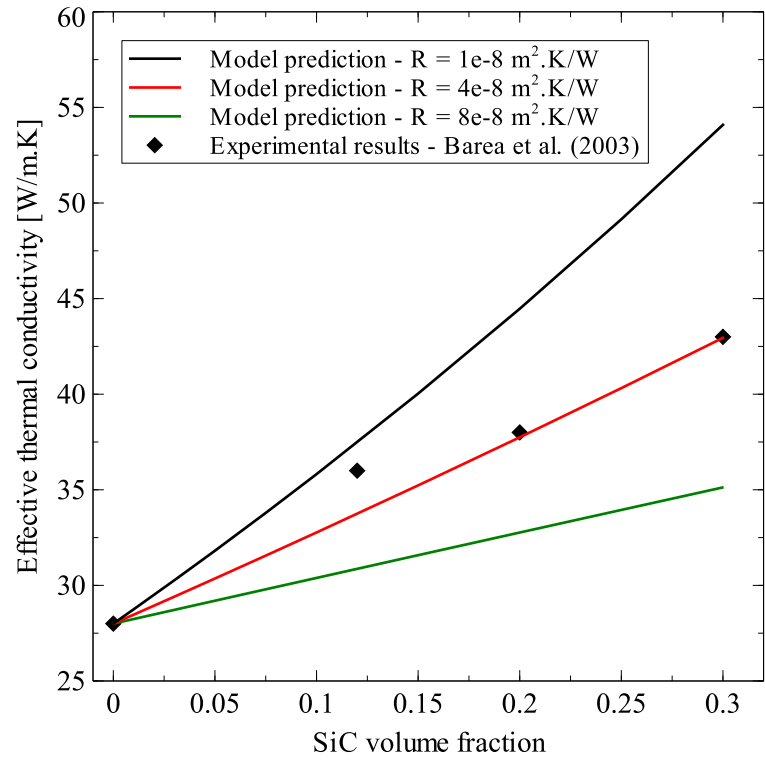


Figure 6.9. Comparison of model predictions with experimental results for Al_2O_3 -SiC composite [156].

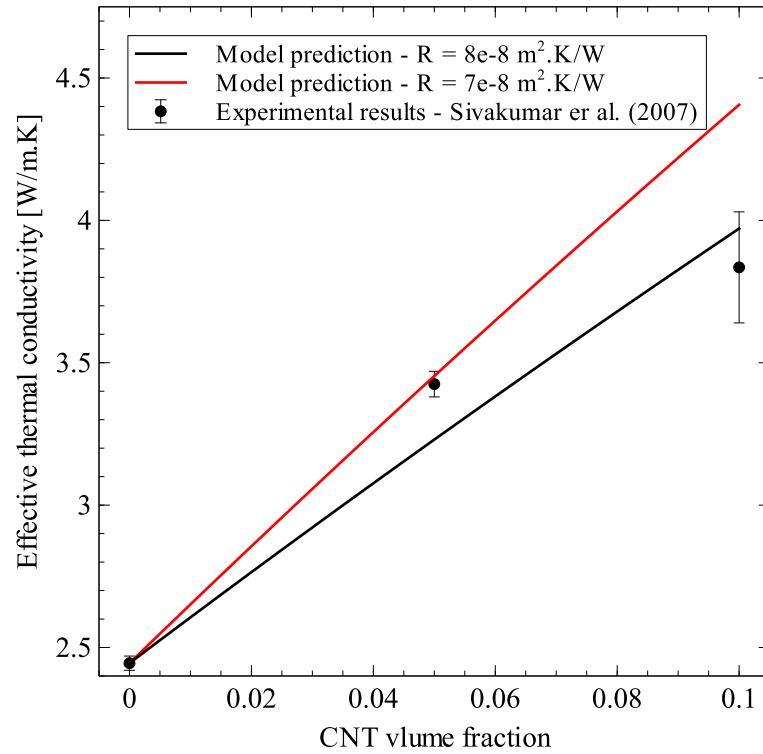


Figure 6.10. Comparison of model predictions with experimental results for SiO₂-CNT composite [157].

6.3.1 Effect of nanometer sized inclusions

The generalized EMT formulated in the current work was applied to two particulate nanocomposites, Ge-Si composites and alumina-CNT composites to study the effect of nanometer sized inclusions on the effective thermal conductivity of the composites.

The Ge-Si composite was studied for a case reported in literature for spherical Si inclusions in Ge matrix. Figure 6.11 shows a comparison of the effective thermal conductivities of Ge-Si composite predicted by the generalized EMT formulation with those predicted by Monte Carlo simulations [86]. The thermal interface resistance, R , was calculated using the diffuse mismatch model given by equation (6.29) and Si and Ge material properties were taken from [86] and are given in Table 6.1.

$$R = \frac{4(C_m v_m + C_p v_p)}{C_m v_m C_p v_p} \quad (6.29)$$

Table 6.1. Properties used for Ge-Si nanocomposite.

	Bulk thermal conductivity [W/m.K]	Bulk phonon mean free path [nm]	Phonon group velocity [m/s]	Volumetric specific heat capacity [J/m ³ .K]
Silicon	150	268	1804	0.93x10 ⁶
Germanium	51.7	171	1042	0.87x10 ⁶

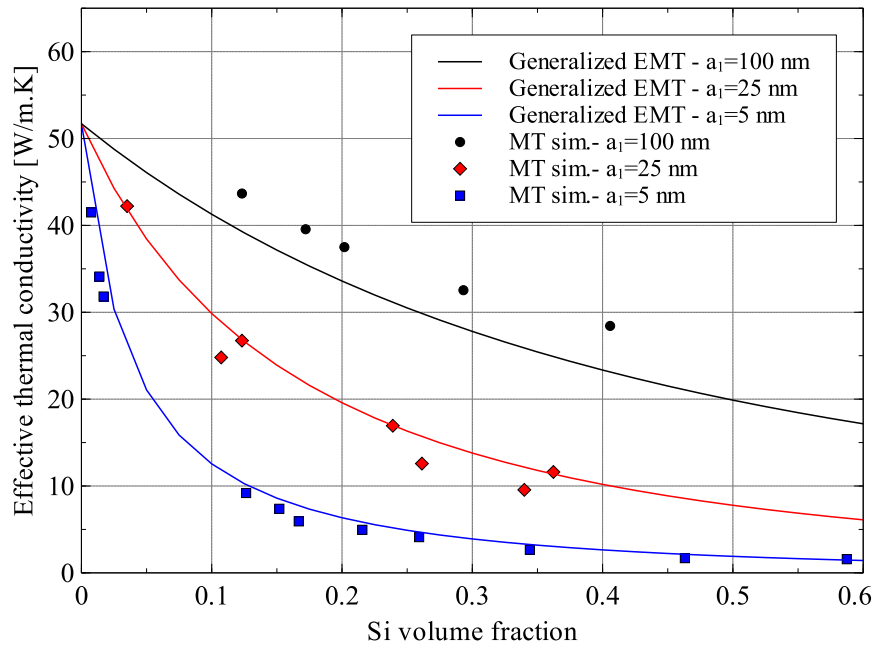


Figure 6.11. Predicted effective thermal conductivity of Ge-Si nanocomposite compared to Monte Carlo (MT) simulations [86].

The results showed that the effective thermal conductivity of Ge–Si nanocomposites is significantly lower than the thermal conductivities of Si and Ge. The effective thermal conductivity falls to less than 5 W/m·K for Si inclusions with a diameter equal to 10 nm and a volume fraction of 20%. This drastic reduction occurs because both Silicon and Germanium have mean-free-paths much greater than the size of the Si inclusion.

The root-mean-squared error (RMSE) in model predictions for the nanocomposite with Si particles of radii 5 nm, 25 nm and 100 nm were 1.68 W/m·K, 2.18 W/m·K, and 4.45 W/m·K, respectively. These translated to normalized errors of 12.72%, 10.22%, and 12.25%, respectively. The RMSE for the case with inclusion size of 100 nm was higher than the other cases because the thermal conductivity of the composite was higher for this case. On the other hand, the normalized root mean squared error all three cases were almost the same. That being said, the difference in the results of the Monte Carlo simulation and the generalized EMT can be attributed to a number of reasons including the difference in the details included in the models and model domain size. Monte Carlo simulations involve the detailed simulation of the transport of a large number of energy carriers through the material whereas the generalized EMT only models the average effect of transport of energy carriers. But because of their complexity, Monte Carlo simulations are extremely computationally intensive and therefore are usually solved over a unit cell containing a single inclusion particle.

The generalized EMT was also applied to the case to alumina and aluminum matrix composites with randomly oriented multi-walled carbon nanotubes (MWCNT). A

comparison between the generalized EMT and Nan and coworkers' model [159] for the two cases is shown in Figure 6.12. Nan and coworkers' model can take into account the effect of size and orientation of CNTs on the effective thermal conductivity of the composite but ignores the effect of CNT size on the thermal conductivity of matrix and CNT inclusion itself. The properties of alumina, aluminum, and MWCNTs used in the current work are shown in Table 6.2.

For comparison between the two models, the value of the thermal interface resistance, R , was varied from 0 to 1×10^{-7} . For high values of thermal interface resistance, a very small difference was observed between the generalized EMT and Nan and coworkers' model for alumina–MWCNT composite. In this case, the effect of interfacial resistance dominated the effect of inclusion size and therefore, the difference is more prominent at lower values of R . On the other hand, the aluminum–MWCNT composites showed dependence on CNT size for all interfacial resistance values. A significant result of the comparison is that the theoretical maximum effective thermal conductivity possible when $R=0$ is reduced from 85 W/m·K to 78 W/m·K for alumina matrix composite and from 298 W/m·K to 278 W/m·K for aluminum matrix composite when the CNT volume fraction is 5%.

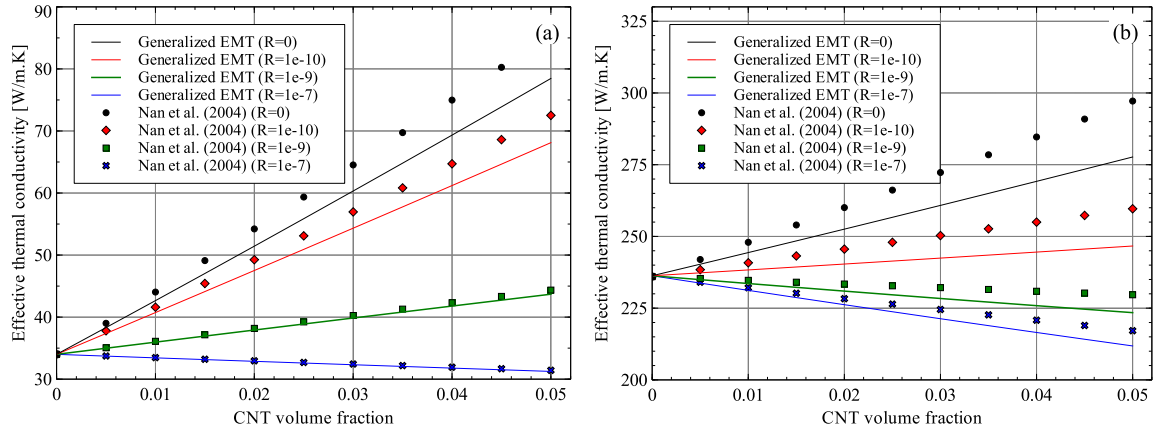


Figure 6.12. Effective thermal conductivity of (a) Alumina-MWCNT and (b) Aluminum-MWCNT nanocomposites.

Table 6.2. Properties for alumina, aluminum and MWCNTs.

	Bulk phonon thermal conductivity [W/m.K]	Bulk electron thermal conductivity [W/m.K]	Bulk phonon mean free path [nm]	Bulk electron mean free path [nm]	Diameter [nm]	Length [μ m]
Alumina	34	-	4.6	-	-	-
Aluminum	11.3	225	2.3	14.1	-	-
MWCNT	3000	-	2.2	-	10	2

To investigate the reason for the difference in the effect of nanometer inclusion sizes on the effective thermal conductivity of alumina–CNT and aluminum–CNT composites, the variation of the reduced thermal conductivities of alumina and aluminum matrices with CNT diameter was analyzed. The results are shown in Figure 6.13. As shown in the figure, the CNT diameter had a minimal effect on the alumina matrix thermal conductivity, which dropped by around 1 W/m·K when the CNT diameter was reduced from 20 nm to 5 nm. For the same change in CNT diameter, the thermal conductivity of the aluminum dropped from 236 W/m·K to 224.5 W/m·K. This large difference between aluminum and alumina in the sensitivity to CNT size can be attributed to the difference in the mean-free-paths of energy carriers for aluminum and alumina. For aluminum, the dominant energy carriers are the electrons whose mean-free-path is 14.1 nm compared to the 4.6 nm phonon mean-free-path for alumina. Since the CNT diameters were larger than the phonon mean-free-path for alumina, the addition of CNTs had little effect on the thermal conductivity of alumina.

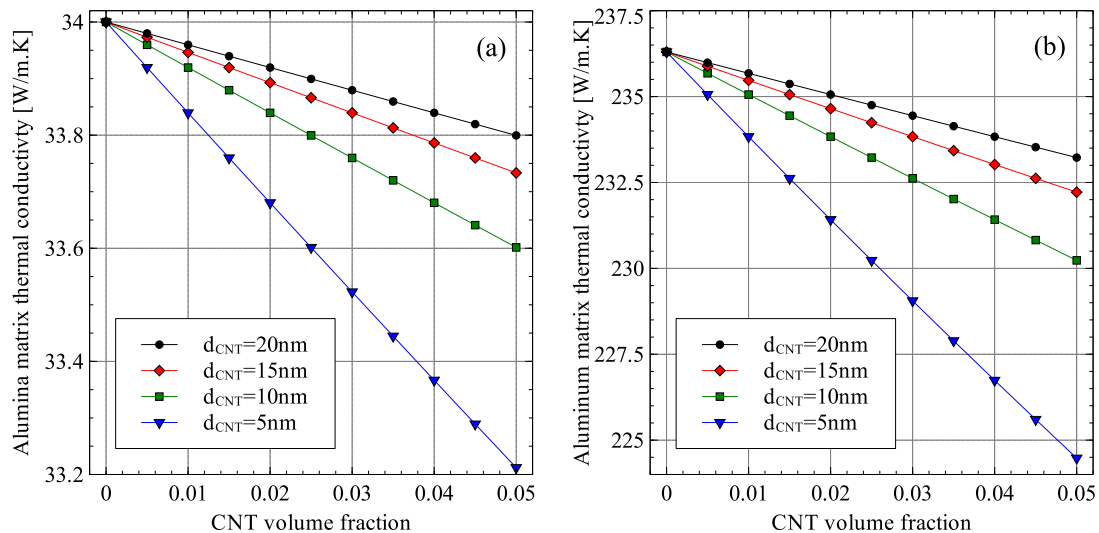


Figure 6.13. Modified (a) Alumina matrix and (b) Aluminum matrix thermal conductivities in MWCNT nanocomposites with randomly oriented CNTs.

6.3.2 Effect of inclusion orientation

The effective thermal conductivity of aligned spheroidal nanometer sized inclusions was estimated by Ordóñez-Miranda et al. [87]. The generalized EMT presented in the current work extends their approach to composites with randomly oriented spheroidal inclusions. A comparison of the axial direction effective thermal conductivity of Ge–Si nanocomposites with aligned and randomly oriented inclusion is presented in Figure 6.14 for two different aspect ratios of inclusions. For oblate inclusions ($p < 1$), the alignment of inclusions in a specific direction resulted in reduced effective thermal conductivity, which is the main purpose of the development of Ge–Si nanocomposites. On the other hand, for prolate inclusions ($p > 1$), the effect was reversed and randomly oriented prolate inclusions were more effective in reducing the thermal conductivity of Ge–Si composites.

The difference in the behavior of oblate and prolate shaped inclusions was because of two reasons. First, the cross-sectional area of the inclusion obstructing the motion of energy carriers in the matrix was reduced due to random orientation of particles in case of oblate inclusions while it increased for prolate inclusions. This resulted in the matrix thermal conductivity to increase due to random orientation of oblate inclusion and reduce due to the random orientation of prolate inclusions. Second, the collision mean-free-path of the energy carriers inside the inclusion increased due to random orientation of oblate inclusions while it reduced due to the random orientation of prolate inclusions. This resulted in an increase in the inclusion thermal conductivity for oblate inclusions and a decrease in the inclusion thermal conductivity for prolate inclusions due to random orientation.

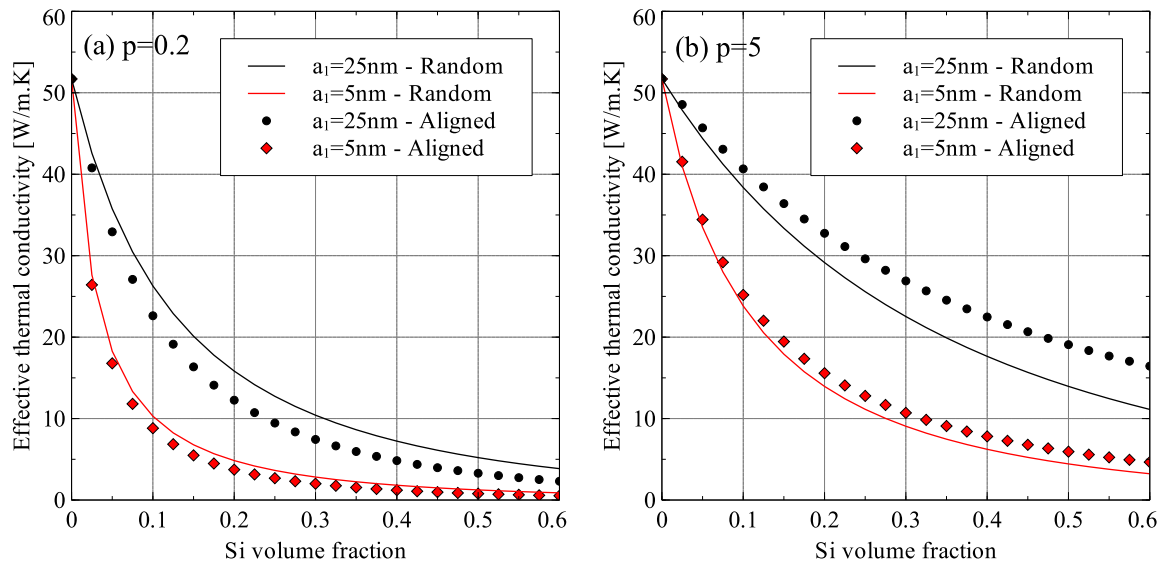


Figure 6.14. Dependence of Ge-Si effective thermal conductivity on inclusion alignment for inclusion aspect ratio p equal to (a) 0.2 and (b) 5.

6.3.3 Effect of non-uniform dispersion of inclusions

The two-scale approach presented in the current was used to study the effect of non-uniform dispersion on the effective thermal conductivity of Ge-Si nanocomposites. Without loss of generality, Ge-Si nanocomposites with 2.5%, 5%, 7.5% and 10% Si inclusions with diameter equal to 10 nm were considered in the study. The results, presented in Figure 6.15, show the effective thermal conductivity of the Ge-Si nanocomposite normalized with effective thermal conductivity of Ge-Si nanocomposite with uniformly dispersed inclusions plotted against the non-uniformity (shown in the figure as the ratio of standard deviation σ_ϕ and average of inclusion volume fraction $\phi_{Si,avg}$) in inclusion distribution. To analyze the variation of results due to randomness, each case was repeated five times by randomly generating an inclusion distribution in the RVE. As can be seen from the figure, the effectiveness of Si inclusions in reducing the effective thermal conductivity of the composite is adversely affected by non-uniformity in inclusion dispersion.

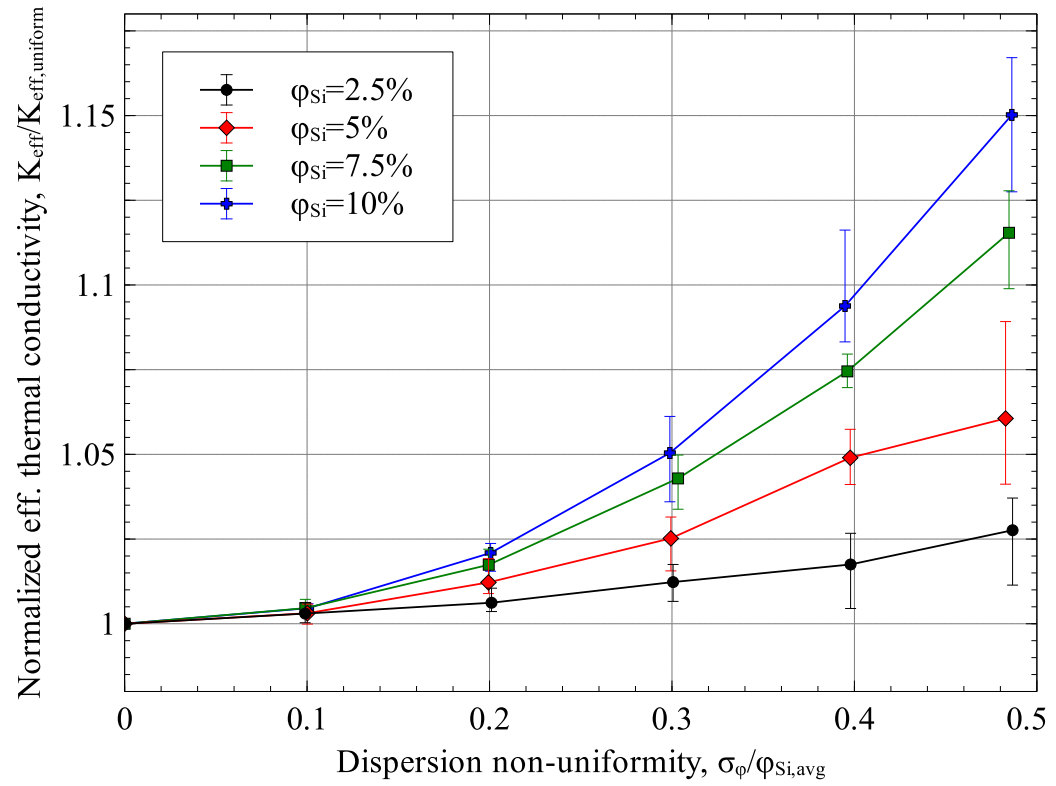


Figure 6.15. Effect of non-uniform dispersion on Ge-Si effective thermal conductivity.

6.4 APPLICATION TO POLYMER MATRIX COMPOSITES WITH HYBRID INCLUSIONS

In case of composites with hybrid inclusions i.e. a combination of platelet and tube type inclusions, the inclusions can form a percolating network that improves the effective thermal conductivity of the composite. In the current work for the case of two inclusions, it is assumed that the higher dimensional inclusion, referred with $i=1$, forms a percolating network through the lower dimensional inclusion, referred with $i=2$.

A recent work on the modeling of the effective thermal conductivity of polymer nanocomposites with hybrid fillers was presented by Chen et al. [160]. They used the effective medium theory and the thermal resistance method to formulate a two-step analytical model for the thermal conductivity of polymer nanocomposites with hybrid inclusions.

Chu et al. [161] modified the EMT model by Nan et al. by replacing φ_1 , the volume fraction of the platelet inclusion, with $(\varphi_1 - \varphi_p^1)^n$ in the numerator of equations (6.1) where φ_p^1 is the percolation threshold and n is the critical exponent. The critical exponent n represents the amount of percolation in the composite and is a function of the volume fraction of the lower dimensional inclusion. A lower value of n indicates higher percolation. Whereas as Chu et al. used a constant value of the exponent n , we propose equation (6.30) for determining n which describes the critical exponent as a function of the

tube-type inclusion volume fraction. The approach uses a single parameter just like the one proposed by Chu et al.

$$n = m + (1 - m) \exp(-10\varphi_2 / \varphi_{2,max}) \quad (6.30)$$

where the parameter m is the maximum value of n , φ_2 is the volume fraction of the tube-type inclusion and $\varphi_{2,max}$ is the total volume fraction of both inclusions combined.

6.4.1 Validation results for polymer matrix nanocomposites

To validate the proposed modeling approach, the experimental work carried by Yu et al. [162] on Epoxy- hybrid CNT-GNP nanocomposites was selected. In their work, Yu et al. fixed the total inclusion weight fraction to 10% and varied the ratio of carbon nanotubes and graphite nanoplatelets. The inclusion dimensions and material properties use in the model are given in Table 6.3. The percolation threshold, φ_p^l , was set at 0.001 as suggested by Chu et al. [161] and the parameter m was set as 0.85. A comparison of the predicted effective thermal conductivity with experimental measurements is shown in Figure 6.16(a). The predicted thermal conductivities by Chen et al.' model, Chu et al.'s model ($n=0.85$) and Nan et al.'s model ($n=1$) are also shown in the figure. As shown in the figure, the proposed model accurately captures the varying level of percolation in the composite providing very accurate estimates for the effective thermal conductivity. The proposed model also accurately predicts the optimum ratio of CNTs and GNPs for maximizing the effective thermal conductivity. On the other hand, the model by Chu et al. over-predicts the thermal conductivity at low levels of percolation (i.e. low weight fraction of CNTs)

because of the use of a constant critical exponent. Nan et al.'s model fails to capture the effect of percolation entirely and predicts a linear dependence of the effective thermal conductivity on the ratio of CNTs and GNPs added.

Interesting insights into the percolating behavior of the hybrid composite can be gained by looking at the dependence of the critical exponent on the amount of CNTs in the composite. This is shown in Figure 6.16(b). The figure shows that the percolation in the composite increases as the CNTs are added and reaches a maximum level well before the maximum amount of CNTs are added in the composite.

Table 6.3. Properties used for Epoxy-Hybrid CNT-GNP nanocomposite.

Material	Thermal	Thermal interface		Aspect ratio
	conductivity	resistance	Diameter	
	[W/m.K]	[10⁻⁸ m².K/W]	[nm]	
Epoxy	0.2	-	-	-
CNT	3000	1	1.4 [162]	350 [162]
GNP	4000 [158]	0.39 [158,163]	500 [162]	250 [162]

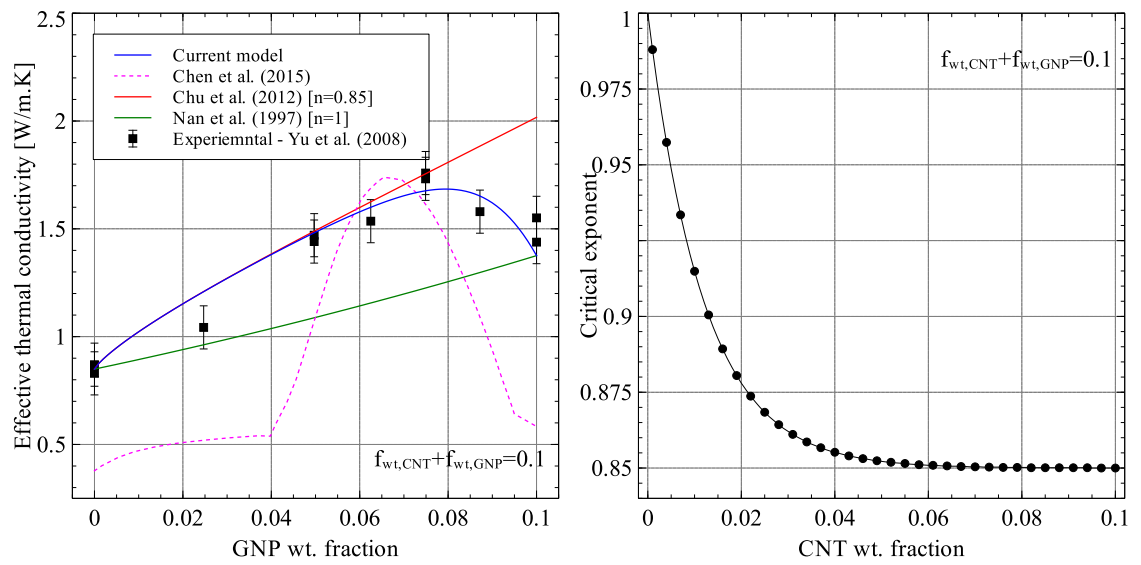


Figure 6.16. (a) Effective thermal conductivity of Epoxy- Hybrid CNT-GNP nanocomposite of Yu et al. (2008) (b) Variation of critical exponent.

To further validate the proposed model, the model was used to predict the effective thermal conductivity of the two composites with hybrid fillers, an epoxy matrix composite with 1% CNT-GNP hybrid filler [164] and an epoxy matrix composite with 1% BNNT-BNNS hybrid filler [165]. CNT and GNP properties were from Table 6.3 and the inclusion dimensions were taken from the experimental work of Yang et al.[164]. For the Epoxy-hybrid BNNT-BNNS nanocomposite, the material properties and inclusion dimension were taken from the experimental work of Yan et al.[165] and are given in Table 6.4. The thermal interface resistance for BNNT and BNNS were assumed to be of the same order as for CNT and GNP inclusions respectively. The comparison of the model predictions with experimentally determined values of thermal conductivity the cases of CNT-GNP hybrid filler ($m=0.8$) and BNNT-BNNS hybrid filler ($m=0.88$) are shown in Figure 6.17 and Figure 6.18 respectively. Estimated effective thermal conductivities using Chu et al.'s model and Nan et al.'s model are also presented for comparison. The usefulness of the model is especially shown in Figure 6.18 for Epoxy-hybrid BNNT-BNNS composite in which the model predicts a higher effective thermal conductivity for a BNNT-BNNS fraction ratio ($\sim 1:4$) not tested by the Yan et al [165].

Table 6.4. Properties used for Epoxy-Hybrid CNT-GNP nanocomposite.

Material	Thermal	Thermal interface		
	conductivity [W/m.K]	resistance [m ² .K/W]	Diameter [μm]	Aspect ratio
Epoxy	0.19	-	-	-
BNNT	200	2×10^{-8}	3×10^{-3}	350
BNNS	200	5×10^{-9}	1	250

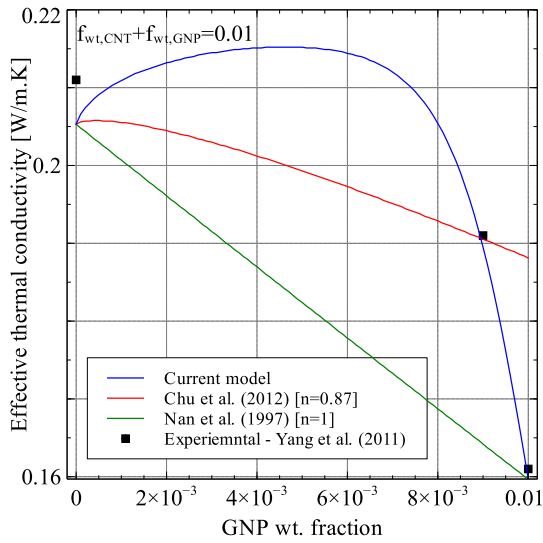


Figure 6.17. Effective thermal conductivity of Epoxy- Hybrid CNT-GNP nanocomposite of Yang et al. (2011).

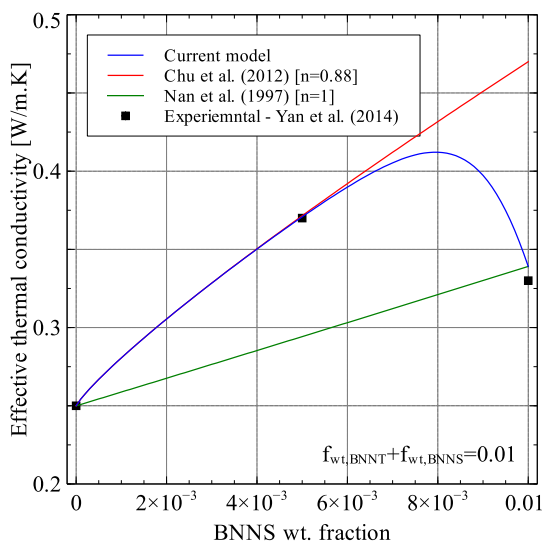


Figure 6.18. Effective thermal conductivity of Epoxy- Hybrid BNNT-BNNS nanocomposite of Yang et al. (2014).

6.5 APPLICATION TO SPARK PLASMA SINTERED HYBRID NANOCOMPOSITES

Current estimation techniques have been shown to overestimate the thermal conductivity of spark plasma sintered particulate nanocomposites [166,167] even when using very high value of Kapitza resistance between the matrix and inclusion particles. Wu et al. [166] compared the predicted thermal conductivity of Al/MWCNT nanocomposites with experimental results obtained using spark-plasma-sintered samples and found that the model over-predicted the effective thermal conductivity of the nanocomposite even when the interfacial thermal resistance was set as infinite. Similar results were found by Ahmed et al. [167] who studied the effective thermal conductivity of spark-plasma-sintered Alumina/MWCNT nanocomposites.

In the current work, the generalized effective medium theory approach was modified for the estimation for the effective thermal conductivity estimation of spark plasma sintered nanocomposites. This was done by first modeling the thermal conductivity of the polycrystalline matrix as a function of its average crystallite size and then using the modified matrix thermal conductivity in the generalized effective medium theory model.

6.5.1 Effective thermal conductivity of polycrystalline matrix

Polycrystalline materials exhibit lower thermal conductivities than the single crystals of the same material due to the existence of grain boundaries and the thermal conductivity of the polycrystals decreases with decreasing crystal size [168–175]. Several efforts have

been made to model the effective thermal conductivity of polycrystals as function of crystallite size. Yang et al. [172] presented a model to relate the isotropic thermal conductivity of polycrystals to their average crystallite size. Their model is shown by equation (6.31).

$$K_{pc} = \frac{K_{large}}{1 + \frac{R_K K_{large}}{d}} \quad (6.31)$$

where K_{pc} and K_{large} are the thermal conductivity of the polycrystalline material and the corresponding material with large grains, R_K is the Kapitza thermal resistance of the grain boundary and d is the average crystallite size in the polycrystalline material.

In cases when the crystallite size approaches the mean free path of the energy carriers in the material, equation (6.31) leads to an over-prediction of the effective thermal conductivity of the polycrystals. Dong et al. [174] formulated a new model to take into account the reduction in the thermal conductivity of the polycrystalline material due to scattering of energy carriers at the grain boundaries. Their model is described by equation (6.32).

$$K_{pc} = \frac{K_{large} / (1 + \Lambda_0 / d^\alpha)}{1 + R_K [K_{large} / (1 + \Lambda_0 / d^\alpha)] / d} \quad (6.32)$$

where Λ_0 is the mean free path of the energy carriers and the parameter α ranging from $1/2$ to $3/4$.

The mean free path of phonons in alumina is around 4.8nm [167] which is much larger than the average crystallite size of the alumina matrix considered in the current work. In the current work, a modified form of equation (6.31), shown in equation (6.33), was used to model the effective thermal conductivity of polycrystalline alumina matrix.

$$K_{pc} = \frac{K_{large}}{1 + \left(\frac{R_K K_{large}}{d} \right)^n} \quad (6.33)$$

6.5.2 Validation and Results

To model the thermal conductivity of polycrystalline alumina as a function of its crystallite size using equation (6.33), the thermal conductivity of dense alumina was estimated using the experimentally measured sample thermal conductivities and relative densities. This was done using the generalized effective medium theory model defined by equations (6.1)-(6.9) by solving for matrix thermal conductivity when the effective thermal conductivity of porous alumina is known. The results of this inverse problem are listed in Table 6.5.

Using the thermal conductivity values of dense alumina along with the corresponding average crystallite size, a parameter estimation was carried out using the Nelder-Mead simplex search algorithm [149] implemented in MATLAB. The fitted model on of thermal conductivity of polycrystalline alumina is given by equation (6.34). A comparison of the modeled thermal conductivity of the polycrystalline alumina with experimental results is shown in Figure 6.19. The figure shows that the model presented

in equation (6.34) is able to very accurately predict the thermal conductivity of polycrystalline alumina.

$$K_{pc} = \frac{34.55[\text{W/ m.K}]}{1 + \left(\frac{(2.195 \times 10^{-9} [\text{m}^2 \cdot \text{K/ W}]) (34.55 [\text{W/ m.K}])}{d[\text{m}]} \right)^{8.814}} \quad (6.34)$$

Table 6.5. Dense material thermal conductivities of sintered alumina samples.

Average crystallite size [nm]	Porosity fraction	Measured sample thermal conductivity [W/m.K]	Dense material thermal conductivity [W/m.K]
69	0.395	5.29	10.50
72.74	0.375	6.00	11.50
66.2	0.335	7.24	12.73
84	0.015	84.00	31.29
115	0.010	31.37	31.85
98	0.009	31.72	32.15
122.5	0.008	32.23	32.64
127.3	0.007	33.84	34.20
125	0.004	34.44	34.65

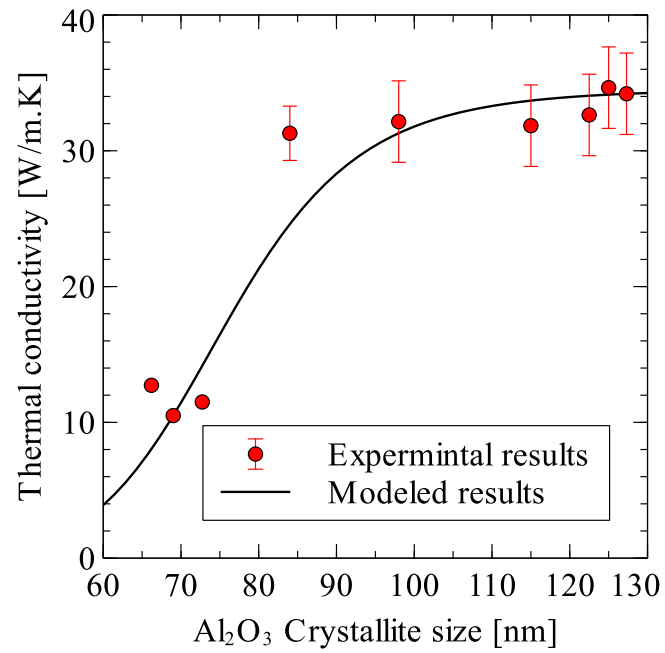


Figure 6.19. Predicted thermal conductivity of alumina as a function of its average crystallite size.

The effective thermal conductivities of sintered hybrid nanocomposites were estimated using the generalized effective medium theory model by taking into account the effect of CNT and SiC inclusions as well as porosity. The inclusion properties used in the model are listed in Table 6.6. The thermal conductivity of the matrix was estimated by inserting the experimentally measured crystallite size of the alumina matrix in the sintered sample in equation (6.34). The results are listed in Table 6.7. A comparison of the predicted thermal conductivities of the samples with experimentally determined values is shown in Figure 6.20. The figure also shows the predicted thermal conductivities of the sintered samples when the matrix thermal conductivity is considered independent of its crystallite size. It can be seen from the results that ignoring the crystallite size dependence of matrix thermal conductivity leads to very large errors and that the errors increase as the matrix crystallite size reduces. Considering the matrix thermal conductivity as a function of the matrix crystallite size improves the prediction accuracy for all cases.

Table 6.6. Material properties of inclusions used in estimation model.

Inclusion	Thermal conductivity	Diameter	
	[W/m.K]	[nm]	Aspect ratio
CNT	3000	20	2500
SiC	120	50	1

Table 6.7. Predicted effective thermal conductivities of sintered hybrid nanocomposite samples.

Sample composition	Average crystallite size [nm]	Prediction dense matrix thermal conductivity [W/m.K]	Experimental sample thermal conductivity [W/m.K]	Predicted results with crystallite size effect [W/m.K]	Predicted results without crystallite size effect [W/m.K]
Pure Al ₂ O ₃	125	34.13	34.44	34.06	33.92
5SiC-1CNT	98	31.28	22.20	27.60	29.99
5SiC-2CNT	93	29.64	21.33	25.60	29.34
10SiC-1CNT	88	27.22	17.75	21.38	26.69
10SiC-2CNT	85	25.29	17.57	19.62	26.30

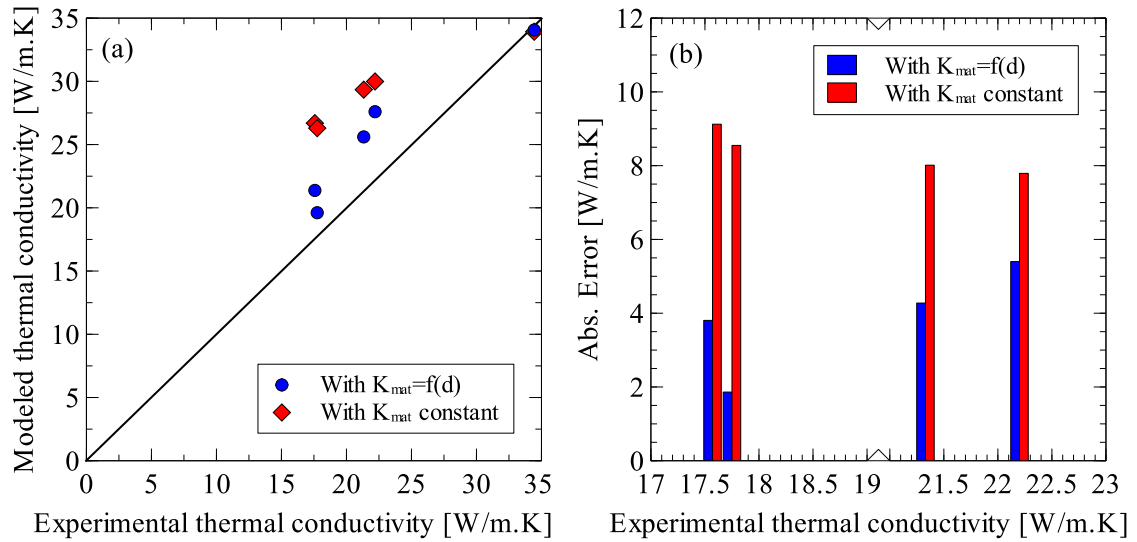


Figure 6.20. (a) Comparison of predicted thermal conductivities of sintered hybrid nanocomposite samples with experimentally measured values (b) Absolute errors in predicted thermal conductivities.

Using the formulated model, the effect of various parameters on the predicted thermal conductivity of the hybrid composite was studied. Figure 6.21 shows the effect of average matrix crystallite size on the effective thermal conductivity of alumina matrix hybrid nanocomposite. The amount of inclusions and porosity considered was kept same as those in the sintered samples. The parametric study shows that the effective thermal conductivity of the alumina matrix nanocomposite is a strong function of matrix crystallite size for crystallite sizes below 100nm. Above 100nm, the effect of crystallite size reduces and becomes negligible above 125nm.

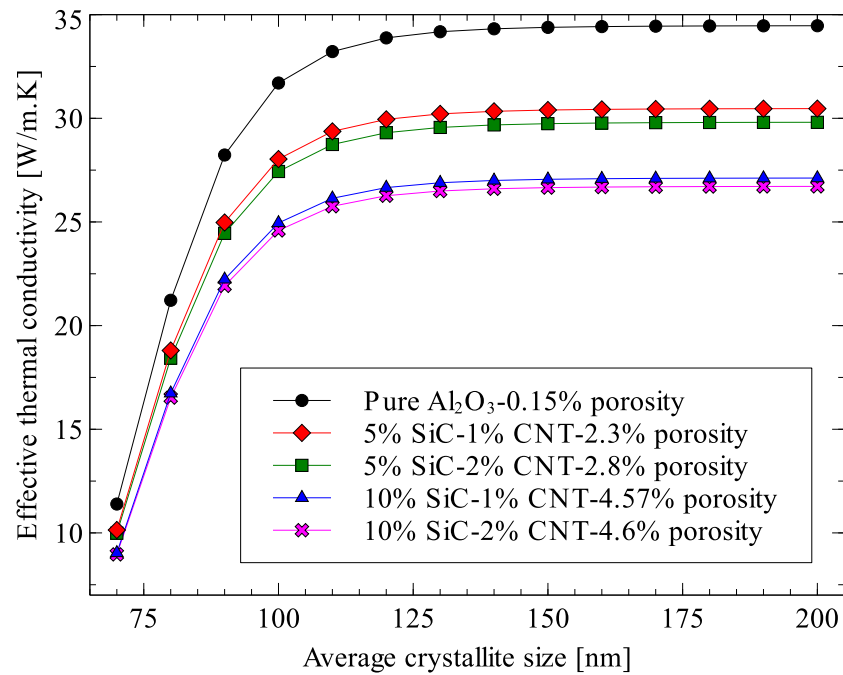


Figure 6.21. Effect of matrix crystallite size on the effective thermal conductivity of sintered hybrid nanocomposite samples.

The effects of inclusion volume fractions and porosity fraction on the effective thermal conductivity of alumina matrix hybrid nanocomposite are shown in Figure 6.22 and Figure 6.23 respectively. For these studies, the matrix crystallite size was set as 100nm. Although the thermal conductivities of CNT and SiC are higher than the thermal conductivity of the alumina matrix, their addition into the matrix results in a reduction in the effective thermal conductivity of the nanocomposite. This is due to the effect of interfacial thermal resistance between the inclusion particles and the matrix.

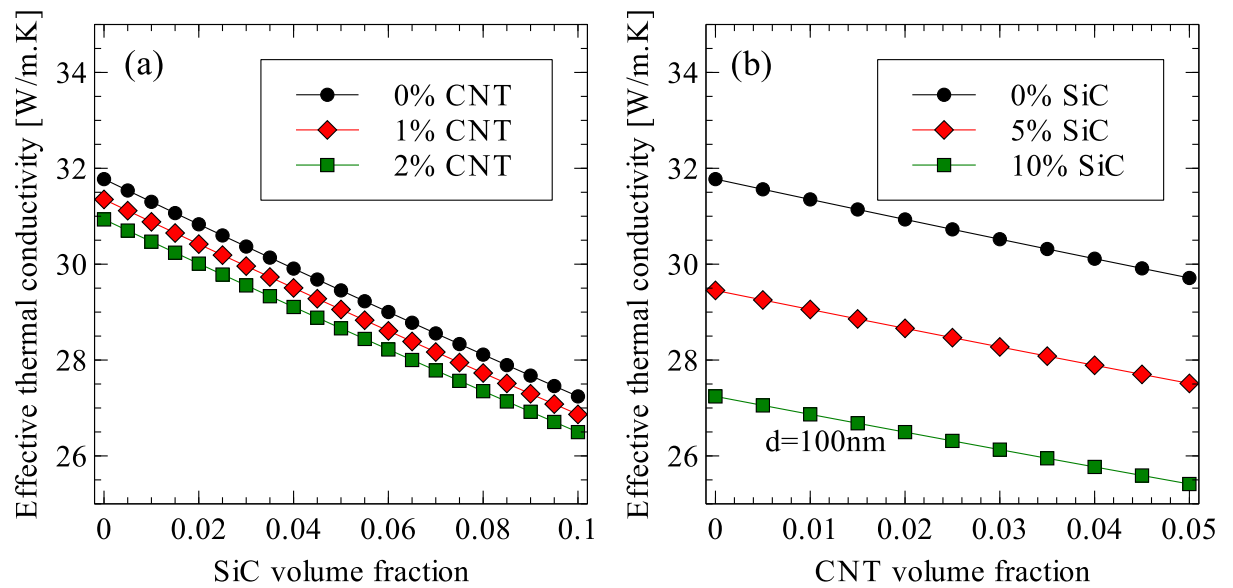


Figure 6.22. Effect of (a) SiC and (b) CNT volume fractions on the effective thermal conductivity of sintered hybrid nanocomposite samples ($d=100\text{nm}$ and porosity fraction=0).

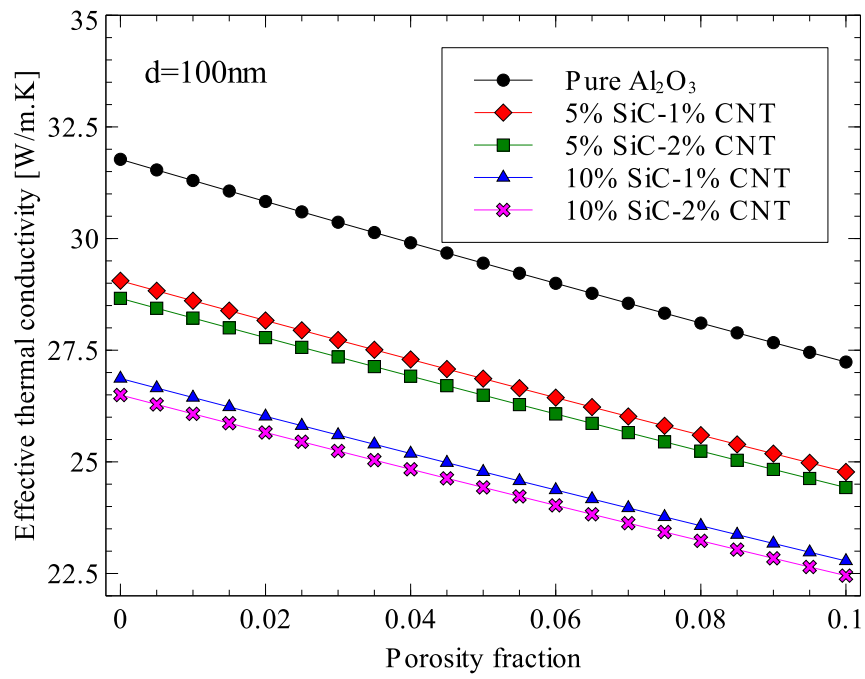


Figure 6.23. Effect of porosity fraction on the effective thermal conductivity of sintered hybrid nanocomposite samples.

6.6 CONCLUSIONS

In this chapter, we presented a generalized effective medium theory for the estimation of the effective thermal conductivity of particulate nanocomposites. The formulated EMT has the capability of incorporating the effects of size, shape, orientation and dispersion non-uniformity of multiple inclusions on the estimated thermal conductivity of particulate composites. Several applications of the formulated EMT were also presented.

For the Ge–Si nanocomposite, it was found that spherical Si inclusions result in better effective thermal conductivity reduction in the nanocomposite. It was also found that aligned oblate inclusions result in better thermal conductivity reduction than randomly oriented oblate inclusions. The effect is reversed for the case of prolate inclusions for which randomly oriented prolate inclusions show better thermal conductivity reduction. Finally, the effective thermal conductivity was found to be strongly dependent on the dispersion uniformity of the inclusion particles for Ge–Si nanocomposites. The effectiveness of nanometer-sized Si particles in reducing the thermal conductivity of Ge matrix reduced with increasing non-uniformity in Si dispersion.

For alumina–MWCNT and aluminum–MWCNT nanocomposites, the effect of high scattering of energy carriers on the effective thermal conductivity increased with reducing interface thermal resistance. Between alumina and aluminum, aluminum showed a greater sensitivity to CNT size due to its relatively large electron mean-free-path.

For polymer composites with hybrid inclusions, the model was found to accurately capture the effect of varying ratio of inclusions in the hybrid mix. Therefore, the formulated model can be a useful tool for material scientists in optimizing the hybrid filler content for composites. For spark plasma sintered nanocomposites, errors in model predictions were found to be reduced when the thermal conductivity of the matrix was taken as a function of its crystallite size.

CHAPTER 7

MULTISCALE MODELING: FORMULATION AND IMPLEMENTATION

7.1 INTRODUCTION

The prediction of the effective constitutive behavior of heterogeneous materials is both a practically and theoretically important problem, which draws input from many different disciplines, including materials science, mechanics and mathematics. Traditionally, the effective response of heterogeneous materials is either determined experimentally and represented as macroscale material model or found by using homogenization approaches. But due to the nonlinear nature of their constituent phases and complex microstructure, the determination of the effective response of such materials is a particularly challenging problem. Additionally, when effective properties of heterogeneous materials are directly used, the microscale information and any accompanying localization effects are lost.

An alternative approach in dealing with such materials is by using multiscale modeling approaches. In these approaches, the systems are represented at various length and/or time

scales. These methods allow the use of information of lower length or time scales to model the constitutive response at the larger scale. Therefore, multiscale methods are of indispensable importance in the design of heterogeneous materials.

An important issue with multiscale approaches is the transition of information between the various scales. Upscaling i.e. bringing information up from a lower scale is done using homogenization. The existing homogenization approaches fall into two main groups. The first approach includes mean-field variational bounding methods which statistically describe the microstructures. Among the techniques employed to solve the mean-field homogenization problem, the self-consistent schemes originally suggested by Kroner [7], the scheme by Mori and Tanaka [8] and the Differential Method [176] have been widely used. The second approach, computational homogenization [3–5], is based on modeling discrete microstructures. Although mean-field homogenization schemes are much more computationally efficient than the computational homogenization schemes, they suffer from several shortcomings. Since mean-field approaches are based on Eshelby's solution [6], the inclusion geometries are limited to regular ellipsoidal shapes. Additionally, mean-field approaches only solve the average fields (stress, strains, etc.) within the microscale model due to which localized effects within the microstructure are lost.

The current work involves the development of an efficient multiscale finite element methodology for the modeling and simulation of heterogeneous materials. The basic ingredients of any such methodology include a macroscale model, a microscale model and a methodology for the transition of information between the two scales.

7.2 OVERALL MULTISCALE MODELING ALGORITHM

The multiscale modeling methodology is based on two assumptions: scale separation and local periodicity. The two assumptions are shown graphically in Figure 7.1. The assumption of scale separation implies that the microscale model is significantly smaller than the macroscale model and, therefore, can represent a single point in the macroscale model. A direct consequence of the assumption is that heterogeneous materials with microscopic phases can be considered homogeneous at the macroscale. This assumption is used in the calculation of the material properties at the integration points in the macroscale model using the solution of microscale problem. The second assumption of local periodicity implies that although the solution of the microscale problem is not assumed to be periodic throughout the macroscale domain, it is assumed to be periodic in the vicinity of each individual macroscopic integration point. This is made possible by the use of a statistically representative microscale model of the heterogeneous microstructure.

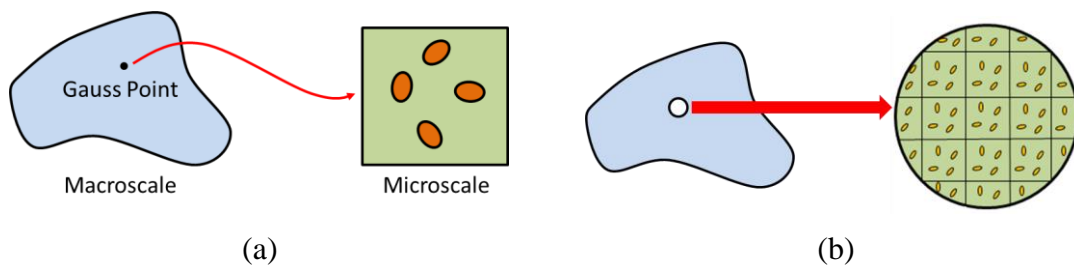


Figure 7.1. Assumption in multiscale methodology (a) Scale Separation (b) Local periodicity

The overall multiscale modeling approach in the context of finite element analysis of structural mechanics is presented in Figure 7.2. The microscale model is coupled with the macroscale model at finite element Gauss points where the constitutive response of the heterogeneous material is required. The macroscale strain solutions at the Gauss points are used to apply boundary conditions to microscale model. After the solution of the microscale boundary value problem, macroscale stresses and tangent stiffness at the macroscale Gauss points are estimated using the microscale solution.

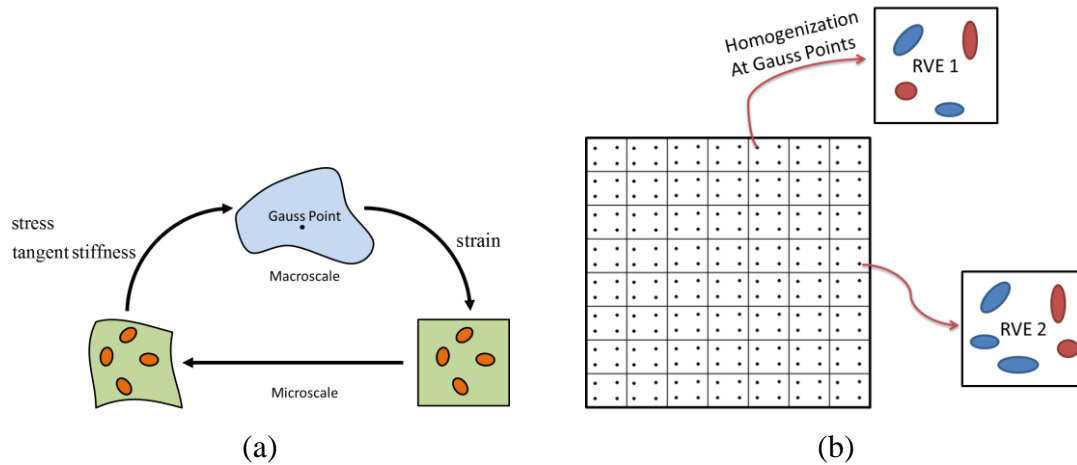


Figure 7.2. (a) Scaling methodology (b) FEM implementation scheme for the Multiscale model

7.3 MACROSCALE MODELING

In a two-scale finite element analysis, the macroscale problem is formulated as a standard finite element model. The constitutive behavior of the macroscale material is predicted using homogenization of the microscale model.

The problem solved for the macroscale is given by equations (7.1)-(7.6).

$$-\nabla \cdot \sigma_M = F_V \quad (7.1)$$

$$F_M = (1 + \nabla u) \quad (7.2)$$

$$J_M = \det(F_M) \quad (7.3)$$

$$\sigma_M = J_M^{-1} F_M S_M F_M^T \quad (7.4)$$

$$\varepsilon_M = \frac{1}{2} \left[(\nabla u)^T + \nabla u + (\nabla u)^T \nabla u \right] \quad (7.5)$$

$$S_M = f(\varepsilon_M) \quad (7.6)$$

where σ is the true stress, F_V is the body load, F is the deformation gradient, u is the displacement field, J is the jacobian, ε is the Green-Lagrange strain, S is the 2nd Piola-Kirchhoff stress and the subscript M refers to macroscale.

It should be noted that no relationship between the 2nd Piola-Kirchhoff stress and the Green-Lagrange strain is defined. The 2nd Piola-Kirchhoff stress tensor is calculated using homogenization of the microscale model associated with a particular integration point.

7.3.1 Macro-Micro Scale Transition

The macro-micro scale transition requires a methodology to apply suitable boundary conditions on the microscale model using either the macroscale stress or strain. To formulate its mathematical form, consider the following [61].

$$\mathbf{F}_m = \left(\vec{\nabla}_{0,m} \vec{x} \right) = \mathbf{F}_M + \left(\vec{\nabla}_{0,m} \vec{w} \right) \quad (7.7)$$

where \mathbf{F}_M is the macroscale deformation gradient, \mathbf{F}_m is the microscale deformation gradient, \vec{w} is a micro-fluctuation field which describes the variation of \mathbf{F}_m from \mathbf{F}_M . The volumetric average of the microscale deformation gradient can be determined using,

$$\bar{\mathbf{F}}_m = \mathbf{F}_M + \frac{1}{V_0} \int_{V_0} \vec{\nabla}_{0,m} \vec{w} dV_0 = \mathbf{F}_M + \frac{1}{V_0} \int_{\Gamma_0} \vec{w} \vec{N} d\Gamma_0 \quad (7.8)$$

Equation (7.8) can also be formulated in terms of an appropriate strain measure instead of the deformation gradient since rigid-body rotations do not contribute to stress.

$$\bar{\boldsymbol{\varepsilon}}_m = \boldsymbol{\varepsilon}_M + \frac{1}{V_0} \int_{\Gamma_0} \tilde{\boldsymbol{\varepsilon}}_m \vec{N} d\Gamma_0 \quad (7.9)$$

where $\bar{\varepsilon}_m$ and ε_M are the volume-average microscale and macroscale Green-Lagrange strain tensors and $\tilde{\varepsilon}_m$ is the microscale fluctuation in the Green-Lagrange strain.

When applying the microscale boundary condition using macroscale deformation gradient, the volumetric average of the microscale deformation gradient is assumed to equal to macroscale deformation gradient. To ensure this condition, the second term in equations (7.8) and (7.9) must vanish i.e.,

$$\begin{aligned} \int_{\Gamma_0} \bar{w} \vec{N} d\Gamma_0 &= 0 \\ \int_{\Gamma_0} \tilde{\varepsilon}_m \vec{N} d\Gamma_0 &= 0 \end{aligned} \quad (7.10)$$

The two basic methods for applying microscale boundary conditions using macroscale solution are:

1. by imposing displacement boundary conditions using the macroscale deformation gradient (Taylor's assumption).

$$\vec{u}_p = (F_M - I) \cdot \vec{X}_p, \quad p = 1, N_p \quad (7.11)$$

where F_M is the macroscale deformation gradient, N_p is the total number of boundary nodes and \vec{X}_p is the position vector of node p in the undeformed frame.

Applying displacement on the entire boundary is equivalent to setting $\bar{w} = 0$. Therefore, equation (7.10) is satisfied.

2. by imposing traction boundary conditions using the macroscale stress (Sachs assumptions).

$$\vec{p} = \vec{n} \cdot \vec{P}_M \text{ on } \Gamma_o \quad (7.12)$$

where \vec{P}_M is the macroscale first-Piola Kirchhoff stress, \vec{n} is the normal to the boundary Γ_o in the undeformed frame and \vec{p} is the traction vector.

These simple transition schemes do not always satisfy the microscale equilibrium conditions and in general either overestimate (Taylor) or underestimate (Sachs) the stiffness of the microscale model. An alternative to these boundary conditions is the periodic boundary condition. Mathematically, it may be expressed as,

$$\vec{x}^+ - \vec{x}^- = \vec{F}_M \cdot (\vec{X}^+ - \vec{X}^-) \quad (7.13)$$

where \vec{X} and \vec{x} are the position vectors of a point in the undeformed and deformed configurations respectively and the superscripts + and – show opposite boundaries.

For a periodic boundary condition, equations (7.10) can be written as,

$$\begin{aligned} \int_{\Gamma_0} \vec{w} \vec{N} d\Gamma_0 &= \int_{\Gamma_0^+} \vec{w}^+ \vec{N}^+ d\Gamma_0 + \int_{\Gamma_0^-} \vec{w}^- \vec{N}^- d\Gamma_0 \\ \int_{\Gamma_0} \tilde{\varepsilon}_m \vec{N} d\Gamma_0 &= \int_{\Gamma_0^+} \tilde{\varepsilon}_m^+ \vec{N}^+ d\Gamma_0 + \int_{\Gamma_0^-} \tilde{\varepsilon}_m^- \vec{N}^- d\Gamma_0 \end{aligned} \quad (7.14)$$

Due to periodicity, this may be written as,

$$\begin{aligned}
\int_{\Gamma_0} \vec{w} \vec{N}^+ d\Gamma_0 &= \int_{\Gamma_0^+} \vec{w}^+ \vec{N}^+ d\Gamma_0 - \int_{\Gamma_0^-} \vec{w}^+ \vec{N}^+ d\Gamma_0 \\
\int_{\Gamma_0} \tilde{\varepsilon}_m \vec{N} d\Gamma_0 &= \int_{\Gamma_0^+} \tilde{\varepsilon}_m^+ \vec{N}^+ d\Gamma_0 - \int_{\Gamma_0^-} \tilde{\varepsilon}_m^+ \vec{N}^+ d\Gamma_0 \\
&= 0
\end{aligned} \tag{7.15}$$

Hence, the second term in equation (7.8) and (7.9) vanishes under periodic boundary condition. It is also important to note that for periodic boundary conditions, the boundary tractions are anti-periodic, i.e.,

$$\vec{P}^+ = -\vec{P}^- \tag{7.16}$$

7.4 MICROSCALE MODELING

In a multiscale algorithm, microscale models are used for determining the stresses and the tangent stiffness for the macroscale model. In the current work, three different approaches to microscale modeling were studied. These were mean-field homogenization based microscale modeling, computational homogenization based microscale modeling and a hybrid approach which combines the features of mean-field and computational homogenization approaches. The details of each modeling approach is presented in the sections 3.2 to 3.4. First, in section 3.1, the micro-macro scale transition is discussed.

7.4.1 Micro-Macro scale transition

The micro-macro transition is based on Hill-Mandel condition [10] of equivalence of virtual work on the macro and microscales. Mathematically, it can be written in terms of first Piola-Kirchhoff stress and the deformation gradient as,

$$P_M : \delta F_M^T = \frac{1}{V_0} \int_{V_0} P_m : \delta F_m^T dV_0 \quad (7.17)$$

The integral on the right-hand side of equation (7.17) can be represented as a boundary integral in the following way.

$$\begin{aligned} P_m : \delta F_m^T &= P_m : \nabla_{0,m} \delta \vec{x} \\ &= \nabla_{0,m} \cdot (P_m^T \cdot \delta \vec{x}) - (\nabla_{0,m} \cdot P_m^T)_m \cdot \delta \vec{x} \end{aligned} \quad (7.18)$$

The equilibrium condition states that,

$$\nabla_{0,m} \cdot P_m^T = 0 \quad (7.19)$$

Therefore, equation (7.17) becomes,

$$P_M : \delta F_M^T = \frac{1}{V_0} \int_{V_0} \nabla_{0,m} \cdot (P_m^T \cdot \delta \vec{x}) dV_0 \quad (7.20)$$

Applying the divergence theorem yields,

$$P_M : \delta F_M^T = \frac{1}{V_0} \int_{\Gamma_0} \vec{N} \cdot (P_m^T \cdot \delta \vec{x}) d\Gamma_0 = \frac{1}{V_0} \int_{\Gamma_0} \vec{P}_m \cdot \delta \vec{x} d\Gamma_0 \quad (7.21)$$

In a similar manner to equation (7.21), the volume-average of first Piola-Kirchhoff can also be represented as a boundary integral.

$$\begin{aligned}
\bar{P}_m &= \int_{V_0} P_m \, dV_0 \\
&= \int_{V_0} P_m \cdot \nabla_{0,m} \vec{X} \, dV_0 \\
&= \int_{V_0} \nabla_{0,m} \cdot (P_m^T \vec{X}) - (\nabla_{0,m} \cdot P_m^T) \vec{X} \, dV_0 \\
&= \int_{V_0} \nabla_{0,m} \cdot (P_m^T \vec{X}) \, dV_0 \\
&= \int_{\Gamma_0} \vec{N} \cdot (P_m^T \vec{X}) \, d\Gamma_0 \\
&= \int_{\Gamma_0} \vec{p}_m \vec{X} \, d\Gamma_0
\end{aligned} \tag{7.22}$$

For periodic boundary condition, the right-hand side of equation (7.21) can be written as,

$$\begin{aligned}
\frac{1}{V_0} \int_{\Gamma_0} \vec{p}_m \cdot \delta \vec{x} \, d\Gamma_0 &= \frac{1}{V_0} \left[\int_{\Gamma_0^+} \vec{p}_m^+ \cdot \delta \vec{x}^+ \, d\Gamma_0 + \int_{\Gamma_0^-} \vec{p}_m^- \cdot \delta \vec{x}^- \, d\Gamma_0 \right] \\
&= \frac{1}{V_0} \left[\int_{\Gamma_0^+} \vec{p}_m^+ \cdot (\delta \vec{x}^+ - \delta \vec{x}^-) \, d\Gamma_0 \right]
\end{aligned} \tag{7.23}$$

Using equation (7.13) for periodic boundary condition,

$$\begin{aligned}
\frac{1}{V_0} \int_{\Gamma_0} \vec{p}_m \cdot \delta \vec{x} \, d\Gamma_0 &= \frac{1}{V_0} \left[\int_{\Gamma_0^+} \vec{p}_m^+ \cdot (\delta F_M \cdot \vec{X}^+ - \delta F_M \cdot \vec{X}^-) \, d\Gamma_0 \right] \\
&= \frac{1}{V_0} \left[\int_{\Gamma_0^+} \vec{p}_m^+ \cdot (\vec{X}^+ - \vec{X}^-) \, d\Gamma_0 \right] : \delta F_M^T \\
&= \frac{1}{V_0} \left[\int_{\Gamma_0} \vec{p}_m \cdot \vec{X} \, d\Gamma_0 \right] : \delta F_M^T
\end{aligned} \tag{7.24}$$

Using equation (7.22), equation (7.24) becomes,

$$\frac{1}{V_0} \int_{\Gamma_0} \vec{p}_m \cdot \delta \vec{x} d\Gamma_0 = \bar{P}_m : \delta F_M^T \quad (7.25)$$

Upon comparing with equation (7.21), we arrive at the relationship between macroscale and microscale stresses.

$$P_M = \bar{P}_m \quad (7.26)$$

Equation (7.26) shows that the macroscale stresses are the volumetric average of microscale stresses.

In addition to the stresses, algorithmic or tangent modulus ($\partial P_M / \partial F_M$ or $\partial S_M / \partial \varepsilon_M$ based on the FEM solution methodology) is also required for the solution of the macroscale finite element problem. Methodologies for its calculations are discussed in the following sections.

7.4.2 Mean-field homogenization based microscale modeling

Mean-field homogenization can be incrementally applied to a nonlinear material to determine the stresses and the tangent modulus at the macroscale Gauss points. In the current work, the incremental mean-field modeling approach of Doghri and Tinel [88] who proposed a two-step mean-field homogenization approach for modeling materials with multiple heterogeneities has been implemented within the multiscale modeling framework. In the first step, the microstructure is divided into pseudo grains each containing only one

inclusion. Mean-field homogenization is carried for all pseudo grains to determine the effective stresses and tangent modulus in each grain. Finally, homogenization is carried out across all grains to determine the overall effective stresses and tangent modulus of the heterogeneous material. The two-step approach of Doghri and Tinel is shown graphically in Figure 7.3.

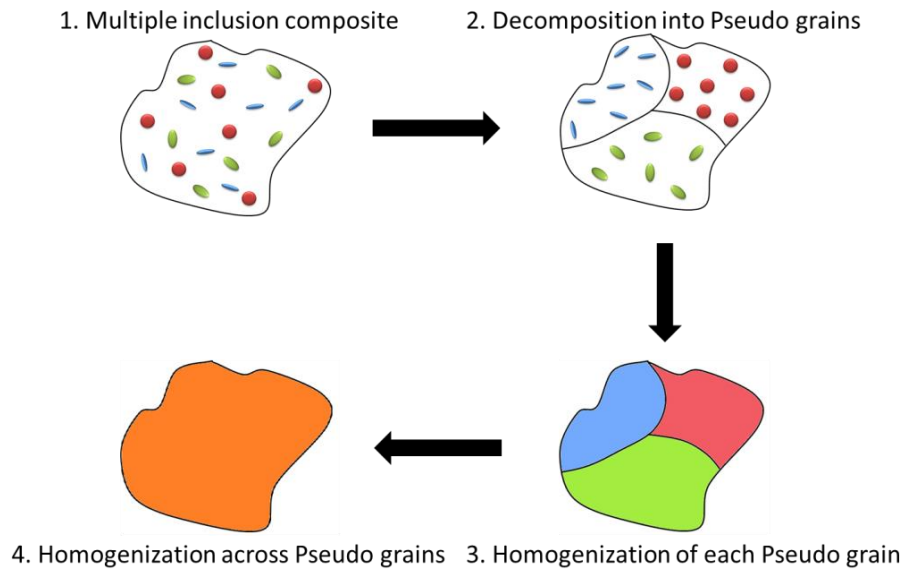


Figure 7.3. Two-step mean-field homogenization approach.

For a microstructure containing N types of inclusions i having volume fractions φ_i , the microstructure is divided into N pseudo grains with each pseudo grain having only one type of inclusion. Within each pseudo grain, the inclusion volume fraction φ_{inc} is set as $(1 - \varphi_0)$, where φ_0 is the volume fraction of the matrix.

The macroscale strain is applied to each pseudo-grain as the boundary condition. Using the mean-field strain localization relations, the strain increments in the inclusion and matrix are estimated using,

$$\begin{aligned}\Delta \varepsilon_{inc} &= A_{inc} \Delta \varepsilon_M \\ \Delta \varepsilon_{mat} &= (\Delta \varepsilon_M - \varphi_{inc} \Delta \varepsilon_{inc}) / (1 - \varphi_{inc})\end{aligned}\quad (7.27)$$

where φ_{inc} is the volume fraction of inclusion phase, A_{mat} and A_{inc} are the strain localization tensors defined by,

$$\begin{aligned}A_{mat} &= \left[(1 - \varphi_{inc}) I_4 + \varphi_{inc} B_a \right]^{-1} \\ A_{inc} &= B_a : A_{mat} \\ B_a &= \left[I_4 + S : C_{mat,alg}^{-1} (C_{inc,alg} - C_{mat,alg}) \right]^{-1}\end{aligned}\quad (7.28)$$

where I_4 is the 4th order identity, S is the Eshelby tensor [6] and $C_{mat,alg}$ and $C_{inc,alg}$ are the algorithmic tangent moduli of the matrix and inclusion for the current strain increment.

Using the matrix and inclusion strain increments, the stresses in the matrix and inclusion and the corresponding tangent moduli are estimated using the constitutive models of the matrix and inclusion. Finally, the effective stress and tangent modulus of the pseudo-grain is estimated using equation (7.29) and (7.30) respectively.

$$\sigma_{eff,i} = \varphi_{inc} \sigma_{eff} + (1 - \varphi_{inc}) \sigma_{mat} \quad (7.29)$$

$$C_{eff,alg,i} = \varphi_{inc} C_{inc,alg} : A_{inc} + (1 - \varphi_{inc}) C_{mat,alg} : A_{mat} \quad (7.30)$$

Since the strain increments and the algorithmic tangent moduli of the matrix and inclusion are implicitly related, an iterative scheme is required to solve for the stress and strain of the pseudo grain. At the start, the inclusion strain increment is assumed to be equal to the macroscale strain increment. Using this value, the entire process is completed once at the end of which the inclusion strain increment is recalculated using the updated parameters. If the difference between the inclusion strain increment at the beginning and the end of the step is within tolerance, the iterative process is stopped. Otherwise, the inclusion strain increment is updated and the step is repeated. The iterative scheme is shown in Figure 7.4.

Once the effective stresses and tangent moduli of all pseudo grains have been calculated the macroscale stresses and tangent modulus are calculated by Voigt homogenization across all the pseudo grains using equations (7.31) and (7.32).

$$\sigma_M = \sum_{i=1}^N \frac{\varphi_i}{1 - \varphi_0} \sigma_{eff,i} \quad (7.31)$$

$$C_{alg,M} = \sum_{i=1}^N \frac{\varphi_i}{1 - \varphi_0} C_{eff,alg,i} \quad (7.32)$$

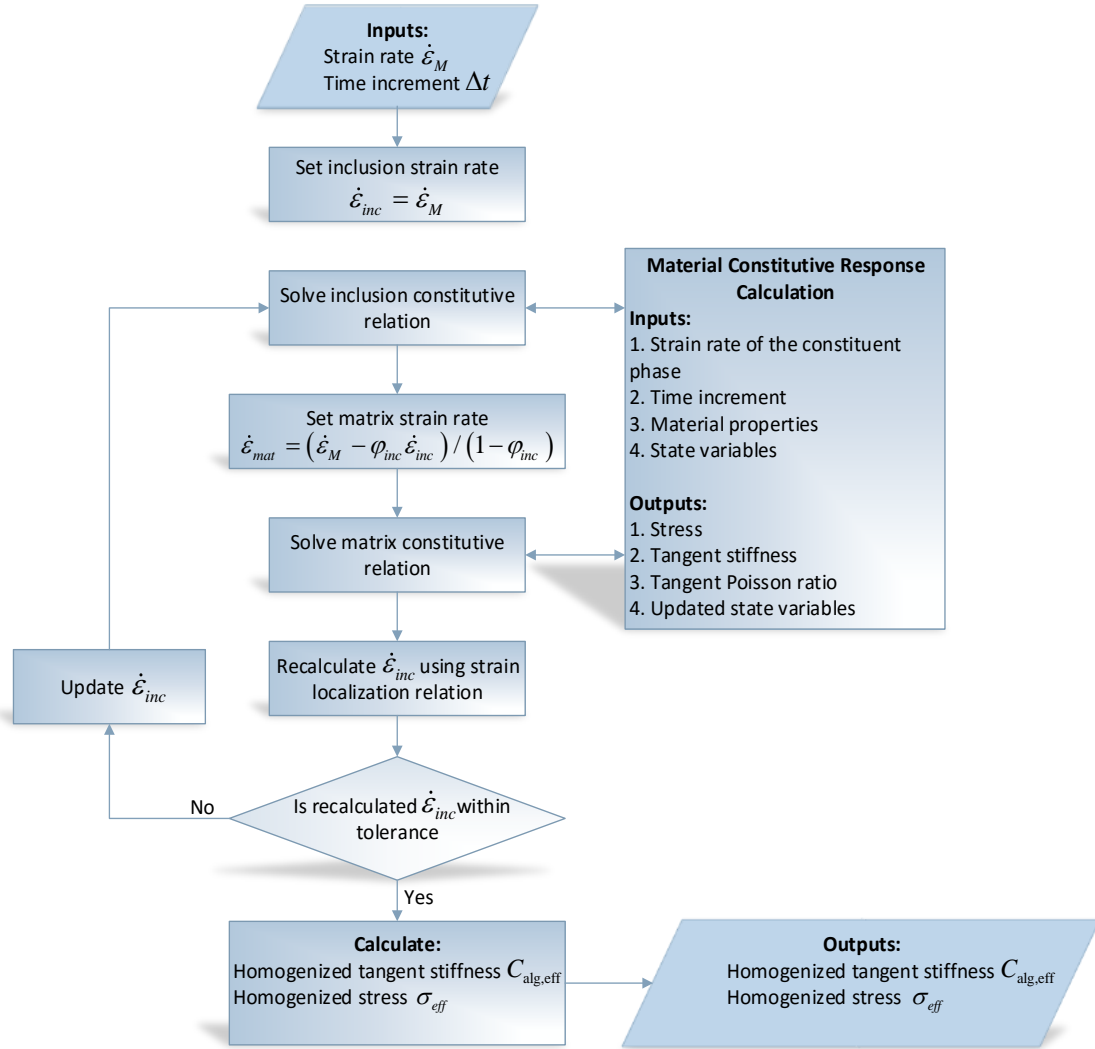


Figure 7.4. Effective stress and tangent Modulus update algorithm for Mean-field homogenization.

7.4.3 Computational homogenization based microscale modeling

In the case of computational homogenization, the microscale problem consists of a finite element model of the representative volume element of the heterogeneous material. The RVE contains all constituent phases of the material and the size of the RVE is statistically determined to accurately represent the overall macroscopic response of the material.

For the microscale model, the constitutive behavior of all phases present in the RVE is defined explicitly. The microscale model is defined by equations (7.33)-(7.40).

$$-\nabla \cdot \sigma_m = F_v \quad (7.33)$$

$$F_m = (1 + \nabla u) \quad (7.34)$$

$$J_m = \det(F_m) \quad (7.35)$$

$$\sigma_m = J_m^{-1} F_m^T S_m F_m \quad (7.36)$$

$$\varepsilon_m = \frac{1}{2} \left[(\nabla u)^T + \nabla u + (\nabla u)^T \nabla u \right] \quad (7.37)$$

$$S_m = C_{e,m} : (\varepsilon_{e,m}) \quad (7.38)$$

$$\varepsilon_{e,m} = (F_{e,m}^T F_{e,m} - I) \quad (7.39)$$

$$F_{e,m} = F_m F_{p,m}^{-1} \quad (7.40)$$

where σ_m is the true stress, F_V is the body load, F_m is the deformation gradient, u is the displacement vector, J_m is the jacobian, ε_m is the Green-Lagrange strain, S_m is the 2nd Piola-Kirchhoff stress and $C_{e,m}$ is the elasticity tensor of the microstructural constituent phases.

Periodic boundary conditions are applied to the microscale model using constraint equations. For a two-dimensional RVE, shown in, the constraint equations are given as equations (7.41)-(7.45). For a three-dimensional RVE, a simple extension of the same method can be used by incorporating a reference node 3 as well. An example geometry for the case of a 3D RVE is shown in Figure 7.5.

$$\vec{u}_2 - \vec{u}_1 - \vec{u}_{ref_1} = 0 \quad (7.41)$$

$$\vec{u}_4 - \vec{u}_1 - \vec{u}_{ref_2} = 0 \quad (7.42)$$

$$\vec{u}_3 - \vec{u}_1 - \vec{u}_{ref_1} - \vec{u}_{ref_2} = 0 \quad (7.43)$$

$$\vec{u}_{right, no\ edges} - \vec{u}_{left, no\ edges} - \vec{u}_{ref_1} = 0 \quad (7.44)$$

$$\vec{u}_{top, no\ edges} - \vec{u}_{bottom, no\ edges} - \vec{u}_{ref_2} = 0 \quad (7.45)$$

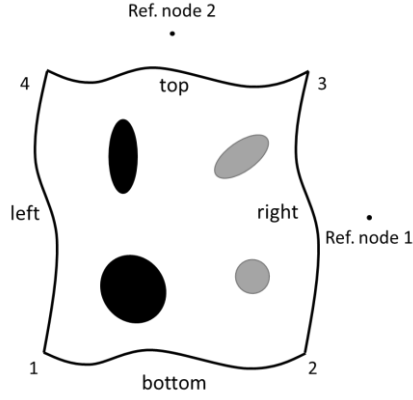


Figure 7.5. Applying periodic boundary conditions to microscale RVE

The displacement of the reference nodes is applied using the macroscale strain ε_M using equations (7.46).

$$\begin{aligned}
 u_1 &= \varepsilon_{xx} L \\
 v_1 &= \varepsilon_{xy} L / 2 \\
 w_1 &= \varepsilon_{xz} L / 2 \\
 u_2 &= \varepsilon_{xy} L / 2 \\
 v_2 &= \varepsilon_{yy} L \\
 w_2 &= \varepsilon_{yz} L / 2 \\
 u_3 &= \varepsilon_{xz} L / 2 \\
 v_3 &= \varepsilon_{yz} L / 2 \\
 w_3 &= \varepsilon_{zz} L
 \end{aligned} \tag{7.46}$$

where L is the edge length of the microscale RVE, (u, v, w) is the displacement field, subscripts 1, 2 and 3 refer to reference nodes 1, 2 and 3 and,

$$\varepsilon_M = \begin{bmatrix} \varepsilon_{xx} & \varepsilon_{xy} & \varepsilon_{xz} \\ \varepsilon_{xy} & \varepsilon_{yy} & \varepsilon_{yz} \\ \varepsilon_{xz} & \varepsilon_{yz} & \varepsilon_{zz} \end{bmatrix} \tag{7.47}$$

For scale transition from the microscale to the macroscale, the macroscale stress at the Gauss points is calculated using the following equation at the microscale.

$$S_{ij,M} = \frac{1}{|V_0|} \int_{V_0} S_{ij} dV \quad (7.48)$$

The tangent modulus $dS_M / d\varepsilon_M$ at the macroscale Gauss points is calculated after the calculation of the macroscale stress. Restarting from the completed solution, six different displacement loads (three in case of two-dimensional models) are applied to the reference nodes of the microscale model. Each load vector, shown below, will provide one column of the tangent modulus.

$$\begin{Bmatrix} \varepsilon_{xx} \\ \varepsilon_{yy} \\ \varepsilon_{zz} \\ \varepsilon_{yz} \\ \varepsilon_{xz} \\ \varepsilon_{xy} \end{Bmatrix} = \begin{Bmatrix} \varepsilon_o \\ 0 \\ 0 \\ 0 \\ 0 \\ 0 \end{Bmatrix}, \begin{Bmatrix} 0 \\ \varepsilon_o \\ 0 \\ 0 \\ 0 \\ 0 \end{Bmatrix}, \begin{Bmatrix} 0 \\ 0 \\ \varepsilon_o \\ 0 \\ 0 \\ 0 \end{Bmatrix}, \begin{Bmatrix} 0 \\ 0 \\ 0 \\ \varepsilon_o \\ 0 \\ 0 \end{Bmatrix}, \begin{Bmatrix} 0 \\ 0 \\ 0 \\ 0 \\ \varepsilon_o \\ 0 \end{Bmatrix}, \begin{Bmatrix} 0 \\ 0 \\ 0 \\ 0 \\ 0 \\ \varepsilon_o \end{Bmatrix} \quad (7.49)$$

where ε_o is a small strain increment.

7.4.4 Hybrid Approach to Microscale Modeling

The two previous approaches to microscale modeling suffer from certain shortcomings. The mean-field homogenization approach is limited by the inherent limitations of the mean-field approaches while the computational homogenization approach suffers from very high computational cost due to the solution of seven microscale problems: one for

solving for macroscale stresses and the remaining six for solving for the tangent modulus at the macroscale. In order to overcome the shortcomings of the previous two approaches, a hybrid approach for the solution of microscale problem was formulated.

Before proceeding with the hybrid modeling approach, it is important to understand the role of the two quantities (stresses and tangent modulus) calculated at the microscale in the macroscale problem solution. In the context of structural mechanics, the finite element method is used to solve the weak form of the equilibrium equation (7.50).

$$\int_{V_0} \delta \varepsilon_M^T : S_M \, dV_0 = \int_{V_0} \delta \varepsilon_M^T \cdot F_V \, dV_0 + \int_{\Gamma_0} \delta u_M^T \cdot p_M \, d\Gamma_0 \quad (7.50)$$

The final solution of the macroscale finite element problem depends only on one quantity calculated at the microscale, i.e. stress. The tangent modulus does not affect the final solution. Instead, the tangent modulus is used in the calculation of stiffness during the solution of the macroscale finite element problem using Newton-Raphson method shown by equation (7.51).

$$[K]^{(i-1)} \{\Delta U\}^{(i)} = \{F\} - \{R\}^{(i-1)} \quad (7.51)$$

where $[K]$ is the stiffness matrix, $\{\Delta U\}$ is the nodal displacement increment vector, $\{F\}$ applied nodal forces vector, $\{R\}$ is the vector of nodal reaction forces and i is the Newton-Raphson iteration. The accuracy of the estimated macroscale tangent modulus only affects the speed of convergence of the Newton-Raphson scheme. Even with the initial tangent modulus, it is possible that a nonlinear finite element problem can be solved. This

point is explained graphically in Figure 7.6 with the help of a simple one-dimensional example.

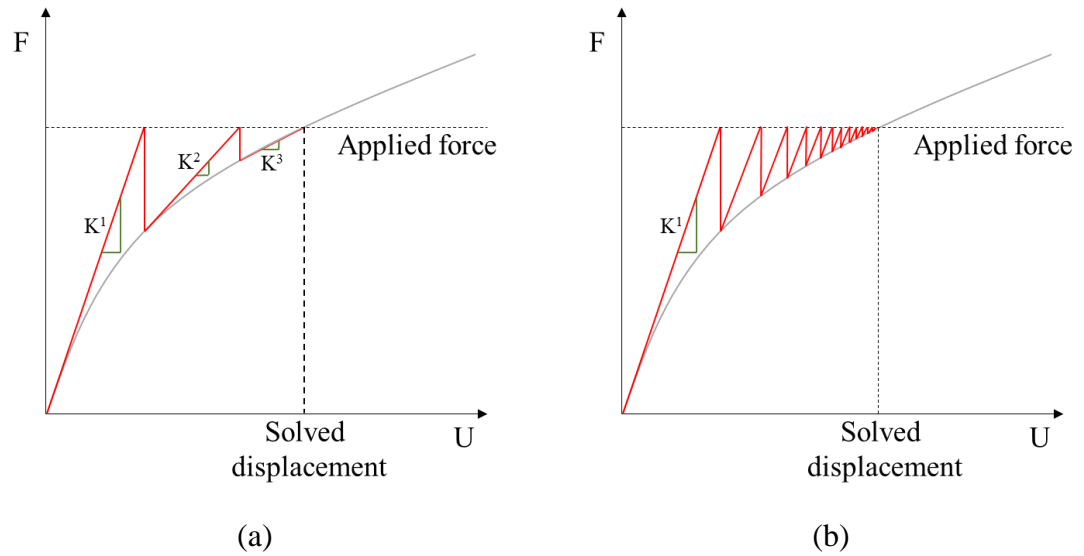


Figure 7.6. One dimensional example of the Newton-Raphson scheme for nonlinear problems using (a) updated stiffness at each iteration and (b) constant stiffness.

Based on the discussion in the preceding paragraphs, it is clear that it is more important to accurately calculate the homogenized macroscale stresses than tangent modulus. Since computational homogenization provides a more accurate estimate of macroscale stresses due to the assumptions involved in mean-field homogenization, it should be used for stress estimate. For tangent modulus calculation, the use of computational homogenization results in high computation time since the microscale problem needs to be solved several times. To reduce the computation time, mean-field homogenization can be used for its estimation.

A hybrid multiscale algorithm which uses both computational homogenization as well as mean-field homogenization was formulated in the current work to provide accurate predictions of stresses while reducing the overall computational time required to solve the microscale problem. In the hybrid approach, the microscale problem is solved in two steps. First, the microscale RVE boundary value problem is solved as discussed in section 7.4.3 and the macroscale stresses are determined using equation (7.48). Once the microscale boundary value problem has been solved under the application of macroscale strain ε_M , the homogenized state variables M of the microscale constituents are determined. In the case elastoplasticity, the state variable is the effective plastic strain which needs to be determined from the homogenized plastic strain tensor of each constituent. It is important to note that since the plastic strain field is localized, it cannot be directly homogenized. Instead, it is determined using homogenized total and elastic strains.

$$\begin{aligned}\bar{\varepsilon}_{mat,ij} &= \frac{1}{V_{mat}} \int_V \varepsilon_{ij} dV \\ \bar{\varepsilon}_{inc,ij}^i &= \frac{1}{V_{inc}^i} \int_V \varepsilon_{ij} dV\end{aligned}\tag{7.52}$$

$$\begin{aligned}\bar{\varepsilon}_{e,mat,ij} &= \frac{1}{V_{mat}} \int_V \varepsilon_{e,ij} dV \\ \bar{\varepsilon}_{e,inc,ij}^i &= \frac{1}{V_{inc}^i} \int_V \varepsilon_{e,ij} dV\end{aligned}\tag{7.53}$$

$$\begin{aligned}\bar{\varepsilon}_{p,mat,ij} &= \bar{\varepsilon}_{mat,ij} - \bar{\varepsilon}_{e,mat,ij} \\ \bar{\varepsilon}_{p,inc,ij} &= \bar{\varepsilon}_{inc,ij} - \bar{\varepsilon}_{e,inc,ij}\end{aligned}\tag{7.54}$$

Using the homogenized state variable, the algorithmic tangent moduli of all phases $C_{alg}(\varepsilon_p)$ is determined. Finally, mean-field homogenization is carried out as detailed in section 7.4.2 .

7.5 MULTISCALE MODEL IMPLEMENTATION IN MATLAB/COMSOL

The multiscale modeling methodologies discussed in the previous sections has been implemented using MATLAB and COMSOL Multiphysics. The methodologies are presented graphically in Figure 7.7 for mean-field homogenization based multiscale modeling, in Figure 7.8 for computational homogenization based multiscale model and in Figure 7.9 for the hybrid multiscale modeling approach.

In order to improve the computational efficiency of the computational homogenization based and hybrid approaches in which the microscale FEM model needs to be solved at each macroscale Gauss point, the MATLAB code has been developed to solve multiple microscale problems in parallel. The details about the implementation of the macroscale model, microscale model and MATLAB functions are given in the following sub-sections.

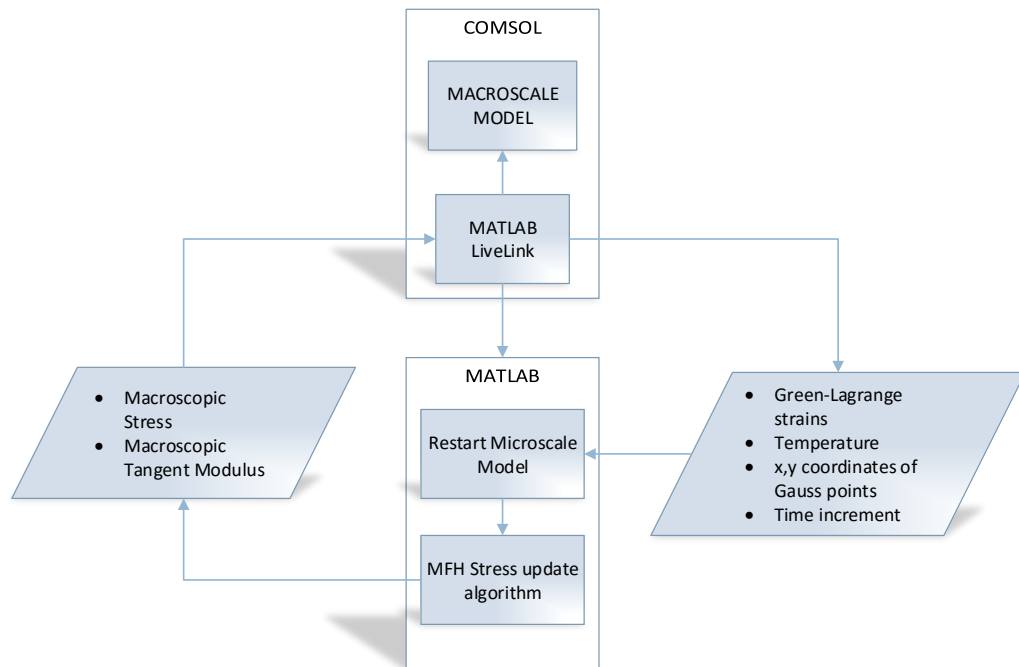


Figure 7.7. Mean-field homogenization based multiscale modeling methodology

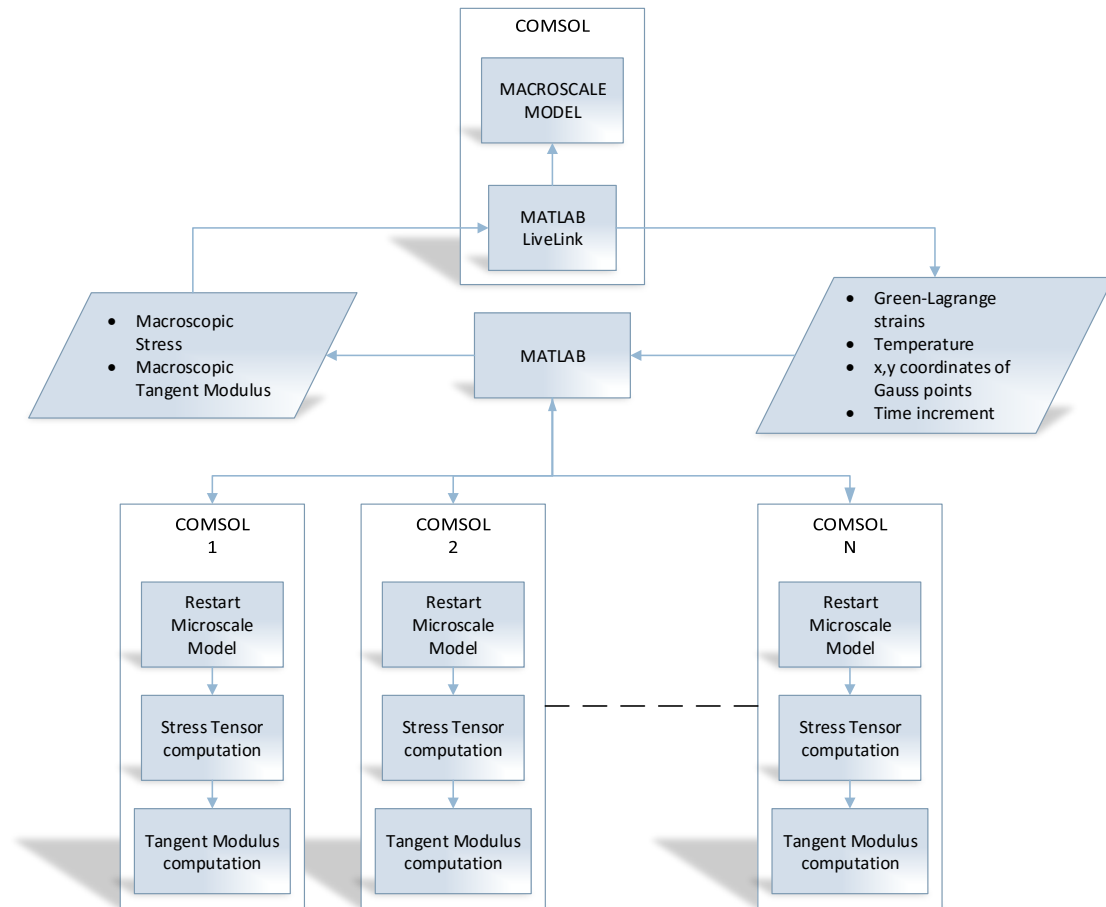


Figure 7.8. Computational homogenization based multiscale modeling methodology

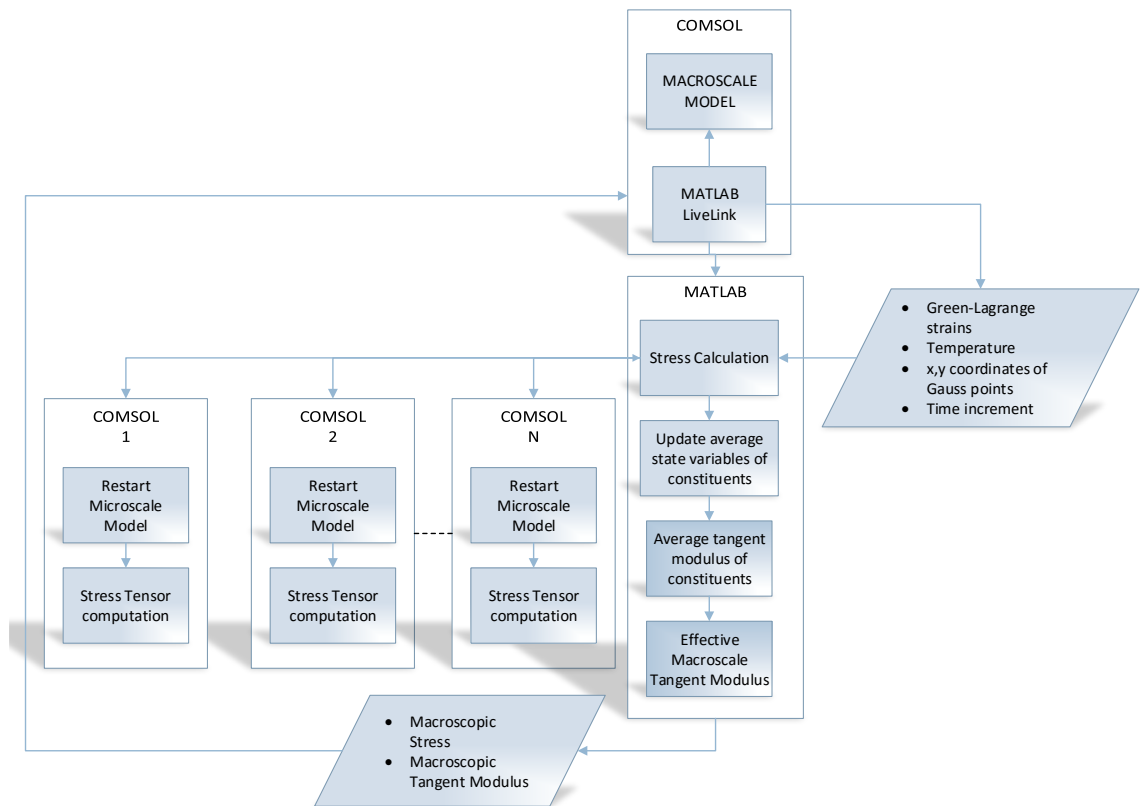


Figure 7.9. Hybrid multiscale modeling methodology

7.5.1 Macroscale model

The finite element model at macroscale is implemented in COMSOL Multiphysics. Since the macroscale stress tensor is calculated using computational homogenization of the microscale model associated with a particular integration point, the standard structural mechanics physics is modified to calculate the stresses using the microscale model. In COMSOL, this is achieved by defining MATLAB functions for the calculation of the components of stress tensor and replacing the default expressions for the stress components with the MATLAB functions. In addition to defining the functions for the stress components, functions are also defined for the derivative for the stress components with the strain components since these are required for the calculation of the jacobian. The modified equations in the structural mechanics physics inside COMSOL are shown in Figure 7.10. The MATLAB functions called from COMSOL are also defined in the macroscale COMSOL model as shown in Figure 7.11 and Figure 7.12.

Equation View

Variables

Name	Expression	Ur
solid.SI11	StressX(x,y,solid.el11,solid.el22,soli...	N/t
solid.SI12	StressXY(x,y,solid.el11,solid.el22,soli...	N/t
solid.SI13	0	N/t
solid.SI22	StressY(x,y,solid.el11,solid.el22,solid...	N/t
solid.SI23	0	N/t
solid.SI33	StressZ(x,y,solid.el11,solid.el22,soli...	N/t
solid.u_ttX	d(root.mod1.uTIME,TIME)	m/
solid.u_ttY	d(root.mod1.vTIME,TIME)	m/
solid.u_ttZ	0	m/
solid.u_tX	root.mod1.uTIME	m/
solid.u_tY	root.mod1.vTIME	m/

Figure 7.10. Modified stress-strain equations for macroscale model.

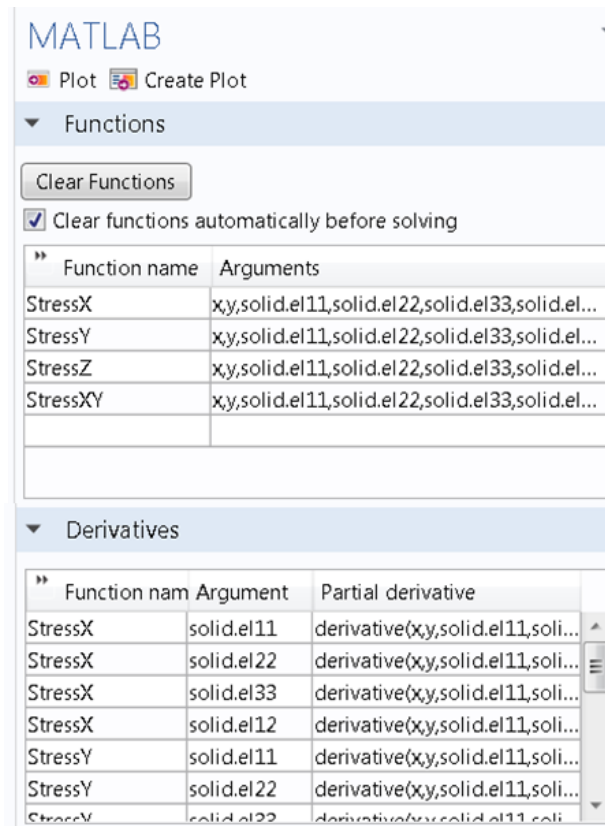


Figure 7.11. MATLAB stress functions calls defined in macroscale model.

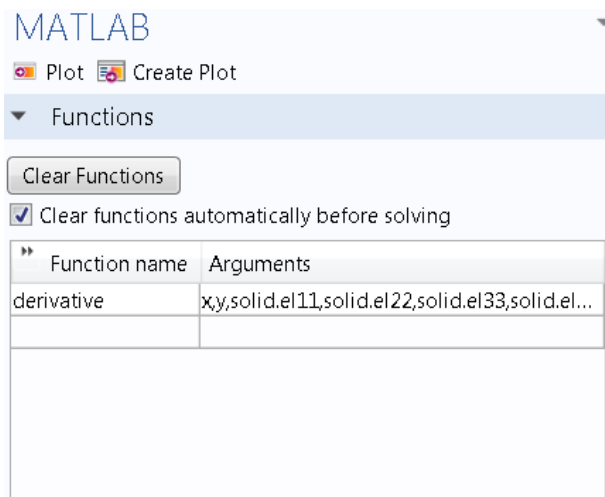


Figure 7.12. MATLAB tangent modulus function call defined in macroscale model.

7.5.2 Microscale model for computational homogenization based and hybrid approach

The microscale finite element model for computational homogenization based and hybrid multiscale approaches is a standard finite element model implemented in COMSOL Multiphysics. An example RVE geometry is shown in Figure 7.13.

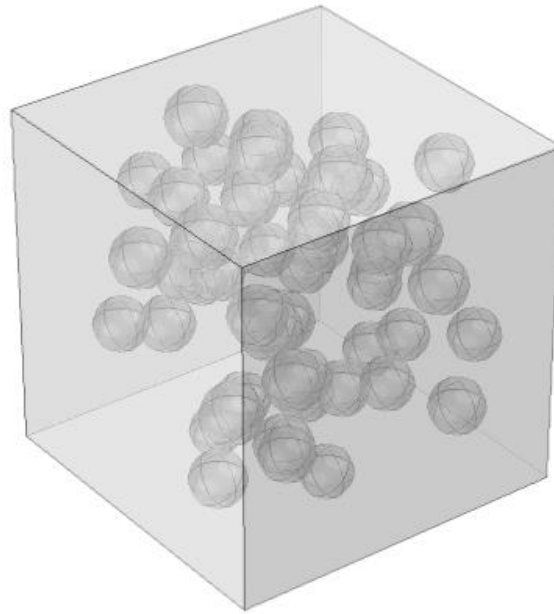


Figure 7.13. An example RVE geometry with 10 vol.% spherical inclusions.

The material constitutive behavior of all microscale constituent phases is explicitly defined in the COMSOL model. The boundary conditions are applied as follows. The vertex at (0,0,0) is fixed to eliminate rigid body motions. Periodic boundary conditions are defined for all surfaces using the *Periodic Condition* option available in COMSOL. The default *Periodic Condition* boundary condition ties the degrees of freedom on the faces where it is applied. Therefore, it does not allow for relative displacements between the

faces and is applicable only for cases when force loads are applied to the model. To make *Periodic Condition* usable with prescribed displacements, the equations for the *Periodic Condition* are modified by introducing nine new parameters, three for each periodic boundary (ref1x, ref1y, ref1z, ref2x ... ref3z). These parameters define the relative displacements of the faces in x, y and z-directions.

7.5.3 MATLAB Functions

MATLAB functions are used to define the stress components and their derivatives in the macroscale problem. The total number of MATLAB functions is equal to the total number of stress components plus one function to calculate derivatives. Therefore, for plane strain and axisymmetric macroscale problems, five MATLAB function need to be defined while for three-dimensional macroscale problems, seven functions need to be defined.

The inputs to the functions are vectors containing the positions of the integration points, final time at the end of the increment and Green-Lagrange strain components at the integration points. In the case of derivative functions, an additional input is required specifying with respect to which strain component the partial derivative of stress is required. Although the inputs are passed to all the functions, the solution of the microscale problem is carried out only in the first stress function called. The remaining functions only read the solution and pass the appropriate output back to COMSOL. The algorithms of the stress function and derivative function are given in Figure 7.14 and Figure 7.15.

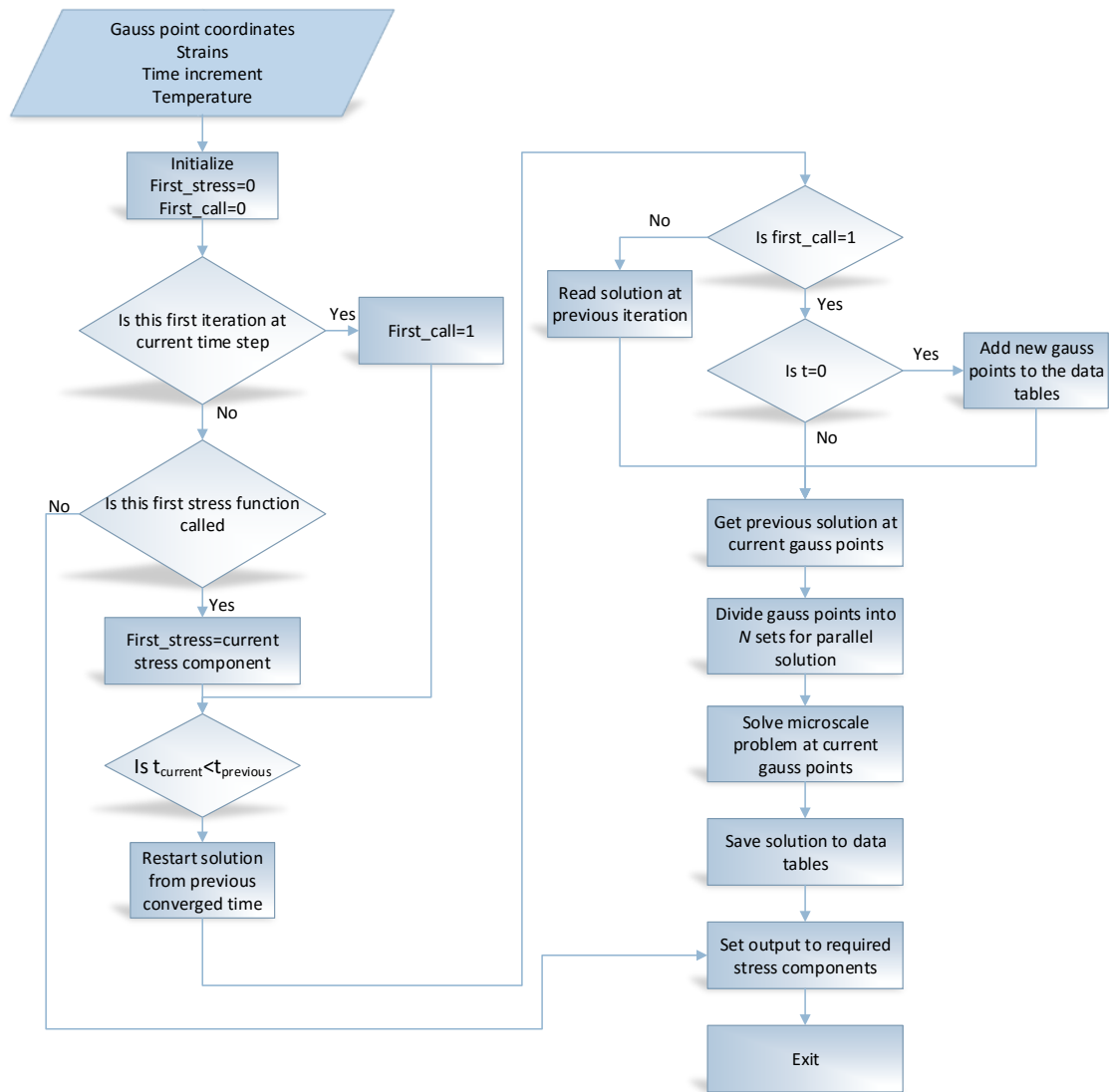


Figure 7.14. MATLAB function to solve microscale problem

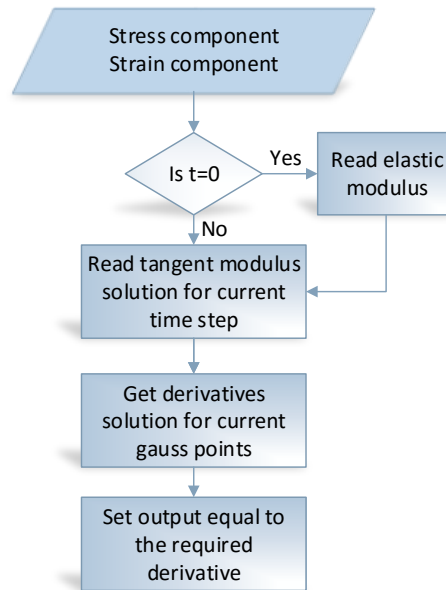


Figure 7.15. MATLAB function to return tangent modulus components using microscale model solution.

7.6 CASE STUDIES

The three multiscale modeling algorithms formulated in the present work were used to simulate the response of a particulate composite plate under two types of loadings, uniaxial extension and bending. The dimensions of the modeled plate is shown in Figure 7.16. The heterogeneous material is taken as an aluminum-10vol.% alumina composite represented by the RVE, shown in Figure 7.13. The plate was modeled as two-dimensional plane-strain problem.

Table 7.1. Material properties used in multiscale simulation.

Material	Elastic modulus [GPa]	Poisson's ratio	Yield stress [MPa]	Tangential modulus [GPa]
Aluminum	65	0.35	70	1
Alumina	370	0.22	-	-



Figure 7.16. Modeled plate dimensions.

7.6.1 Uniaxial extension

Under the plane strain assumption, a uniform strain of 1% was applied to the plate in the x-direction using displacement boundary condition. As a result, stresses in the x- and z-directions are generated in the plate. The applied boundary conditions are shown in Figure 7.17 and the solution of the uniaxial extension problem using the three multiscale algorithms is shown in Figures 7.18, 7.19 and 7.20. The computational homogenization based multiscale algorithm and the hybrid multiscale algorithm provide very close results while the mean-field homogenization based multiscale algorithm provides higher stresses.

In case of computational homogenization based and hybrid multiscale modeling algorithms, the solution at the microscale can also be analyzed. A representative RVE solution for the computational homogenization based multiscale model is shown in Figure 7.21. Although σ_y and σ_{xy} are produced in the RVE, their volume averages are zero and therefore, there are no macroscale stress in these directions.



Figure 7.17. Applied boundary conditions for uniaxial extension



Figure 7.18. Solution to the uniaxial tension problem using computational homogenization based multiscale model.



Figure 7.19. Solution to the uniaxial tension problem using hybrid multiscale model.



Figure 7.20. Solution to the uniaxial tension problem using mean field homogenization based multiscale model.

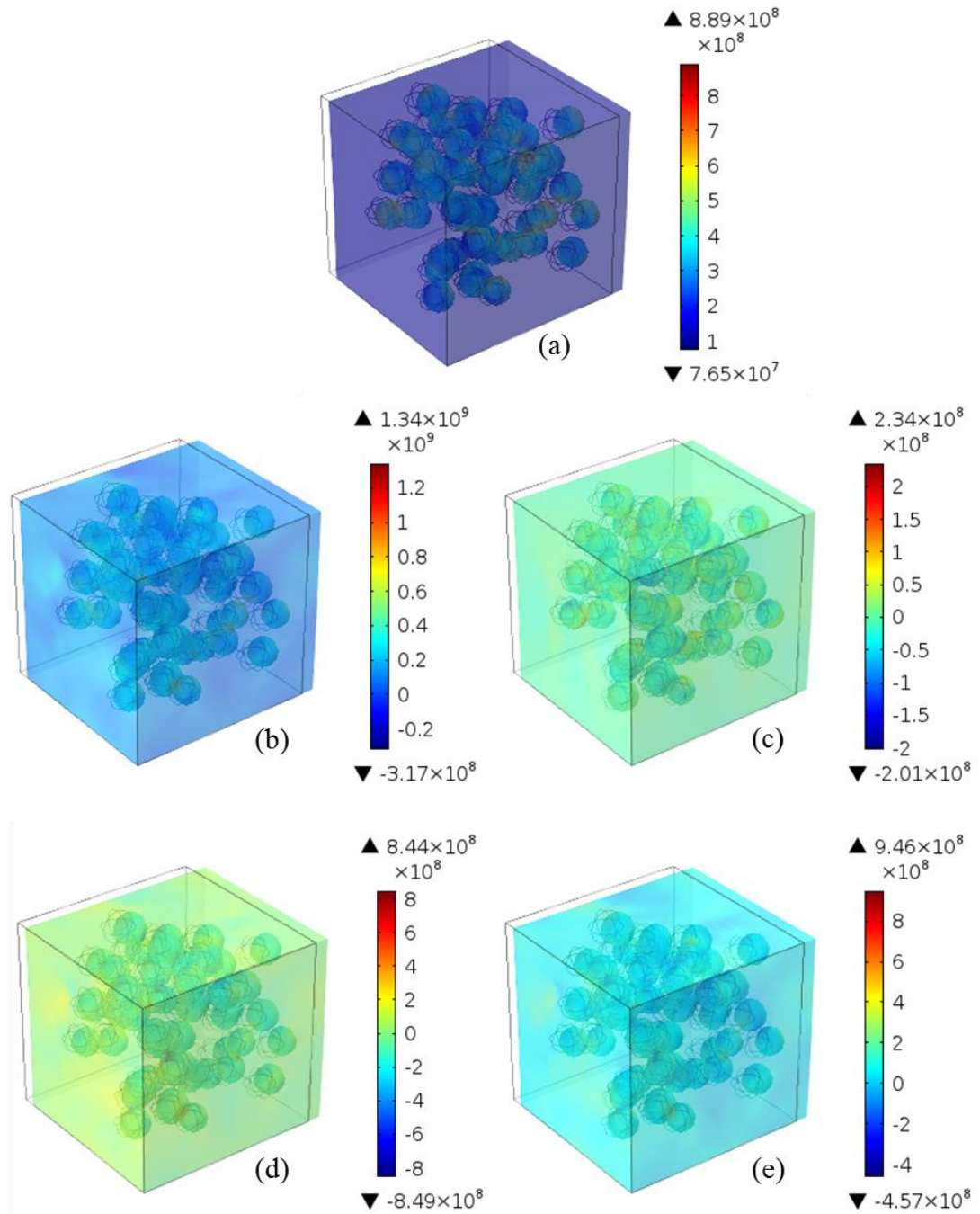


Figure 7.21. Computational homogenization based multiscale algorithm RVE solution for Gauss point at coordinates (0.003028,0.005528). (a) von Mises stress (b) Normal stress in x-direction (c) Normal stress in z-direction (d) Normal stress in y-direction (e) Shear stress in xy-direction.

7.6.2 Bending

For this case, a point load of -20 kN was applied to one end of the plate while the other end was fixed. The applied load and boundary conditions are shown in Figure 7.22.



Figure 7.22. Applied boundary conditions for bending

The von Mises stress distribution in bent plate is shown in Figure 7.23. Similar to the case of uniaxial extension, computation homogenization based algorithm and the hybrid algorithm provide the same result. The stress calculated using mean-field homogenization based algorithm are slightly higher.

Unlike the uniaxial extension problem, the microscale RVEs for the bending problem are undergoing different types of deformation at different locations. Four representative RVE solutions are shown in Figure 7.24 in which the von Mises stress is plotted in the deformed RVE.

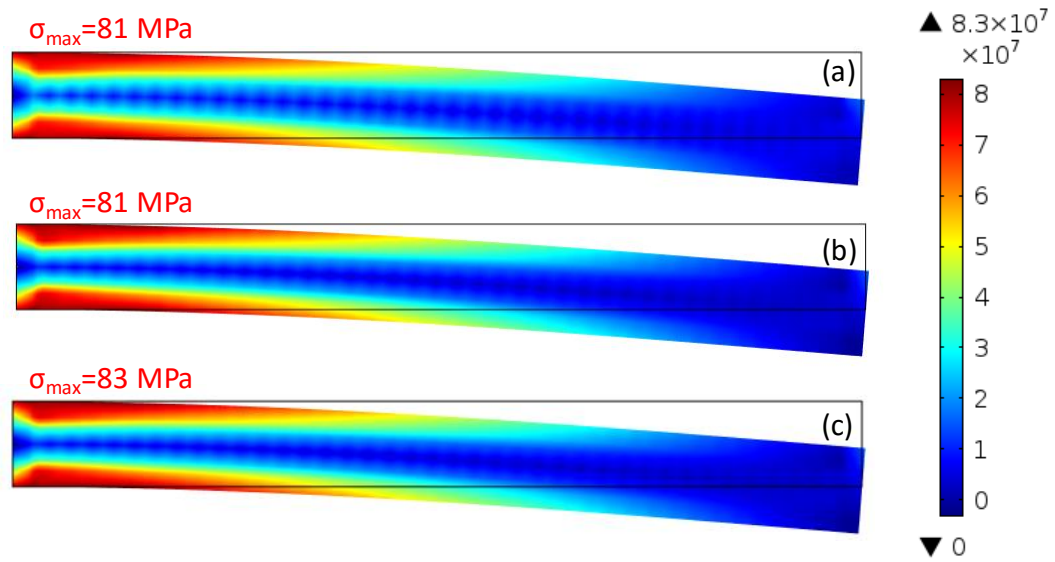


Figure 7.23. von Mises stress distribution in the plate under bending. (a) Computational homogenization based algorithm (b) Hybrid algorithm and (c) mean-field homogenization based algorithm.

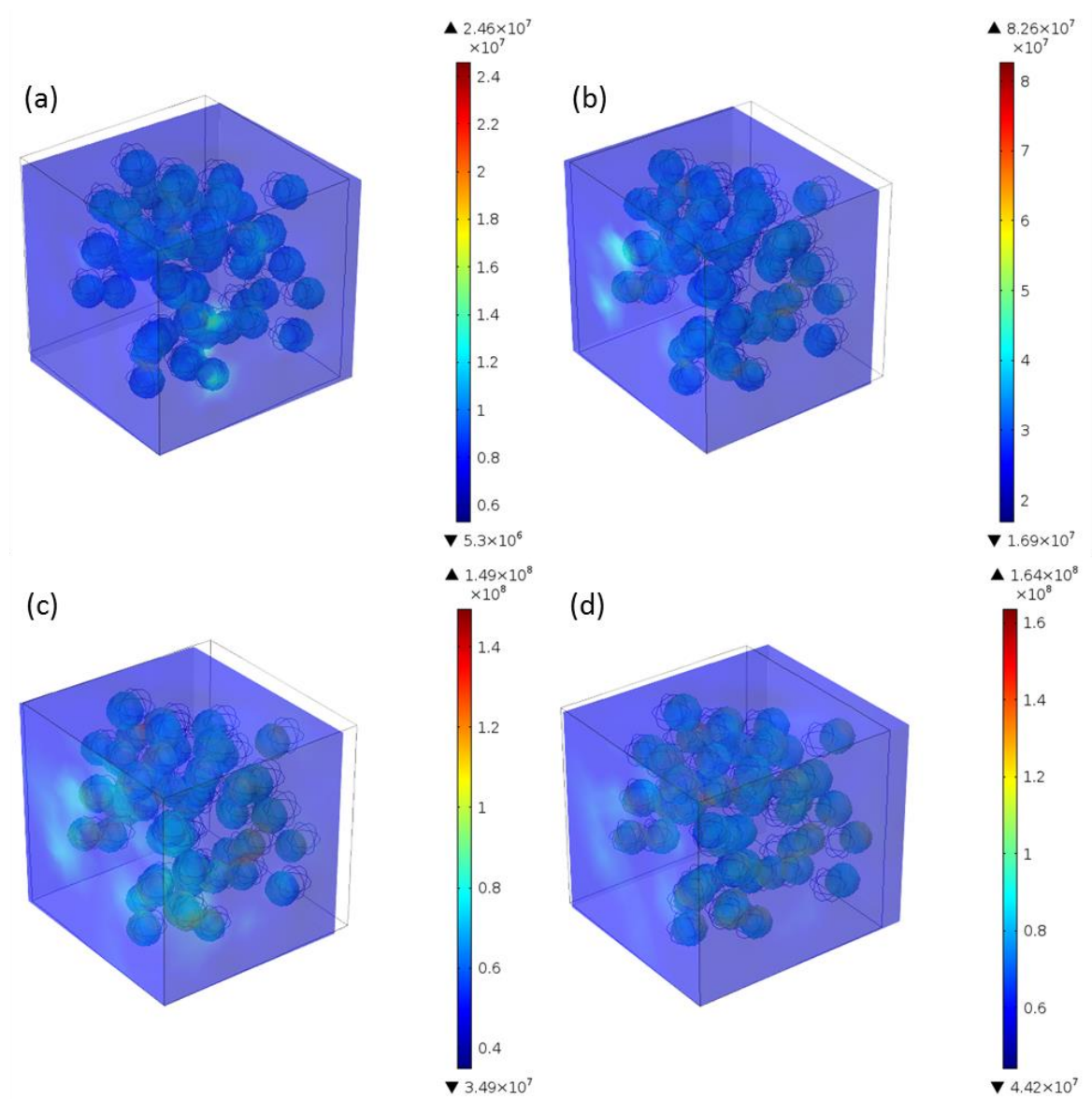


Figure 7.24. Representative RVE solutions for the plate bending problem.

7.6.3 Computational efficiency of multiscale algorithms

In order to compare the computational efficiency of multiscale algorithms, the uniaxial extension and bending problems were solved multiple times for different number of total degrees of freedom. The total degrees of freedom in a multiscale model can be defined as,

$$N_{dof, total} = N_{dof, macroscale} + N_{macroelements} N_{gausspoint per macroelement} N_{dof, microscale} \quad (7.55)$$

The microscale degrees of freedom remain unchanged at 24372 and the number of gauss points per macroscale element is 4 since linear interpolation function are used. The total number of degrees of freedom is therefore controlled by the number of macroscale elements. When only 160 macroscale elements are used, the total number of degrees of freedom are above 15 million.

In the current work, all simulations were carried out on a Dell Precision 7610 workstation having dual Intel Xeon 2670v2 processors and 64 GB RAM and running windows 7 x64. The simulation times for the computational homogenization based algorithm and the hybrid algorithm are shown in Figure 7.25. During these simulations, four microscale RVE problems were solved in parallel with each microscale solution using 5 processor cores. As seen from the figure, the hybrid algorithm provides an improvement of 26.9% and 46.1% for the uniaxial extension and bending problems. In comparison to these, the mean-field homogenization based algorithm solves the problems in under 5 minutes for 160 macroscale elements.

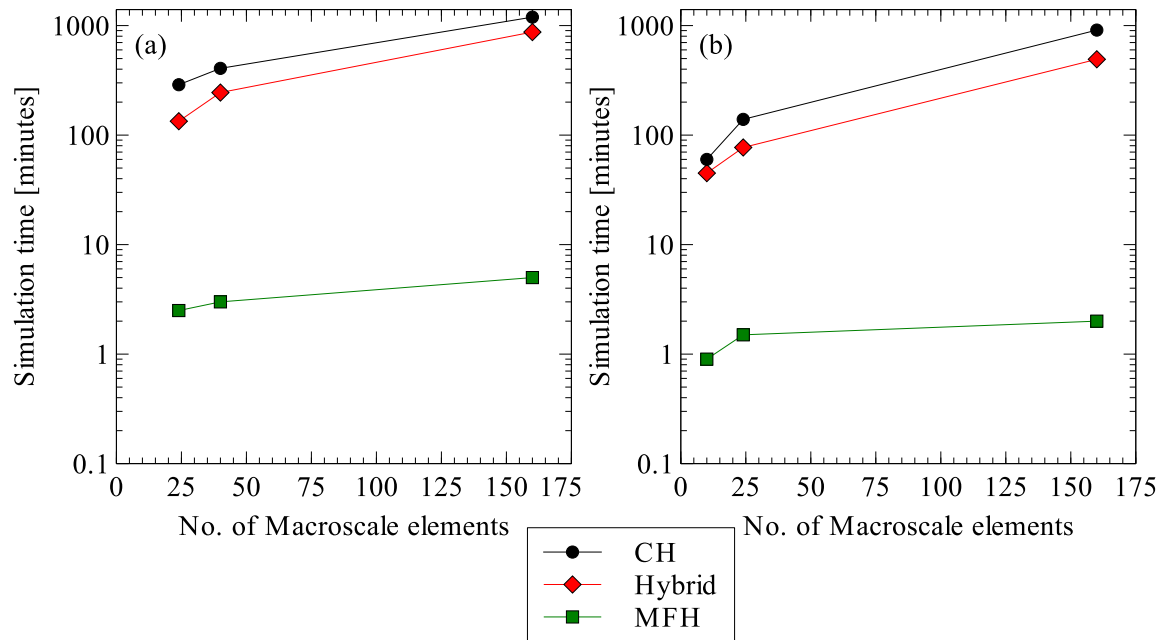


Figure 7.25. Simulation times for (a) uniaxial extension and (b) bending problems using computational homogenization (CH) based algorithm, hybrid algorithm and mean-field homogenization (MFH) based algorithm.

To see the effect of number of parallel microscale solutions, the uniaxial extension problem was resolved for eight parallel solutions each utilizing 3 cores. Therefore, the total number of cores being used for microscale solution increased from 20 to 24. The number of cores per solution needed to be reduced because of the total number of cores available in the workstation. The comparison is shown in Figure 7.26. Increasing the number of parallel microscale solutions from four to eight reduced the simulation times by 8.8% and 6.7% for computational homogenization based algorithm and hybrid algorithm respectively. The improvement is lower than expected since there is a 16.7% increase in the number of processor cores being used. The reduced improvement can be attributed to the increased amount of data being read and written to the hard drive after each solution.

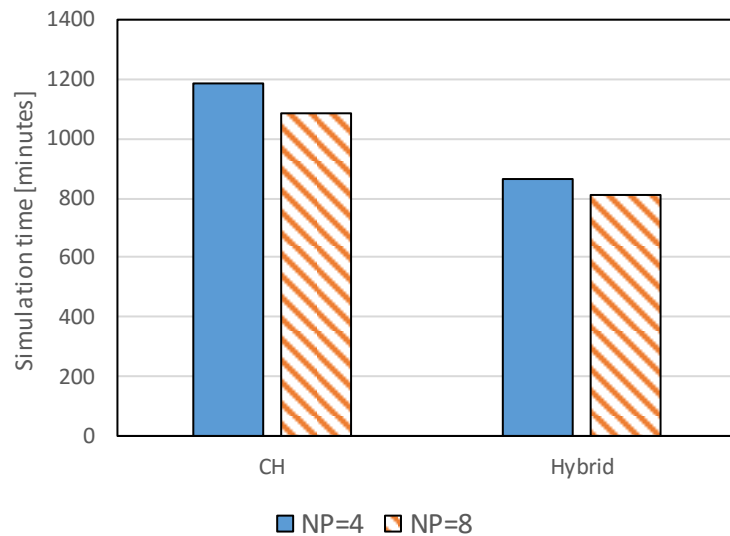


Figure 7.26. Effect of number of parallel microscale solution (NP) on simulation time using computational homogenization (CH) based algorithm and hybrid algorithm.

7.7 CONCLUSION

In the present work, three multiscale modeling methodologies and their implementation in COMSOL/MATLAB were presented. The multiscale modeling methodologies were used to simulate the response of a particulate composite plate under two types of loading. From the results, the following conclusions can be drawn.

- Computational homogenization based algorithm and the hybrid algorithm provided the same solution for the two problems studied. The mean-field homogenization based algorithm provided results which were around 4% higher than the results for computational homogenization.
- Hybridizing the computation homogenization and mean-field homogenization algorithms helped reduce the simulation times significantly. For the uniaxial extension and bending, an improvement of 27% and 46% in computational time was achieved when the hybrid algorithm was used.
- Increasing the number of parallel solutions on the microscale did not significantly improve the computational efficiency of the algorithm. This was due to the limitations of using a single workstation for the simulation in which the number of available processor cores is limited.
- Although the simulation times for the computational homogenization based algorithms was reduced using the hybrid approach, the simulation times were still around two orders of magnitude higher than the mean-field homogenization based multiscale modeling approach.

CHAPTER 8

MULTISCALE MODELING: APPLICATION TO

THERMAL BARRIER COATING

8.1 INTRODUCTION

Finite element method is a widely applied technique for the analysis of coatings. These include works which focus on the modeling of the coating deposition process [177], works which simulate the residual and thermal stress developing in the coating [178–180] and works which focus on the analysis of the failure mechanisms in the coating [2,181,182]. Ward et al. [177] used a commercial FE code ABAQUS to simulate the stress developing in coatings during the deposition process in which the strain development was simulated using a FORTRAN subroutine. Asghari et al. [178] analyzed the stresses developing in the TBC system under thermal cycling using a unit cell model. Haider et al. [179] used an axisymmetric model to study the stresses developing in a thin coating due to thermal mismatch when the coated substrate was cooled from the deposition temperature to the room temperature. Limarga et al. [180] studied the residual stresses developing in Zirconia

TBC using finite element analysis and compared the results with experimental measurements from Raman spectroscopy. They found that the numerical and the experimental results showed considerable difference which they attributed to the assumptions involved in the numerical model as well as the calculation of stress from strain measurements. Al-Athel et al. [2] studied the debonding of the top coat in a thermal barrier coating due to the development of a thermally grown oxide layer at the interface. For their study, they used a unit cell model capable of simulating the thermal, chemical and structural behavior of the thermal barrier coating. Bhatnagar et al. [181,182] studied the effect of various material and geometric parameters on the initiation and propagation of cracks in EB-PVB thermal barrier coatings using a unit cell based FE model.

Most applications of FEM to coatings focus on the study of a micromechanical unit cell or representative volume element. The results of these micromechanical models are usually considered to be applicable to the entire coating. This approach, however, presents certain difficulties. Practically, the loads and boundary conditions are not uniform through the entire coating. Therefore, the application of realistic boundary conditions and loads on the microscale model presents a difficulty. Most works employ simplified structural boundary conditions such as periodic or symmetry boundary conditions which may lead to unrealistic results. Bobzin et al. [183] studied the influence of the size of the RVE on the prediction of the homogenized properties of TBC system and found that if the size of the RVE is not correctly defined, the property prediction can show large variations. Studies on actual turbine blades coated with TBC are very limited. Yang et al. [184] carried out finite element simulations on TBC coated turbine blade to identify critical regions of the blades

where TBC failure can occur. They also used the maximum principal stress to predict the number of cycles to TBC failure as a function of turbine working temperature. There have also been a few studies to study the thermal performance of turbine blades [185,186].

An alternate to using only a unit cell model is multiscale finite element method of a coated blade. In such an approach, a multiscale constitutive model can be used to describe the behavior of the coating. Several approaches to multiscale modeling of materials have been reported in literature. Geers et al. [3,26,61,187,96] developed multiscale schemes based on computational homogenization. They also developed a methodology for the computational homogenization and multiscale modeling of multi-layered thin sheets [97]. As shown in the previous chapter, computational homogenization based multiscale models can lead to extremely high computational times even for very simple macroscale finite element models. Mean-field homogenization [40,53,93] based multiscale modeling provides a good compromise between the computational efficiency and the level of details considered in the model.

Although a vast body of literature is available on the multiscale modeling of materials, applications to the study of coating performance have not been reported. Since coating thicknesses are usually much smaller than the dimensions of the substrate material, multiscale modeling can prove to be an effective tool for modeling coated materials. In the current work, a thermo-mechanical finite element model of turbine blade coated with thermal barrier coating was developed. A multiscale methodology was also formulated to model the creep behavior of porous top coat. The developed model was used to study the

thermo-mechanical performance of a turbine blade under serving conditions. The effect of porosity in yttria-stablized-zirconia top coat on the performance of the TBC blade was also analyzed.

8.2 CONSTITUTIVE MODELING – THERMO-ELASTO-VISCOPLASTICITY OF POROUS TOP COAT

In the current work, the incrementally affine mean-field modeling approach of Doghri et al. [53] was extended for thermo-elasto-viscoplastic materials and used for the modeling of the constitutive response of porous top coat. For the estimation of constitutive response, the mean-field homogenization methodology was incrementally applied to the top coat during the finite element simulation in order to determine the stresses and the tangent modulus of the composite. The mean-field homogenization methodology is presented in section 8.2.1 and its application to Perzyna-type viscoplasticity and creep is presented in section 8.2.2 . Section 8.2.3 presents the details of implementation of the homogenization methodology as a user material in ABAQUS/Standard.

8.2.1 Mean-field homogenization of thermo-elasto-viscoplastic materials

This section presents the details of the mean-field homogenization methodology in the context of thermo-elasto-viscoplasticity. The foundation of the mean-field homogenization scheme is the strain localization relation. Equation (8.1) shows the strain localization relations in the context of thermo-elastoplasticity.

$$\begin{aligned}\Delta\boldsymbol{\varepsilon}_{inc} &= \mathbf{A}_{inc}\Delta\boldsymbol{\varepsilon}_M + \mathbf{a}_{inc}\Delta\theta_M \\ \Delta\boldsymbol{\varepsilon}_{mat} &= (\Delta\boldsymbol{\varepsilon}_M - \varphi_{inc}\Delta\boldsymbol{\varepsilon}_{inc}) / (1 - \varphi_{inc})\end{aligned}\quad (8.1)$$

where φ is the volume fraction of inclusion phase, \mathbf{A} and \mathbf{a} are the inclusion strain localization and inclusion thermal strain localization tensors, $\Delta\boldsymbol{\varepsilon}$ is the strain increment and $\Delta\theta$ is the temperature increment. Subscripts M , inc and mat denote macroscale, inclusion and matrix respectively.

$$\begin{aligned}\mathbf{A}_{inc} &= \mathbf{B}_a : \mathbf{A}_{mat} \\ \mathbf{a}_{inc} &= (\mathbf{A}_{inc} - \mathbf{I}_4) : (\mathbf{C}_{inc,alg} - \mathbf{C}_{mat,alg})^{-1} : (\boldsymbol{\beta}_{inc} - \boldsymbol{\beta}_{mat})\end{aligned}\quad (8.2)$$

where,

$$\begin{aligned}\mathbf{A}_{mat} &= [(1 - \phi_{inc})\mathbf{I}_4 + \phi_{inc}\mathbf{B}_a]^{-1} \\ \mathbf{B}_a &= [\mathbf{I}_4 + \mathbf{S} : \mathbf{C}_{mat,alg}^{-1} (\mathbf{C}_{inc,alg} - \mathbf{C}_{mat,alg})]^{-1} \\ \boldsymbol{\beta}_x &= -\mathbf{C}_{x,alg} : \boldsymbol{\alpha}_x\end{aligned}\quad (8.3)$$

and \mathbf{I}_4 is the 4th order tensor identity, \mathbf{S} is the Eshelby tensor [6], $\mathbf{C}_{x,alg}$ are the algorithmic tangent moduli of the matrix and inclusion for the current strain increment, $\boldsymbol{\alpha}$ is the coefficient of thermal expansion tensor. Subscript x can be either inc or mat .

It is important to note here that the algorithmic tangent moduli of the matrix and inclusion which are required to determine the localized strains in the inclusion and matrix are not known at the beginning of the step. Therefore, an iterative scheme is needed to determine the localized strains.

The strain localization relation (8.1) for elastoplasticity can lead to over-stiff solution for rate-dependent material behavior [52,53]. Doghri et al. [53] and Pierard and Doghri [52] have presented incremental affine homogenization schemes to carry out mean-field homogenization for elasto-viscoplastic material behavior. Their proposed solution involves the inclusion of an affine strain term in the strain localization relation. The exact form of affine strain term depends on the viscoplastic constitutive relation under consideration. In the current work, the formulation of Doghri et al [53] has been extended to include the effect of temperature change on the strain localization relation of elasto-viscoplastic materials.

$$\Delta \varepsilon_{inc} = A_{inc} : \Delta \varepsilon_M + \Delta \varepsilon^* \quad (8.4)$$

where,

$$\Delta \varepsilon^* = (A_{inc} - I_4) : (C_{inc,alg} - C_{mat,alg})^{-1} : \left\{ (\beta_{inc} - \beta_{mat}) \Delta \theta - (C_{inc,alg} : \Delta \varepsilon_{inc}^{aff} - C_{mat,alg} : \Delta \varepsilon_{mat}^{aff}) \right\} \quad (8.5)$$

where $\Delta \varepsilon_x^{aff}$ depends on the constitutive model of the inclusion and matrix and will be further discussed in the next section in the context of J₂-elastoviscoplasticity and creep.

Using the matrix and inclusion strain increments, the stresses in the matrix and inclusion and the corresponding tangent moduli are estimated using the constitutive models of the matrix and inclusion. Finally, the effective stress and tangent modulus of the heterogeneous material are estimated using equation (8.6) and (8.7) respectively.

$$\sigma_{eff} = \varphi_{inc} \sigma_{inc} + (1 - \varphi_{inc}) \sigma_{mat} \quad (8.6)$$

$$C_{eff,alg} = \varphi_{inc} C_{inc,alg} : A_{inc} + (1 - \varphi_{inc}) C_{mat,alg} : A_{mat} \quad (8.7)$$

The effective thermal expansion coefficient of the heterogeneous material is estimated using equation (8.8).

$$\alpha_{eff} = (-C_{eff,alg})^{-1} : \left[(1 - \varphi_{inc}) \beta_{mat} + \varphi_{inc} \beta_{inc} + \varphi_{inc} (C_{inc,alg} - C_{mat,alg}) : a_{inc} \right] \quad (8.8)$$

8.2.2 Application to J₂-elasto-viscoplasticity and creep models

This section presents the application of the mean-field homogenization methodology presented in the previous section to the J₂ elasto-viscoplasticity and creep constitutive behaviors. The J₂ elasto-viscoplasticity model is represented by equations (8.9)-(8.13).

$$\sigma = E : \varepsilon^{el} \quad (8.9)$$

$$\varepsilon = \varepsilon^{el} + \varepsilon^{vp} \quad (8.10)$$

$$f(\sigma_{eq}, p) = \sigma_{eq} - \sigma_y - R(p) \quad (8.11)$$

$$\dot{\varepsilon}^{vp} = \dot{\gamma} \frac{\partial f}{\partial \sigma} \quad (8.12)$$

$$\dot{\gamma} = \begin{cases} 0 & \text{if } f \leq 0 \\ g_v(\sigma_{eq}, p) & \text{if } f > 0 \end{cases} \quad (8.13)$$

where σ and ε are the stress and strain tensors, f is the yield function, p is the effective viscoplastic strain, $\dot{\gamma}$ is the plastic multiplier and g_v is the viscoplastic or creep function. The function $R(p)$ is the hardening function. In the current work, a voce-type hardening law, given by equation (8.14), has been used.

$$R(p) = \sigma_y + (\sigma_A - \sigma_y)(1 - \exp(-p / \varepsilon_0)) + mp \quad (8.14)$$

In the current work, two functions were used for $g_v(\sigma_{eq}, p)$. Equation (8.15) is Norton's power law viscoplastic function and equation (8.16) is the Norton's power law creep function.

$$g_v(\sigma_{eq}, p) = A \left(\frac{f}{\sigma_y + R(p)} \right)^n \quad (8.15)$$

$$g_v(\sigma_{eq}, p) = A(\sigma_{eq})^n \quad (8.16)$$

Using the results presented by Doghri et al. [53], the affine strain increments is given by equation (8.17).

$$\Delta \varepsilon^{af} = \dot{\gamma}(t_n)(\Delta t) \left[N(t_n) + N(t_{n+1}) \frac{g_{v,p}(t_{n+1})\Delta t}{1 - g_{v,p}(t_{n+1})\Delta t} \right] \quad (8.17)$$

where the derivative $g_{v,p}$ is given by equations (8.18) and (8.19) for the viscoplastic function and creep function respectively.

$$g_{v,p} = \frac{n\sigma_{eq} A \frac{dR}{dp} \left(\frac{f}{\sigma_y + R(p)} \right)^{n-1}}{(\sigma_y + R(p))^2} \quad (8.18)$$

$$g_{v,p} = 0 \quad (8.19)$$

8.2.3 Implementation approach in FEM

The material model for porous top coat has been implemented in ABAQUS/Standard as a user-defined material subroutine (UMAT). The inputs to the subroutine include the material properties of the constituent phases, the current strain tensor and temperature, strain and temperature increments, current time and time increment and the current state variables. The state variables include the total strain tensor, viscoplastic strain tensor, effective viscoplastic strain and the algorithmic tangent modulus of each phase. Using this information, the subroutine calculates the new homogenized stress tensor, the homogenized algorithmic tangent operator, the homogenized tensor representing the dependence of stress on temperature and the updated state variables.

The first step carried out in the material subroutine is to determine the mechanical strain increments in the inclusion phase using equation (8.20).

$$\Delta \varepsilon_{inc}^{mech} = A_{inc} : \Delta \varepsilon_M + (\Delta \varepsilon^* - \alpha_{inc} \Delta \theta_M) \quad (8.20)$$

Using the mechanical strain increment in the inclusion, its constitutive model is solved to determine the average stress in the inclusion. Next, equation (8.21) is used to determine

the mechanical strain increment in the matrix phase where $\Delta\epsilon_{mat}$ is calculated using equation (8.1). Using the mechanical strain increment in the matrix, its constitutive relation is solved.

$$\Delta\epsilon_{mat}^{mech} = \Delta\epsilon_{mat} - \alpha_{mat} \Delta\theta_M \quad (8.21)$$

Using the updated inclusion and matrix properties, equation (8.20) is solved again for $\Delta\epsilon_{inc}^{mech}$. If the difference between the previous and updated values is within the tolerance limit, the solution is considered to be converged and the homogenized stresses, tangent modulus and stress-temperature tensor are determined. Otherwise, the process is repeated with the updated value of $\Delta\epsilon_{inc}^{mech}$.

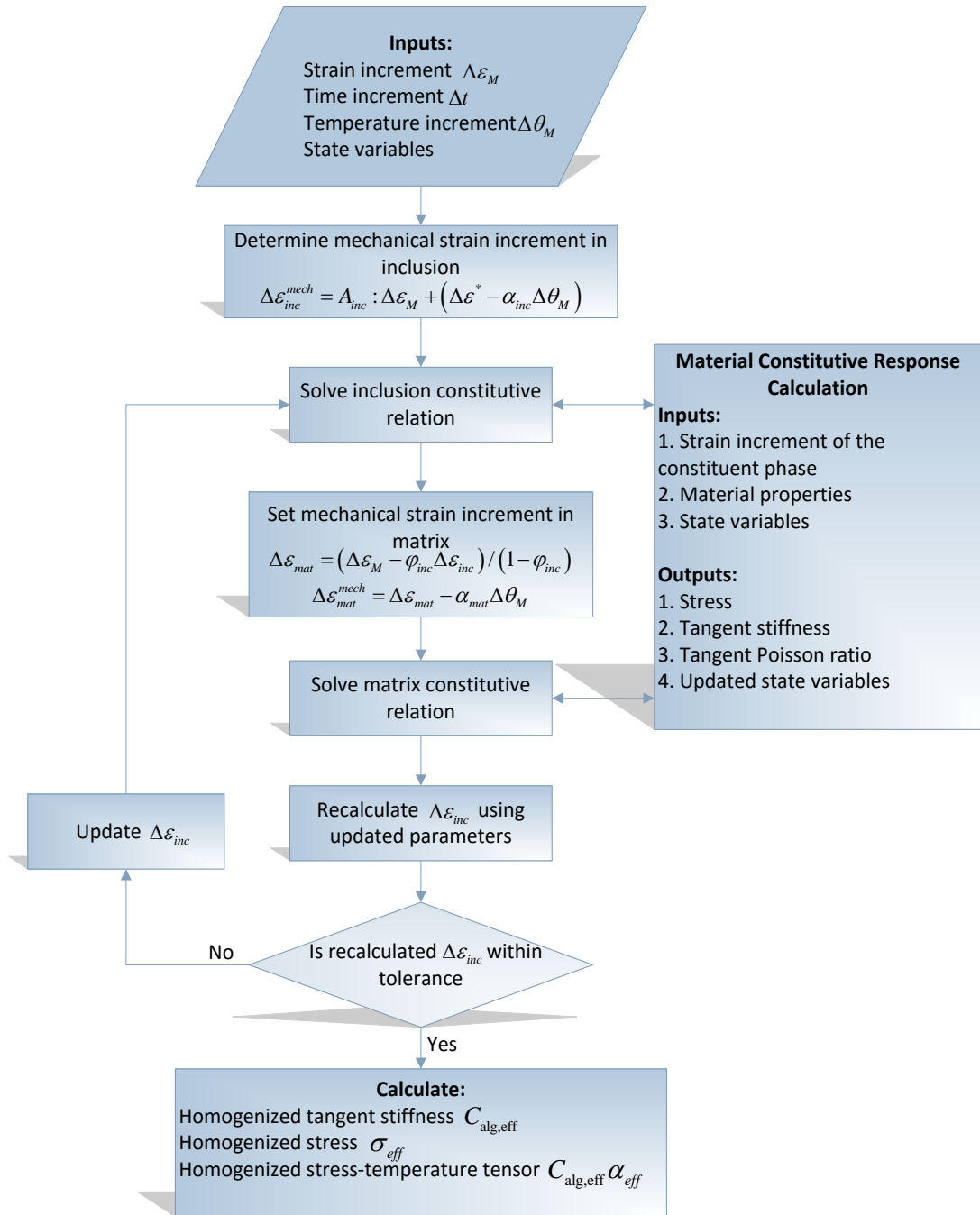


Figure 8.1. Iterative algorithm for the determination of homogenized stress, tangent modulus and stress-temperature tensor.

8.2.4 Validation of methodology

The implemented user material was validated against full-field finite element simulation for the case of viscoplastic-viscoplastic composite and porous viscoplastic material using the power law viscoplastic function given by equation (8.15). Both of these cases were simulated for 5%, 10% and 20% volume fractions of the secondary phase and multiple strain rates. The finite element models used to carry out the validation are shown in Figure 8.2. The material properties of the viscoplastic matrix and inclusion phases are given in Table 8.1. In case of porous viscoplastic material, the pores were modeled as elastic materials with an elastic modulus of 0.1 MPa and a Poisson's ratio equal to 0.3.

The results of the validation are presented in Figure 8.3. The results show good agreement between the homogenized stress-strain response and full-field finite element simulations. In addition to accurate prediction, the mean-field homogenization based approach provides orders-of-magnitude reduction in simulation time compared to the finite element model.

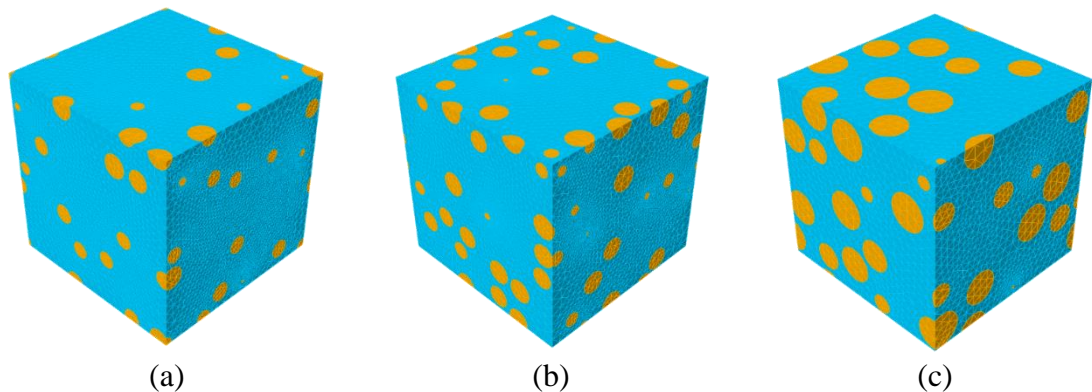


Figure 8.2. Finite element models for validation containing (a) 5% (b) 10% and (c) 20% secondary phase.

Table 8.1. Material properties used for model validation.

Property	Matrix	Inclusion
E [GPa]	70	200
ν [1]	0.33	0.3
σ_y [MPa]	50	100
σ_A [MPa]	100	200
m [GPa]	1	0.5
ε_0 [1]	0.01	0.02
A [1]	0.001	0.001
n [1]	1	1

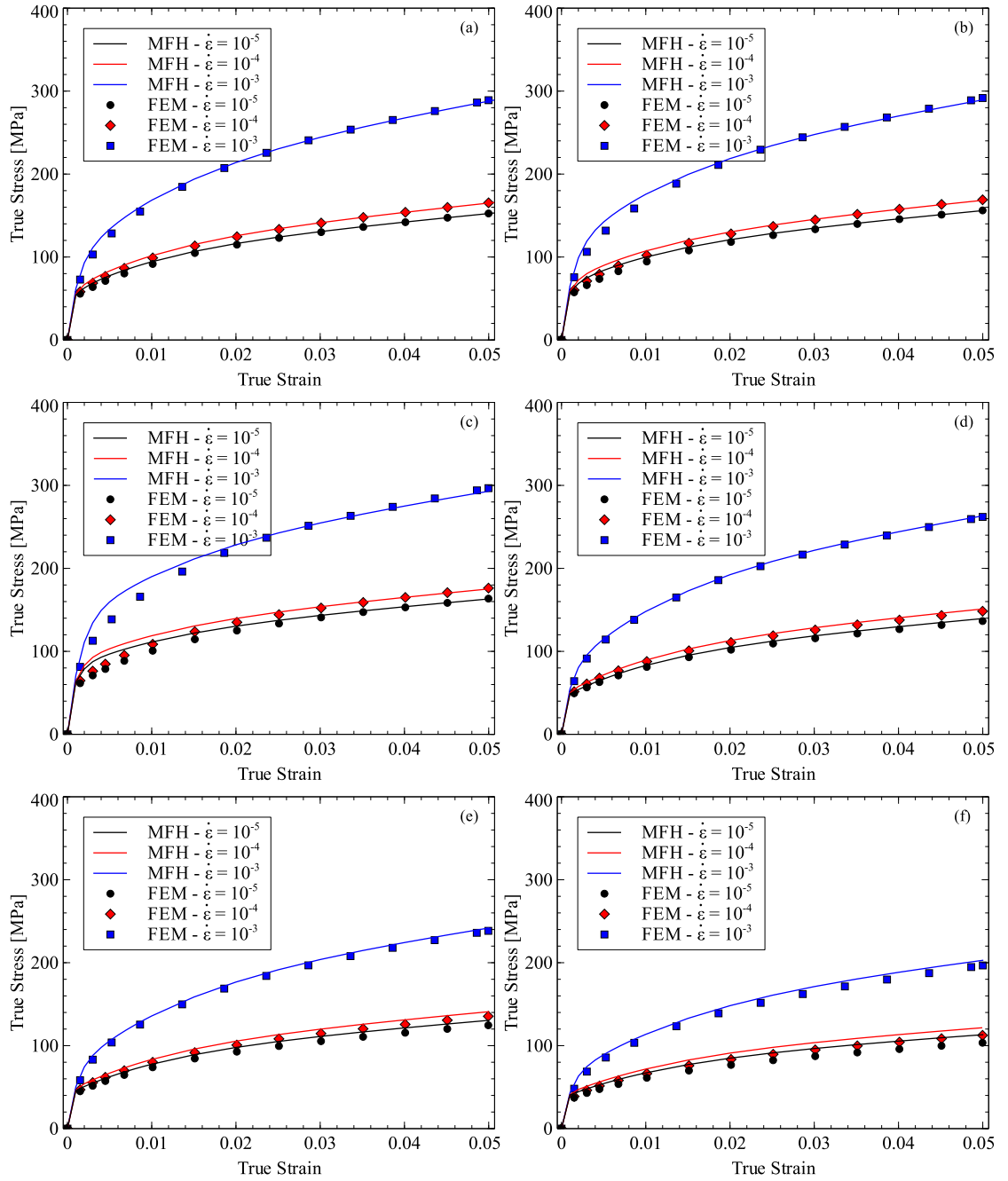


Figure 8.3. Validation of homogenization methodology. Cases (a)-(c) are for 5%, 10% and 20% viscoplastic-viscoplastic composite respectively and cases (d)-(f) are for porous viscoplastic materials with 5%, 10% and 20% porosity fractions respectively.

8.3 MODEL FORMULATION

This section presents the details of the developed finite element model used for the study of a turbine blade coated with TBC. The model was used to carry out a fully coupled transient thermal-quasi static structural analysis of the TBC coated blade under serving conditions.

8.3.1 Geometry and FE model

The shape of actual turbine blades is shown in Figure 8.4. In order to study the response of the coated blade under thermal loading, two FE models were developed. The geometries of the two models used in the current work are shown in Figure 8.5. The simplified model was used to carry out initial studies regarding the behavior of TBC coated materials under thermal loads. The detailed model of the coated turbine blade was then used to study the effect of blade shape and cooling through the internal channels on the thermos-mechanical performance of the blade.

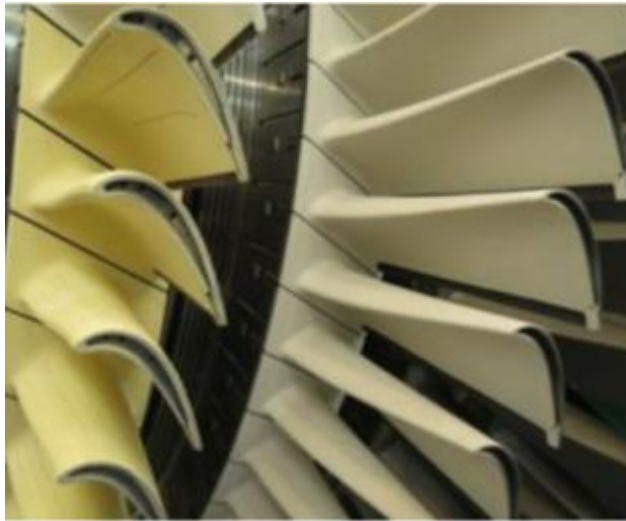
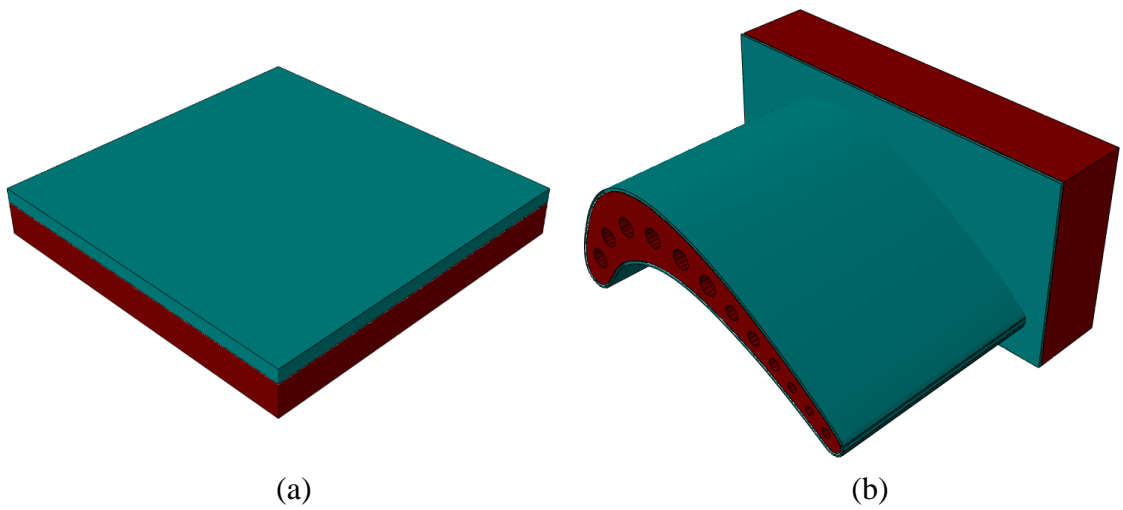


Figure 8.4. Actual turbine blade [188]



(a) (b)
Figure 8.5. (a) Simplified model (b) Model of actual turbine blade

The finite element model was implemented in ABAQUS/Standard. Since there exists a large difference in the size of the blade and the thickness of each layer in the TBC system, the coating was modeled as a layered SHELL part while the blade substrate was modeled as a SOLID part. The shell and the solid parts were tied together using the TIE constraint option in ABAQUS. Simpson's rule was used to carry out the integration across the three layers of shell elements with five integration points considered in each layer. A schematic representation of the arrangement of materials in the coated blade is shown in Figure 8.6.

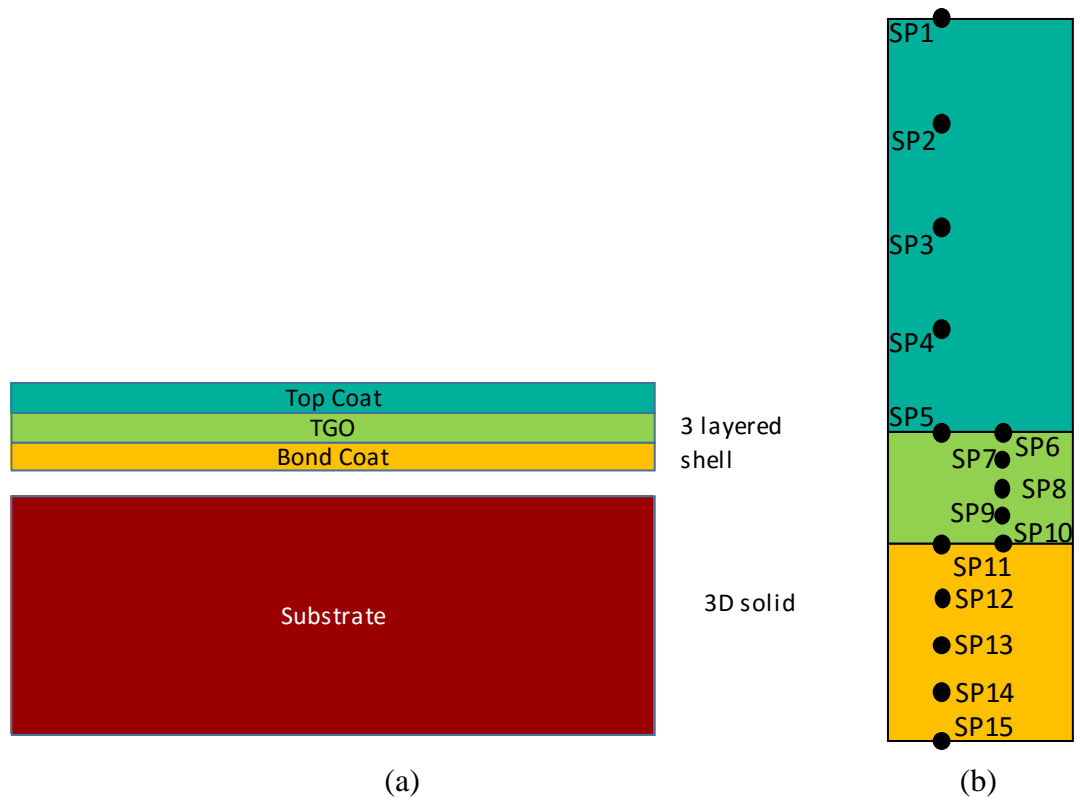


Figure 8.6. (a) Schematic representation of the various materials in the coated blade (b) Arrangement of integration point through the thickness of layered shell elements.

8.3.2 Loadings and boundary conditions

Roller boundary conditions were applied to three sides of the substrate part in order to stop rigid body motion while ensuring that the model is not over-constrained. Convective boundary conditions were applied to the top surface of the top coat to model the heating of the coated blade when exposed to the high temperature environment of the turbine. The effect of cooling of the blade was modeled by applying convective boundary conditions to the lower surface of the substrate in the simplified model and inside the cooling channels in the detailed model. All boundary conditions and loadings are shown in Figure 8.7

The ambient temperature used for both heating and cooling convections was increased from 25°C to its maximum value over a period of 60 seconds. The maximum temperature on the heating side was taken as 1300°C and on the cooling side was taken as 200°C. For analysis of a single cycle, the temperature was maintained at the maximum value for 1 hour and was reduced back to 25°C over a period of 60 seconds. For analysis of the model under thermal cycling, the dwell time was reduced to 10 minutes. The convective heat transfer coefficients on the heating and cooling sides were taken as 800 W/m².K and 400 W/m².K respectively. The variation of temperatures of the hot environment and the cooling air with time is shown graphically in Figure 8.8.

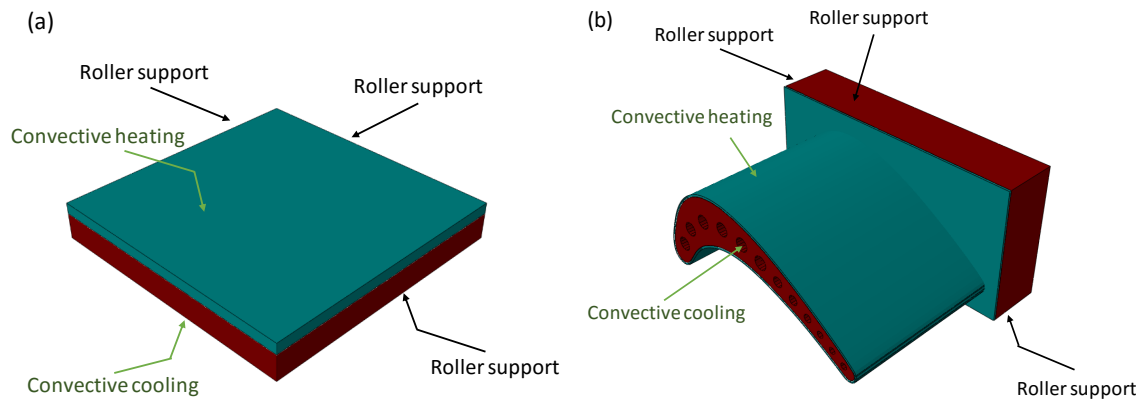


Figure 8.7. Loading and boundary conditions on (a) simplified model (b) Turbine blade model.

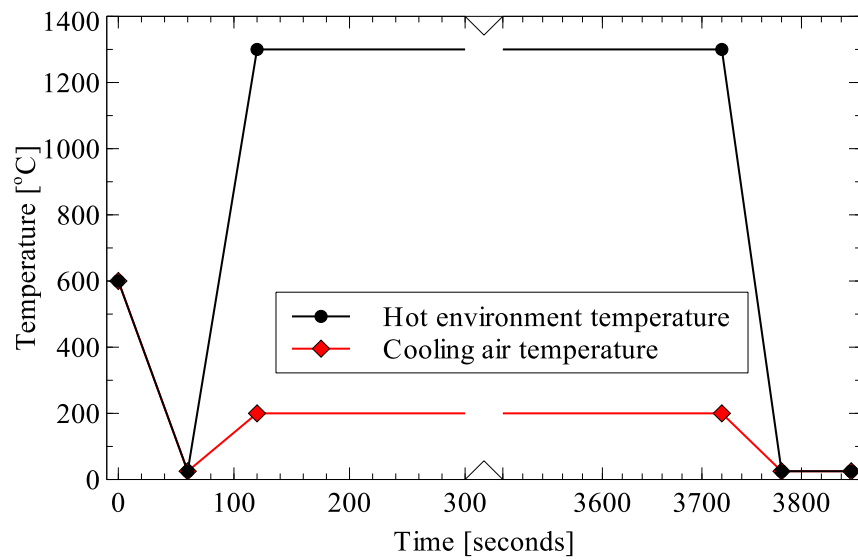


Figure 8.8. Variation of ambient temperatures in convective boundary conditions.

8.3.3 Material models

The substrate, bond coat and thermally grown oxide layer were considered to be isotropic and homogeneous materials. The Ytria-stabilized Zirconia top coat layer was considered as a porous material. Temperature dependent material properties were used for all materials used in the finite element model. Creep was modeled in the three materials of the TBC while elasto-plasticity was considered for the two metal alloys in the model, the bond coat and the substrate. The temperature dependent mechanical properties of the various materials are given in Tables 8.2 to 8.5. Table 8.6 lists the creep parameters for all layers in the TBC coating.

Table 8.2. Mechanical properties of bond coat [189].

Temperature [°C]	E [GPa]	ν	α [$\mu\text{m}/\text{m.K}$]	σ_y [MPa]
20	200	0.3	12.30	426.00
200	190	0.3	13.20	412.00
400	175	0.31	14.20	396.00
600	160	0.31	15.20	362.00
800	145	0.32	16.30	284.00
1000	120	0.33	17.20	202.00
1100	110	0.33	17.70	114.00

Table 8.3. Mechanical properties of dense top coat [189].

Temperature [°C]	E [GPa]	ν	α [$\mu\text{m}/\text{m.K}$]
20	48	0.1	9.70
200	47	0.1	9.80
400	44	0.1	9.90
600	40	0.11	9.90
800	34	0.11	10.0
1000	26	0.12	10.1
1100	22	0.12	10.1

Table 8.4. Mechanical properties of TGO layer [189].

Temperature [°C]	E [GPa]	v	α [$\mu\text{m}/\text{m.K}$]
20	400	0.23	8.00
200	390	0.23	8.20
400	380	0.24	8.40
600	370	0.24	8.70
800	355	0.25	9.00
1000	325	0.25	9.30
1100	320	0.25	9.50

Table 8.5. Mechanical properties of substrate [190].

Temperature [°C]	E [GPa]	v	α [$\mu\text{m}/\text{m.K}$]
25	211	0.3	12.50
200	201	0.3	13.60
400	188	0.3	-
600	173	0.3	14.00
800	157	0.3	15.40
1000	139	0.3	16.30

Table 8.6. Creep parameters for TBC materials [191].

Material	Creep Parameter		Creep Parameter <i>n</i>
	<i>A</i> [MPa ^{−<i>n</i>} s ^{−1}]		
	1000°C	1150°C	
Dense Top Coat	2.57×10 ^{−8}	2.92×10 ^{−7}	3.0
TGO	7.3×10 ^{−4}	4.2×10 ^{−2}	1.0
Bond coat	1.39×10 ^{−7}	2.35×10 ^{−6}	3.0

For the constitutive behavior of porous top coat, the methodology presented in the previous section was used. Using the material properties of dense top coat mentioned in Tables 8.3 and 8.6, the uniaxial tension response of the top coat material was tested for various levels of porosities at a strain rate of 10^{-5} s^{-1} and a temperature of 1000°C . The results are shown in Figure 8.9.

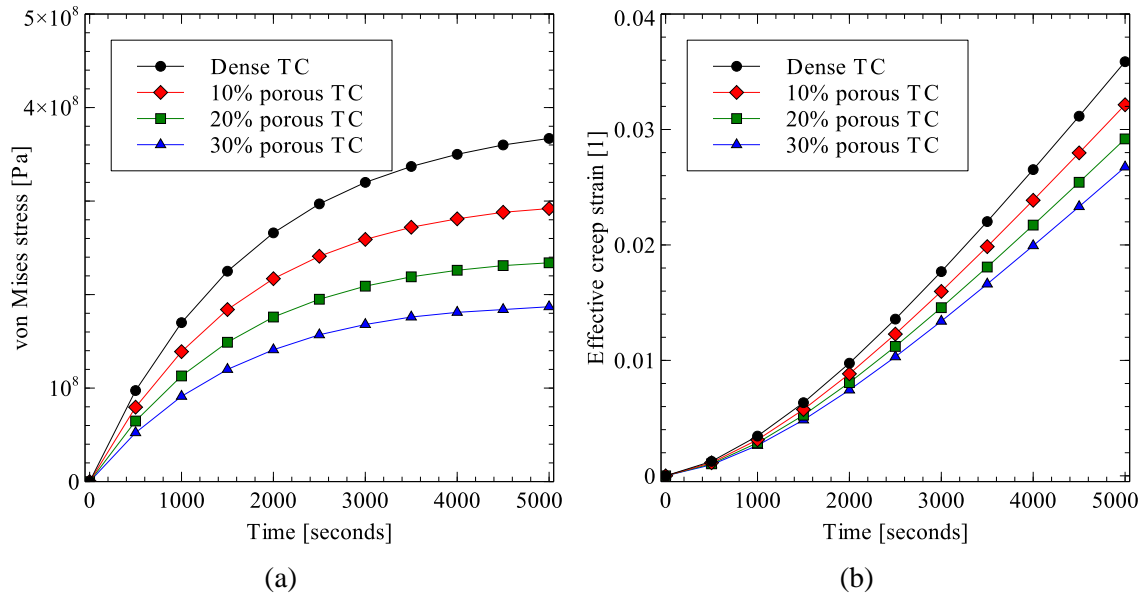


Figure 8.9. Uniaxial tension test of porous top coat at a strain rate of 10^{-5} s^{-1} and a temperature of 1000°C .

(a) von Mises stress (b) effective creep strain.

Table 8.7 lists the thermal properties of all materials. The thermal conductivity of porous top was estimated using the generalized effective medium theory model by Siddiqui and Arif [192]. The predicted thermal conductivities of the porous yttria-stabilized zirconia show good agreement with those found experimentally by Schlichting et al. [193].

Table 8.7. Thermal properties of all materials [184].

	BC	TGO	Substrate	TC (dense)	TC (10%)	TC (20%)	TC (30%)
Density [kg/m ³]	7380	3984	8500	3610.00	3249	2888	2527
Thermal conductivity (20°C) [W/m.K]	5.8	10	88	2	1.71	1.45	1.22
Thermal conductivity (1600°C) [W/m.K]	17	4	69	1.7	1.46	1.24	1.04
Specific heat capacity [J/m ³ .K]	450	755	440	505	454.5	404	353.5

8.4 RESULTS AND DISCUSSION

The following sections present the analysis of the thermo-mechanical performance of the TBC coated blade using the simplified model and the detailed model of the turbine blade. Both models were studied considering four levels of porosity in the top coat: 0%, 10%, 20% and 30%.

8.4.1 Simplified Model

For the simplified model, the steady-state temperature drop through the thickness of the TBC coating is shown in Figure 8.10. Since the heat transfer only occurred through thickness, no in-plane temperature distribution was present. Among the three layers of the TBC, the top coat was responsible for the majority of the temperature drop. The temperature drop across the top coat increased with increasing porosity inside the top coat. The temperature drop across the top coat was 45.9°C for the dense top coat and increased to 73.1°C for the 30% porous top coat. An interesting observation from the results shown in Figure 8.10 is that the temperature at the outer surface of the top coat actually increased with increasing level of porosity. Increasing the porosity from 0% to 30% increased the surface temperature by 9°C. The overall temperature drops across the TBC coating were 49°C, 56.4°C, 65.1°C and 76.2°C for the cases with dense, 10% porous, 20% and 30% porous top coats respectively. This represents an increase of 55% for the 30% porous top coat over the dense top coat.

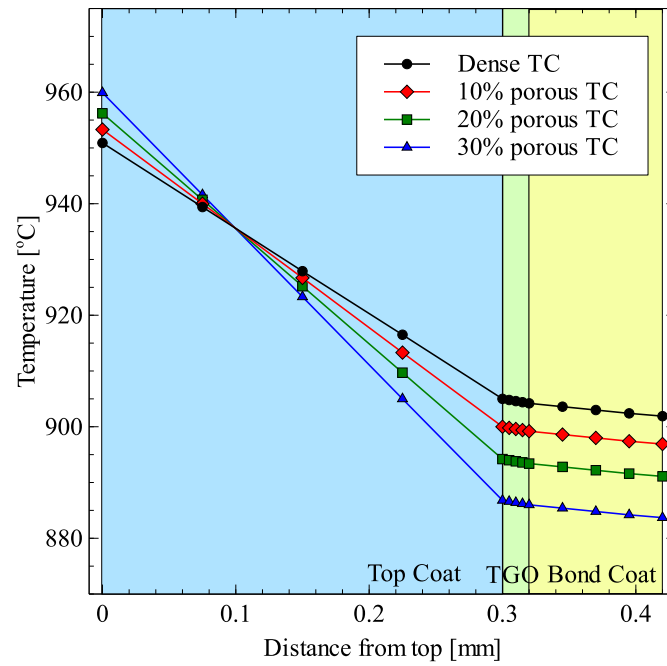


Figure 8.10. Steady-state temperature drops across the TBC for various amounts of top coat porosities.

The variation of the 1st principle stress in the bond coat and the top coat at the interface with TGO layer as a result of the thermal loading shown in Figure 8.8 are shown in Figures 8.11 and 8.12 respectively. The interface with the TGO was chosen to show the stresses because the stresses were maximum at the TGO interface. The figures show the stress variation in the layers for the models with 0% porous, 10% porous, 20% porous and 30% porous top coat and at two times: at the end of initial heating and at the end of final cooling. The results show that at the end of initial heating (120 seconds), the bond coat had compressive stresses while the top coat experienced tensile stresses. In Figures 8.11 and 8.12, the stresses away from the boundary need to be observed to ignore the effect of boundary conditions applied in the model. The 1st principle stress in the bond coat layer at the TGO interface were -65 MPa at the end of heating for the model with dense top coat. The stress was reduced to -57 MPa when a 30% porous top coat was used. For the top coat, the 1st principle stress at the TGO interface reduced from 45 MPa to 26 MPa due the presence of 30% porosity.

After the dwell time of 1 hour and the cool-down to room temperature, the stresses in the bond coat switched to tensile and the stresses in the top coat switched to compressive in nature. After the cool down to room temperature, the tensile 1st principle stress in the bond coat reduced from 128 MPa to 97 MPa when the porosity in the top coat was increased from 0% to 30%. For the top coat layer, the 1st principle stress at the TGO interface was -127 MPa for the dense top coat. It was reduced to 75 MPa for the 30% porous top coat.

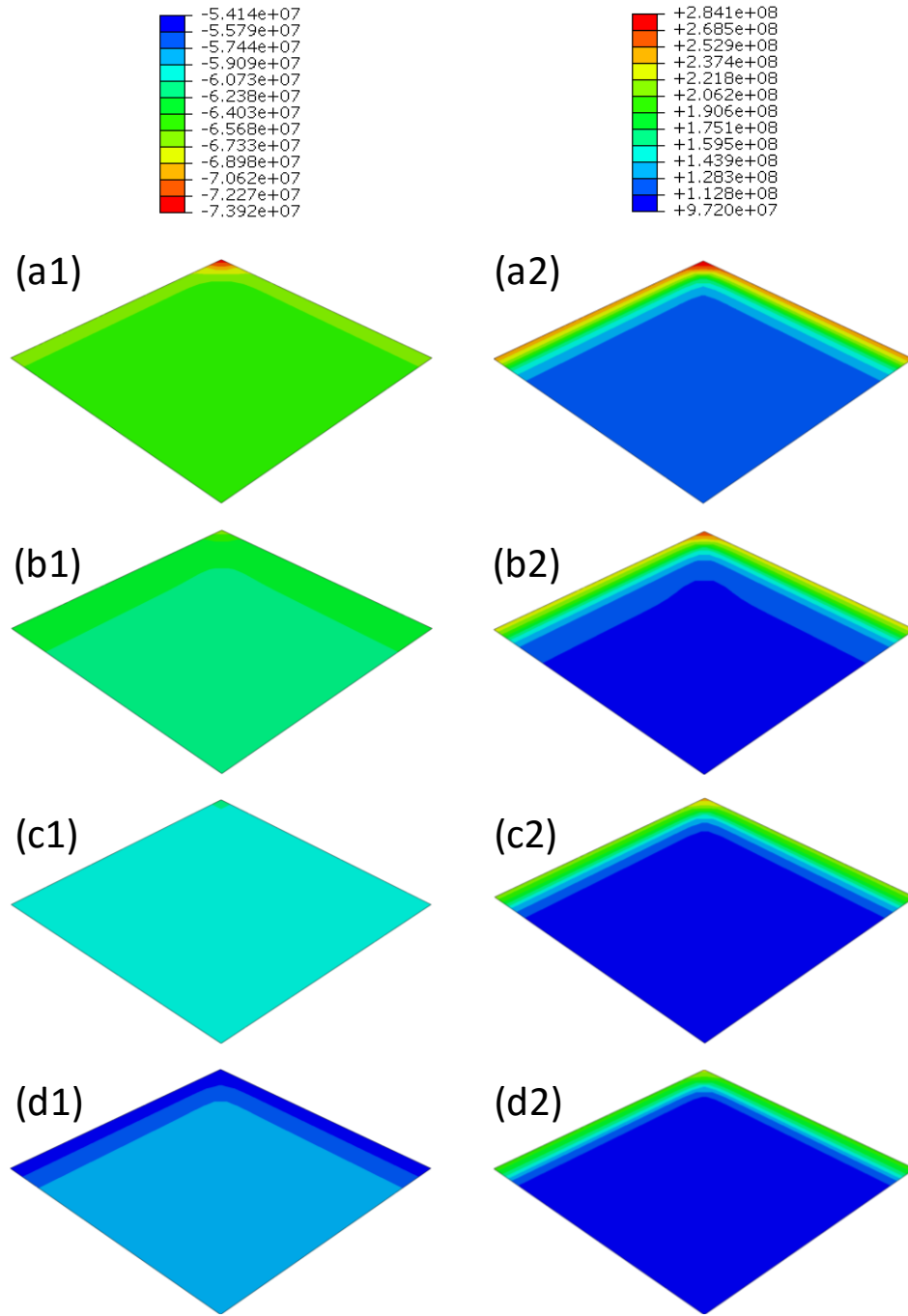


Figure 8.11. 1st principle stress in the bond coat at the TGO interface. (a), (b), (c) and (d) represent 0%, 10%, 20% and 30% porosity in the top coat. (1) and (2) represent results at the end of heating and the end of cooling.

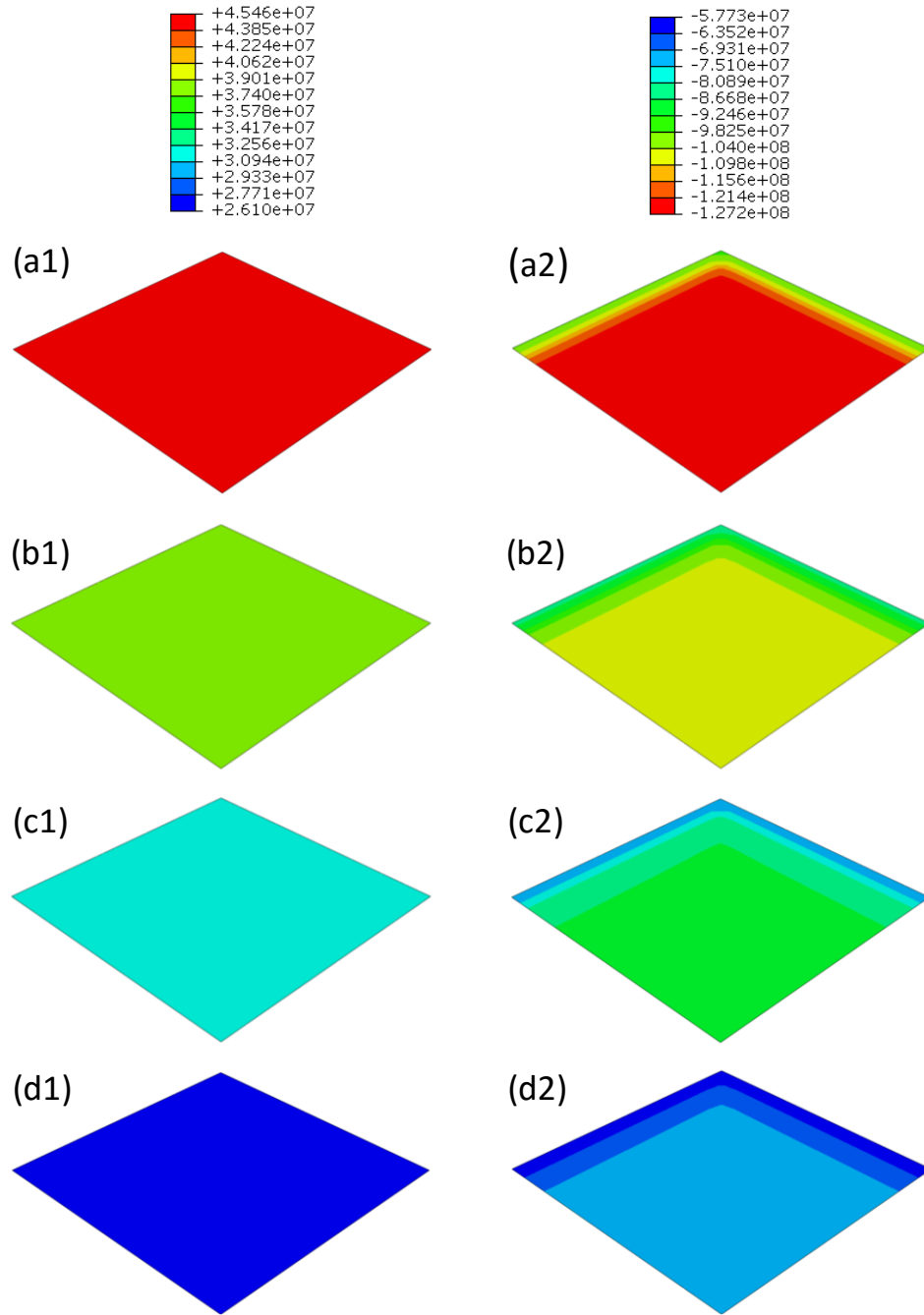


Figure 8.12. 1st principle stress in the top coat at the TGO interface. (a), (b), (c) and (d) represent 0%, 10%, 20% and 30% porosity in the top coat. (1) and (2) represent results at the end of heating and the end of cooling.

The evolution of creep strains in the thermal barrier coating layers is shown in Figure 8.13. As shown in the figure, the top coat and bond coat showed strong dependence of the creep strain on top coat porosity. The TGO layer does show a dependence of creep strain on top coat porosity but the effect is lower than the other two layers.

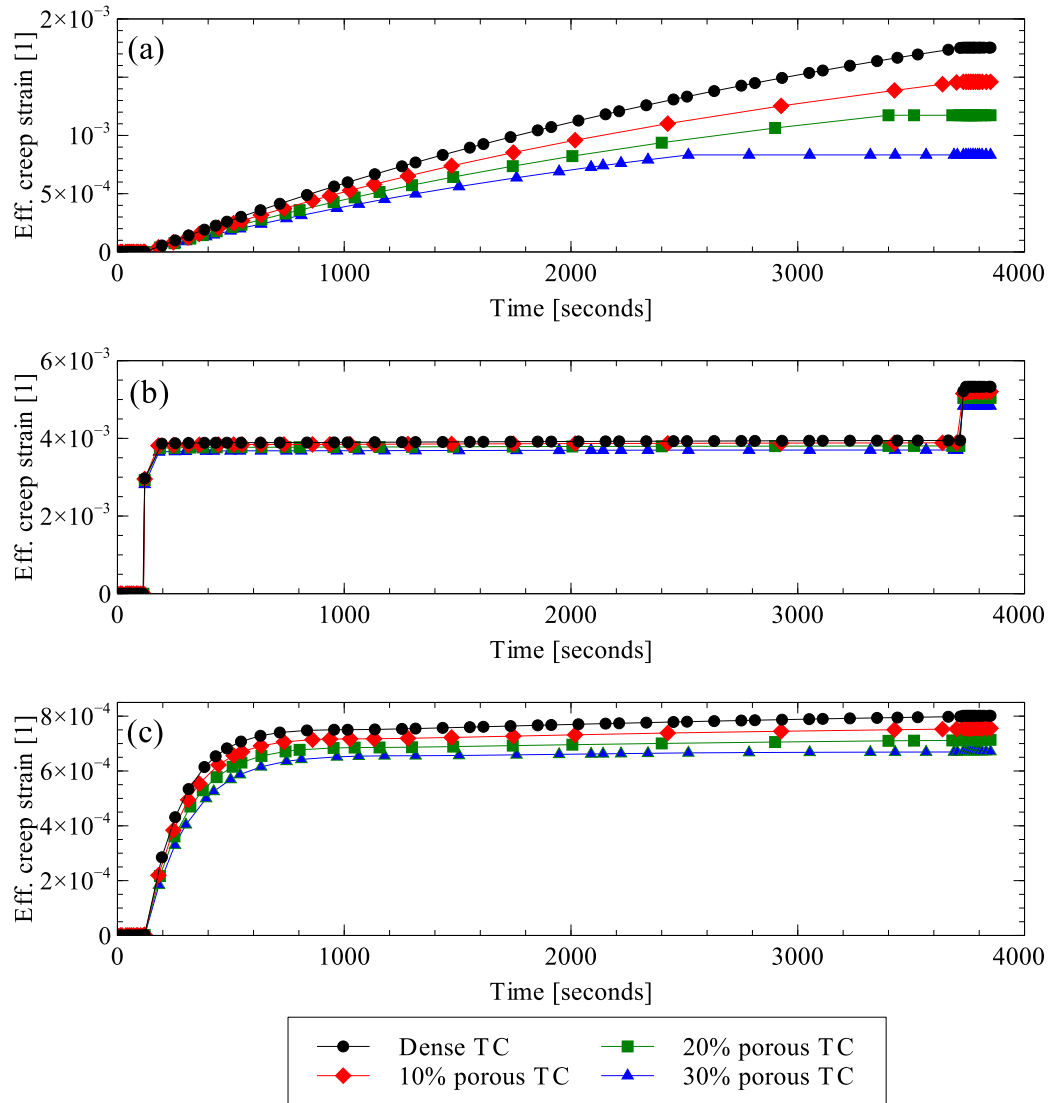


Figure 8.13. Effective creep strain evolution during a single thermal cycle in (a) top coat (b) TGO and (c) bond coat using the simplified model (TC: top coat).

8.4.2 Turbine blade model

In case of the detailed model of the blade turbine, the heat transfer within the model was three-dimensional. Figures 8.14, 8.15 and 8.16 show the spatial variation in temperature at the steady-state for the top surface of the top coat, bond coat-substrate interface and the blade substrate respectively. Similar to the simplified model, the temperature at the top surface of the top coat increased with increasing porosity level in the top coat. The maximum surface temperatures in case of dense top coat and 30% porous top coat were 1053 °C and 1057°C. But due to a reduction in thermal conductivity due to porosity, the temperature drop through the TBC increases with an increase in top coat porosity. This is shown in Figure 8.15 for the bond coat-substrate interface. The maximum interface temperatures in case of dense top coat and 30% porous top coat were 1019°C and 1002°C respectively. The positive effect of top coat porosity in increasing the temperature drop through the TBC is also shown in Figure 8.16 which shows the spatial variation in temperature of the blade substrate.

Using Figures 8.14 and 8.15, four different regions of the turbine blade can be identified. These regions, shown in Figure 8.17, are the trailing edge, leading edge, suction side and pressure side. Temperature drop through the TBC coating in these four regions is shown in Figure 8.18. The effect of porosity in increasing the temperature drop through the TBC is visible in all regions. The hottest part of the turbine blade was found to be the trailing edge while the suction side had the lowest temperature. These findings agree with Liu et al. [186] who carried out a CFD analysis of convective cooling of a turbine blade coated with TBC.

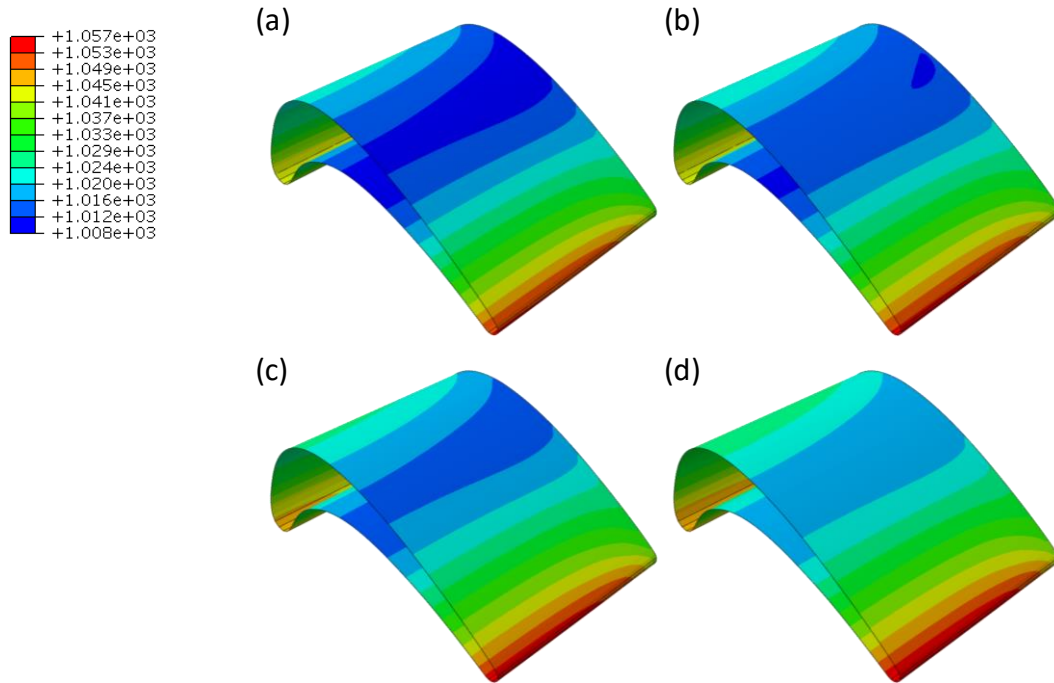


Figure 8.14. Steady-state temperature distribution on the top coat outer surface. (a), (b), (c) and (d) represent 0%, 10%, 20% and 30% porosity in the top coat.

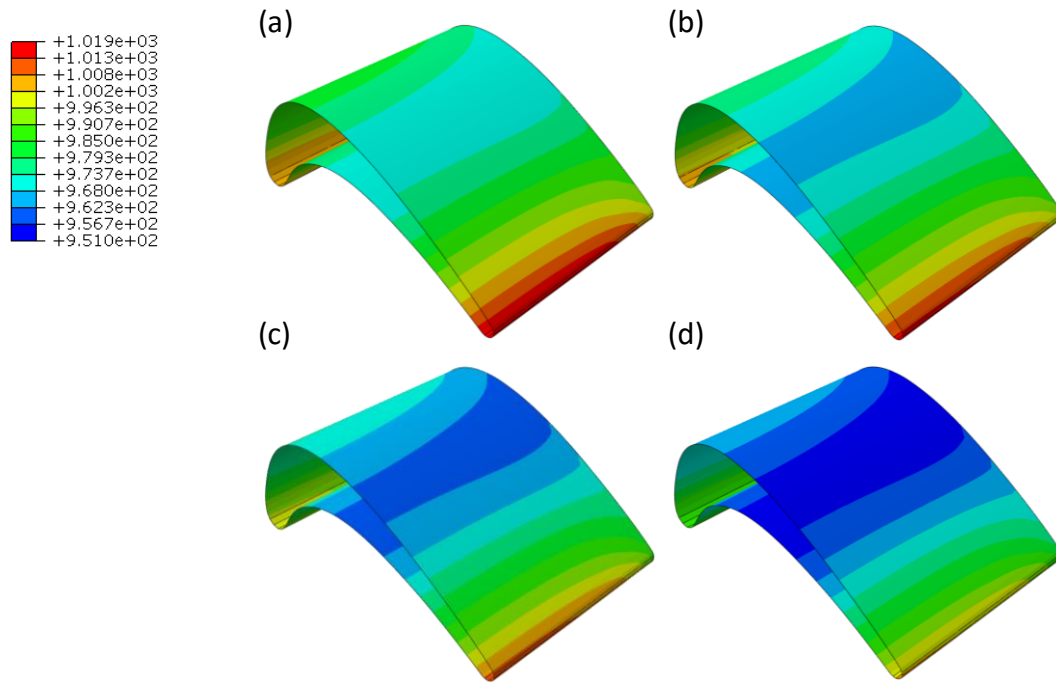


Figure 8.15. Steady-state temperature distribution at the bond-substrate interface. (a), (b), (c) and (d) represent 0%, 10%, 20% and 30% porosity in the top coat.

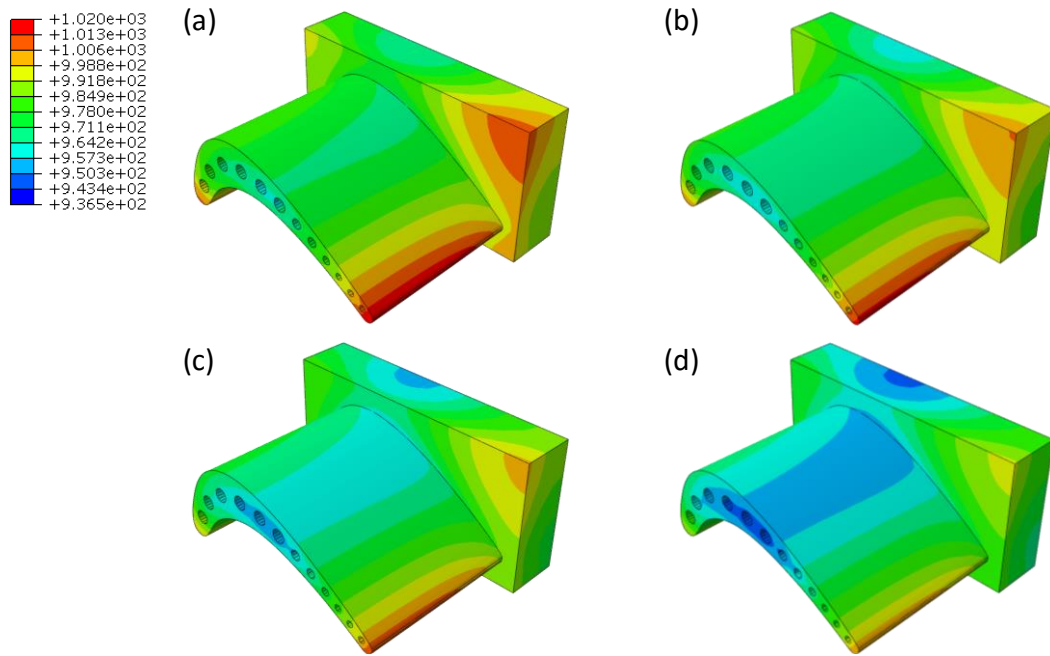


Figure 8.16. Steady-state temperature distribution in the blade substrate. (a), (b), (c) and (d) represent 0%, 10%, 20% and 30% porosity in the top coat.

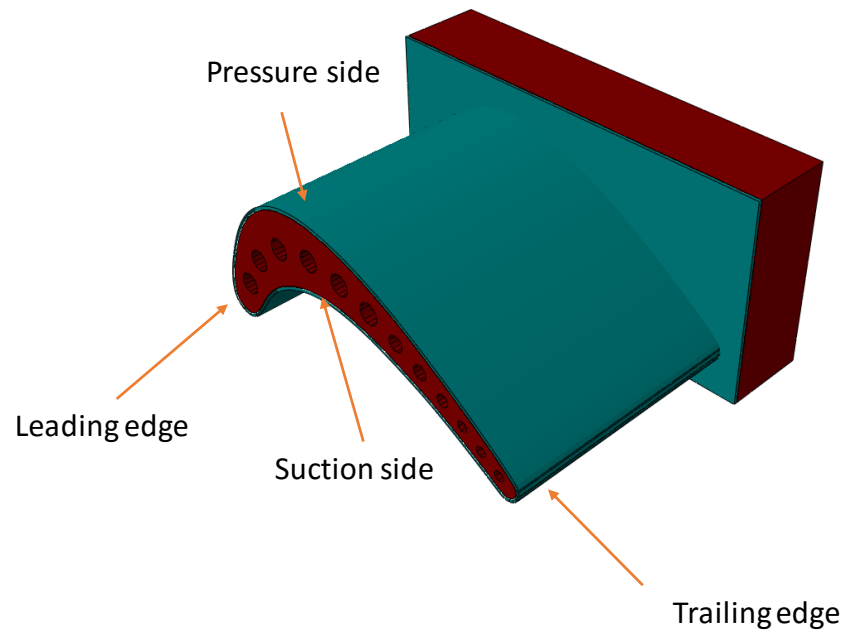


Figure 8.17. Characteristic regions in a turbine blade.

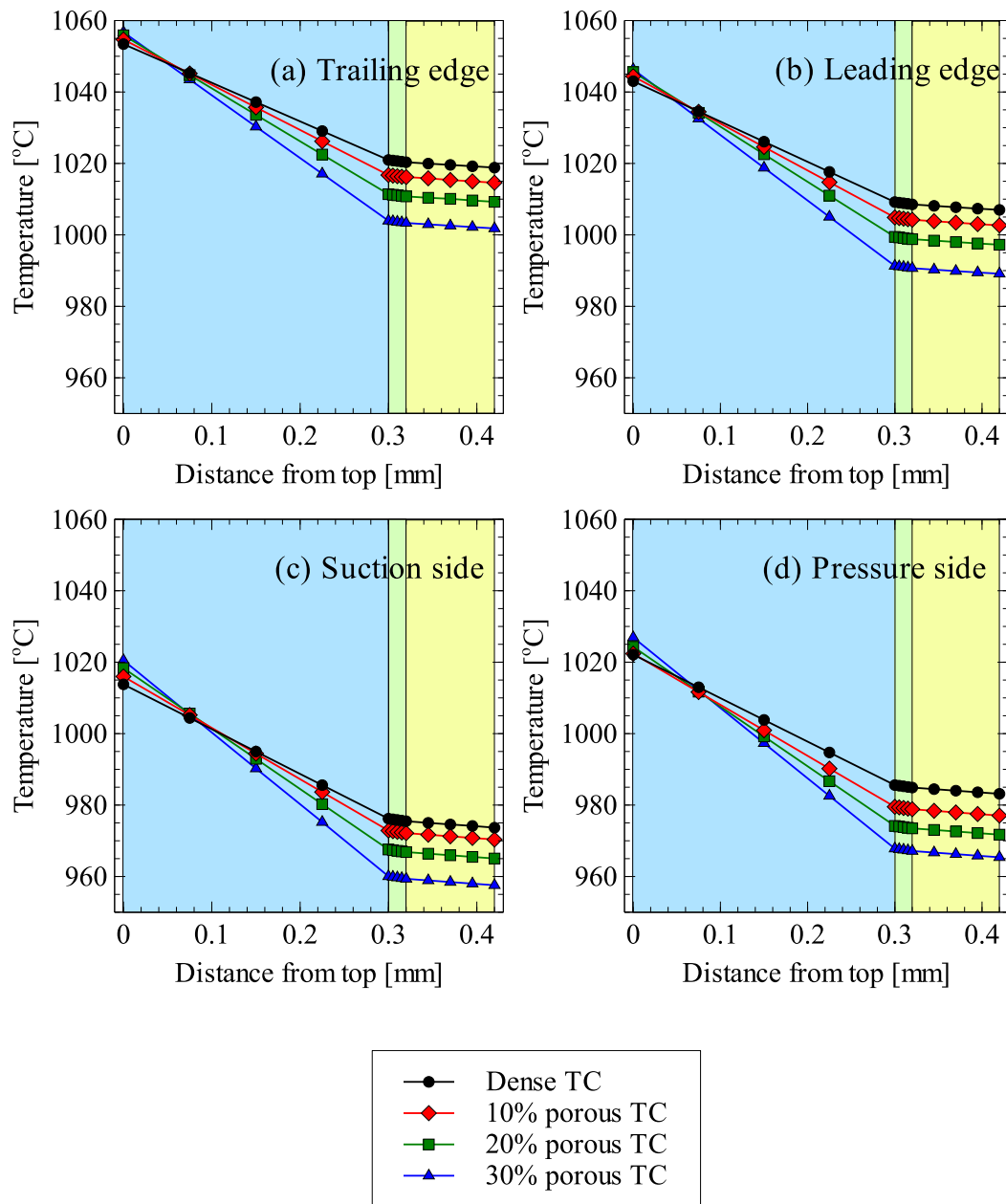


Figure 8.18. Steady-state temperature distribution on (a) trailing edge, (b) the leading edge, (c) the suction side and (d) the pressure side.

Figures 8.19 and 8.20 show the spatial variation of 1st principle stress at the TGO interface for the bond coat and top coat respectively. The results are presented for three different times: end of initial cooling from coating deposition temperature, end of heating and end of final cooling. The effect of top coat porosity on the stresses developed is shown for both top coat and bond coat. As shown in the two figures, the state of stress in the coated blade is more complex than the simplified model. In addition, both compressive and tensile stresses exist in the bond coat as well as the top coat at the same time. This is because of geometric factors and non-uniform cooling of the turbine blade.

At the end of initial cooling, the bond coat is under a combination of tensile and compressive stresses with the maximum stresses occurring at the corner on the trailing edge that meets the base of the blade. The maximum tensile stresses in the bond coat at this time reduces from 363 MPa to 331 MPa when porosity is increased from 0% to 30%. At the end of the final cooling, the state of stress in the bond coat is entirely tensile in nature and the maximum stress in the bond coat reduces from 492 MPa to 400 MPa when porosity is increased from 0% to 30%. The maximum compressive stress in the top coat at the end of initial cooling was found to be -81 MPa for the case of dense top coat. It reduced to 48 MPa for the case of 30% porous top coat. These stress values agree well with those reported in literature where compressive stress of around -100 to -120 MPa have been reported [194,195]. At the end of heating, the stresses in the top coat are mainly tensile. The maximum tensile stresses in the top coat were around 74 MPa for the dense top coat. They were reduced to 30 MPa for the case of 30% porous top coat. At the end of the final cooling, the stress state in the top coat was entirely compressive. The maximum compressive stress

in the top coat was -180 MPa for the dense top coat which reduced to -96 MPa for the case of 30% porous top coat.

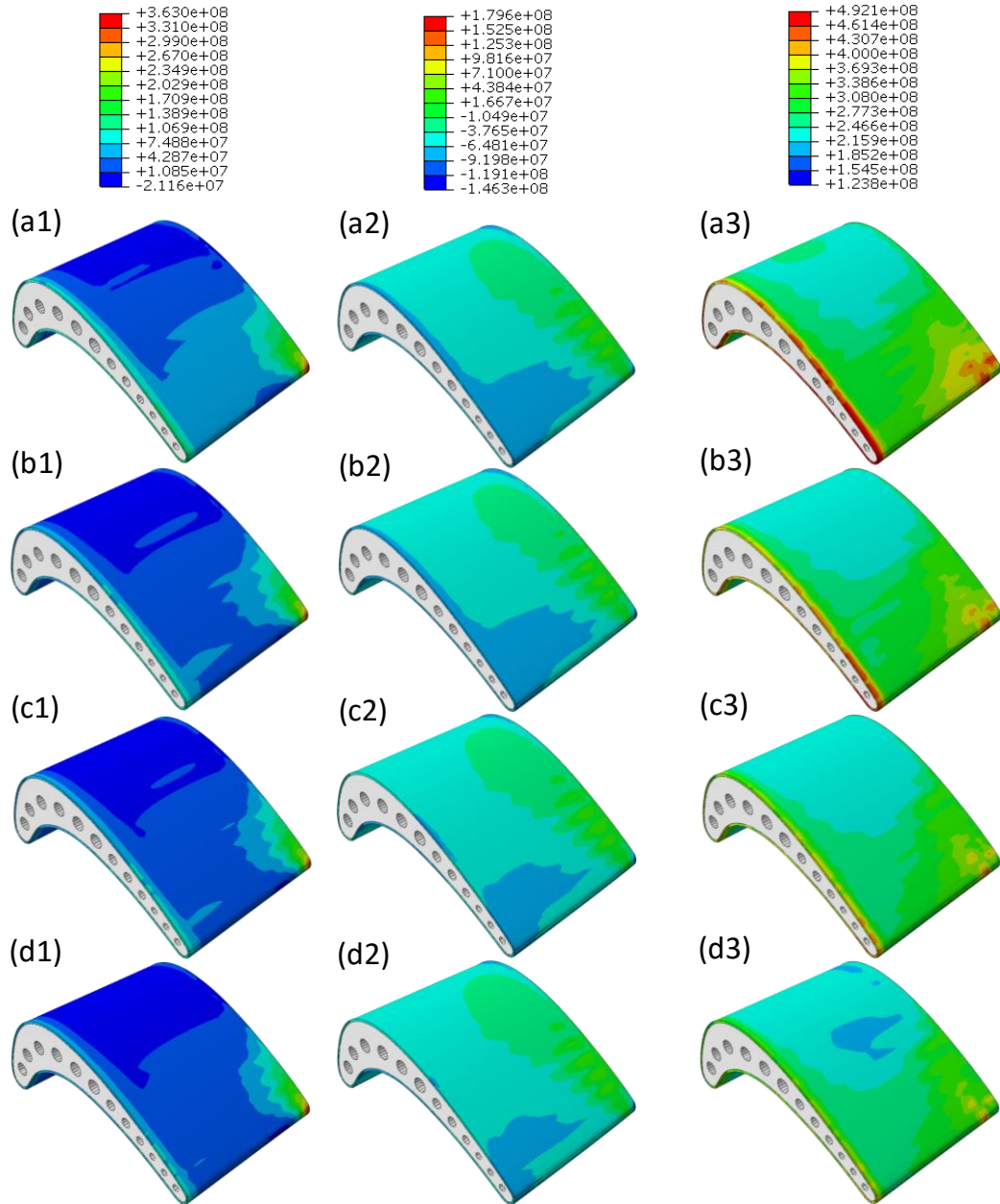


Figure 8.19. 1st principle stress in the bond coat at the TGO interface. (a), (b), (c) and (d) represent 0%, 10%, 20% and 30% porosity in the top coat. (1), (2) and (3) represent times at the end of initial cooling, at the end of heating and the end of final cooling.

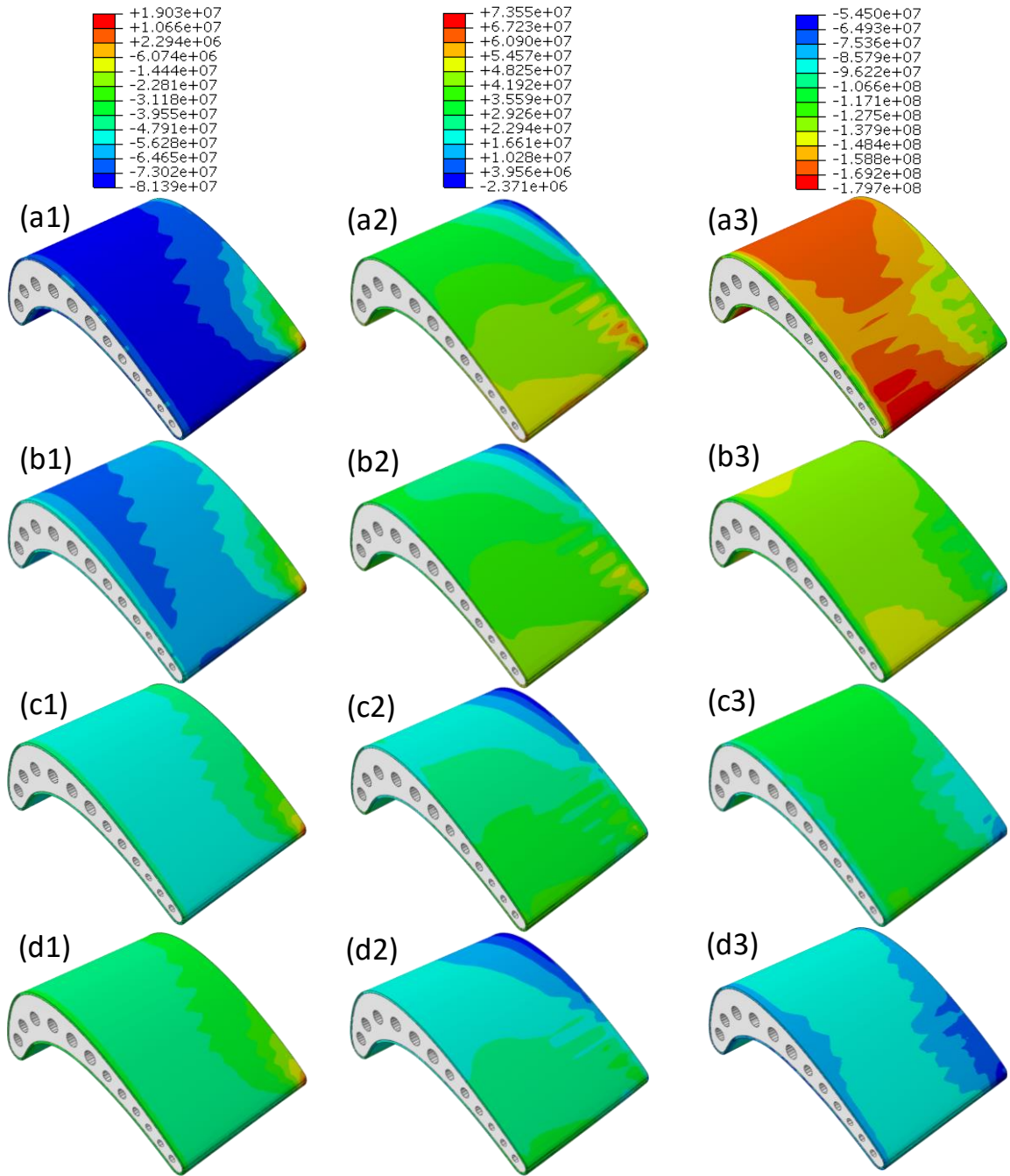


Figure 8.20. 1st principle stress in the top coat at the TGO interface. (a), (b), (c) and (d) represent 0%, 10%, 20% and 30% porosity in the top coat. (1), (2) and (3) represent times at the end of initial cooling, at the end of heating and the end of final cooling.

Figure 8.21 show the variation of 1st principle stress in the yttria-stabilized-zirconia (YSZ) phase of the top coat at the top coat-TGO interface for the four cases of porosities i.e., 0%, 10%, 20% and 30%. The results are presented for the trailing edge of the turbine blade at a point where the blade meets the base part. The maximum tensile stresses in the top coat occurred at around 180 seconds. The stress magnitude in the YSZ at this time were around 86 MPa for the dense top coat. These were reduced to 67 MPa in the presence of 30% porosity in the top coat. The maximum tensile stresses developed 30 seconds after the cooling started. The final compressive stresses at the considered point were -119 MPa for dense top coat and -93 MPa for the 30% porous top coat.

During the final cooling of the turbine blade, it was observed that the top coat initially developed tensile stresses which turned compressive upon further cooling. To further investigate this, the stress in all TBC layers was plotted against time for the case of dense top coat. The results are shown in Figure 8.22. The figure presents that all three layers show variation in the stresses from tensile to compressive either during initial cooling from deposition temperature or during the final cooling after dwell time. The reason for this type of behavior is the temperature dependent properties of the materials and the nonlinear creep strains developing in the layers. Since the stresses developing in the layers are a function of the elastic moduli, coefficient of thermal expansions and these properties are a function of temperature, the interaction of the various layers changes during the cooling of turbine blade.

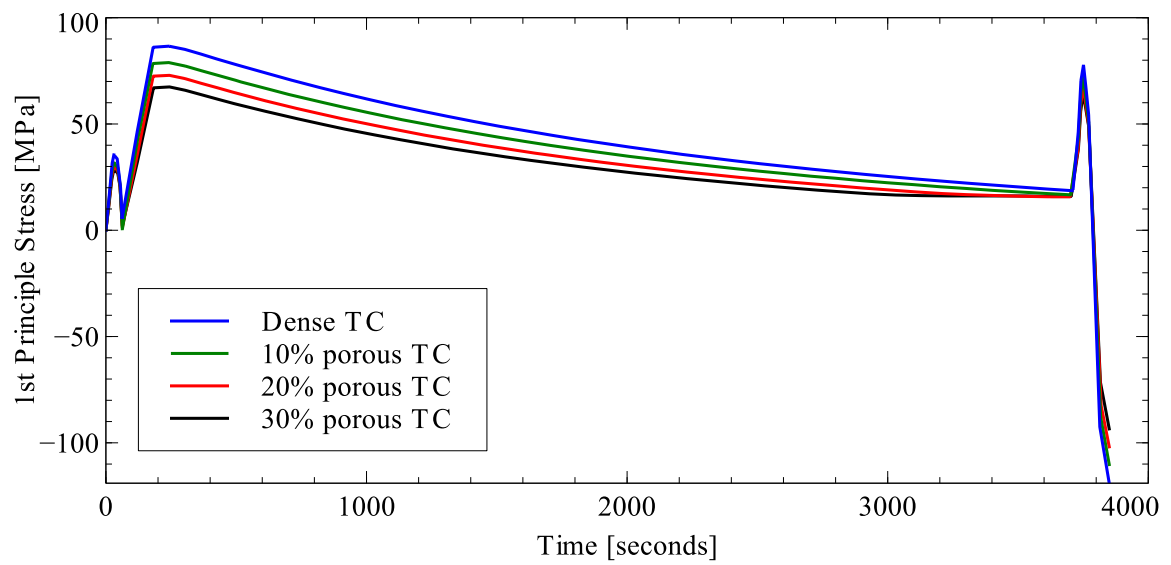


Figure 8.21. Variation of 1st principle stress with time in the YSZ phase of top coat at a point on the trailing edge. (TC: top coat)

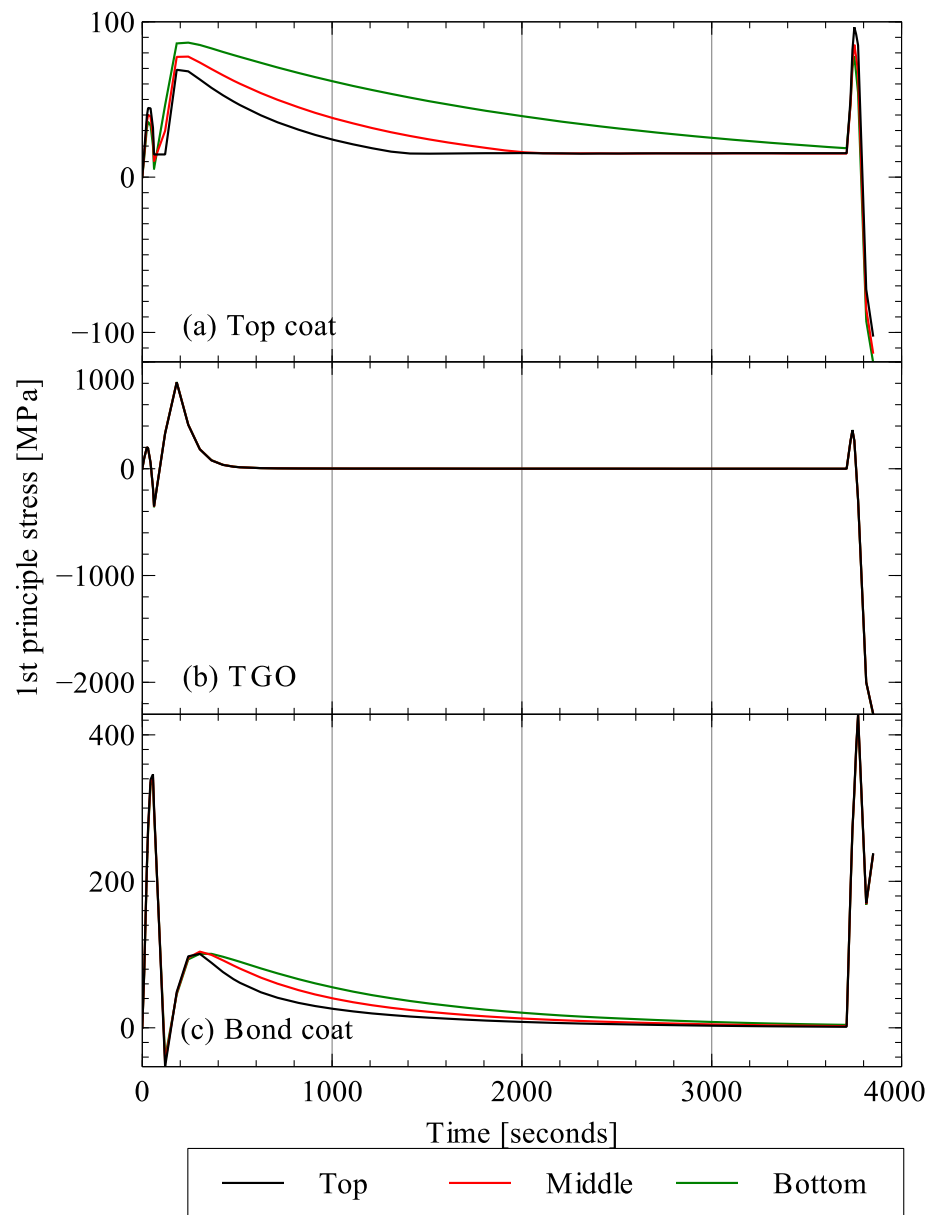


Figure 8.22. Variation of 1st principle stress with time in the (a) top coat (b) TGO and (c) bond coat for TBC system with dense top coat at a point on the trailing edge.

The compressive strength of yttria-stabilized-zirconia is around 500 MPa while its tensile strength is 117 MPa [184]. Tensile stresses higher than the tensile strength of the YSZ material can result in cracking with the top coat. To study the effect of thermal cycling on the stresses developing in the top coat, another study was conducted. The results are presented in Figure 8.23. The figure shows the maximum tensile stress within the YSZ phase of the top coat during each cycle. As can be seen from the figure, the tensile stresses in the dense top coat exceed the YSZ tensile strength during the fifth cycle thermal. The presence of porosity results in the maximum tensile stresses in the YSZ phase of top coat to be always lower than its tensile strength.

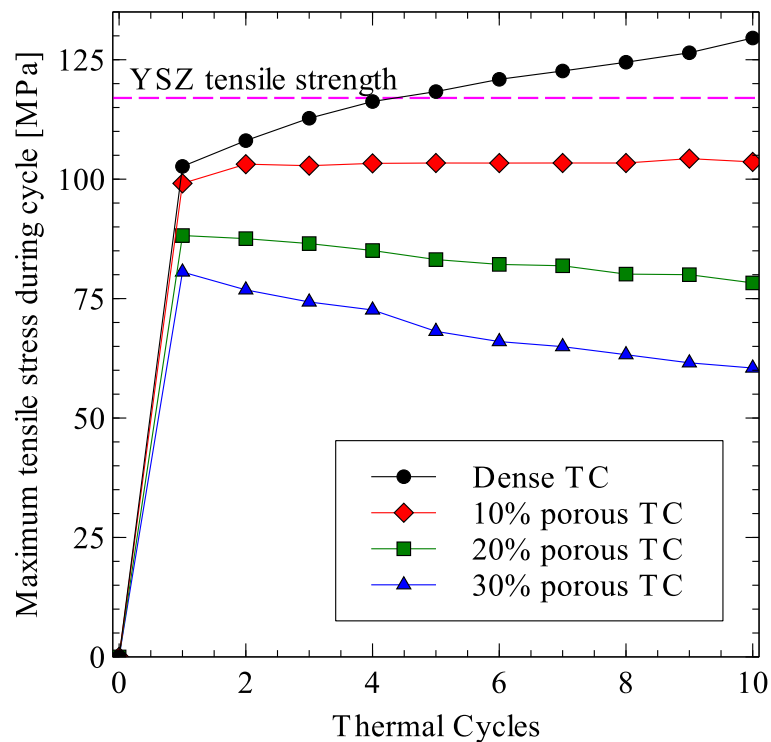


Figure 8.23. Maximum tensile stress variation with number of thermal cycles for the YSZ phase of top coat.
(TC: top coat).

Figures 8.24 to 8.26 show the spatial distribution of effective creep strain in the top coat, TGO and bond coat respectively at the end of final cooling. In all three layers, the maximum creep strains were developed at the trailing edge since the temperatures were maximum there and creep is a temperature activated process. The time evolution of creep strains in the three layers of the TBC system at a point on the trailing edge is shown in Figure 8.27. Similar to the results in the simplified model, the bond coat and top coat layers show strong influence of top coat porosity on the developed creep strains. The TGO layer does show the effect of top coat porosity but the effect is low. Whereas the creep strains reduce from 3.75×10^{-3} to 1.96×10^{-3} in the top coat and from 1.64×10^{-3} to 1.04×10^{-3} in the bond coat, they only reduce from 5.95×10^{-3} to 5.67×10^{-3} for the TGO layer. This behavior of TGO can be explained by considering the magnitudes of stresses developing in the TGO layer as shown in Figure 8.28. For all four levels of porosity in the top coat, the stresses in the TGO layer were of the order of 10^3 MPa. The maximum effect of top coat porosity on TGO stresses was present at the end of final cooling when a reduction of 140 MPa was seen when porosity was increased from 0% to 30%. However, 140 MPa represented a difference of only 6%.

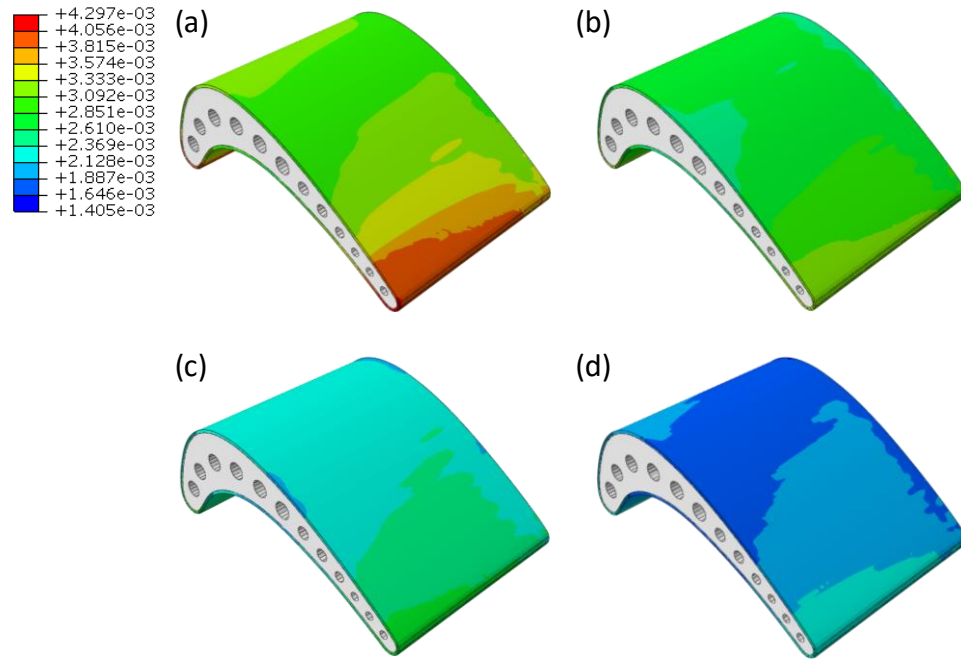


Figure 8.24. Effective creep strain in the top coat at the end of final cooling. (a), (b), (c) and (d) represent 0%, 10%, 20% and 30% porosity in the top coat.

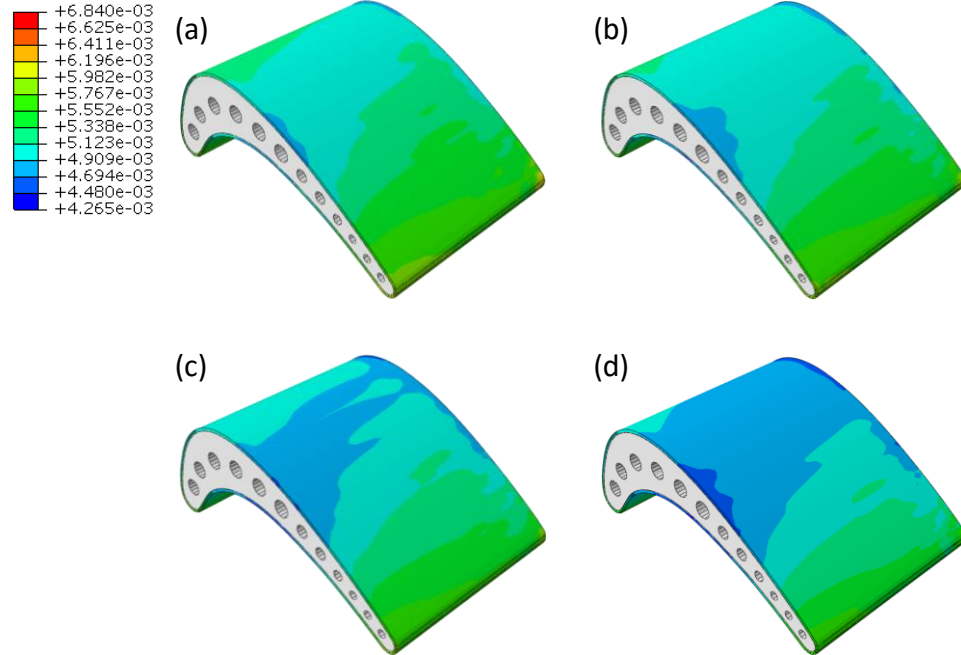


Figure 8.25. Effective creep strain in the TGO layer at the end of final cooling. (a), (b), (c) and (d) represent 0%, 10%, 20% and 30% porosity in the top coat.

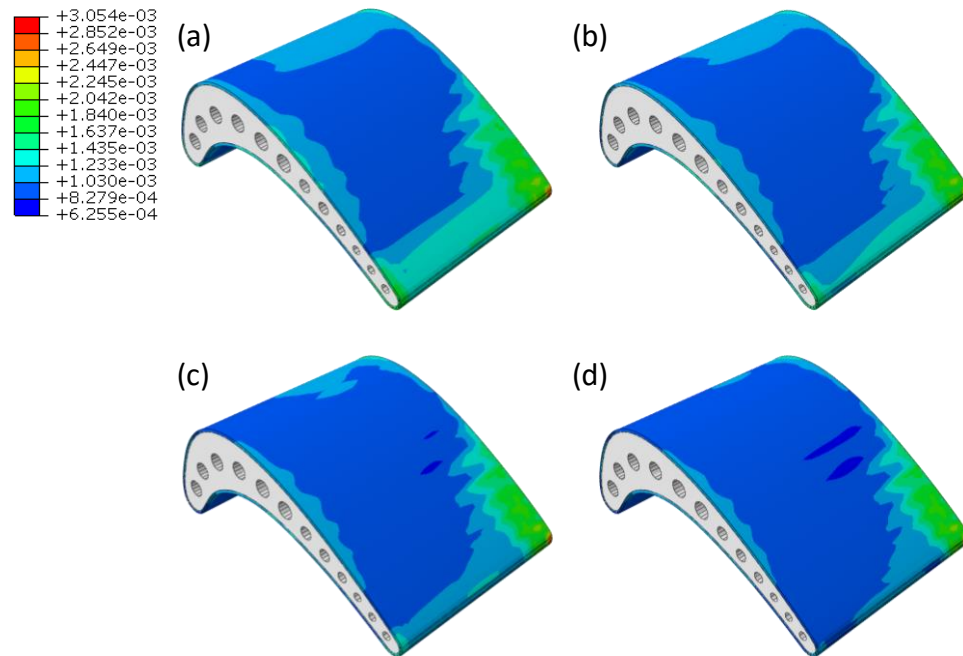


Figure 8.26. Effective creep strain in the bond coat at the end of final cooling. (a), (b), (c) and (d) represent 0%, 10%, 20% and 30% porosity in the top coat.

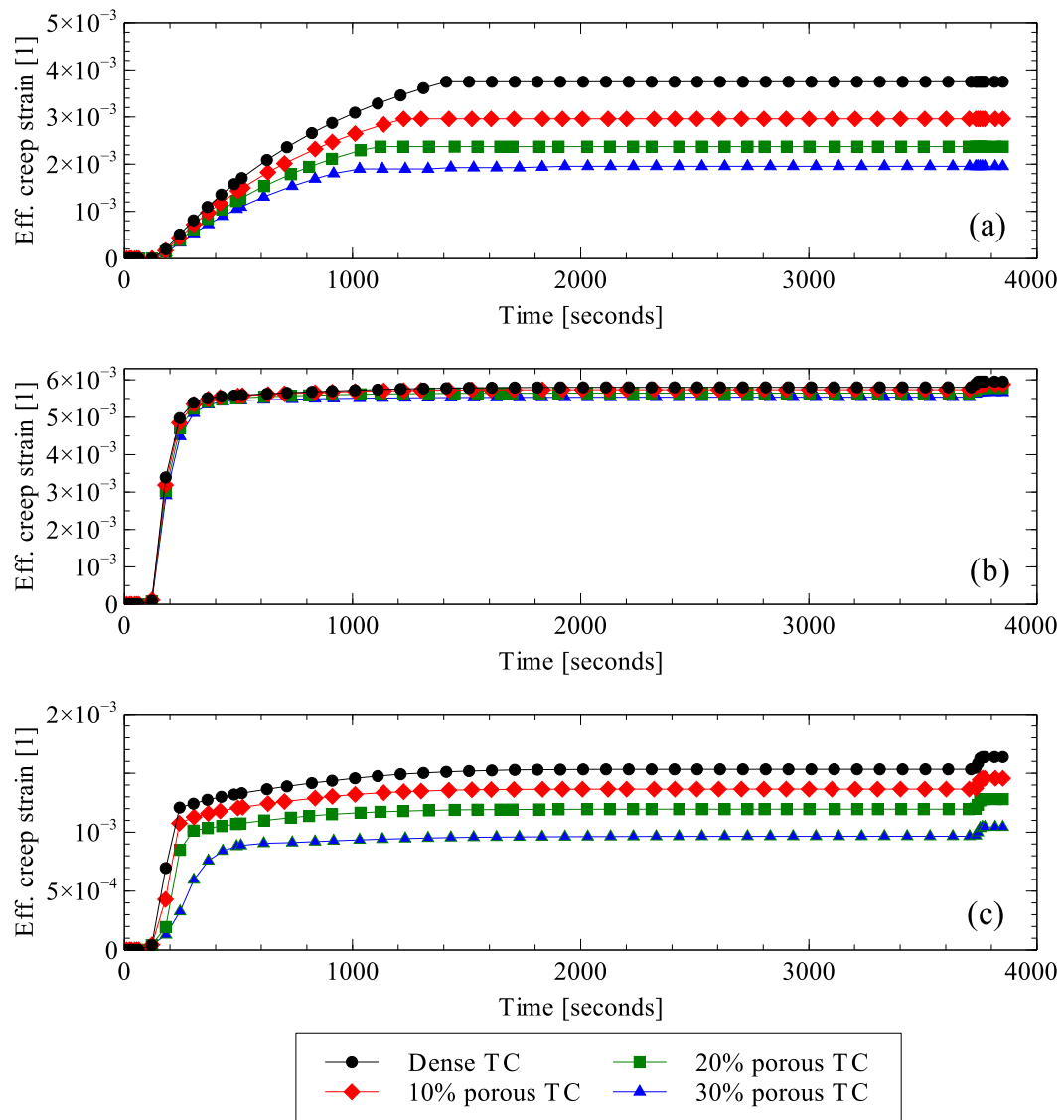


Figure 8.27. Effective creep strain evolution at the trailing edge during a single thermal cycle in (a) top coat (b) TGO and (c) bond coat using the turbine blade model (TC: top coat).

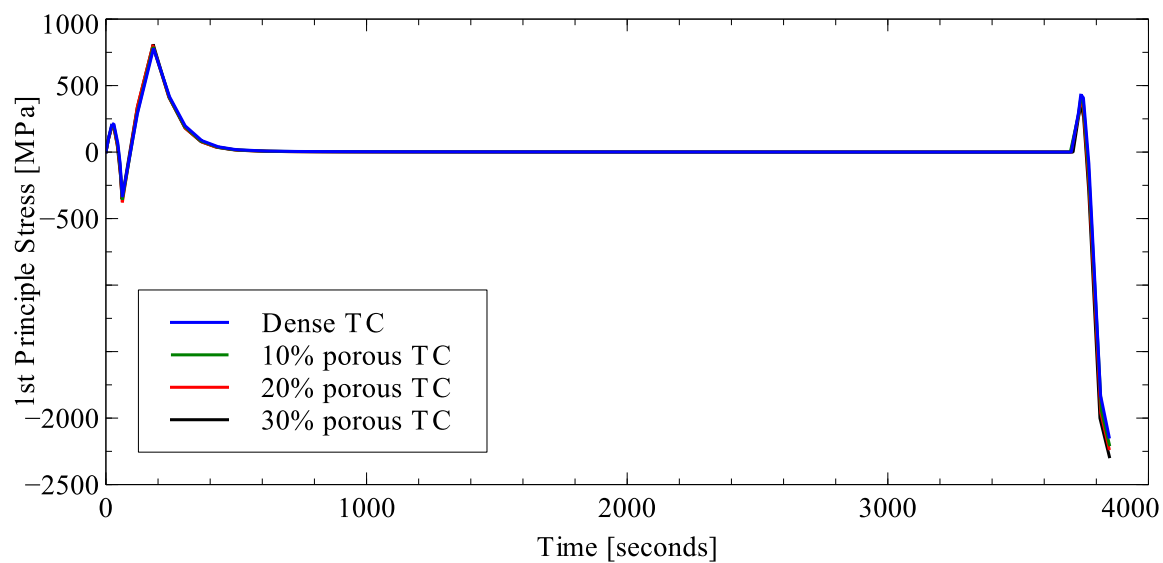


Figure 8.28. Variation of 1st principle stress with time in the TGO layer at a point on the trailing edge.

(TC: top coat)

8.5 CONCLUDING REMARKS

In this chapter, a mean-field homogenization based multiscale modeling methodology for thermo-elasto-viscoplasticity was presented and validated. The methodology was applied to study the thermo-mechanical performance of a turbine blade coated with a thermal barrier coating. Using the multiscale model, the effect of porosity in the top coat on the performance of the blade was studied. From the study conducted, the following conclusions were drawn.

- The increase in porosity in top coat resulted in an increase in the temperature drop across the TBC. It also resulted in an increase in the temperature of the outer surface of the top coat. The critical part of the blade in terms of high temperatures was found to be the trailing edge of the blade.
- Stresses in the top coat and bond coat showed a strong influence of porosity in the top coat layer while the TGO layer showed no significant effect of it. The maximum stresses in the top coat were found to occur at the top coat-TGO interface. The maximum tensile stresses in top coat which can cause cracking occurred during the cooling of the turbine blade.
- Like the stresses, the creep strains in the top coat and bond coat also showed strong influence of top coat porosity. On the other hand, the creep strains in TGO layer showed no influence of porosity in the top coat layer. The reasons for this were high magnitude of stresses in the TGO layer and faster creep

- It was also found that during thermal cycling, the porosity in top coat played a very strong role of the stresses developing the TBC system. Using the average stress in the YSZ phase of top coat estimated using the mean-field homogenization scheme, it was found that the top coat will start to crack after 5 thermal cycles. For the three cases of porous top coat, the average stress in YSZ remained lower than the tensile strength of YSZ.

CHAPTER 9

PERFORMANCE MODELING OF MEMBRANES

9.1 INTRODUCTION

Microfiltration and ultrafiltration are widely used techniques in applications ranging from wastewater treatment to biomedical applications and the food industry. In water desalination, for example, the use of ultrafiltration membranes instead of conventional pre-treatment improves the RO feed quality and provide stable permeability.

Microfiltration and ultrafiltration membranes are generally made using organic polymers such as polytetrafluoroethylene (PTFE), polyethylene terephthalate (PET), polyvinylidene fluoride (PVDF), polypropylene (PP), polyethylene (PE), polysulfone (PS) and polyether sulfone (PES). Microfiltration membranes are prepared by track-etching, stretching, or phase inversion techniques while ultrafiltration membranes are prepared exclusively by phase inversion techniques. The microstructures of phase-inversion and track-etched membranes are shown in Figure 9.1. Most membrane used for ultrafiltration and microfiltration are very thin (0.1 to 1 μm) and structurally weak. Therefore, they are

supported by one or more thicker layers with larger pores. However, the support layer plays no role in the sieving mechanism during the filtration process.

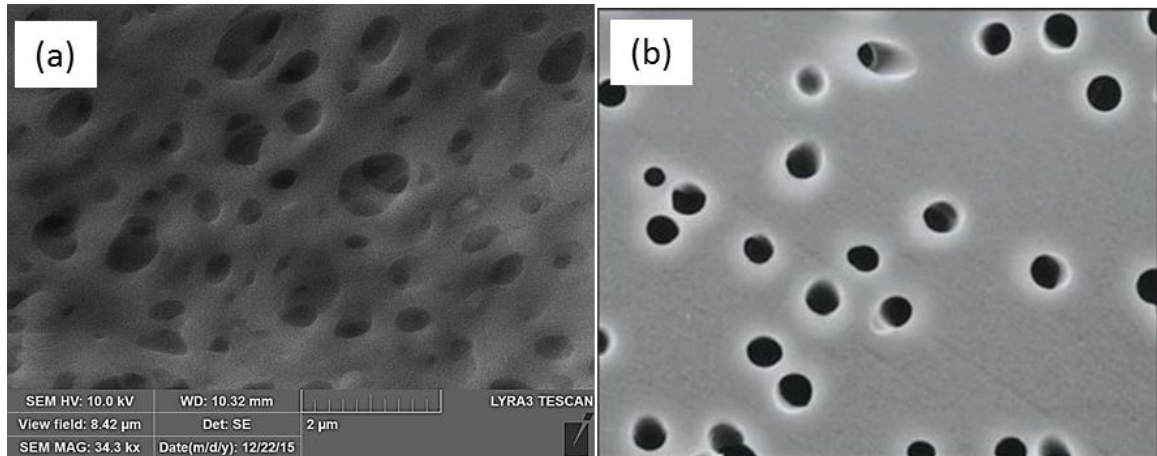


Figure 9.1. Microstructure of a (a) phase-inversion PES membrane (b) track-etched membrane [196].

Microfiltration and ultrafiltration are pressure driven processes that work by removing particles larger than the pore size of the membrane through a sieving mechanism. The quality of separation is normally expressed by the rejection factor or the separation of the membrane for a given solute. The rejection factor is defined as $1 - c_p / c_f$ while the separation factor is defined as c_f / c_p (where c_p = permeate concentration and c_f = feed concentration). Ideally, a membrane should combine high permeability and high rejection rate. Practically, this is not the case as permeability and rejection rate cannot both be increased at the same time [197].

In order to understand and predict the performance of microfiltration and ultrafiltration membranes, several efforts have also been made to formulate models the membrane performance under the influence of fouling [198–201], pore size distribution [197,202] and

pore shape [203,204]. Variation in pore sizes has been found to affect membrane performance significantly. Effect of pore size distribution in track-etched membranes on the permeability-selectivity characteristics of ultrafiltration membranes was studied by Mehta and Zydney [197] for circular pores and by Kanani et al. [204] for slot-shaped pores. Kanani et al. also found that using slot-shaped pores (very high aspect ratio) resulted in higher permeate flux compared to circular pores for same rejection ratios. Increased aspect ratio has also been linked to reduced fouling rates in membranes [205].

To take advantage of improved membrane performance when pore aspect ratio is high, studies have also been conducted to see the effect of artificially increasing pore aspect ratio by uniaxial stretching [206–208]. Morehouse et al. [206,207] and Worrel [208] carried out experimental and numerical studies to study the effect of uniaxial stretching on the pore geometry and performance of PET track-etched membranes and phase-inversion PES and PVDF membranes respectively. Both found that an increase in the pore aspect ratio resulted in improved permeate flux, but no definite trend in the rejection rate of the solutes was observed as the uniaxial strain applied to the membrane was increased.

Although, models of membrane performance that take into account pore size distribution have been published for various pore geometries, they are not applicable real membranes. As is evident from Figure 9.1, conventional membrane preparation methods do not result in well-defined pore shapes. For example, the track-etched membrane in Figure 9.1(b), not only has pore size distribution but also pore aspect ratio distribution. Similarly, the process of membrane stretching will also introduce an aspect ratio

distribution in the membrane. Currently, no model is available that can predict the permeability-selectivity characteristics of microfiltration and ultrafiltration membranes taking into account the pore size as well as pore aspect ratio distributions.

In the current work, three major tasks are carried out. First, a model to study permeability-selectivity trade-off of membranes with pore size and aspect ratio distribution is formulated and is used to study the effect of aspect ratio and size distribution on the permeability-selectivity trade-off. Second, a finite element model for porous membrane is developed using the computational microstructure generation algorithm and is used to study the effect of membrane stretching on pore size and aspect ratio distributions and on the permeability-selectivity trade-off. Finally, the effect of porosity dispersion quality on the performance of stretched membrane is studied.

9.2 PERMEABILITY-SELECTIVITY ANALYSIS

A methodology to carry out permeability-selectivity analysis of ultrafiltration and microfiltration membranes has been presented by Mehta and Zydney [197] for membranes with circular pores of variable sizes and later extended by Kanani et al. [204] for slot pores. The following development was done by Mehta and Zydney [197] to determine the permeability of the solvent through a membrane with circular pores and is presented here for the sake of completeness with some additional intermediate steps.

9.2.1 Circular pores with size distribution

Under the assumption of a convection dominated process, the velocity of all impurities in the feed is the same as the solvent and the separation coefficient of the membrane for the large solute to be filtered is defined as,

$$\alpha = \frac{S_{small}}{S_{large}} \quad (9.1)$$

where S_{large} is the selectivity of the larger solute that needs to be separated and S_{small} is the selectivity of the small solutes that pass through the membrane without any hindrance.

The selectivity of the larger solute that needs to be filtered can be determined using the expression developed by Zeman and Wales [209].

$$S_a(r) = (1 - \lambda)^2 (2 - (1 - \lambda)^2) \exp(-0.7146\lambda^2) \quad (9.2)$$

where $\lambda = r_s / r$ and r and r_s are the pore and solute radii.

The permeability of the solvent through the membrane can be determined assuming that the pores are perfect cylinders. Under this condition, the Hagen–Poiseuille equation is valid. The volumetric flow rate of the solvent through the membrane is,

$$Q = \frac{\Delta P}{8\mu\delta_m} N_p \pi r^4 \quad (9.3)$$

where Q is the flow rate (m^3/s), ΔP is the pressure drop (Pa) across the membrane, μ is the viscosity (Pa.s) of the solvent, δ_m is the membrane thickness (m) and N_p is the number of pores in the membrane. The volumetric flux through the membrane becomes,

$$J_v = Q/A_{mem} \quad (9.4)$$

where A_{mem} is the membrane area defined by,

$$A_{mem} = \frac{N_p \pi r^2}{\phi} \quad (9.5)$$

and ϕ is the porosity fraction in the membrane.

Using equations (9.3), (9.4) and (9.5), the permeability of the solvent through the membrane can be defined using,

$$L_p = \frac{J_v}{\Delta P} = \frac{\phi r^2}{8\mu\delta_m} \quad (9.6)$$

Equations (9.2) and (9.6) can be used to generate the permeability-selectivity curves for membranes. The effect of variation in the pore radius can also be included in the equations for permeability and selectivity. This is done by averaging the permeability and selectivity over the entire range of pore radii. Mochizuki and Zydney [202] carried out a theoretical analysis to determine the average permeability and selectivity of membranes. The average permeability and selectivity are given by equations (9.7) and (9.8) respectively.

$$\bar{L}_p = \frac{\varphi}{8\mu\delta_m} \frac{\int_0^\infty n(r)r^4 dr}{\int_0^\infty n(r)r^2 dr} \quad (9.7)$$

$$\bar{S}_a = \frac{\int_0^\infty S_a(r)n(r)r^4 dr}{\int_0^\infty n(r)r^4 dr} \quad (9.8)$$

where $n(r)$ is the probability density function of pore radii.

9.2.2 Elliptical pores with size and aspect ratio distribution

Using a similar approach to Mehta and Zydney [197], the permeability of a solvent through a membrane with elliptical pores was also derived. The solution of the Hagen–Poiseuille equation for elliptical cross-section leads to the following equation for solvent flow rate,

$$Q = \frac{N_p \Delta P}{4\mu\delta_m} \frac{\pi a^3 b^3}{a^2 + b^2} \quad (9.9)$$

where a and b are the major and minor axes half lengths of the elliptical cross section of the pore. The permeability of the solvent through the membrane is therefore,

$$L_p = \frac{\varphi}{4\mu\delta_m} \frac{a^2 b^2}{a^2 + b^2} \quad (9.10)$$

To take into account variation in the pore sizes in the membrane, area weighted average of equation (9.10) is taken. The average permeability through the membrane is given by equation (9.11).

$$\bar{L}_p = \frac{\varphi}{4\mu\delta_m} \frac{\int_0^\infty \int_0^\infty n(a)n(b) \frac{a^3 b^3}{a^2 + b^2} da db}{\int_0^\infty \int_0^\infty n(a)n(b) ab da db} \quad (9.11)$$

where $n(a)$ and $n(b)$ are the probability density functions of major and minor axes half lengths of the pores.

To determine the average selectivity of the membrane, it is noted that the selectivity will depend on the minor axis length of the pore cross section. Setting $\lambda = r_s/b$ and assuming equation (9.2) is still valid for determining selectivity, the average selectivity of membranes with elliptical pores of variable sizes can be determined using,

$$\bar{S}_a = \frac{\int_0^\infty S_a(b)n(b)b^2 db}{\int_0^\infty n(b)b^2 db} \quad (9.12)$$

9.3 EFFECT OF PORE GEOMETRY ON MEMBRANE PERFORMANCE

In order to study the effect of pore aspect ratio on the permeability-selectivity performance of microfiltration and ultrafiltration membranes, a study was conducted in which aspect ratio of the pores was changed keeping the pore cross section area constant.

The parameters used in the model were solute radius $r_a=3.65nm$ for bovine serum albumin protein, membrane porosity fraction $\phi=0.3$, membrane thickness $\delta=0.3\mu m$ and solvent viscosity $\mu=0.001 Pa.s$. The log-normal probability distribution function was used to describe the pore size variation within the membrane [202].

$$n(x) = \frac{n_0}{x\sqrt{2\pi}} \left[\ln \left(1 + \left(\frac{\sigma}{\bar{x}} \right)^2 \right) \right]^{-1/2} \exp \left\{ - \frac{\left(\ln(x/\bar{x}) \left[1 + \left(\frac{\sigma}{\bar{x}} \right)^2 \right]^{1/2} \right)^2}{2 \ln \left[1 + \left(\frac{\sigma}{\bar{x}} \right)^2 \right]} \right\} \quad (9.13)$$

where σ is the standard deviation of x , \bar{x} is the mean value of x and n_0 is the maximum possible value of $n(x)$. The two parameters that control the distribution are mean \bar{x} and the normalized standard deviation σ/\bar{x} .

Two studies were conducted: first, to see the effect of average aspect ratio on permeability-selectivity trade-off for different normalized standard deviations of pore sizes a and b , and second, to see the effect of normalized standard deviations of pore sizes a and b on the performance for different aspect ratios. The results are shown in Figure 9.2 and Figure 9.3. Each point in the figures was generated by selecting an average pore radius r , calculating the average major and minor axes half lengths under the condition that the pore area remains same for all aspect ratios and calculating permeability and selectivity using equations (9.11) and (9.12) respectively.

As can be seen from Figure 9.2, increasing the average aspect ratio improves the performance of microfiltration and ultrafiltration membranes for all size distributions. In

other words, for the same separation factor, a higher permeate flux can be obtained if the pore aspect ratio is increased. This result agrees with the experimental findings of Worrel [208] and Morehouse et al. [206,207] who found the same effect of increasing aspect ratio of permeate flux. This strengthens confidence in the theoretical development carried out in the current work.

The effect of pore size distribution on the membrane performance is shown in Figure 9.3. The figure shows the detrimental effect of non-uniform pore size on the permeability-selectivity trade-off curve. Having a larger standard deviation of pore sizes results in lower separation factor for all aspect ratios. In order to achieve the same separation factor, the pore size needs to be reduced which reduces the permeability.

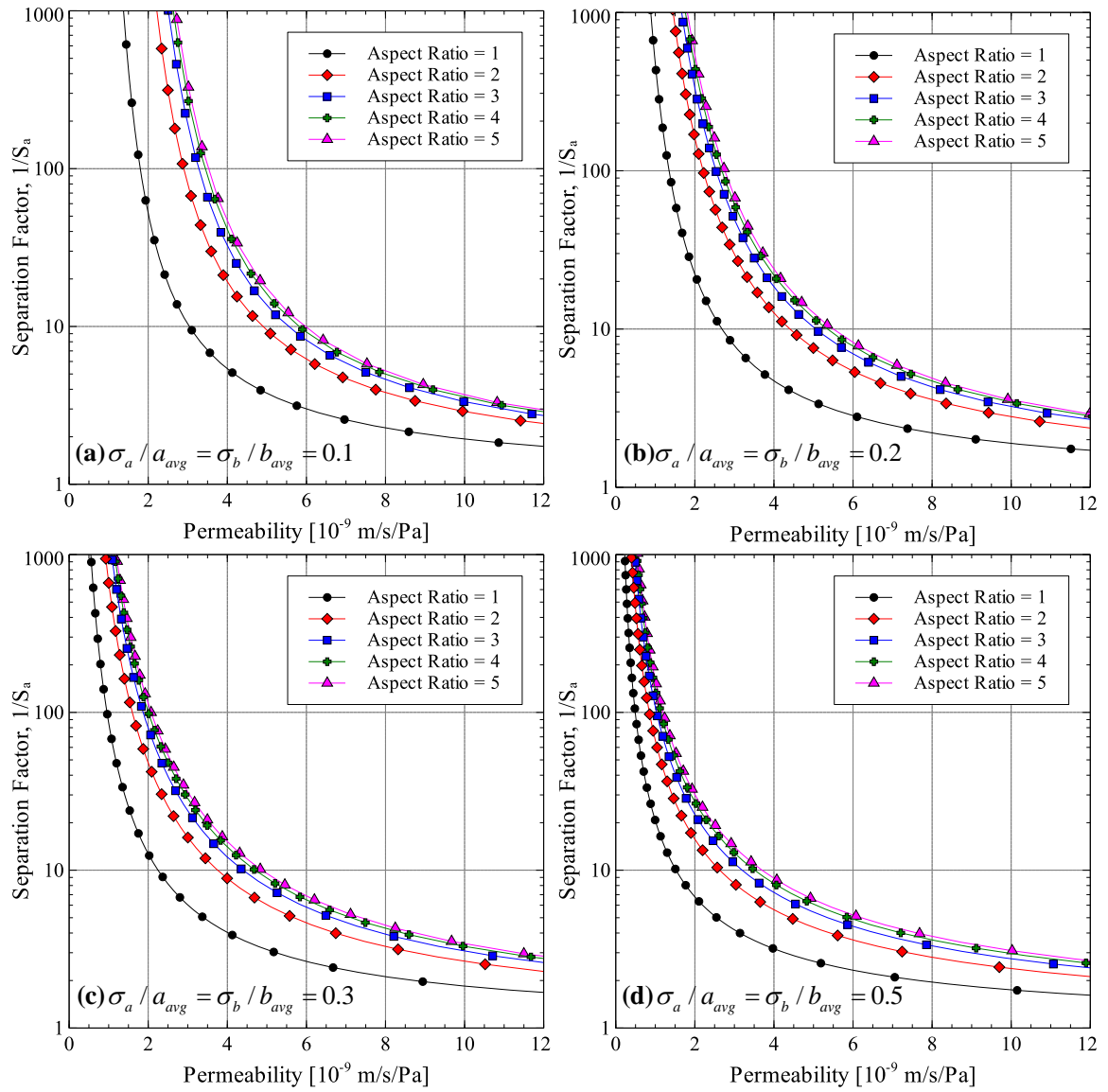


Figure 9.2. Effect of pore aspect ratio on permeability-selectivity trade-off.

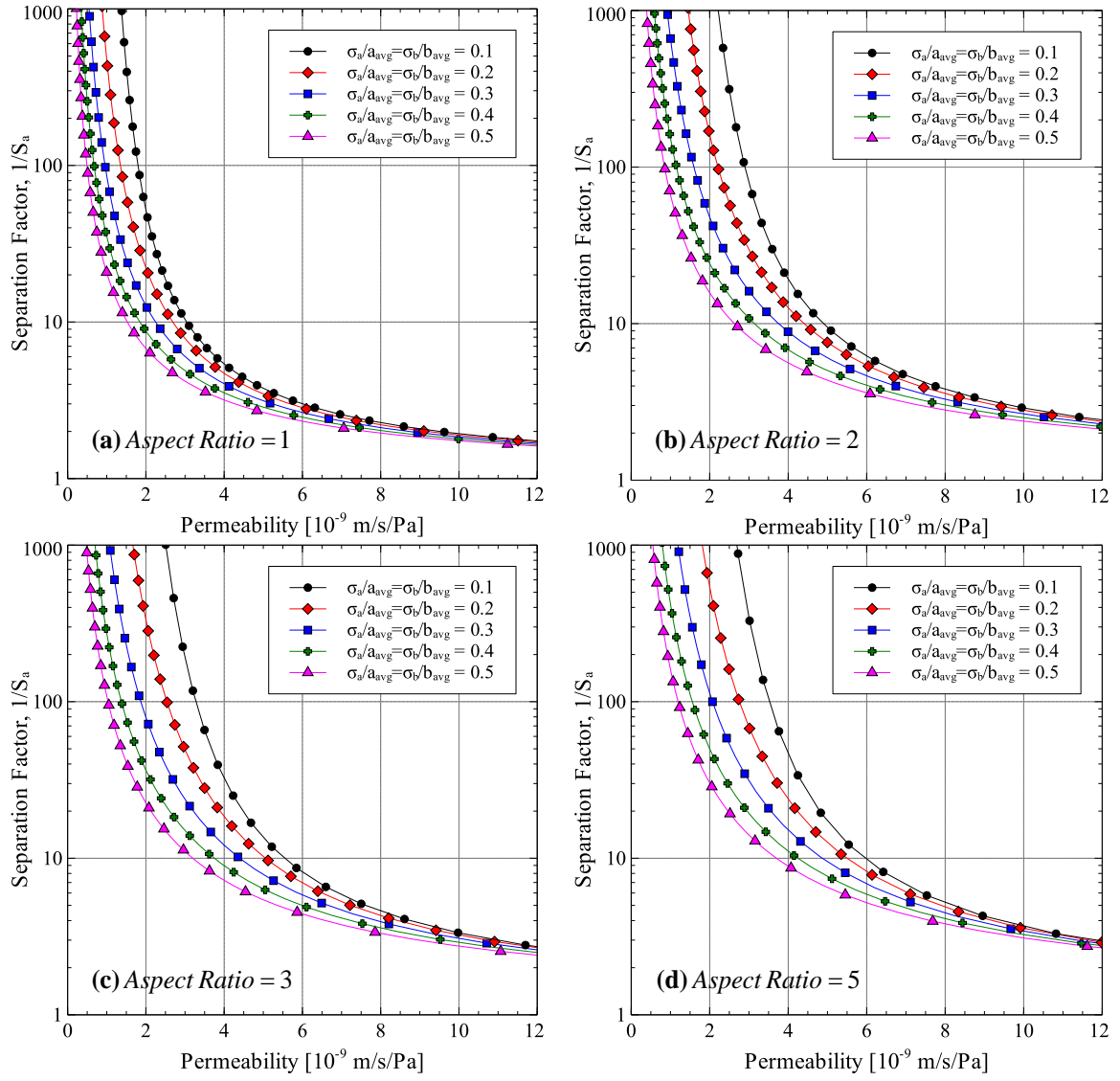


Figure 9.3. Effect of pore size distribution on permeability-selectivity trade-off.

9.4 MEMBRANE STRETCHING

Previous studies show that membrane stretching can have a positive effect on membrane permeability [206–208]. On the other hand, the effect of stretching on the separation factor could not be properly identified as experiments showed that there were cases in which the separation factor increased, remained unchanged or even reduced [208].

In the current work, a finite element model of a microfiltration membrane was developed to analyze the effect of membrane stretching on the size distribution on pores in the stretched membrane. Using the results of the finite element model, the effect of membrane stretching on the permeability-selectivity trade-off curve was also analyzed. This section presents the development of the finite element model and the resulting pore sizes due to membrane stretching. The effect of membrane stretching on its performance is analyzed in the next section.

9.4.1 Finite element model for membrane stretching

The membrane stretching problem consists of a finite element model of the representative volume element (RVE) of the porous membrane. The constitutive behavior of the membrane material is defined explicitly as viscoelastic-rate-independent plastic. The geometry of a 30% porous membrane with an average pore size of $0.1\mu\text{m}$ was generated using an in-house code and is shown in Figure 9.4 along with the finite element mesh. The microscale model is defined by equations (9.14).

$$-\nabla \cdot (1 + \nabla u) S = F_v \quad (9.14)$$

$$S = C : \varepsilon_{el} + S_q \quad (9.15)$$

$$\varepsilon_{el} = \varepsilon - \varepsilon_{pl} \quad (9.16)$$

$$\varepsilon = \frac{1}{2} \left[(\nabla u)^T + \nabla u + (\nabla u)^T \nabla u \right] \quad (9.17)$$

where u is the displacement field, S is the second Piola Kirchhoff stress, F_v is the body load, C is the elasticity tensor, S_q is the relaxation stress due to viscoelasticity and $\varepsilon, \varepsilon_{el}$ and ε_{pl} are the total, elastic and plastic strain tensors.

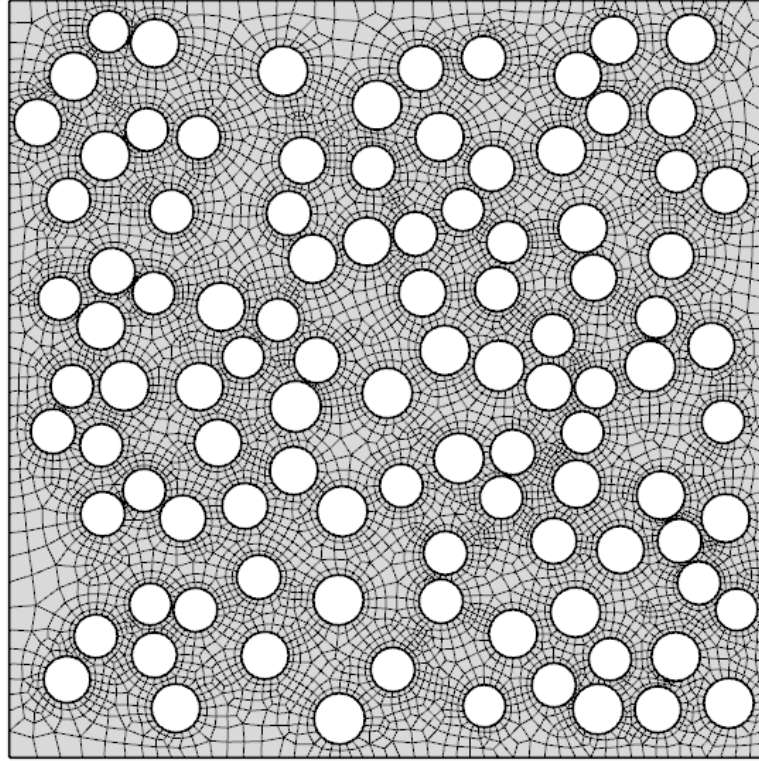


Figure 9.4. Membrane geometry with finite element mesh.

For viscoelasticity, the bulk modulus was assumed to be constant while the shear modulus was assumed to be defined by the generalized Maxwell model. The model consists of several spring-damper branches in parallel each of which is defined by a shear modulus and a relaxation time. Considering m parallel branches, the viscoelasticity model can be described using equations (9.18) and (9.19) .

$$S_q = \sum_m 2G_{vm} (e_{el,dev} - \varepsilon_{vm}) \quad (9.18)$$

$$\tau_{vm} \dot{\varepsilon}_{vm} + \varepsilon_{vm} = \varepsilon_{el,dev} \quad (9.19)$$

where G_{vm} is the shear modulus in branch m , τ_{vm} is the relaxation time of branch m , ε_{vm} is the viscoplastic strain of branch m and $\varepsilon_{el,dev}$ is the deviatoric part of the elastic strain tensor.

The rate-independent plasticity of the membrane material was modeled using the bilinear isotropic hardening model. The model is described by equations (5.10)-(5.13) .

$$\dot{\varepsilon}_p = \dot{\varepsilon}_{p,eff} \frac{\partial F}{\partial S} \quad (9.20)$$

$$F = \sigma_{mises} - \sigma_{ys} \quad (9.21)$$

$$\sigma_{ys} = \sigma_{y0} + \frac{E_{T,iso}}{1 - \frac{E_{T,iso}}{E}} \varepsilon_{p,eff} \quad (9.22)$$

$$\dot{\varepsilon}_{p,eff} \geq 0, F(\sigma, \sigma_{ys}) \leq 0, \dot{\varepsilon}_{p,eff} F = 0 \quad (9.23)$$

where ε_p is the plastic strain tensor, $\varepsilon_{p,eff}$ is the von Mises effective plastic strain, σ_{mises} is the von Mises stress, σ_{y0} and σ_y are the initial and current yield stress and E and E_T are the elastic and tangential moduli.

Since the finite element model represents a part of a larger membrane, periodic boundary conditions are applied to the model using constraint equations. For a two-dimensional model, shown in Figure 4.1, the constraint equations are given as equations (9.24)-(9.28). Uniaxial stretching is applied to the membrane by controlling the displacement of reference node 1.

$$\vec{u}_2 - \vec{u}_1 - \vec{u}_{ref_1} = 0 \quad (9.24)$$

$$\vec{u}_4 - \vec{u}_1 - \vec{u}_{ref_2} = 0 \quad (9.25)$$

$$\vec{u}_3 - \vec{u}_1 - \vec{u}_{ref_1} - \vec{u}_{ref_2} = 0 \quad (9.26)$$

$$\vec{u}_{right, no\ edges} - \vec{u}_{left, no\ edges} - \vec{u}_{ref_1} = 0 \quad (9.27)$$

$$\vec{u}_{top, no\ edges} - \vec{u}_{bottom, no\ edges} - \vec{u}_{ref_2} = 0 \quad (9.28)$$

In the current work, the membrane material was assumed to be PET. The properties used in the current work were determined by Hanks et al. [210] who experimentally determined the stress-strain response and the viscoelastic material properties of dense PET. The properties are listed in Table 9.1.

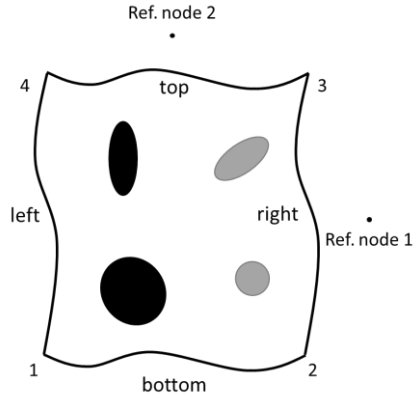


Figure 9.5. Applying periodic boundary conditions to a microscale RVE.

Table 9.1. Material properties of dense PET used in finite element model.

Property	Value	
Bulk modulus, K	0.162 GPa	
Initial Shear modulus, G_{init}	0.075 GPa	
Tangent modulus, E_T	5.95 MPa	
Viscoelasticity		
Branch	Shear modulus ratio, G_{vm} / G_{init}	Relaxation time [s]
1	0.0402	10^{-5}
2	0.0468	10^{-4}
3	0.0572	10^{-3}
4	0.1805	10^{-2}
5	0.0487	10^{-1}
6	0.0988	10^0
7	0.0205	10^1
8	0.1394	10^2
9	0.0000	10^3
10	0.1283	10^4
11	0.0470	10^5
12	0.1005	10^6

The stretching process was carried out at 160°C by applying the total strain over a period of 5 minutes. This was followed by a holding time of 10 minutes to allow stress relaxation followed by cooling the membrane to room temperature over a period of five minutes. Finally, the applied strain load was released to remove any elastic strains within the membrane. The membrane temperature and applied strain load are shown in Figure 9.6.

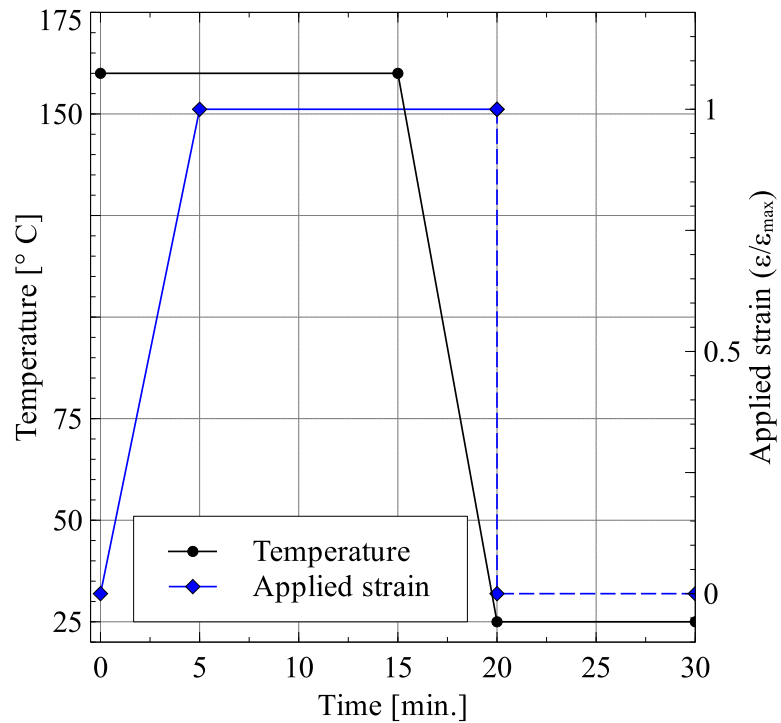


Figure 9.6. Applied temperature and strain load.

9.4.2 Finite element modeling results

For the membrane geometry presented in Figure 9.4, the cases of 15%, 30%, 40% and 50% uniaxial stretch were solved and analyzed. A summary of pore sizes after membrane stretching is presented in Table 9.2 while Figure 9.7 shows the distribution of major and minor axis sizes. The deformed geometries for the four cases solved are shown in Figure 9.8.

As expected, increasing the uniaxial strain applied to the membrane increases the pore aspect ratios. The average pore aspect ratio increases from 1.374 for 15% stretch to 2.732 for 50% stretch. The stretching process also affects the distribution of pore sizes as increasing stretching strains result in larger standard deviations in pore sizes. The maximum normalized standard deviation was observed for the 50% stretch case with values of 0.201 and 0.256 for major and minor axes sizes. As was shown in Figure 9.2 and Figure 9.3, increasing the aspect ratio improves the membrane performance while a wider distribution of pore sizes results in a degradation of membrane performance. Since membrane stretching results in an increase in pore aspect ratios as well as the width of distribution of sizes, stretching will not necessarily result in an improved permeability-selectivity trade-off.

Table 9.2. Size distribution parameters for stretched membranes.

Stretch	Avg. major axis size, a_{avg} [μm]	Avg. minor axis size, b_{avg} [μm]	Major axis size distribution, σ/a_{avg}	Major axis size distribution, σ/b_{avg}	Average pore aspect ratio
Unstretched	0.097	0.097	0.060	0.060	1
15%	0.129	0.095	0.142	0.094	1.374
30%	0.162	0.087	0.191	0.156	1.866
40%	0.180	0.084	0.194	0.196	2.256
50%	0.199	0.079	0.201	0.256	2.732

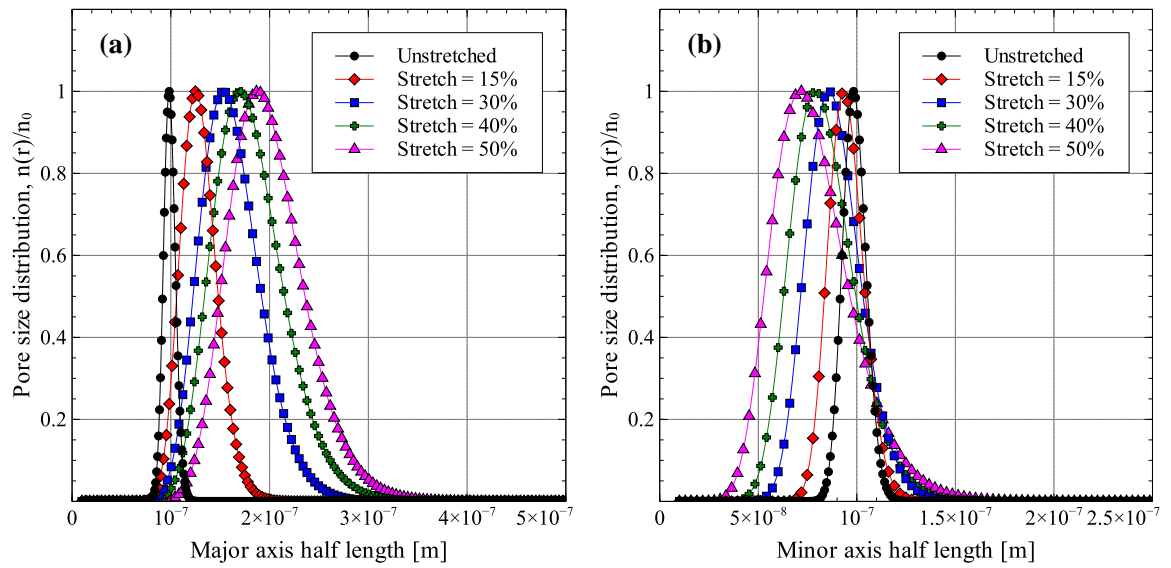
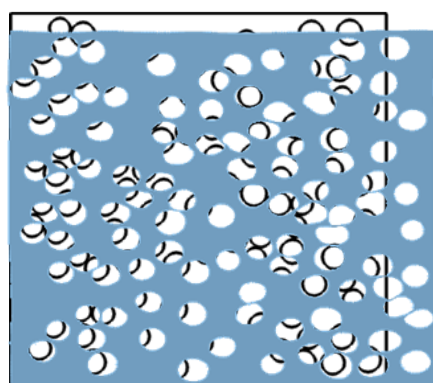
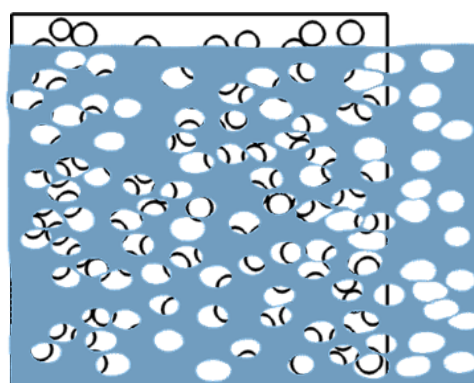


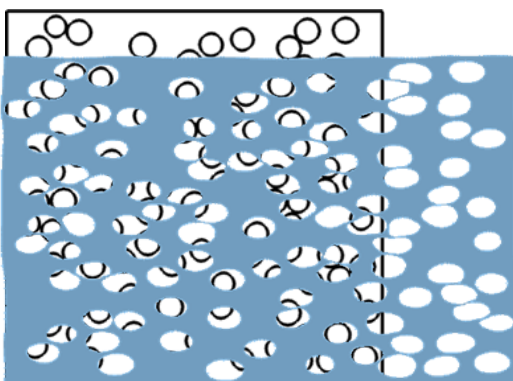
Figure 9.7. (a) Major and (b) minor axes size distribution for stretched membranes.



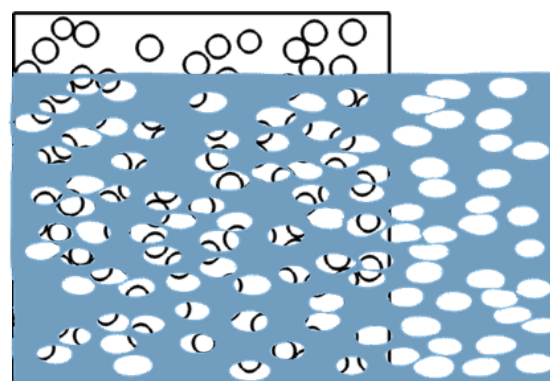
(a) Stretch=15%



(b) Stretch=30%



(c) Stretch=40%



(d) Stretch=50%

Figure 9.8. Deformed geometries of stretched membranes for (a) 15% stretch, (b) 30% stretch, (c) 40% stretch and (d) 50% stretch.

9.5 EFFECT OF STRETCHING ON MEMBRANE PERFORMANCE

Using the finite element model results of section 4 and the permeability and selectivity models formulated in section 9.2, the effect of membrane stretching on their permeability-selectivity trade-off was analyzed. As was discussed in section 9.4.2, there are two competing effects of stretching that modify the membrane performance. First, stretching causes the pore aspect ratios to increase which improves performance. Second, the width of pore size dispersion is also increased which degrades membrane performance. Their combined effect on membrane performance for the stretching cases considered in section 9.4 is shown in Figure 9.9. Each point in the figure is generated by taking an initial pore radius r and applying the average major and minor axes stretches to it. The normalized standard deviation was assumed to be independent of the average pore size. The figure shows that the cases of 15% and 30% stretches show positive effect of the permeability-selectivity trade-off curve. The performance starts to degrade at higher stretches which is easily observable at high selectivity values. The degradation of performance can be associated to the large width of pore size distribution which is numerically presented as the normalized standard deviation in Table 9.2.

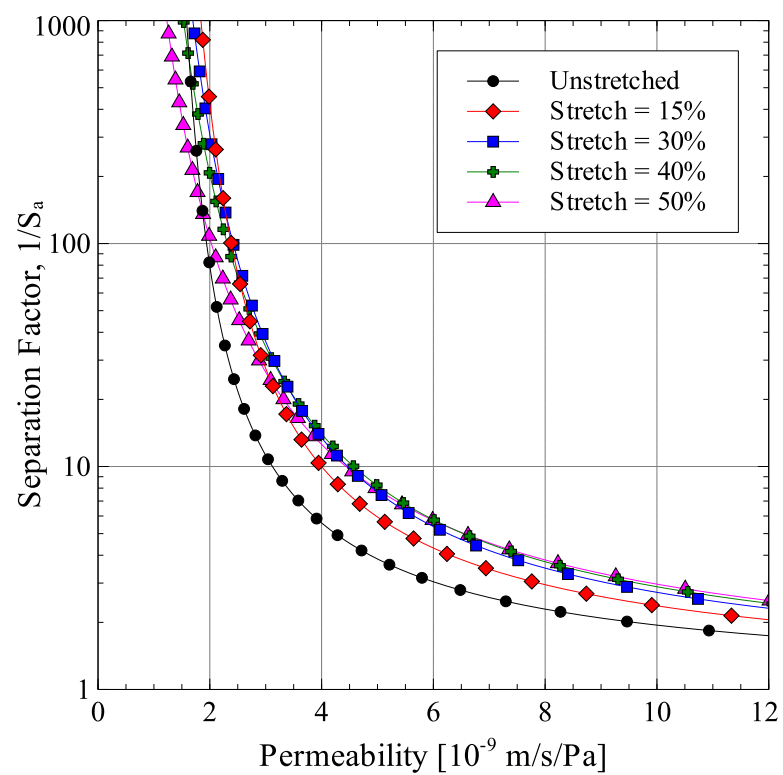


Figure 9.9. Effect of membrane stretching on permeability-selectivity trade-off.

9.5.1 Effect of porosity dispersion quality on membrane performance

The results in Figure 9.9 show that at higher stretch level, the effect of size distribution dominates the effect of pore aspect ratio. This results in a worse performance than the case of a lower stretch. In this section, a study is presented that was conducted to test the hypothesis that the pore size distribution after stretching is related to the uniformity of pore dispersion.

To start, four porous membrane RVEs were generated with different pore dispersion uniformities. The dispersion quality for each microstructure was quantified by first calculating nearest neighbor distances (calculated from center to center) for all pores and representing them as the normalized average nearest neighbor distance and its standard deviation. A higher average nearest neighbor distance and a lower standard deviation represents better dispersion. The four membrane RVEs along with the dispersion quality parameters are shown in Figure 9.10 in which case (b) is the one studied in previous sections. The dispersion quality is increasing from case (a) to (d). The distributions of normalized nearest neighbor distances in the four RVEs are shown in Figure 9.11.

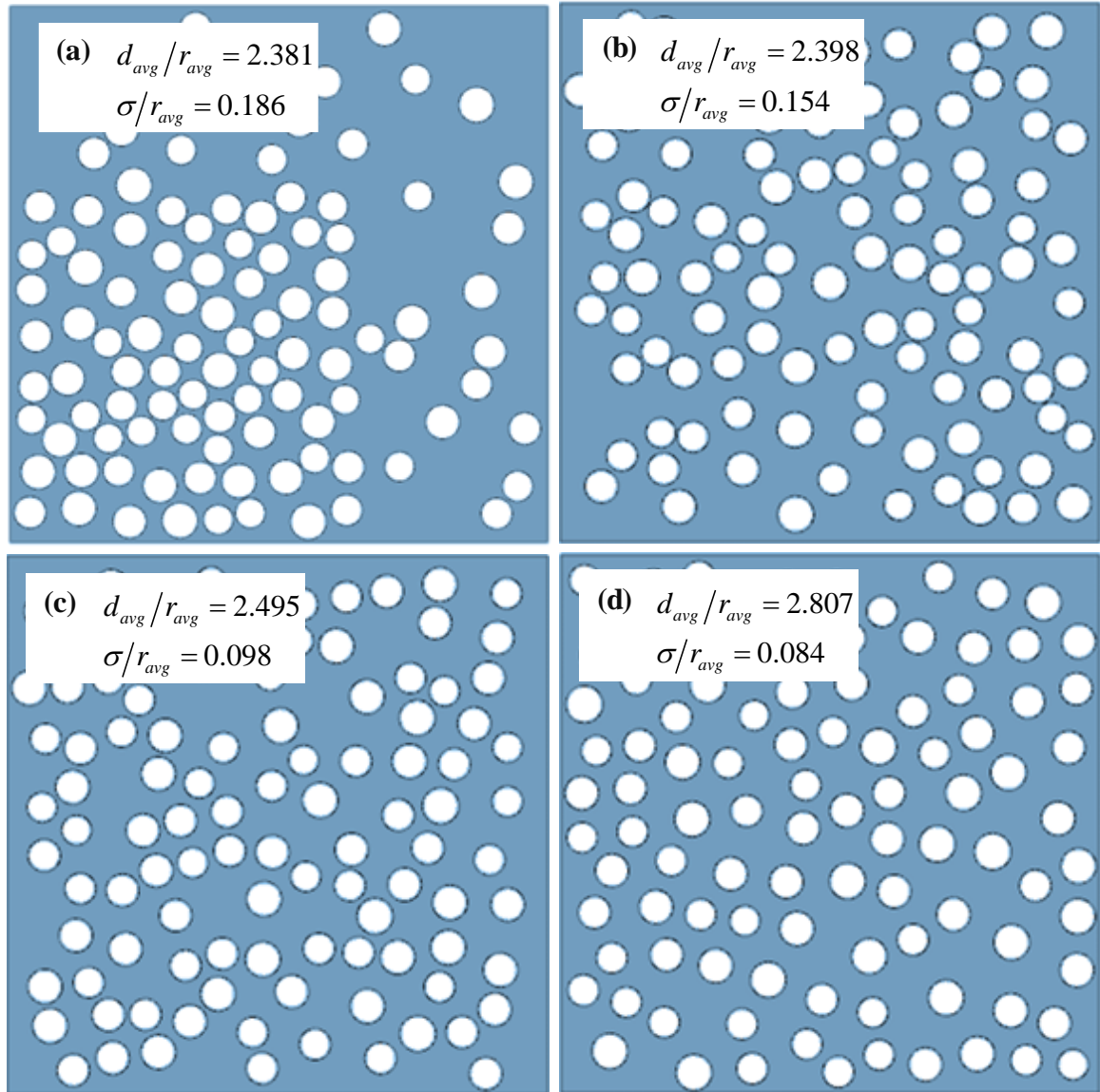


Figure 9.10. Porous membrane RVEs with controlled porosity dispersion.

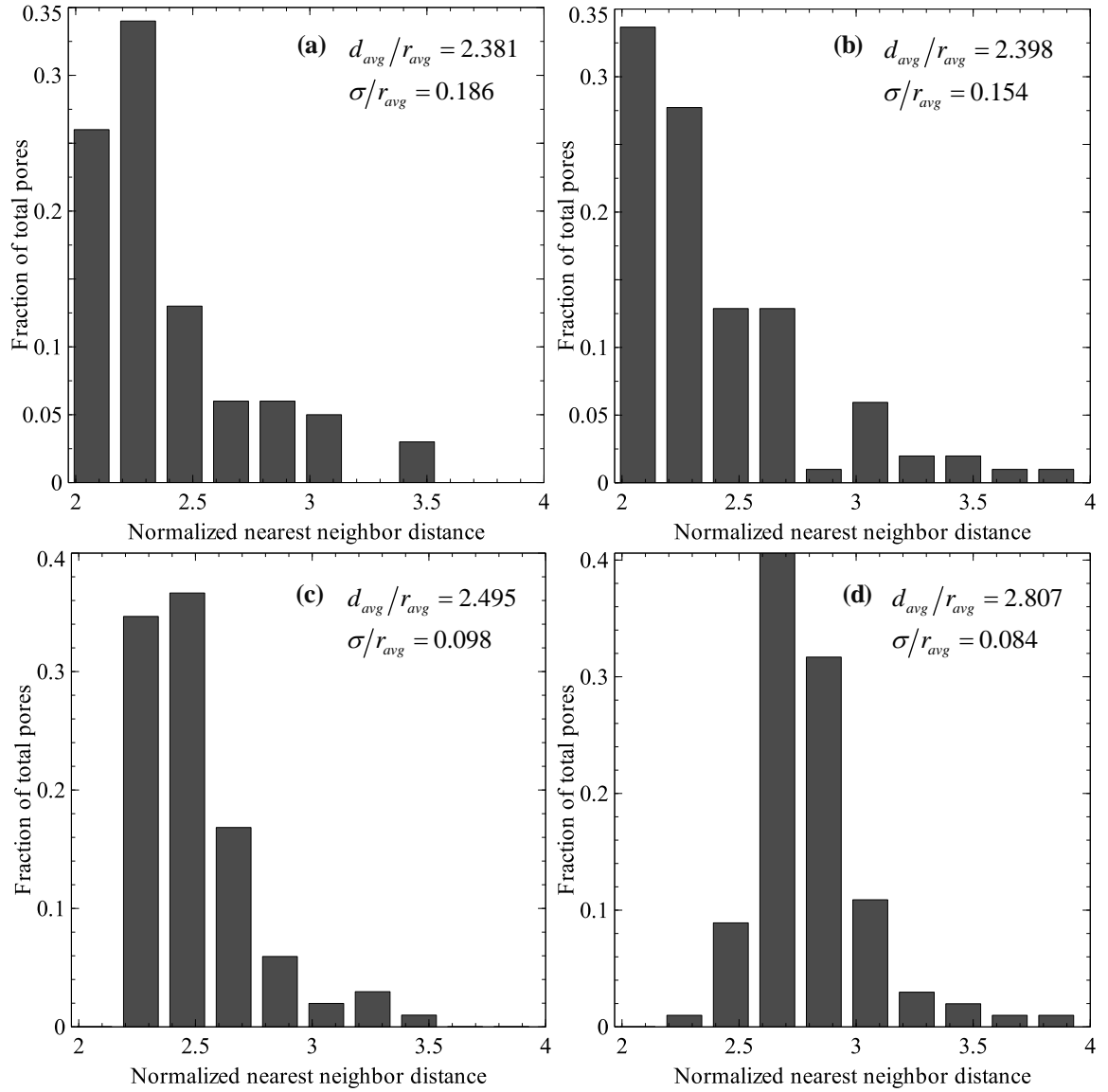


Figure 9.11. Normalized nearest neighbor distances in membrane RVEs with controlled porosity dispersion.

Using the four RVEs, the cases for 30% and 50% stretches were solved using finite element analysis and the permeability-selectivity trade-off curves were generated which are shown in Figure 9.12. The figure shows the significant effect that porosity dispersion quality can have on the performance of stretched membrane. As dispersion quality is improved, the selectivity of stretched membranes improves for same permeability.

The results presented in this section are significant as they can help explain why previous experimental studies with stretched membranes showed that the separation factor increased, stayed the same or even reduced for stretched membranes [208].

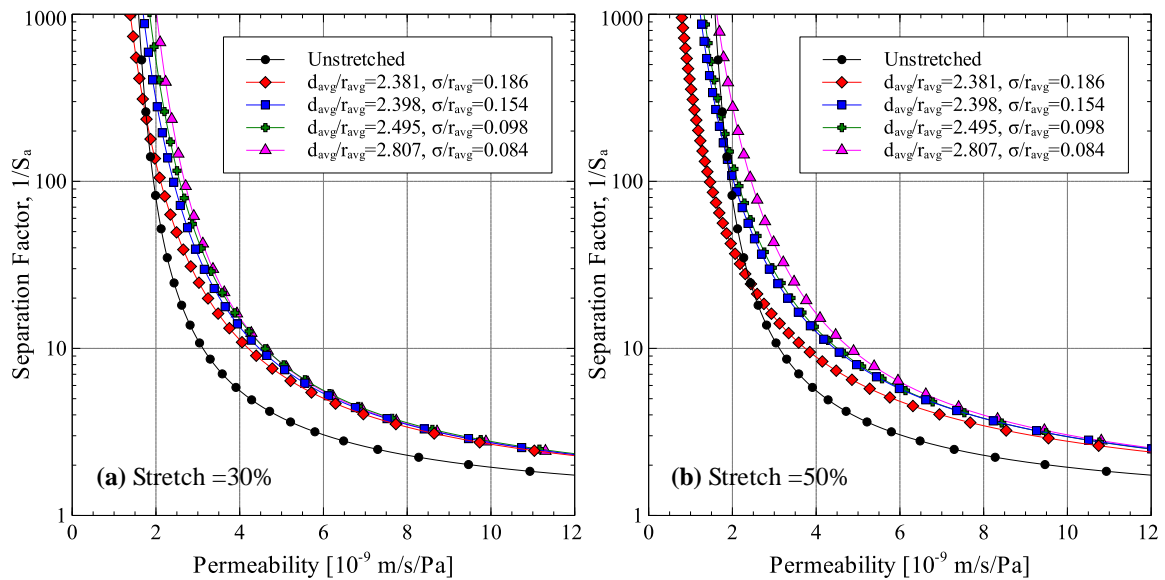


Figure 9.12. Effect of porosity dispersion on permeability-selectivity trade-off for (a) 30% stretch and (b) 50% stretch.

9.6 CONCLUSION

Permeability-selectivity tradeoff analysis provides a simple tool for the analysis and comparison of performance of microfiltration and ultrafiltration membranes. In the current work, a model to carry out permeability-selectivity analysis is formulated that takes into considered the distribution of pore sizes and aspect ratios. Using the model, the effect of pore aspect ratio and size distribution on membrane performance was studied. It was found that increasing pore aspect ratio improves membrane performance while increasing the width of pore size distribution deteriorates the performance.

The effect of uniaxial stretching on membrane performance was also studied by using a finite element model of a porous membrane in conjunction with the permeability-selectivity model. For the porous membrane modeled, improvement was observed for 15% and 30% uniaxial stretching. Further stretching deteriorated the membrane performance. The key factor in the deterioration of performance was found to be the width of the pore size distribution which became larger with stretch. Porosity dispersion was found to play a key role in pore size distribution of stretched membranes. Using the finite element model, it was determined that membranes with well dispersed pores had less size distribution around the average value. This minimized the negative effect of pore size distribution on membrane performance. As a result, membranes with well-dispersed porosity had better performance improvement after stretching.

CHAPTER 10

CONCLUSIONS AND RECOMMENDATIONS

10.1 CONCLUSIONS

The aim of the current work was to develop property estimation and multiscale modeling methodologies for multi-physics problems that are easy to deploy in commercial finite element codes. In this regards, computational tools have been developed for the estimation of thermo-mechanical properties of heterogeneous materials. A multi-scale modeling approach has also been formulated that can utilize homogenization techniques to predict the constitutive response of materials at integration points of finite element models. Applications of the developed tools and methodologies have been shown for various applications such as composites, membranes and coatings.

- For the estimation of mechanical properties of heterogeneous materials, two homogenization methodologies were used. These the computational homogenization and the mean-field homogenization approaches.
 - Since the computational homogenization approach solves a boundary value problem on a microstructural domain, algorithms for the generation of

computational microstructures for heterogeneous materials were formulated and implemented. A methodology to determine the minimum RVE size required for correct property estimation was also presented.

- Application of the computational homogenization approach was shown for metal matrix composites for which elastic and rate-independent elastoplastic properties were determined. The approach was validated against results from literature and experiments carried out in the current work.
- In the current work, the approach of mean-field homogenization has been extended for the application to metal matrix nanocomposites. The novel approach is capable of accurately predicting the elastoplastic behavior of metal matrix nanocomposites as a function of matrix grain size, inclusion particle size, inclusion volume fraction and porosity fraction.
 - The formulated methodology incorporates the effect of Hall-Petch strengthening, Orowan strengthening, dislocation density strengthening, load transfer strengthening and porosity on the elastoplastic response of metal matrix nanocomposites.
 - A metal matrix crystallite size, inclusion particle size and inclusion volume fraction plasticity hardening function for the metal matrix was also formulated and validated.

- A grain growth model for spark-plasma-sintering was also formulated that can estimate the average matrix crystallite size as a function of sintering time, sintering temperature, inclusion size and inclusion volume fraction.
- To estimate the effective thermal conductivity of particulate nanocomposites, the capabilities of existing effective medium theories reported in the literature have been extended to include effects previously missing from these models. These include the ability to include randomly oriented nanometer sized inclusions, the ability to include multiple nanometer sized inclusions and the ability to handle non-uniformly dispersed inclusions.
 - Additional improvements were made to the EMT model specifically for predicting the thermal conductivity of polymer composites with hybrid inclusions. With the improvements, the model was found to accurately capture the effect of varying ratio of inclusions in the hybrid mix.
 - For spark plasma sintered nanocomposites, the effect of crystallite size of matrix material was incorporated into the model using a model for the thermal conductivity of polycrystalline materials. It was found that the errors in model predictions reduced when the thermal conductivity of the matrix was taken as a function of its crystallite size.
- In the present work, three multiscale modeling methodologies and their implementation in Comsol/MATLAB were presented. The multiscale modeling methodologies were used to simulate the response of a particulate composite plate under two types of loading.

- Computational homogenization based algorithm and the hybrid algorithm provided the same solution for the two problems studied. The mean-field homogenization based algorithm provided results which were around 4% higher than the results for computational homogenization.
- Hybridizing the computation homogenization and mean-field homogenization algorithms helped reduce the simulation times significantly. For the uniaxial extension and bending, an improvement of 27% and 46% in computational time was achieved when the hybrid algorithm was used.
- Increasing the number of parallel solutions on the microscale did not significantly improve the computational efficiency of the algorithm. This was due to the limitations of using a single workstation for the simulation in which the number of available processor cores is limited.
- Although the simulation times for the computational homogenization based algorithms was reduced using the hybrid approach, the simulation times were still around two orders of magnitude higher than the mean-field homogenization based multiscale modeling approach.
- A multiscale model of a turbine blade coated with a thermal barrier coating was formulated in the current work and was applied to study the thermo-mechanical performance of the coated blade. Using the multiscale model, the effect of porosity in the top coat on the performance of the blade was studied. From the study conducted, the following conclusions were drawn.

- The increase in porosity in top coat resulted in an increase in the temperature drop across the TBC. The critical part of the blade in terms of high temperatures was found to be the trailing edge of the blade. Stresses and creep strains in the top coat and bond coat showed a strong influence of porosity in the top coat layer while the TGO layer showed no significant effect of it.
- It was also found that during thermal cycling, the porosity in top coat played a very strong role of the stresses developing the TBC system. Using the average stress in the YSZ phase of top coat estimated using the mean-field homogenization scheme, it was found that the top coat will start to crack after 5 thermal cycles. For the three cases of porous top coat, the average stress in YSZ remained lower than the tensile strength of YSZ. Further investigation using microscale FE model of the TBC system is needed in this regard.

10.2 RECOMMENDATIONS FOR FUTURE WORK

The computational tools developed in the current work can be extended in a variety of directions. Below is a list of recommendations for possible future work based on this dissertation.

- The homogenization methodologies formulated in the current work can be extended to include effects present in specific heterogeneous materials. For example, the effect of surface treatment and functionalization of inclusions can be added to the model for effective thermal conductivity.
- The grain growth model for spark-plasma-sintering process presented in Chapter 5 need to be further explored. In the current work, the model was validated against aluminum data. Other materials need to be tested. Additionally, the experimental data used in the current work did not include variation of inclusion particle size. Therefore, model's effectiveness in capturing the effect of inclusion particle size needs to be investigated.
- The multiscale model of turbine blade coated with TBC needs to be coupled with a finite element model for coating deposition in order to take into account residual stresses that develop in the coating during the deposition process.

REFERENCES

- [1] G. Geandier, A. Hazotte, S. Denis, A. Mocellin, E. Maire, Microstructural analysis of alumina chromium composites by X-ray tomography and 3-D finite element simulation of thermal stresses, *Scr. Mater.* 48 (2003) 1219–1224. doi:10.1016/S1359-6462(02)00531-6.
- [2] K. Al-Athel, K. Loeffel, H. Liu, L. Anand, Modeling decohesion of a top-coat from a thermally-growing oxide in a thermal barrier coating, *Surf. Coatings Technol.* 222 (2013) 68–78. doi:10.1016/j.surfcoat.2013.02.005.
- [3] V.G. Kouznetsova, M.G.D. Geers, W. a. M. Brekelmans, Multi-scale second-order computational homogenization of multi-phase materials: a nested finite element solution strategy, *Comput. Methods Appl. Mech. Eng.* 193 (2004) 5525–5550. doi:10.1016/j.cma.2003.12.073.
- [4] V.P. Nguyen, M. Stroeve, L.J. Sluys, An enhanced continuous–discontinuous multiscale method for modeling mode-I cohesive failure in random heterogeneous quasi-brittle materials, *Eng. Fract. Mech.* 79 (2012) 78–102. doi:10.1016/j.engfracmech.2011.10.005.
- [5] P.J. Sánchez, P.J. Blanco, A.E. Huespe, R.A. Feijóo, Failure-Oriented Multi-scale Variational Formulation: micro-structures with nucleation and evolution of softening bands, *Comput. Methods Appl. Mech. Eng.* 257 (2012) Accepted Manuscript. doi:10.1016/j.cma.2012.11.016.
- [6] J.D. Eshelby, The determination of the elastic field of an ellipsoidal inclusion, and related problems, *Proc. R. Soc. Lond. A. Math. Phys. Sci.* 241 (1957) 376–396.
- [7] E. Kröner, Berechnung der elastischen Konstanten des Vielkristalls aus den Konstanten des Einkristalls, *Zeitschrift Für Phys.* 151 (1958) 504–518.
- [8] T. Mori, K. Tanaka, Average stress in matrix and average elastic energy of materials with misfitting inclusions, *Acta Metall.* 21 (1973) 571–574. doi:10.1016/0001-

6160(73)90064-3.

- [9] B. Klusemann, B. Svendsen, Homogenization methods for multi-phase elastic composites : Comparisons and benchmarks, *Tech. Mech.* 30 (2010) 374–386.
- [10] R. Hill, Elastic properties of reinforced solids: some theoretical principles, *J. Mech. Phys. Solids.* 11 (1963) 357–372.
- [11] Z. Shan, A. Gokhale, Representative volume element for non-uniform micro-structure, *Comput. Mater. Sci.* 24 (2002) 361–379. doi:10.1016/S0927-0256(01)00257-9.
- [12] X.L. Chen, Y.J. Liu, Square representative volume elements for evaluating the effective material properties of carbon nanotube-based composites, *Comput. Mater. Sci.* 29 (2004) 1–11. doi:10.1016/S0927-0256(03)00090-9.
- [13] Z. Li, P. Steinmann, RVE-based studies on the coupled effects of void size and void shape on yield behavior and void growth at micron scales, *Int. J. Plast.* 22 (2006) 1195–1216. doi:10.1016/j.ijplas.2005.07.004.
- [14] B.R. Kim, H.K. Lee, An RVE-based micromechanical analysis of fiber-reinforced composites considering fiber size dependency, *Compos. Struct.* 90 (2009) 418–427. doi:10.1016/j.compstruct.2009.04.025.
- [15] M. Stroeve, H. Askes, L.J. Sluys, Numerical determination of representative volumes for granular materials, *Comput. Methods Appl. Mech. Eng.* 193 (2004) 3221–3238. doi:10.1016/j.cma.2003.09.023.
- [16] I.M. Gitman, H. Askes, L.J. Sluys, Representative volume: Existence and size determination, *Eng. Fract. Mech.* 74 (2007) 2518–2534. doi:10.1016/j.engfracmech.2006.12.021.
- [17] Y. Liu, X. Chen, Evaluations of the effective material properties of carbon nanotube-based composites using a nanoscale representative volume element, *Mech. Mater.* 35 (2003) 69–81. doi:10.1016/S0167-6636(02)00200-4.

- [18] P. Raghavan, S. Ghosh, Concurrent multi-scale analysis of elastic composites by a multi-level computational model, *Comput. Methods Appl. Mech. Eng.* 193 (2004) 497–538. doi:10.1016/j.cma.2003.10.007.
- [19] C. Toulemonde, R. Masson, J. El Gharib, Modeling the effective elastic behavior of composites: a mixed Finite Element and homogenisation approach, *Comptes Rendus Mécanique*. 336 (2008) 275–282. doi:10.1016/j.crme.2007.11.024.
- [20] M. Galli, J. Botsis, J. Janczak-Rusch, An elastoplastic three-dimensional homogenization model for particle reinforced composites, *Comput. Mater. Sci.* 41 (2008) 312–321. doi:10.1016/j.commatsci.2007.04.010.
- [21] J.R. Cho, Y.J. Kang, K.Y. Jeong, Y.J. Noh, O.K. Lim, Homogenization and thermoelastic analysis of heterogenous materials with regular and random microstructures, *Compos. Part B Eng.* 43 (2012) 2313–2323. doi:10.1016/j.compositesb.2011.11.074.
- [22] S.S. Vel, A.J. Goupee, Multiscale thermoelastic analysis of random heterogeneous materials Part 1: Microstructure characterization and homogenization of material properties, *Comput. Mater. Sci.* 48 (2010) 22–38. doi:10.1016/j.commatsci.2009.11.015.
- [23] D.V. Griffiths, J. Paiboon, J. Huang, G. a. Fenton, Homogenization of geomaterials containing voids by random fields and finite elements, *Int. J. Solids Struct.* 49 (2012) 2006–2014. doi:10.1016/j.ijsolstr.2012.04.006.
- [24] Y. Dong, D. Bhattacharyya, A simple micromechanical approach to predict mechanical behaviour of polypropylene/organoclay nanocomposites based on representative volume element (RVE), *Comput. Mater. Sci.* 49 (2010) 1–8. doi:10.1016/j.commatsci.2010.03.049.
- [25] F.J. Vernerey, M. Kabiri, An adaptive concurrent multiscale method for microstructured elastic solids, *Comput. Methods Appl. Mech. Eng.* 241–244 (2012) 52–64. doi:10.1016/j.cma.2012.04.021.

- [26] M.G.D. Geers, V.G. Kouznetsova, W. a. M. Brekelmans, Multi-scale computational homogenization: Trends and challenges, *J. Comput. Appl. Math.* 234 (2010) 2175–2182. doi:10.1016/j.cam.2009.08.077.
- [27] M.R. Ayatollahi, S. Shadlou, M.M. Shokrieh, Multiscale modeling for mechanical properties of carbon nanotube reinforced nanocomposites subjected to different types of loading, *Compos. Struct.* 93 (2011) 2250–2259. doi:10.1016/j.compstruct.2011.03.013.
- [28] K.I. Tserpes, P. Papanikos, G. Labeas, S.G. Pantelakis, Multi-scale modeling of tensile behavior of carbon nanotube-reinforced composites, *Theor. Appl. Fract. Mech.* 49 (2008) 51–60. doi:10.1016/j.tafmec.2007.10.004.
- [29] Y. Ni, M.Y.M. Chiang, Prediction of elastic properties of heterogeneous materials with complex microstructures, *J. Mech. Phys. Solids.* 55 (2007) 517–532. doi:10.1016/j.jmps.2006.09.001.
- [30] Y.U. Wang, Y.M.M. Jin, A.G. Khachaturyan, Phase field microelasticity theory and modeling of elastically and structurally inhomogeneous solid, *J. Appl. Phys.* 92 (2002) 1351–1360. doi:10.1063/1.1492859.
- [31] N. Takano, K. Kimura, M. Zako, F. Kubo, Three-dimensional microstructural modeling and homogenization of porous alumina with needle-like pores, *JSME.* 46 (2002) 519–526. <https://sciencelinks.jp/j-east/article/200220/000020022002A0687317.php> (accessed November 30, 2012).
- [32] N. Takano, M. Zako, F. Kubo, K. Kimura, Microstructure-based stress analysis and evaluation for porous ceramics by homogenization method with digital image-based modeling, *Int. J. Solids Struct.* 40 (2003) 1225–1242. doi:10.1016/S0020-7683(02)00642-X.
- [33] M. Galli, J. Cugnoni, J. Botsis, Numerical and statistical estimates of the representative volume element of elastoplastic random composites, *Eur. J. Mech. - A/Solids.* 33 (2012) 31–38. doi:10.1016/j.euromechsol.2011.07.010.

- [34] X. Li, J. Zhang, X. Zhang, Micro-macro homogenization of gradient-enhanced Cosserat media, *Eur. J. Mech. - A/Solids*. 30 (2011) 362–372. doi:10.1016/j.euromechsol.2010.10.008.
- [35] X. Li, Q. Liu, J. Zhang, A micro–macro homogenization approach for discrete particle assembly – Cosserat continuum modeling of granular materials, *Int. J. Solids Struct.* 47 (2010) 291–303. doi:10.1016/j.ijsolstr.2009.09.033.
- [36] F. Fritzen, S. Forest, T. Böhlke, D. Kondo, T. Kanit, Computational homogenization of elasto-plastic porous metals, *Int. J. Plast.* 29 (2012) 102–119. doi:10.1016/j.ijplas.2011.08.005.
- [37] F. Fritzen, S. Forest, D. Kondo, T. Böhlke, Computational homogenization of porous materials of Green type, *Comput. Mech.* (2012). doi:10.1007/s00466-012-0801-z.
- [38] K. Danas, N. Aravas, Numerical modeling of elasto-plastic porous materials with void shape effects at finite deformations, *Compos. Part B Eng.* 43 (2012) 2544–2559. doi:10.1016/j.compositesb.2011.12.011.
- [39] R. Brenner, Computational approach for composite materials with coupled constitutive laws, *Zeitschrift Für Angew. Math. Und Phys.* 61 (2009) 919–927. doi:10.1007/s00033-009-0045-8.
- [40] I. Doghri, a. Ouaar, Homogenization of two-phase elasto-plastic composite materials and structures, *Int. J. Solids Struct.* 40 (2003) 1681–1712. doi:10.1016/S0020-7683(03)00013-1.
- [41] Z. Yuan, J. Fish, Toward realization of computational homogenization in practice, *Int. J. Numer. Methods Eng.* (2008) 361–380. doi:10.1002/nme.
- [42] N. Benseddiq, N. Belayachi, M. Naït Abdelaziz, Multiscale approach to the behaviour and damage of the heterogeneous elastic–viscoplastic materials, *Theor. Appl. Fract. Mech.* 46 (2006) 15–25. doi:10.1016/j.tafmec.2006.05.001.
- [43] G. Haasemann, V. Ulbricht, Numerical evaluation of the viscoelastic and

- viscoplastic behavior of composites, *Tech. Mech.* 30 (2010) 122–135.
http://141.44.1.20/ifme/zeitschrift_tm/2010_Heft1_3/09_Haasemann.pdf (accessed December 17, 2013).
- [44] N. Ohno, K. Ikenoya, D. Okumura, T. Matsuda, Homogenized elastic–viscoplastic behavior of anisotropic open-porous bodies with pore pressure, *Int. J. Solids Struct.* 49 (2012) 2799–2806. doi:10.1016/j.ijsolstr.2012.02.014.
- [45] O. Van Der Sluis, P. Schreurs, H. Meijer, Effective properties of a viscoplastic constitutive model obtained by homogenisation, *Mech. Mater.* 31 (1999) 743–759.
<http://www.sciencedirect.com/science/article/pii/S0167663699000289> (accessed December 17, 2013).
- [46] M. Tsuda, E. Takemura, T. Asada, N. Ohno, T. Igari, Homogenized elastic–viscoplastic behavior of plate-fin structures at high temperatures: Numerical analysis and macroscopic constitutive modeling, *Int. J. Mech. Sci.* 52 (2010) 648–656. doi:10.1016/j.ijmecsci.2009.06.007.
- [47] N. Carrere, F. Feyel, S. Kruch, Multi-scale modelling of silicon carbide reinforced titanium MMCs: Application to advanced compressor design, *Aerosp. Sci. Technol.* 7 (2003) 307–315. doi:10.1016/S1270-9638(03)00028-2.
- [48] F. Feyel, J. Chaboche, FE 2 multiscale approach for modelling the elastoviscoplastic behaviour of long fibre SiC/Ti composite materials, *Comput. Methods Appl. Mech. Eng.* 183 (2000) 309–330.
<http://www.sciencedirect.com/science/article/pii/S0045782599002248> (accessed May 18, 2014).
- [49] F. Feyel, A multilevel finite element method (FE2) to describe the response of highly non-linear structures using generalized continua, *Comput. Methods Appl. Mech. Eng.* 192 (2003) 3233–3244. doi:10.1016/S0045-7825(03)00348-7.
- [50] K. a. Khan, A.H. Muliana, A multi-scale model for coupled heat conduction and deformations of viscoelastic functionally graded materials, *Compos. Part B Eng.* 40

- (2009) 511–521. doi:10.1016/j.compositesb.2009.02.003.
- [51] K. Matou, A. Maniatty, Multiscale modeling of elasto-viscoplastic polycrystals subjected to finite deformations, *Interact. Multiscale Mech.* 2 (2009) 375–396. <http://www.scorec.rpi.edu/REPORTS/2009-22.pdf> (accessed April 15, 2014).
 - [52] O. PIERARD, I. DOGHRI, An enhanced affine formulation and the corresponding numerical algorithms for the mean-field homogenization of elasto-viscoplastic composites, *Int. J. Plast.* 22 (2006) 131–157. doi:10.1016/j.ijplas.2005.04.001.
 - [53] I. Doghri, L. Adam, N. Bilger, Mean-field homogenization of elasto-viscoplastic composites based on a general incrementally affine linearization method, *Int. J. Plast.* 26 (2010) 219–238. doi:10.1016/j.ijplas.2009.06.003.
 - [54] A. Molinari, S. Ahzi, R. Kouddane, On the self-consistent modeling of elastic-plastic behavior of polycrystals, *Mech. Mater.* 26 (1997) 43–62. doi:10.1016/S0167-6636(97)00017-3.
 - [55] S. Mercier, a. Molinari, Homogenization of elastic–viscoplastic heterogeneous materials: Self-consistent and Mori-Tanaka schemes, *Int. J. Plast.* 25 (2009) 1024–1048. doi:10.1016/j.ijplas.2008.08.006.
 - [56] S. Mercier, a Molinari, S. Berbenni, M. Berveiller, Comparison of different homogenization approaches for elastic–viscoplastic materials, *Model. Simul. Mater. Sci. Eng.* 20 (2012) 24004. doi:10.1088/0965-0393/20/2/024004.
 - [57] S. Mercier, N. Jacques, A. Molinari, Validation of an interaction law for the Eshelby inclusion problem in elasto-viscoplasticity, *Int. J. Solids Struct.* 42 (2005) 1923–1941. doi:10.1016/j.ijsolstr.2004.08.016.
 - [58] S. Ghosh, J. Bai, P. Raghavan, Concurrent multi-level model for damage evolution in microstructurally debonding composites, *Mech. Mater.* 39 (2007) 241–266. doi:10.1016/j.mechmat.2006.05.004.
 - [59] B.R. Kim, H.K. Lee, Elastoplastic modeling of circular fiber-reinforced ductile matrix composites considering a finite RVE, *Int. J. Solids Struct.* 47 (2010) 827–

836. doi:10.1016/j.ijsolstr.2009.11.015.

- [60] V.P. Nguyen, O. Lloberas-Valls, M. Stroeve, L.J. Sluys, Homogenization-based multiscale crack modelling: From micro-diffusive damage to macro-cracks, *Comput. Methods Appl. Mech. Eng.* 200 (2011) 1220–1236. doi:10.1016/j.cma.2010.10.013.
- [61] M.G.D. Geers, V.G. Kouznetsova, W.A.M. Brekelmans, Computational Homogenization, in: R. Pippan, P. Gumbsch (Eds.), *Multiscale Model. Plast. Fract. by Means Dislocation Mech.*, 2010: pp. 327–394.
- [62] V. Uthaisangsuk, U. Prahl, W. Bleck, Modelling of damage and failure in multiphase high strength DP and TRIP steels, *Eng. Fract. Mech.* 78 (2011) 469–486. doi:10.1016/j.engfracmech.2010.08.017.
- [63] F. Greco, L. Leonetti, P. Lonetti, A two-scale failure analysis of composite materials in presence of fiber/matrix crack initiation and propagation, *Compos. Struct.* 95 (2013) 582–597. doi:10.1016/j.compstruct.2012.08.035.
- [64] A.J. Goupee, S.S. Vel, Multiscale thermoelastic analysis of random heterogeneous materials Part II: Direct micromechanical failure analysis and multiscale simulations, *Comput. Mater. Sci.* 48 (2010) 39–53. doi:10.1016/j.commatsci.2009.10.004.
- [65] T. Wu, İ. Temizer, P. Wriggers, Computational thermal homogenization of concrete, *Cem. Concr. Compos.* 35 (2013) 59–70. doi:10.1016/j.cemconcomp.2012.08.026.
- [66] V.P. Nguyen, M. Stroeve, L.J. Sluys, Multiscale failure modeling of concrete: Micromechanical modeling, discontinuous homogenization and parallel computations, *Comput. Methods Appl. Mech. Eng.* 201–204 (2012) 139–156. doi:10.1016/j.cma.2011.09.014.
- [67] R. Glüge, M. Weber, A. Bertram, Comparison of spherical and cubical statistical volume elements with respect to convergence , anisotropy , and localization behavior, *Comput. Mater. Sci.* 63 (2012) 91–104.

doi:10.1016/j.commatsci.2012.05.063.

- [68] A. Salahouelhadj, H. Haddadi, Estimation of the size of the RVE for isotropic copper polycrystals by using elastic–plastic finite element homogenisation, *Comput. Mater. Sci.* 48 (2010) 447–455. doi:10.1016/j.commatsci.2009.12.014.
- [69] J. Maxwell, *A Treatise on Electricity and Magnetism*, 2nd ed., Oxford University Press, 1904.
- [70] Lord Rayleigh, On the influence of obstacles arranged in rectangular order upon the properties of a medium, *Philos. Mag. Ser. 5.* 34 (1892) 481–502. doi:10.1080/14786449208620364.
- [71] D.P.H. Hasselman, L.F. Johnson, Effective Thermal Conductivity of Composites with Interfacial Thermal Barrier Resistance, *J. Compos. Mater.* 21 (1987) 508–515. doi:10.1177/002199838702100602.
- [72] Y. Benveniste, Effective thermal conductivity of composites with a thermal contact resistance between the constituents: Nondilute case, *J. Appl. Phys.* 61 (1987) 2840. doi:10.1063/1.337877.
- [73] C.-W. Nan, R. Birringer, D.R. Clarke, H. Gleiter, Effective thermal conductivity of particulate composites with interfacial thermal resistance, *J. Appl. Phys.* 81 (1997) 6692–6699. doi:10.1063/1.365209.
- [74] D.A.G. Bruggeman, Berechnung verschiedener physikalischer Konstanten von heterogenen Substanzen. I. Dielektrizitätskonstanten und Leitfähigkeiten der Mischkörper aus isotropen Substanzen, *Ann. Phys.* 416 (1935) 636–664. doi:10.1002/andp.19354160705.
- [75] A.G. Every, Y. Tzou, D.P.H. Hasselman, R. Raj, The effect of particle size on the thermal conductivity of ZnS/diamond composites, *Acta Metall. Mater.* 40 (1992) 123–129. doi:10.1016/0956-7151(92)90205-S.
- [76] W. Jiajun, Y. Xiao-Su, Effects of interfacial thermal barrier resistance and particle shape and size on the thermal conductivity of AlN/PI composites, *Compos. Sci.*

- Technol. 64 (2004) 1623–1628. doi:10.1016/j.compscitech.2003.11.007.
- [77] A. El Moumen, T. Kanit, A. Imad, H. El Minor, Computational thermal conductivity in porous materials using homogenization techniques: Numerical and statistical approaches, *Comput. Mater. Sci.* 97 (2015) 148–158.
 - [78] W. Tian, R. Yang, Thermal conductivity modeling of compacted nanowire composites, *J. Appl. Phys.* 101 (2007) 22–27. doi:10.1063/1.2653777.
 - [79] M.-S. Jeng, R. Yang, D. Song, G. Chen, Modeling the Thermal Conductivity and Phonon Transport in Nanoparticle Composites Using Monte Carlo Simulation, *J. Heat Transfer.* 130 (2008) 42410. doi:10.1115/1.2818765.
 - [80] H.M. Duong, D. V Papavassiliou, K.J. Mullen, S. Maruyama, Computational modeling of the thermal conductivity of single-walled carbon nanotube-polymer composites., *Nanotechnology.* 19 (2008) 65702. doi:10.1088/0957-4484/19/6/065702.
 - [81] R. Yang, G. Chen, Thermal conductivity modeling of periodic two-dimensional nanocomposites, *Phys. Rev. B - Condens. Matter Mater. Phys.* 69 (2004) 1–10. doi:10.1103/PhysRevB.69.195316.
 - [82] T.Y. Hsieh, J.Y. Yang, Z.C. Hong, Thermal conductivity modeling of compacted type nanocomposites, *J. Appl. Phys.* 106 (2009). doi:10.1063/1.3182803.
 - [83] Y. Xu, G. Li, Strain effect analysis on phonon thermal conductivity of two-dimensional nanocomposites, *J. Appl. Phys.* 106 (2009). doi:10.1063/1.3259383.
 - [84] P. Lee, R. Yang, K. Maute, An Extended Finite Element Method for the Analysis of Submicron Heat Transfer Phenomena, in: *Multiscale Methods Comput. Mech.*, 2011: pp. 195–212. doi:10.1007/978-90-481-9809-2.
 - [85] K. Maute, S. Kreissl, D. Makhija, R. Yang, Topology optimization of heat conduction problems, in: *9th World Congr. Struct. Multidiscip. Optim.*, Shizouka, Japan, 2010: pp. 1–17.

- [86] A. Minnich, G. Chen, Modified effective medium formulation for the thermal conductivity of nanocomposites, *Appl. Phys. Lett.* 91 (2007) 4–7. doi:10.1063/1.2771040.
- [87] J. Ordonez-Miranda, R. Yang, J.J. Alvarado-Gil, On the thermal conductivity of particulate nanocomposites, *Appl. Phys. Lett.* 98 (2011) 2009–2012. doi:10.1063/1.3593387.
- [88] I. Doghri, L. Tinel, Micromechanical modeling and computation of elasto-plastic materials reinforced with distributed-orientation fibers, *Int. J. Plast.* 21 (2005) 1919–1940. doi:10.1016/j.ijplas.2004.09.003.
- [89] V. Phu Nguyen, O. Lloberas-Valls, M. Stroeven, L. Johannes Sluys, On the existence of representative volumes for softening quasi-brittle materials – A failure zone averaging scheme, *Comput. Methods Appl. Mech. Eng.* 199 (2010) 3028–3038. doi:10.1016/j.cma.2010.06.018.
- [90] F. Dinzart, H. Sabar, Homogenization of the viscoelastic heterogeneous materials with multi-coated reinforcements: an internal variables formulation, *Arch. Appl. Mech.* 84 (2014) 715–730. doi:10.1007/s00419-014-0828-z.
- [91] M.I. El Ghezal, Y. Maalej, I. Doghri, Micromechanical models for porous and cellular materials in linear elasticity and viscoelasticity, *Comput. Mater. Sci.* 70 (2013) 51–70. doi:10.1016/j.commatsci.2012.12.021.
- [92] N. Lahellec, P. Suquet, Effective behavior of linear viscoelastic composites: A time-integration approach, *Int. J. Solids Struct.* 44 (2007) 507–529. doi:10.1016/j.ijsolstr.2006.04.038.
- [93] C. Friebel, I. Doghri, V. Legat, General mean-field homogenization schemes for viscoelastic composites containing multiple phases of coated inclusions, *Int. J. Solids Struct.* 43 (2006) 2513–2541. doi:10.1016/j.ijsolstr.2005.06.035.
- [94] O. Pierard, J. LLorca, J. Segurado, I. Doghri, Micromechanics of particle-reinforced elasto-viscoplastic composites: Finite element simulations versus affine

- homogenization, *Int. J. Plast.* 23 (2007) 1041–1060. doi:10.1016/j.ijplas.2006.09.003.
- [95] A. Molinari, Averaging Models for Heterogeneous Viscoplastic and Elastic Viscoplastic Materials, *J. Eng. Mater. Technol.* 124 (2002) 62. doi:10.1115/1.1421052.
- [96] M.G.D. Geers, E.W.C. Coenen, V.G. Kouznetsova, Multi-scale computational homogenization of structured thin sheets, *Model. Simul. Mater. Sci. Eng.* 15 (2007) S393–S404. doi:10.1088/0965-0393/15/4/S06.
- [97] E. Coenen, Computational homogenization for heterogeneous thin sheets, *Int. J. Numer. Methods Eng.* (2010) 1180–1205. doi:10.1002/nme.
- [98] M. Rintoul, S. Torquato, Reconstruction of the Structure of Dispersions, *J. Colloid Interface Sci.* 186 (1997) 467–76. doi:10.1006/jcis.1996.4675.
- [99] B.D. Lubachevsky, F.H. Stillinger, Geometric properties of random disk packings, *J. Stat. Phys.* 60 (1990) 561–583. doi:10.1007/BF01025983.
- [100] B.D. Lubachevsky, F.H. Stillinger, E.N. Pinson, Disks vs. spheres: Contrasting properties of random packings, *J. Stat. Phys.* 64 (1991) 501–524. doi:10.1007/BF01048304.
- [101] E. Ghossein, M. Lévesque, A fully automated numerical tool for a comprehensive validation of homogenization models and its application to spherical particles reinforced composites, *Int. J. Solids Struct.* 49 (2012) 1387–1398. doi:10.1016/j.ijsolstr.2012.02.021.
- [102] S. Patel, R. Vaish, V.S. Chauhan, C. Bowen, Microstructural Finite Element Modeling and Simulation on Al – MgO Composites, *Int. J. Comput. Methods.* 12 (2015) 1550030. doi:10.1142/S0219876215500309.
- [103] A. Asgari, B.F. Rolfe, P.D. Hodgson, Microstructure modeling and prediction of the mechanical properties of advanced high strength steels, *Int. J. Comput. Methods.* 11 (2014) 1344009. doi:10.1142/S021987621344009X.

- [104] Y. Feng, M. Denng, J. Cui, X. Guan, A two-scale finite element analysis of the thermo-elastic effects in composites, *Int. J. Comput. Methods.* 11 (2014) 1350066. doi:10.1142/S0219876213500667.
- [105] O. Pierard, C. Friebel, I. Doghri, Mean-field homogenization of multi-phase thermo-elastic composites: a general framework and its validation, *Compos. Sci. Technol.* 64 (2004) 1587–1603. doi:10.1016/j.compscitech.2003.11.009.
- [106] G.R. Liu, A step-by-step method of rule-of-mixture of fiber- and particle-reinforced composite materials, *Compos. Struct.* 40 (1997) 313–322. doi:10.1016/S0263-8223(98)00033-6.
- [107] Critical values of chi-square distribution, (n.d.). <http://www.itl.nist.gov/div898/handbook/eda/section3/eda3674.htm> (accessed August 11, 2016).
- [108] P. Gudlur, A. Muliana, M. Radovic, The effect of microstructural morphology on the elastic , inelastic , and degradation behaviors of aluminum – alumina composites, *Mech. Res. Commun.* 57 (2014) 49–56. doi:10.1016/j.mechrescom.2014.02.003.
- [109] N. Chawla, Y.-L. Shen, Mechanical Behavior of Particle Reinforced Metal Matrix Composites, *Adv. Eng. Mater.* 3 (2001) 357–370. doi:10.1002/1527-2648(200106)3:6<357::AID-ADEM357>3.0.CO;2-I.
- [110] R. Casati, *Aluminum Matrix Composites Reinforced with Alumina*, Springer, Milano, Italy, 2016. doi:10.1007/978-3-319-27732-5.
- [111] I. Aliyu, N. Saheb, S. Hassan, N. Al-Aqeeli, Microstructure and Properties of Spark Plasma Sintered Aluminum Containing 1 wt.% SiC Nanoparticles, *Metals (Basel).* 5 (2015) 70–83. doi:10.3390/met5010070.
- [112] D.C. Van Aken, P.E. Krajewski, G.M. Vyletel, J.E. Allison, J.W. Jones, Recrystallization and grain growth phenomena in a particle-reinforced aluminum composite, *Metall. Mater. Trans. A.* 26 (1995) 1395–1405. doi:10.1007/BF02647590.

- [113] Y.C. Kang, S.L.I. Chan, Tensile properties of nanometric Al₂O₃ particulate-reinforced aluminum matrix composites, *Mater. Chem. Phys.* 85 (2004) 438–443. doi:10.1016/j.matchemphys.2004.02.002.
- [114] A. Mazahery, M. Ostadshabani, Investigation on mechanical properties of nano-Al₂O₃-reinforced aluminum matrix composites, *J. Compos. Mater.* 45 (2011) 2579–2586. doi:10.1177/0021998311401111.
- [115] A. Mazahery, H. Abdizadeh, H.R. Baharvandi, Development of high-performance A356/nano-Al₂O₃ composites, *Mater. Sci. Eng. A.* 518 (2009) 61–64. doi:10.1016/j.msea.2009.04.014.
- [116] F. Mirza, D. Chen, A Unified Model for the Prediction of Yield Strength in Particulate-Reinforced Metal Matrix Nanocomposites, *Materials (Basel)*. 8 (2015) 5138–5153. doi:10.3390/ma8085138.
- [117] C.S. Goh, J. Wei, L.C. Lee, M. Gupta, Ductility improvement and fatigue studies in Mg-CNT nanocomposites, *Compos. Sci. Technol.* 68 (2008) 1432–1439. doi:10.1016/j.compscitech.2007.10.057.
- [118] Z. Zhang, D. Chen, Consideration of Orowan strengthening effect in particulate-reinforced metal matrix nanocomposites: A model for predicting their yield strength, *Scr. Mater.* 54 (2006) 1321–1326. doi:10.1016/j.scriptamat.2005.12.017.
- [119] F. Shehata, A. Fathy, M. Abdelhameed, S.F. Moustafa, Preparation and properties of Al₂O₃ nanoparticle reinforced copper matrix composites by in situ processing, *Mater. Des.* 30 (2009) 2756–2762. doi:10.1016/j.matdes.2008.10.005.
- [120] N. Saheb, I.K. Aliyu, S.F. Hassan, N. Al-Aqeeli, Matrix structure evolution and nanoreinforcement distribution in mechanically milled and spark plasma sintered Al-SiC nanocomposites, *Materials (Basel)*. 6 (2014) 6748–6767. doi:10.3390/ma7096748.
- [121] S. Kamrani, R. Riedel, S.M. Seyed Reihani, H.J. Kleebe, Effect of Reinforcement Volume Fraction on the Mechanical Properties of Al-SiC Nanocomposites

- Produced by Mechanical Alloying and Consolidation, *J. Compos. Mater.* 44 (2010) 313–326. doi:10.1177/0021998309347570.
- [122] M. Rahimian, N. Ehsani, N. Parvin, H.R. Baharvandi, The effect of particle size, sintering temperature and sintering time on the properties of Al-Al₂O₃ composites, made by powder metallurgy, *J. Mater. Process. Technol.* 209 (2009) 5387–5393. doi:10.1016/j.jmatprotec.2009.04.007.
- [123] Y. Wu, G.Y. Kim, Carbon nanotube reinforced aluminum composite fabricated by semi-solid powder processing, *J. Mater. Process. Technol.* 211 (2011) 1341–1347. doi:10.1016/j.jmatprotec.2011.03.007.
- [124] K. Morsi, A.M.K. Esawi, S. Lanka, A. Sayed, M. Taher, Spark plasma extrusion (SPE) of ball-milled aluminum and carbon nanotube reinforced aluminum composite powders, *Compos. Part A Appl. Sci. Manuf.* 41 (2010) 322–326. doi:10.1016/j.compositesa.2009.09.028.
- [125] H. Choi, J. Shin, B. Min, J. Park, D. Bae, Reinforcing effects of carbon nanotubes in structural aluminum matrix nanocomposites, *J. Mater. Res.* 24 (2011) 2610–2616. doi:10.1557/jmr.2009.0318.
- [126] R. Casati, M. Vedani, Metal Matrix Composites Reinforced by Nano-Particles—A Review, *Metals (Basel)*. 4 (2014) 65–83. doi:10.3390/met4010065.
- [127] E.O. Hall, The Deformation and Ageing of Mild Steel: III Discussion of Results, *Proc. Phys. Soc. Sect. B.* 64 (1951) 747–753. doi:10.1088/0370-1301/64/9/303.
- [128] N.J. Petch, The Cleavage Strength of Polycrystals, *J. Iron Steel Inst.* 174 (1953) 25–28. doi:10.1007/BF01972547.
- [129] A. Sanaty-Zadeh, Comparison between current models for the strength of particulate-reinforced metal matrix nanocomposites with emphasis on consideration of Hall-Petch effect, *Mater. Sci. Eng. A.* 531 (2012) 112–118. doi:10.1016/j.msea.2011.10.043.
- [130] D.J. Dunstan, A.J. Bushby, Grain size dependence of the strength of metals: The

- Hall-Petch effect does not scale as the inverse square root of grain size, *Int. J. Plast.* 53 (2014) 56–65. doi:10.1016/j.ijplas.2013.07.004.
- [131] A.S. Khan, Y.S. Suh, X. Chen, L. Takacs, H. Zhang, Nanocrystalline aluminum and iron: Mechanical behavior at quasi-static and high strain rates, and constitutive modeling, *Int. J. Plast.* 22 (2006) 195–209. doi:10.1016/j.ijplas.2004.07.008.
- [132] A.S. Khan, B. Farrokh, L. Takacs, Effect of grain refinement on mechanical properties of ball-milled bulk aluminum, *Mater. Sci. Eng. A.* 489 (2008) 77–84. doi:10.1016/j.msea.2008.01.045.
- [133] B. Farrokh, A.S. Khan, Grain size, strain rate, and temperature dependence of flow stress in ultra-fine grained and nanocrystalline Cu and Al: Synthesis, experiment, and constitutive modeling, *Int. J. Plast.* 25 (2009) 715–732. doi:10.1016/j.ijplas.2008.08.001.
- [134] N. Saheb, M. Shahzeb Khan, A.S. Hakeem, Effect of Processing on Mechanically Alloyed and Spark Plasma Sintered Al-Al₂O₃ Nanocomposites, *J. Nanomater.* 2015 (2015) 1–13. doi:10.1155/2015/609824.
- [135] Y. Li, A.J. Bushby, D.J. Dunstan, The Hall-Petch effect as a manifestation of the general size effect, arXiv:1507.01223 [Cond-Mat.mtrl-Sci]. (2015) 1–33.
- [136] H.J. Choi, S.W. Lee, J.S. Park, D.H. Bae, Tensile behavior of bulk nanocrystalline aluminum synthesized by hot extrusion of ball-milled powders, *Scr. Mater.* 59 (2008) 1123–1126. doi:10.1016/j.scriptamat.2008.07.030.
- [137] N. Kamikawa, X. Huang, N. Tsuji, N. Hansen, Strengthening mechanisms in nanostructured high-purity aluminium deformed to high strain and annealed, *Acta Mater.* 57 (2009) 4198–4208. doi:10.1016/j.actamat.2009.05.017.
- [138] N. Tsuji, Y. Ito, Y. Saito, Y. Minamino, Strength and ductility of ultrafine grained aluminum and iron produced by ARB and annealing, *Scr. Mater.* 47 (2002) 893–899. doi:10.1016/S1359-6462(02)00282-8.
- [139] C.Y. Yu, P.W. Kao, C.P. Chang, Transition of tensile deformation behaviors in

- ultrafine-grained aluminum, *Acta Mater.* 53 (2005) 4019–4028. doi:10.1016/j.actamat.2005.05.005.
- [140] D. Hull, An introduction to composite materials, Igarss 2014. (2014) 1–5. doi:10.1007/s13398-014-0173-7.2.
- [141] K.R. Phaneesh, A. Bhat, P. Mukherjee, K.T. Kashyap, On the Zener limit of grain growth through 2D Monte Carlo simulation, *Comput. Mater. Sci.* 58 (2012) 188–191. doi:10.1016/j.commatsci.2012.02.013.
- [142] G.N. Hassold, E. Holm, Effects of particle size on inhibited grain growth, *Scr Met. Mater.* 24 (1990) 11–13. <http://en.scientificcommons.org/854714%5Cnpapers2://publication/uuid/D1AD592A-FB73-4124-869B-8C758E4B0D74>.
- [143] Suk-Joong L.Kang, Sintering Densification, Grain Growth, and Microstructure, 2005. doi:<http://dx.doi.org/10.1016/B978-075066385-4/50009-1>.
- [144] F. Zhou, J. Lee, S. Dallek, E.J. Lavernia, High grain size stability of nanocrystalline Al prepared by mechanical attrition, *J. Mater. Res.* 16 (2011) 3451–3458. doi:10.1557/JMR.2001.0474.
- [145] J. Ye, L. Ajdelsztajn, J.M. Schoenung, Bulk nanocrystalline aluminum 5083 alloy fabricated by a novel technique: Cryomilling and spark plasma sintering, *Metall. Mater. Trans. A Phys. Metall. Mater. Sci.* 37 (2006) 2569–2579. doi:10.1007/BF02586229.
- [146] N. Chawla, Y.-L. Shen, Mechanical Behavior of Particle Reinforced Metal Matrix Composites, *Adv. Eng. Mater.* 3 (2001) 357–370. doi:10.1002/1527-2648(200106)3:6<357::AID-ADEM357>3.3.CO;2-9.
- [147] M.A. Muñoz-Morris, C.G. Oca, D.G. Morris, An analysis of strengthening mechanisms in a mechanically alloyed, oxide dispersion strengthened iron aluminide intermetallic, *Acta Mater.* 50 (2002) 2825–2836. doi:10.1016/S1359-6454(02)00101-5.

- [148] G. Forsythe, M. Malcolm, C. Moler, *Computer Methods for Mathematical Computations*, Prentice-Hall, New Jersey, 1977.
- [149] J.C. Lagarias, J.A. Reeds, M.H. Wright, P.E. Wright, Convergence Properties of the Nelder--Mead Simplex Method in Low Dimensions, *SIAM J. Optim.* 9 (1998) 112–147. doi:10.1137/S1052623496303470.
- [150] G. Chen, Particularities of heat conduction in nanostructures, *J. Nanoparticle Res.* 2 (2000) 199–204. doi:10.1023/A:1010003718481.
- [151] R. Prasher, P.E. Phelan, P. Bhattacharya, Effect of Aggregation Kinetics on the Thermal Conductivity of Nanoscale Colloidal Solutions (Nanofluid), *Nano Lett.* 6 (2006) 1529–1534. doi:10.1021/nl060992s.
- [152] R. Prasher, W. Evans, P. Meakin, J. Fish, P. Phelan, P. Keblinski, Effect of aggregation on thermal conduction in colloidal nanofluids, *Appl. Phys. Lett.* 89 (2006) 88–90. doi:10.1063/1.2360229.
- [153] W. Evans, R. Prasher, J. Fish, P. Meakin, P. Phelan, P. Keblinski, Effect of aggregation and interfacial thermal resistance on thermal conductivity of nanocomposites and colloidal nanofluids, *Int. J. Heat Mass Transf.* 51 (2008) 1431–1438. doi:10.1016/j.ijheatmasstransfer.2007.10.017.
- [154] X. Huang, X. Huai, S. Liang, X. Wang, Thermal transport in Si/Ge nanocomposites, *J. Phys. D: Appl. Phys.* 42 (2009) 95416. doi:10.1088/0022-3727/42/9/095416.
- [155] C.-W. Nan, Physics of inhomogeneous inorganic materials, *Prog. Mater. Sci.* 37 (1993) 1–116. doi:10.1016/0079-6425(93)90004-5.
- [156] R. Barea, M. Belmonte, M.I. Osendi, P. Miranzo, Thermal conductivity of Al₂O₃/SiC platelet composites, *J. Eur. Ceram. Soc.* 23 (2003) 1773–1778. doi:10.1016/S0955-2219(02)00449-1.
- [157] R. Sivakumar, S. Guo, T. Nishimura, Y. Kagawa, Thermal conductivity in multi-wall carbon nanotube/silica-based nanocomposites, *Scr. Mater.* 56 (2007) 265–268. doi:10.1016/j.scriptamat.2006.10.025.

- [158] A. a Balandin, Thermal properties of graphene and nanostructured carbon materials., *Nat. Mater.* 10 (2011) 569–581. doi:10.1038/nmat3064.
- [159] C.-W. Nan, G. Liu, Y. Lin, M. Li, Interface effect on thermal conductivity of carbon nanotube composites, *Appl. Phys. Lett.* 85 (2004) 3549–3551. doi:doi:10.1063/1.1808874.
- [160] L. Chen, Y.-Y. Sun, J. Lin, X.-Z. Du, G.-S. Wei, S.-J. He, et al., Modeling and analysis of synergistic effect in thermal conductivity enhancement of polymer composites with hybrid filler, *Int. J. Heat Mass Transf.* 81 (2015) 457–464. doi:10.1016/j.ijheatmasstransfer.2014.10.051.
- [161] K. Chu, W. Li, C. Jia, F. Tang, Thermal conductivity of composites with hybrid carbon nanotubes and graphene nanoplatelets, *Appl. Phys. Lett.* 101 (2012) 211903. doi:10.1063/1.4767899.
- [162] A. Yu, P. Ramesh, X. Sun, E. Bekyarova, M.E. Itkis, R.C. Haddon, Enhanced thermal conductivity in a hybrid graphite nanoplatelet - Carbon nanotube filler for epoxy composites, *Adv. Mater.* 20 (2008) 4740–4744. doi:10.1002/adma.200800401.
- [163] N.K. Mahanta, M.R. Loos, I. Manas Zloczower, A.R. Abramson, Graphite–graphene hybrid filler system for high thermal conductivity of epoxy composites, *J. Mater. Res.* 30 (2015) 959–966. doi:10.1557/jmr.2015.68.
- [164] S.Y. Yang, W.N. Lin, Y.L. Huang, H.W. Tien, J.Y. Wang, C.C.M. Ma, et al., Synergetic effects of graphene platelets and carbon nanotubes on the mechanical and thermal properties of epoxy composites, *Carbon N. Y.* 49 (2011) 793–803. doi:10.1016/j.carbon.2010.10.014.
- [165] H. Yan, Y. Tang, J. Su, X. Yang, Enhanced thermal-mechanical properties of polymer composites with hybrid boron nitride nanofillers, *Appl. Phys. A Mater. Sci. Process.* 114 (2014) 331–337. doi:10.1007/s00339-013-8149-6.
- [166] J. Wu, H. Zhang, Y. Zhang, X. Wang, Mechanical and thermal properties of carbon

- nanotube/aluminum composites consolidated by spark plasma sintering, *Mater. Des.* 41 (2012) 344–348. doi:10.1016/j.matdes.2012.05.014.
- [167] K. Ahmad, P. Wei, C. Wan, Thermal conductivities of alumina-based multiwall carbon nanotube ceramic composites, *J. Mater. Sci.* 49 (2014) 6048–6055. doi:10.1007/s10853-014-8327-8.
- [168] C.-W. Nan, R. Birringer, Determining the Kapitza resistance and the thermal conductivity of polycrystals: A simple model, *Phys. Rev. B.* 57 (1998) 8264–8268. doi:10.1103/PhysRevB.57.8264.
- [169] M. Singh, K.K. Hlabana, S. Singhal, K. Devlal, Grain-size effects on the thermal conductivity of nanosolids, *J. Taibah Univ. Sci.* 10 (2015) 375–380. doi:10.1016/j.jtusci.2015.04.006.
- [170] S. Wang, Thermal Conductivity of Nanocrystalline Nickel by Thermal Conductivity of Nanocrystalline Nickel, University of Toronto, 2011.
- [171] H.-S. Yang, J.A. Eastman, L.J. Thompson, G.-R. Bai, Grain-Size-Dependent Thermal Transport Properties in Nanocrystalline Yttria-Stabilized Zirconia, *Mat. Res. Soc. Symp. Proc.* 703 (2002) V4.7.1-6.
- [172] H.S. Yang, G.R. Bai, L.J. Thompson, J.A. Eastman, Interfacial thermal resistance in nanocrystalline yttria-stabilized zirconia, *Acta Mater.* 50 (2002) 2309–2317. doi:10.1016/S1359-6454(02)00057-5.
- [173] Z. Wang, J.E. Alaniz, W. Jang, J.E. Garay, C. Dames, Thermal conductivity of nanocrystalline silicon: Importance of grain size and frequency-dependent mean free paths, *Nano Lett.* 11 (2011) 2206–2213. doi:10.1021/nl1045395.
- [174] H. Dong, B. Wen, R. Melnik, Relative importance of grain boundaries and size effects in thermal conductivity of nanocrystalline materials., *Sci. Rep.* 4 (2014) 7037. doi:10.1038/srep07037.
- [175] C.-F. Chen, M.E. Perisse, A.F. Ramirez, N.P. Padture, Effect of grain boundary phase on the thermal conductivity of aluminium nitride ceramics, *J. Mater. Sci.* 29

(1994) 1595–1600.

- [176] R. Roscoe, No Title, *Brit. J. Appl. Phys.* 3 (1952) 267. <http://stacks.iop.org/0508-3443/1/i=11/a=303>.
- [177] D.. Ward, R.. Arnell, Finite element modelling of stress development during deposition of ion assisted coatings, *Thin Solid Films*. 420–421 (2002) 269–274. doi:10.1016/S0040-6090(02)00934-3.
- [178] S. Asghari, M. Salimi, Finite element simulation of thermal barrier coating performance under thermal cycling, *Surf. Coatings Technol.* 205 (2010) 2042–2050. doi:10.1016/j.surfcoat.2010.08.099.
- [179] J. Haider, M. Rahman, B. Corcoran, M.S.J. Hashmi, Simulation of thermal stress in magnetron sputtered thin coating by finite element analysis, *J. Mater. Process. Technol.* 168 (2005) 36–41. doi:10.1016/j.jmatprotec.2004.09.093.
- [180] A.M. Limarga, R. Vaßen, D.R. Clarke, Stress Distributions in Plasma-Sprayed Thermal Barrier Coatings Under Thermal Cycling in a Temperature Gradient, *J. Appl. Mech.* 78 (2011) 11003. doi:10.1115/1.4002209.
- [181] H. Bhatnagar, S. Ghosh, M.E. Walter, A parametric study of damage initiation and propagation in EB-PVD thermal barrier coatings, *Mech. Mater.* 42 (2010) 96–107. doi:10.1016/j.mechmat.2009.09.004.
- [182] H. Bhatnagar, S. Ghosh, M.E. Walter, Parametric studies of failure mechanisms in elastic EB-PVD thermal barrier coatings using FEM, *Int. J. Solids Struct.* 43 (2006) 4384–4406. doi:10.1016/j.ijsolstr.2005.07.037.
- [183] K. Bobzin, N. Bagcivan, D. Parkot, T. Kashko, G. Laschet, J. Scheele, Influence of the Definition of the Representative Volume Element on Effective Thermoelastic Properties of Thermal Barrier Coatings with Random Microstructure, *J. Therm. Spray Technol.* 18 (2009) 988–995. doi:10.1007/s11666-009-9351-0.
- [184] L. Yang, Q.X. Liu, Y.C. Zhou, W.G. Mao, C. Lu, Finite Element Simulation on Thermal Fatigue of a Turbine Blade with Thermal Barrier Coatings, *J. Mater. Sci.*

- Technol. 30 (2014) 371–380. doi:10.1016/j.jmst.2013.11.005.
- [185] W. Wang, J. Gao, X. Shi, L. Xu, Cooling performance analysis of steam cooled gas turbine nozzle guide vane, *Int. J. Heat Mass Transf.* 62 (2013) 668–679. doi:10.1016/j.ijheatmasstransfer.2013.02.080.
- [186] J.H. Liu, Y.B. Liu, X. He, L. Liu, Study on TBCs insulation characteristics of a turbine blade under serving conditions, *Case Stud. Therm. Eng.* 8 (2016) 250–259. doi:10.1016/j.csite.2016.08.004.
- [187] V. Kouznetsova, An approach to micro-macro modeling of heterogeneous materials, *Comput. Mech.* 27 (2001) 37–48. <http://link.springer.com/article/10.1007/s004660000212> (accessed June 5, 2013).
- [188] L. Wang, D.C. Li, J.S. Yang, F. Shao, X.H. Zhong, H.Y. Zhao, et al., Modeling of thermal properties and failure of thermal barrier coatings with the use of finite element methods: A review, *J. Eur. Ceram. Soc.* 36 (2016) 1313–1331. doi:10.1016/j.jeurceramsoc.2015.12.038.
- [189] L. Chen, L. Yueming, Interface stress evolution considering the combined creep–plastic behavior in thermal barrier coatings, *Mater. Des.* 89 (2016) 245–254. doi:10.1016/j.matdes.2015.09.146.
- [190] M. Ranjbar-Far, J. Absi, G. Mariaux, F. Dubois, Simulation of the effect of material properties and interface roughness on the stress distribution in thermal barrier coatings using finite element method, *Mater. Des.* 31 (2010) 772–781. doi:10.1016/j.matdes.2009.08.005.
- [191] J. Rösler, M. Bäker, M. Volgmann, Stress state and failure mechanisms of thermal barrier coatings: Role of creep in thermally grown oxide, *Acta Mater.* 49 (2001) 3659–3670. doi:10.1016/S1359-6454(01)00283-X.
- [192] M.U. Siddiqui, A.F.M. Arif, Generalized Effective Medium Theory for Particulate Nanocomposite Materials, *Materials (Basel)*. 9 (2016) 694. doi:10.3390/ma9080694.

- [193] K.W. Schlichting, N.P. Padture, P.G. Klemens, Thermal conductivity of dense and porous yttria-stabilized zirconia, *J. Mater. Sci.* 36 (2001) 3003–3010. doi:10.1023/A:1017970924312.
- [194] W.G. Mao, Y.C. Zhou, L. Yang, X.H. Yu, Modeling of residual stresses variation with thermal cycling in thermal barrier coatings, *Mech. Mater.* 38 (2006) 1118–1127. doi:10.1016/j.mechmat.2006.01.002.
- [195] K. Suzuki, T. Shobu, Internal Stress in EB-PVD Thermal Barrier Coating under Heat Cycle, *Mater. Sci. Forum.* 638–642 (2010) 906–911. doi:10.4028/www.scientific.net/MSF.638-642.906.
- [196] Etching the Tracks in a Track-etched Membrane Filter / Sterlitech Blog, (n.d.). <http://www.sterlitech.com/blog/2013/07/29/etching-the-tracks-in-a-polycarbonate-track-etched-membrane-filter/> (accessed April 27, 2016).
- [197] A. Mehta, A.L. Zydney, Permeability and selectivity analysis for ultrafiltration membranes, *J. Memb. Sci.* 249 (2005) 245–249. doi:10.1016/j.memsci.2004.09.040.
- [198] Y.S. Polyakov, A.L. Zydney, Ultrafiltration membrane performance: Effects of pore blockage/constriction, *J. Memb. Sci.* 434 (2013) 106–120. doi:10.1016/j.memsci.2013.01.052.
- [199] C. Ho, A. Zydney, A Combined Pore Blockage and Cake Filtration Model for Protein Fouling during Microfiltration., *J. Colloid Interface Sci.* 232 (2000) 389–399. doi:10.1006/jcis.2000.7231.
- [200] G. Bolton, D. LaCasse, R. Kuriyel, Combined models of membrane fouling: Development and application to microfiltration and ultrafiltration of biological fluids, *J. Memb. Sci.* 277 (2006) 75–84. doi:10.1016/j.memsci.2004.12.053.
- [201] C. Duclos-Orsello, W. Li, C.C. Ho, A three mechanism model to describe fouling of microfiltration membranes, *J. Memb. Sci.* 280 (2006) 856–866. doi:10.1016/j.memsci.2006.03.005.

- [202] S. Mochizuki, A.L. Zydney, Theoretical analysis of pore size distribution effects on membrane transport, *J. Memb. Sci.* 82 (1993) 211.
- [203] P.L. Hanks, C.A. Forscher, D.R. Lloyd, Sieve mechanism estimations for microfiltration membranes with elliptical pores, *J. Memb. Sci.* 322 (2008) 91–97. doi:10.1016/j.memsci.2008.05.031.
- [204] D.M. Kanani, W.H. Fissell, S. Roy, A. Dubnisheva, A. Fleischman, A.L. Zydney, Permeability-selectivity analysis for ultrafiltration: Effect of pore geometry, *J. Memb. Sci.* 349 (2010) 405–410. doi:10.1016/j.memsci.2009.12.003.
- [205] T. Knoell, J. Safarik, T. Cormack, R. Riley, S.W. Lin, H. Ridgway, Biofouling potentials of microporous polysulfone membranes containing a sulfonated polyether-ethersulfone/polyethersulfone block copolymer: Correlation of membrane surface properties with bacterial attachment, *J. Memb. Sci.* 157 (1999) 117–138. doi:10.1016/S0376-7388(98)00365-2.
- [206] J.A. Morehouse, The effect of uni-axial stretching on microporous phase separation membrane, University of Texas at Austin, 2006.
- [207] J.A. Morehouse, L.S. Worrel, D.L. Taylor, D.R. Lloyd, B.D. Freeman, D.F. Lawler, The effect of uni-axial orientation on macroporous membrane structure, *J. Porous Mater.* 13 (2006) 61–72. doi:10.1007/s10934-006-5491-5.
- [208] L.S. Worrel, Modification of Track-etched Membrane Structure and Performance via Uniaxial Stretching, The University of Texas at Austin, 2005.
- [209] L. ZEMAN, M. WALES, Polymer Solute Rejection by Ultrafiltration Membranes, in: A.F. Turbak (Ed.), *Synth. Membr. Vol. II*, AMERICAN CHEMICAL SOCIETY, WASHINGTON, D. C., 2009: pp. 411–434. doi:10.1021/bk-1981-0154.
- [210] P.L. Hanks, K.J. Kaczorowski, E.B. Becker, D.R. Lloyd, Modeling of uni-axial stretching of track-etch membranes, *J. Memb. Sci.* 305 (2007) 196–202. doi:10.1016/j.memsci.2007.08.003.

VITAE

Name: Muhammad Usama Siddiqui
Date of Birth: August 9, 1985
Present Address: KFUPM P. O. Box 8119, King Fahd University of Petroleum and Mineral, Dhahran-31261, Saudi Arabia.
Permanent Address: H. No. 129/3, Street 22, Model Colony, Karachi-75100, Pakistan.
Email Address: musiddiqui@kfupm.edu.sa
musiddiqui@gmail.com

Educational Qualification:

M.S (Mechanical Engineering)

January, 2012

King Fahd University of Petroleum & Minerals,

Dhahran, Saudi Arabia.

B.E. (Mechanical Engineering)

June, 2008

National University of Sciences & Technology,

Karachi, Pakistan.

Publications

Journal Papers

1. **Siddiqui, Muhammad Usama** and Abul Fazal M. Arif. 2016. "Generalized Effective Medium Theory for Particulate Nanocomposite Materials." *Materials* 9(8):694.
2. **Siddiqui, M. U.** and Abul Fazal M. Arif. 2016. "A Computational Approach for the Constitutive Modeling of Elastoplastic Behavior of Metal Matrix Composites". *International Journal of Computational Methods* 14(2): 1750058.

3. **Siddiqui, Muhammad Usama**, Abul Arif, and Salem Bashmal. 2016. "Permeability-Selectivity Analysis of Microfiltration and Ultrafiltration Membranes: Effect of Pore Size and Shape Distribution and Membrane Stretching." *Membranes* 6(3):40.
4. Nouari Saheb, Najam Ul Qadir, **Muhammad Usama Siddiqui**, Abul Fazal Muhammad Arif, Syed Sohail Akhtar and Nasser Al-Aqeeli. 2014. "Characterization of Nanoreinforcement Dispersion in Inorganic Nanocomposites: A Review." *Materials* 7:4148–81.

Conference Proceedings

1. **Siddiqui, M. U.** and A. F. M. Arif. 2014. "Computational Homogenization of Metal Matrix Composites." in *Proceedings of the 25th CANCAM*. London, Ontario, Canada.
2. **Siddiqui, M. U.** and A. F. M. Arif. 2016. "Estimation of Thermal Conductivity of Nanocomposites with Non-Uniformly Distributed Inclusions." in *24th International Congress of Theoretical and Applied Mechanics (ICTAM 2016)*. Montréal, Québec, Canada.
3. Akhtar, S. S., A. Bin Ali, **M. U. Siddiqui**, A. F. M. Arif, and Amir Al-Ahmad. 2016. "Development of Graphene-Filled Polymer Nanocomposites for Enhanced Thermal Conductivity." in *3rd International Conference on Structural Nano Composites (NANOSTRUC 2016)*. Aberdeen, Scotland.
4. Akhtar, S. S., A. F. M. Arif, **M. U. Siddiqui**, H. K. R. Chishti, and L. T. Kareem. 2016. "Computational Design and Development of Alumina-Nickel Droplet Composites." in *Proceedings of the ASME 2016 International Mechanical Engineering Congress & Exposition*. Phoenix, AZ, USA.